

A STUDY OF VERTICAL TURBULENT FILM
BOILING AND INTERFACIAL EFFECTS

A Dissertation
Presented to
THE FACULTY OF THE DEPARTMENT OF CHEMICAL ENGINEERING
UNIVERSITY OF HOUSTON

In Partial Fulfillment
of the Requirements for the Degree
Doctor of Philosophy

by
Glenn Coury
August, 1968

477751

Acknowledgements

I would like to express my appreciation for financial support provided by:

The United States Department of Interior, Office of Saline Water,
under Grant No. 14-01-001-667;

The National Aeronautics and Space Agency, under
Institutional Grant No. 44-005-02; and

The National Science Foundation.

In addition, my gratitude must be extended to those whose support and assistance were so valuable to me. Moye Wicks III and Affonso da Silva Telles created the intellectual atmosphere necessary for advanced studies. At critical stages in the experimental work, Jim Bennett turned a temperamental boiler into a leak-free and dependable piece of equipment, and John Cole ferreted out and eliminated the seemingly ubiquitous sources of electronic noise. I would like to especially thank Professor A. E. Dukler for his guidance and friendship during the arduous years of this research.

This dissertation is dedicated to

Anny, Clifford and Rina

A STUDY OF VERTICAL TURBULENT FILM
BOILING AND INTERFACIAL EFFECTS

Abstract of a Dissertation

Presented to

THE FACULTY OF THE DEPARTMENT OF CHEMICAL ENGINEERING
UNIVERSITY OF HOUSTON

In Partial Fulfillment
of the Requirements for the Degree
Doctor of Philosophy

by

Glenn Coury

August, 1968

Abstract

Theoretical and experimental studies were made of vertical, turbulent film boiling. The physical process is characterized by vapor moving within a thin, continuous vapor film next to a heated wall under the influence of buoyancy and pressure forces. Liquid in the bulk phase is separated from the heater wall by the vapor layer, but interfacial waves strongly influence the momentum and energy transport processes.

It was shown that this complex process could be modeled mathematically by a two step analysis. First, a quasi-steady state model led to predictions of the heat transfer rates at any instant based on the velocity and temperature profiles that exist at that instant. The results of the quasi-steady state solution were then applied to the unsteady state condition, which is characterized by interfacial waves and a continually changing vapor film thickness, to determine the heat transfer rates at each instant of time. These results were averaged over time and space to give local and overall heat transfer rates expressed in dimensionless form. The analysis considers the effects of both the interfacial velocity and the interfacial roughness. The theory correlated data taken from systems where large waves were encountered and from relatively wave-free systems.

Experimental measurements were made of the instantaneous, local surface heat flux by means of a low mass, surface thermocouple and a heat meter. Interfacial waves were found to be so large under some conditions as to cause occasional liquid-solid contact. Spectral analysis showed that the surface heat flux variations were random and caused by interfacial activity, and that the spectrum of these variations covered a broad frequency range from about 10 to 100 cps.

TABLE OF CONTENTS

CHAPTER	PAGE
I. Introduction	1
II. A Review of Previous Work	9
A. Theoretical Studies of Film Boiling	9
B. Previous Experimental Studies	14
C. Some Aspects of the Literature on Waves	21
III. Theoretical Development - Quasi-Steady State Model	33
A. The Physical Model	33
B. The Transport Equations	37
C. The Eddy Diffusivities	40
1. Smooth Tube Eddy Viscosity	40
2. Rough Tube Eddy Viscosity	42
3. Eddy Conductivity	44
D. Integration of the Transport Equations	44
1. Division of the Flow Field into a Rough and a Smooth Side	44
2. Formulation of the Separate Equations	49
E. The Matching Procedure	72
1. Matching for Momentum Transport	73
2. Matching for Energy Transport	75
F. The Interfacial Velocity	79
G. Evaluation of the Pressure Drop	86
H. The Effects of Radiant Heat Transfer	88
I. Application of the Theory to Design	89

CHAPTER	PAGE
1. Constant Wall Temperature	90
2. Constant Heat Flux	97
J. The Average Vapor Temperature	99
K. Summary of the Quasi-Steady State Model	101
IV. Theoretical Development - The Effect of Large Amplitude Waves	102
A. The Complete Equations of Motion	102
B. Correction of the Steady State Theory	108
C. The Effect of Wave Shape	110
D. Evaluation of the Unsteady- State Model	116
E. Theoretical Calculation of the Wave Amplitude	119
F. Stability of Film Boiling	120
V. Experimental Equipment and Procedure	124
A. The Boiler Construction	124
B. The Overall Flow System	129
C. Time Average Measurements	130
D. Instantaneous Surface Temperature Measurements	133
E. The Heat Meter	137
F. The Wave Form Analyzer	141
G. Measurements of the Interfacial Structure	142
VI. Evaluation of the Data and the Theories	159
A. Time-Average Local Measurements	159
B. Instantaneous Local Measurements	190
C. Spectral Densities and Average Values of the Fluctuations	222

CHAPTER	PAGE
D. Wave Shape and Amplitude	236
1. A Sinusoidal Interface	236
2. A Square-Pulse Type Interfacial Wave	249
3. Application of the Large Wave Corrections	252
E. Liquid - Solid Contact	253
1. Experimental Evidence	253
2. Theory of Hamill and Bankoff	256
3. Theory of Bankoff and Mehra	258
4. Other Considerations	259
F. Measurements of Interfacial Characteristics	260
G. Theoretical Time Average Characteristics of the Vapor Film	267
H. Evaluation of Other Work from the Literature	277
1. The Data and Theory of Dougall and Rohsenow	279
2. The Data of Class et al	283
3. The Theory of Hsu	284
VII. Conclusions and Recommendations	290
APPENDIGES	
A. Forced Convection Film Boiling in a Vertical Conduit with Laminar Flow of Both Phases	292
B. The Nature of the Roughness Parameter	300
C. True Average Vapor Space Temperature	304
D. Theory and Construction of the Heat Meter	309
A. Simplification of the System	309
B. The Electrical Analogy	312

APPENDICES	PAGE
C. Lumped Parameter Approximation to the Heat Meter	317
D. Testing the Heat Meter	322
E. Summary	323
E. Details of Other Theoretical Studies	325
A. The Theory of Dougall and Rohsenow	325
B. The Theory of Hsu	329
1. The Case of Constant ΔT	330
2. The Case of Negligible Acceleration Effects	333
F. Physical Properties	337
G. Bibliography	341
H. Nomenclature	348

INDEX OF TABLES

TABLE		PAGE
5-1	Location of Thermocouples in Heater Wall	132
6-1	Summary of Test Runs Arranged in Order of Increasing Heat Flux	162
6-2	Summary of Experimental Data	178
6-3	Peak Instantaneous Values of Fluctuating Components of Surface Heat Flux and Temperature	193
6-4	RMS Average of the Fluctuating Component of the Surface Heat Flux	230
6-5	Relative Wave Amplitude and Heat Transfer Coefficient Correction Factor for Sinusoidal Waves	240
6-6	Ratio of Predicted Peak Values in Instantaneous Heat Flux for Sinusoidal Waves to Measured Peak Values	248
6-7	Relative Wave Amplitudes and Heat Transfer Coefficients for Square Pulse Type Waves	251
6-8	Properties of the Vapor Film for Freon-113; $u_i/u_m=0$	272
6-9	Properties of the Vapor Film for Freon-113; $u_i/u_m=0$	273
6-10	Predicted Amplitude of Interfacial Ripples for Specified Values of ϵ/ν for Freon-113	276
F-1	Physical Properties of Nickel-200 and "Pyrex" Glass	338
F-2	Physical Properties of Freon-113 at One Atmosphere	339

INDEX OF FIGURES

FIGURE		PAGE
1-1	Typical Boiling Curve	3
1-2	Flow Regimes for Boiling Within a Conduit with High Vaporization Rates	6
3-1	Interfacial Structure and Boundary-Layer Development in Vertical Film Boiling	34
3-2	Typical Velocity Profiles for the Vapor and Liquid Phases in Vertical Film Boiling	36
3-3	Control Volumes for Momentum and Energy Balances	38
3-4	Comparison of Predicted Temperatures and Temperature Gradients with Experimental Data of Sage	45
3-5	Division of the Vapor Film into a Smooth Side and a Rough Side	48
3-6a	Typical Dimensionless Velocity Profiles for Smooth and Rough Surfaces	53
3-6b	Typical Dimensionless Velocity Profiles for Smooth and Rough Surfaces	54
3-7	Maximum Dimensionless Velocity versus y_{\max}^+ and ϵ/ν	55
3-8	Local Vapor Film Reynolds Number versus y_{\max}^+ and ϵ/ν for Symmetrical Flow Fields	57
3-9	Typical Dimensionless Temperature Profiles for Smooth and Rough Surfaces: Effect of ϵ/ν	59
3-10	Typical Dimensionless Temperature Profiles for Smooth and Rough Surfaces: Effect y_m^+	60
3-11	Typical Dimensionless Temperature Profiles for Smooth and Rough Surfaces: Effect of Pr. No.	61
3-12	Dimensionless Local Heat Transfer Parameter versus Local Vapor Film Reynolds Number for Symmetrical Flow Fields: Pr. No. = 0.2	65

FIGURE		PAGE
3-13	Dimensionless Local Heat Transfer Parameter versus Local Vapor Film Reynolds Number for Symmetrical Flow Fields: Pr. No. = 0.4	66
3-14	Dimensionless Local Heat Transfer Parameter versus Local Vapor Film Reynolds Number for Symmetrical Flow Fields: Pr. No. = 0.7	67
3-15	Dimensionless Local Heat Transfer Parameter versus Local Vapor Film Reynolds Number for Symmetrical Flow Fields: Pr. No. = 0.8	68
3-16	Dimensionless Local Heat Transfer Parameter versus Local Vapor Film Reynolds Number for Symmetrical Flow Fields: Pr. No. = 1.0	69
3-17	Dimensionless Local Heat Transfer Parameter versus Local Vapor Film Reynolds Number for Symmetrical Flow Fields: Pr. No. = 1.2	70
3-18	Dimensionless Local Heat Transfer Parameter versus Local Vapor Film Reynolds Number for Symmetrical Flow Fields: Pr. No. = 1.4	71
3-19	Local Vapor Film Reynolds Number for Non-Symmetrical Flow Field versus Smooth Side Dimensionless Film Thickness: $u_i/u_m = 0$	76
3-20	Local Vapor Film Reynolds Number for Non-Symmetrical Flow Field versus Smooth Side Dimensionless Film Thickness: $u_i/u_m = 0.5$	77
3-21	Dimensionless Local Heat Transfer Parameter versus Local Vapor Film Reynolds Number for Non-Symmetrical Flow Field: Pr. No. = 0.4	80
3-22	Dimensionless Local Heat Transfer Parameter versus Local Vapor Film Reynolds Number for Non-Symmetrical Flow Field: Pr. No. = 0.7	81
3-23	Dimensionless Local Heat Transfer Parameter versus Local Vapor Film Reynolds Number for Non-Symmetrical Flow Field: Pr. No. = 1.0	82
3-24	Dimensionless Local Heat Transfer Parameter versus Local Vapor Film Reynolds Number for Non-Symmetrical Flow Field: Pr. No. = 1.4	83

FIGURE		PAGE
3-24b	Effect of Interfacial Velocity on CC Number versus Re Number Relationship	83b
3-25	Boundary Layer Development over Continuous and Finite Surfaces	85
3-26	Dimensionless Heat Transfer Parameter Averaged over Entire Heating Surface versus Local Vapor Film Reynolds Number at Heater Exit for Constant Wall Temperature: Pr = 0.40	94
3-27	Dimensionless Heat Transfer Parameter Averaged over Entire Heating Surface versus Local Vapor Film Reynolds Number at Heater Exit for Constant Wall Temperature: Pr = 0.7	95
3-28	Dimensionless Heat Transfer Parameter Averaged over Entire Heating Surface versus Local Vapor Film Reynolds Number at Heater Exit for Constant Wall Temperature: Pr = 1.0	96
4-1	The Formation and Disappearance of Vapor Cavities within the Liquid at the Interface	112
4-2	Geometry of a Periodic Pulse-Type Wave	115
5-1	Experimental Equipment for Film Boiling Measurements	145
5-2	Boiler in Place before Installation of Glass	145
5-3	Components of Boiler before Assembly	146
5-4	Sliding Seal in Top Wall of Boiler	146
5-5	Gasket Separating Nickel and Brass	146
5-6	Assembled Boiler with Glass in Place	147
5-7	Boiler with Mineral Wool Insulation in Place	147
5-8	Lines of Constant Potential between Surfaces at E_0 and E_1 , for Two-Dimensional Electrical Conductor with Same Shape as Boiler	148
5-9a	Cross-Sectional View of Boiler	149
5-9	Details of Fastening Brass Section to Nickel Heater Block	150

FIGURE		PAGE
5-10	Details of Clamping Glass Side Walls to Boiler	151
5-11	Schematic View of Flow System, Showing Measuring Stations	152
5-12	x50 Photomicrograph of Tip of Surface Thermocouple	153
5-13	Micrometer Drive Mechanism for Film Thickness Probe	153
5-14	Cut-Away View of Screw Containing Surface Thermocouple	154
5-15	Circuit for Monitoring Signal from Surface Thermocouple	155
5-16	Heat Meter Design	156
5-17	Pressure Sensing Probe and Auxiliary Equipment	157
5-18	Circuit for Monitoring Signal from Pressure Sensing Probe	158
6-1	Temperature Profiles at Surface of Nickel Heater	163
6-2	Temperature Profiles at Surface of Nickel Heater	164
6-3	Effect of Heat Flux on Experimental CC Number	166
6-4	Effect of Heat Flux on Experimental CC Number	167
6-5	Effect of Heat Flux on Experimental CC Number	168
6-6	Effect of Heat Flux on Experimental CC Number	169
6-7	Effect of Heat Flux on Experimental CC Number for Almost Constant Reynolds Number	171
6-8	Comparison of Experimental and Theoretical Results	173
6-9	Comparison of Experimental and Theoretical Results	174
6-10	Comparison of Experimental and Theoretical Results	175
6-11	Comparison of Experimental and Theoretical Results	176
6-12a through 6-12z	Instantaneous Surface Temperature and Heat Flux Records	196
6-13	Spectral Density of Surface Temperature Fluctuations	223

FIGURE		PAGE
6-14a	Spectral Density of Surface Heat Flux; No. 1 Surface Thermocouple, Subcooled Runs	226
6-14b	Spectral Density of Surface Heat Flux; No. 1 Surface Thermocouple	227
6-14c	Spectral Density of Surface Heat Flux; No. 2 Surface Thermocouple	228
6-14d	Spectral Density of Surface Heat Flux; No. 3 Surface Thermocouple	229
6-15	Mean Square Average of Fluctuating Component of Surface Heat Flux vs. Time Average Heat Flux	233
6-16	Mean Square Average of Fluctuating Component of Surface Heat Flux vs. Wall-to-Liquid Temperature Difference	234
6-17	Mean Square Average of Fluctuating Component of Surface Heat Flux vs. Local Vapor Film Reynolds Number	235
6-18	Relative Intensity of Fluctuations in Surface Heat Flux	237
6-19	Calculated Values of \bar{h}/h_s and η_o for Sinusoidal Waves	241
6-20	CC Number vs. Re Number. Experimental Points from Surface Thermocouples with Corrected Values Based on Sinusoidal Waves	243
6-21a	Spectral and Cross-Spectral Densities of Signals from Pressure Probe and No. 3 Surface Thermocouple: Probe 20 mils from Wall	262
6-21b	Spectral and Cross-Spectral Densities of Signals from Pressure Probe and No. 3 Surface Thermocouple: Probe 70 mils from Wall	263
6-21c	Phase Angle Between Signals from Pressure Probe and No. 3 Surface Thermocouple	264
6-22	Typical Signals from Pressure Probe	266
6-23	Temperature Effect on Dimensionless Groups for Freon-113	270
6-24	Local Dimensionless Heat Transfer Parameter versus Local Vapor Film Reynolds Number: Comparison of Laminar and Turbulent Theory	278

FIGURE		PAGE
6-25	Data of Dougall and Rohsenow and Theoretical Curves of this Work	280
6-26	Data and Theoretical Curves of Dougall and Rohsenow	282
6-27	Hsu's Model of Film Boiling	285
6-28	Theoretical Curves from Hsu's Theory	288
A-1	Symmetrical Film Boiling with Laminar Forced Convection Flow Between Parallel Plates	293
D-1	Preliminary Design of Heat Meter	318

CHAPTER I

INTRODUCTION

Film boiling is characterized by the presence of a discrete layer of vapor that separates a hot surface from the boiling liquid, so that vaporization occurs at the liquid-vapor interface rather than at the solid surface. When the surface temperature is much greater than the liquid boiling point, film boiling will normally result. This circumstance has become more common with increasing usage of cryogenic fluids in recent years, and theoretical and experimental interest in film boiling has expanded correspondingly. This dissertation is concerned with turbulent film boiling on a vertical surface. Because much of the previous work has been conducted with horizontal surfaces, a brief review of the geometric and hydrodynamic factors that affect film boiling will be presented.

Two broad categories of film boiling may be discerned: pool boiling and conduit boiling. Pool boiling occurs when the volume of liquid in the heater is very large compared to the amount of vapor formed. In this case, liquid and vapor motion may occur either by natural convection where gravity is the driving force, or by forced convection where the liquid's primary movement is independent of the vaporization process. Boiling in a conduit, which is by

definition a relatively small reservoir of liquid, must involve forced convection flow of the liquid or all the liquid would soon be vaporized. Of course, there will be situations where this distinction between pool and conduit boiling is not easily made, but the principles to be discussed below will still apply.

Consider a horizontal heater submerged in a pool of liquid with boiling taking place on the upper surface of the heater. If the heat source is one of constant temperature, the relationship between heat flux and surface temperature will be as shown in Figure 1-1. Nucleate boiling will occur until the critical heat flux is reached at point A on the curve. Then, in the transition region, the heat flux will decrease as the surface temperature is increased. This region is characterized by a blanket of vapor on the surface with violent interfacial activity and, perhaps, liquid-solid contact. When the surface temperature is increased to point B, the Leidenfrost temperature, stable film boiling begins and interfacial agitation decreases markedly with increasing surface temperatures. Film boiling in this geometry is largely controlled by the dynamics of vapor release from the interface as discrete bubbles.

When the heat source provides a constant heat flux, as is the case with most electrical heaters, the transition region is not a stable one. Any attempt to increase the heat flux beyond the critical level at point A with this type of heater will lead to film boiling at the same heat flux but at the very high temperature, C. Subsequent lowering of the heat flux below that at point B will result

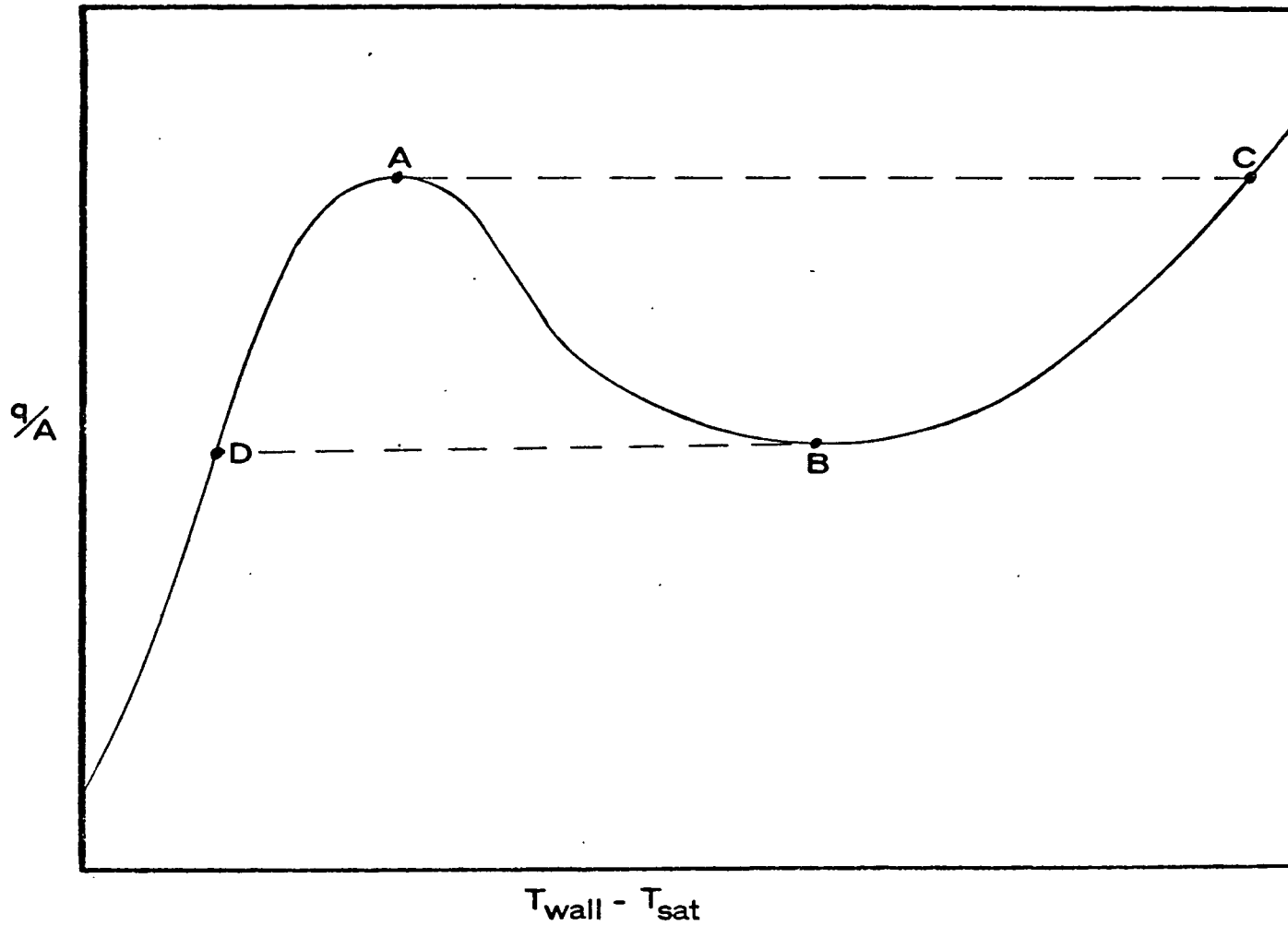


FIGURE 1-1. TYPICAL BOILING CURVE

in nucleate boiling at temperature D.

If the heating surface is now placed vertically in the pool of liquid, "natural" or "free" convection boiling occurs. The heat flux-surface temperature relationship of Figure 1-1 will still apply in general and nucleate, transition or film boiling may be attained. However, the controlling mechanisms for the film boiling regime are considerably different from the horizontal case. Vapor now moves upward in a continuous film bounded by the heated surface on one side and the liquid interface on the other. The vapor film develops in the manner of a boundary layer because of the increasing generation of vapor in the direction of flow. A boundary layer will also develop within the liquid adjacent to the interface. Interfacial waves will be much more violent than for horizontal film boiling and liquid-solid contact is more likely, with the nature of the heating system largely controlling the extent of such contact. Vapor bubbles may break off from the interface and enter the liquid, thereby reducing the amount of vapor in the film and affecting the heat transfer rates.

In natural convection pool boiling discussed above, the only liquid motion is that induced by the interfacial drag force of the vapor. Pool film boiling can also occur with forced convection flow of the liquid, which may be further subdivided into the areas of vertical and horizontal flow. For the vertical case, the vapor motion is influenced both by buoyancy forces and liquid drag at the interface, and the vapor velocity may be greater than the liquid velocity. For the horizontal case, liquid drag is the only cause

of vapor motion and the liquid velocity is the greater of the two.

Forced convection conduit flow may have a significantly different effect on film boiling than does forced convection with pool-boiling. Flow in a conduit implies that a limited amount of liquid is locally available to be vaporized. As the quantity of vapor generated increases in the direction of flow, less room is available for liquid flow. As the vaporization rate increases, this situation will eventually prove unstable. Stable film boiling, with its vapor blanket between the bulk liquid and the hot surface, will give way to a dispersed two-phase flow regime. In this case, vapor will be the continuous phase within the conduit and liquid stringlets or droplets will be carried along by the vapor. This applies to both the horizontal and vertical cases. Horizontal film boiling in a conduit is further complicated by the tendency of the vapor to flow upwards around the periphery of the conduit and concentrate under the upper surface.

When nucleate boiling in a conduit gives way to the dispersed phase flow regime, as shown in Figure 1-2, the heat transfer coefficient will markedly decrease over the distance ΔX . With a constant heat flux boiler, the wall temperature must increase correspondingly over the same short distance. This large temperature change with respect to position has sometimes been considered analogous to the temperature change with respect to time that occurs when the critical heat flux is exceeded. Following the analogy, the dispersed phase flow regime has been called film boiling. However, the pro-

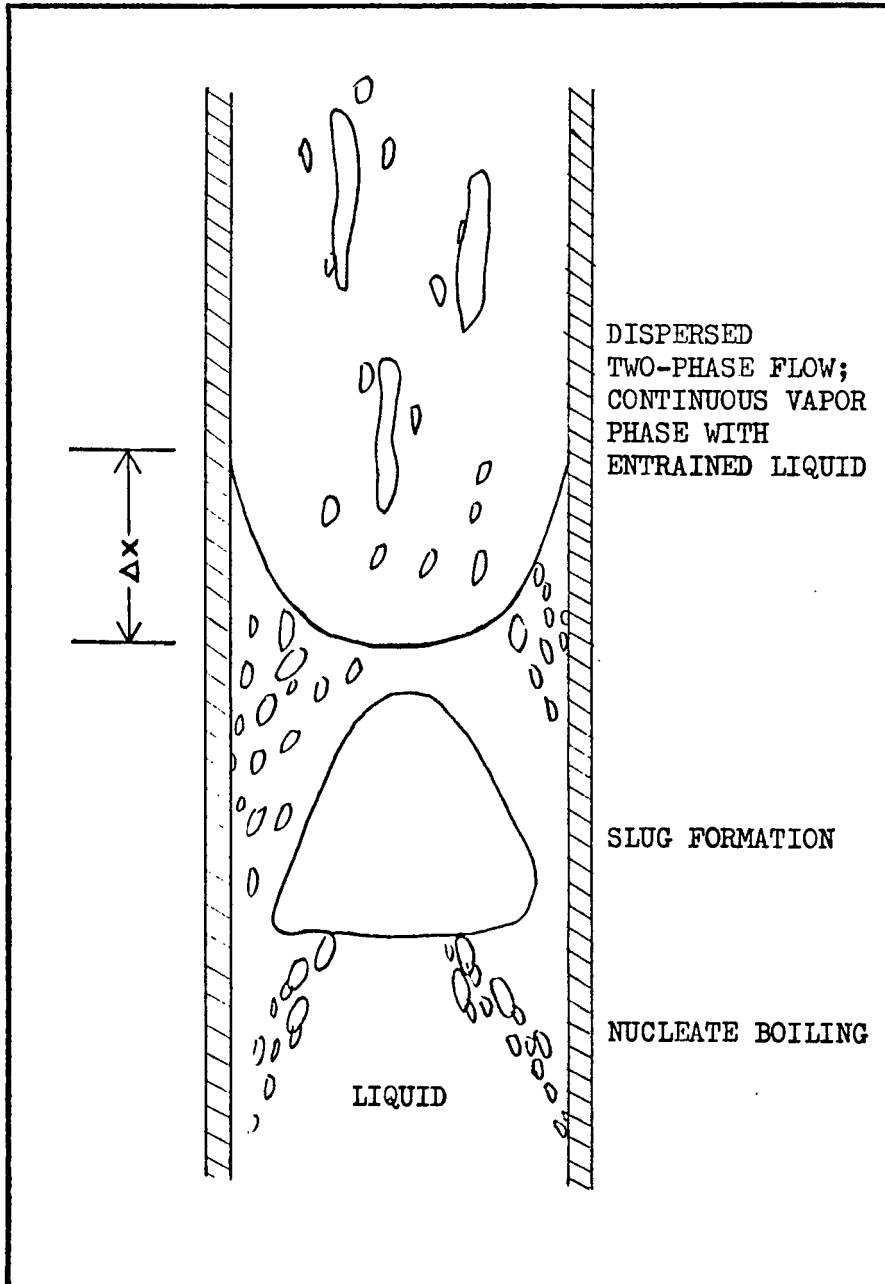


FIGURE 1-2. FLOW REGIMES FOR BOILING WITHIN A CONDUIT WITH HIGH VAPORIZATION RATES

cesses are obviously quite different.

Vertical film boiling may also be classified according to whether vapor motion within the film is laminar or turbulent. Laminar flow will persist only with very short heating surfaces of less than an inch. For longer plates with a turbulent boundary layer, there is some doubt as to whether a laminar region exists even near the leading edge. If this laminar region does exist, the transport rates there would be much higher than normally encountered with laminar flows, because interfacial waves propagating back from the upper turbulent region would provide considerable agitation.

Three different heat transfer coefficients are important with respect to film boiling. The instantaneous local coefficient is significant because it is a direct result of the point conditions and may be of great value in determining mechanisms. The time-average local heat transfer coefficient is more easily measured, and it is required for evaluating theoretical models and for calculating space average coefficients. Finally, an overall heat transfer coefficient, averaged over time and over the entire heat transfer surface, is required by the designer but is of limited usefulness for evaluating the mechanisms of the transport processes.

Earlier theoretical and experimental studies of film boiling will be discussed in the next chapter. The theoretical developments of this dissertation will be presented in Chapters III and IV. Chapter V contains a description of the experimental work conducted for this dissertation. These theoretical and experimental investiga-

tions are then evaluated in Chapter VI.

CHAPTER II

A REVIEW OF PREVIOUS WORK

The work that has been reported in the literature will be discussed in three parts: theoretical studies of film boiling, experimental studies of film boiling, and studies of waves in general.

A. THEORETICAL STUDIES OF FILM BOILING

Historically, the bulk of film boiling studies have been concerned with boiling from above horizontal surfaces or from horizontal small diameter wires. This type of film boiling is profoundly affected by the mechanics of bubble release from the interface as is shown graphically by the photographs of Westwater (W-2). Theories of horizontal film boiling generally revolve about the bubble dynamics, as illustrated by the work of Zuber (Z-1) who used Taylor stability criteria to predict bubble spacing, bubble frequency and heat flux. On the other hand, vertical film boiling is characterized by vapor in a boundary layer flow moving in a continuous film. Horizontal film boiling may have this characteristic feature if the liquid is moving by forced convection, thereby inducing vapor motion in the direction of a growing boundary layer. The discussion from this point will be directed toward vertical film boiling or film boiling in a horizontal boundary-layer situation.

Several solutions for the case of laminar film boiling have been presented. These began with the work of Bromley (B-8) which paralleled Nusselt's investigation of laminar film condensation. This approach involves the assumption that the convective acceleration terms are negligible. Later, several attempts to attain a more exact solution were developed which may be summarized by the works of Koh (K-3) for saturated liquid and of Nishikawa and Ito (N-1) for subcooled liquid. Both papers presented similarity solutions to the boundary layer equations and considered simultaneous development of the boundary layer in both phases, but the vapor-liquid interface was assumed to be smooth. These solutions were for the case of natural convection pool boiling.

Some solutions have been presented for the case of laminar forced convection of the liquid. Bromley, et al (B-10) have considered liquid with a uniform velocity moving upwards around a horizontal tube about which film boiling is occurring. The assumptions are consistent with those in reference (B-8), except that the interfacial velocity is taken to be that of the bulk liquid. Cess and Sparrow (C-6,7) presented an approximate similarity type solution of the boundary layer equations for forced convection film boiling. An exact similarity solution for this case was later made by Padilha (P-1). Both of these studies, however, were carried out for horizontal forced convection flows where buoyancy forces on the vapor are absent. There does not appear to be an exact treatment of laminar flow where both natural and forced convection effects

are considered. All of these studies for laminar flow are of limited value to design work, because in most practical situations the flow very soon becomes turbulent. However, for film boiling on the outside of small diameter (less than one inch) horizontal tubes, laminar flow may be maintained.

Borishanskii and Fokin (B-3) took a different approach to predicting heat transfer rates in vertical film boiling. They assumed that the transport rates are controlled by pear-shaped bubbles such as they observed at the vapor-liquid interface. They calculated the flow characteristics of the bubbles as though they were single bubbles rising through a liquid unhindered by solid surfaces. Their model and their empirical correlations are based on data (B-4) taken with very small wires (about 0.1 inches in diameter and 3 inches long) where the thickness of the vapor film was of the same order as the wire diameter. It appears that both their correlation and their data are suitable only for similar heaters.

Most theoretical studies of turbulent film boiling neglect the acceleration effects. The primary exception is Cashler's similarity type solution of the turbulent boundary layer equations (C-5). He considered both horizontal and vertical forced convection film boiling where the vapor phase was assumed in turbulent flow while the liquid phase was considered laminar. However, his vertical work seems to have been somewhat in error since it allowed a velocity profile with maximas in both the liquid and vapor phase. Appendix A contains a qualitative discussion of this matter.

Hsu (H-5) was the first to treat turbulent vertical film boiling. He accounted for the acceleration effects in a simplified way by using an average vapor velocity. He also tried to account for the effect of the wavy interface by using an empirical relationship for the interfacial shear stress. This correlation was developed from data taken with a stratified air-water flow system. However, his theoretical development was strongly dependent upon the assumption that all the resistance to momentum and energy transport is contained in a laminar sublayer next to the heated wall. This probably leads to an understatement of the resistances involved, and, in fact, his theoretical heat transfer coefficients appear much larger than experimental values.

Dougall and Rohsenow (D-5) developed a theory for turbulent film boiling in which it was assumed that the universal velocity profile as determined for pipe flow existed in the vapor film. The flow field was considered to be symmetrical with the interfacial shear stress equal to the wall shear stress and the interfacial velocity equal to zero. The temperature profile was calculated from the eddy viscosity distribution implied by the universal velocity profile, assuming that the eddy viscosity and conductivity are equal. Their assumption of symmetrical velocity and temperature profiles led to predicted heat transfer coefficients that were lower than measured values. This discrepancy was attributed to the interfacial waves, neglected thus far, that would tend to increase the rate of energy transfer. The theory was modified accordingly by assuming

that the laminar sublayer and the buffer region near the interface did not exist for the temperature field, thus reducing the resistance to heat transfer and indirectly accounting for the effects of the waves. Their theoretical heat transfer coefficients approach an almost constant value as the vapor film Reynolds number gets large. As their data indicate that the heat transfer rates increase at higher Reynolds numbers, it was assumed that film boiling becomes unstable at this point and breaks up into a dispersed two-phase flow regime. A Nusselt type heat transfer relationship was then developed for the dispersed flow system. More data are needed to determine just when this type of instability occurs for forced convection film boiling in a conduit. For pool boiling, however, dispersed flow does not exist.

Laverty and Rohsenow (L-2) developed a two-step sequential heat transfer theory for what is called film boiling. However, the physical model really describes a continuous vapor phase within the conduit in which stringlets of liquid are flowing. This is the dispersed two-phase flow regime rather than film boiling, and the data correlated by the theory are apparently also in the dispersed flow regime.

Morgan (M-6) solved the turbulent boundary layer equations for vertical film boiling in a pool. His solution was based on the integral analysis of von Karman wherein it was necessary to assume the shape of the velocity and temperature profiles. Several sets of profiles were tried and some appeared to lead to a reasonable agreement

with data in the literature. The velocity profiles that worked best were unrealistic for poolfilm boiling in that they postulated a zero shear stress at the interface. However, this is the point at which the shear stress would be expected to have its maximum value.

The theoretical developments described above have increased our understanding of the mechanisms underlying vertical film boiling. However, none of these studies considers directly the effect of the shape and motion of the interface. In the theoretical approach taken in this work, an attempt is made to extend this understanding to include the complexities of interfacial action. To this end, the effects of the interface are considered in two parts: the roughness effects of the relatively small-scale ripples on the interface, and the effects of the relatively large amplitude waves.

B. PREVIOUS EXPERIMENTAL STUDIES

Experimental data for film boiling on the outside of small diameter horizontal tubes, such as the data of Bromley (B-8), are in reasonable agreement with the laminar theory of Bromley. However, when relatively long vertical surfaces (from about 3 to 48 inches in length) were used, the vapor film became turbulent and significantly higher heat transfer coefficients were observed. These data in turbulent flow are discussed in this section.

Because of equipment design problems, the data from many of these studies are characteristic only of the particular equipment

used and are of little value for quantitative evaluation of a film boiling theory. These problems point up the very great difficulty, especially for the first workers in a specialized area, of making reliable measurements in two-phase flow systems. This is discussed at length by Dukler and Wicks (D-7). These problems are magnified when heat transfer also occurs, especially for film boiling where the very large temperature differences create imposing mechanical problems.

Some of the earliest data were reported by Ellion (E-3) who measured heat transfer coefficients averaged over the entire heating surface. His system was a one-quarter inch O.D. by three inch long electrically heated tube with forced convection boiling on the outside. From photographic measurements he was able to estimate some interesting aspects of stable film boiling of water. These include a vapor thickness of the order of 0.02 inches and a Reynolds number for transition from laminar to turbulent vapor flow on the order of 100, based on the definition: $Re = 2 \bar{u} \rho \nu^{-1}$ (some studies have used other constants in the definition). However, his data do not appear suitable for quantitative evaluation of theoretical correlations because of problems associated with equipment design. The electrical bus bars attached to the heater tube apparently disturbed the flow field and contributed to heat losses at the ends of the heater.

Hsu (H-5) measured overall space-average heat transfer coefficients during pool film boiling on the outside of short, verti-

cal bayonet-type steam heaters. The heaters ranged in size from 2 to 6.25 inches in length and $3/8$ to $3/4$ inches in diameter. They entered the pool boiler from the bottom, and the tips of the heaters were about two inches below the surface of the liquid. The fluids studied were methanol, benzene, carbon tetrachloride, nitrogen and argon. Movies taken of these experiments (W-3) are very valuable for elucidation of the mechanisms involved, but they may be valid only for pool boiling with a saturated liquid. In particular, they indicate that there are occasional large bursts of vapor into the bulk liquid, with these bursts being connected by a thin substrate of vapor. The vapor in these bursts rarely breaks off into bubbles but usually flows back into the vapor film. However, the movies also show great agitation where the vapor reaches the tip of the heater. Here the vapor must break off into bubbles to reach the free liquid surface two inches above. The heat transfer due to this end effect could easily have been a significant fraction of the total heat transfer. In addition, low surface to fluid temperature differences of 150 to 320 degrees F. were experienced with the three organic liquids. As a result, it is likely that some liquid-solid contact took place. Such contacts, as discussed in Section F of Chapter IV, would greatly increase the heat transfer rates over those to be expected in stable film boiling.

Forced convection film boiling of Freon-113 and methanol on the inside wall of a vertical, steam-heated tube was studied by Rankin (R-1). A heat transfer coefficient averaged over the entire tube

was measured. The heater was $3\frac{1}{2}$ feet long by one inch in diameter. The average liquid velocity at the heater inlet ranged from one to nine feet per second, but this velocity could not be correlated with the heat transfer rate. The pressure gradient measured across the entire heater was frequently less than the hydrostatic liquid head. Rankin attributed this to entrainment of vapor in the liquid. The temperature differences in Rankin's work ranged from 120 to 320 degrees F. As mentioned before, considerable liquid-solid contact could be expected for these conditions, and the possibility exists that transition boiling rather than film boiling was the mode for many runs. Extensive liquid-solid contact could lead to vapor entrainment within the liquid, since nucleate boiling probably takes place during these contacts. Stable film boiling is most likely to have occurred in Rankin's tests when the temperature difference was greater than 200 degrees F.

Class et al (C-9) measured local time average heat transfer coefficients for hydrogen pool boiling from a vertical electrical heating strip. Because of the unusual physical properties of hydrogen, these data, if valid, would provide a good test of the correlating parameters that are derived from a film boiling theory. The heater strip used by Class was one inch wide by 22 inches high and was embedded in a larger flat wall. In a similar experiment by Morgan (M-6) with a four-inch wide heater strip, high speed motion pictures showed that liquid contact with the strip at the long edges caused excessive instabilities and greater heat transfer rates than would be expected

for film boiling. Class et al did not make visual observations so these instabilities were not reported, but they probably were present. Morgan concluded that his own data were not suitable for evaluation of theoretical models.

Bradfield et al (B-6) studied unsteady-state film boiling by quenching several hydrodynamic shapes in water, trichloroethylene and liquid nitrogen. They took high speed motion pictures of the various boiling regimes that evolved as the solid cooled.

Dougall (D-5) measured local time-average heat transfer coefficients for Freon -113 in forced-convection film boiling on the inside of electrically heated vertical tubes (0.41 and 0.18 inches in diameter by 15 inches long). Qualitative visual studies were also made with an electrically heated transparent tube. Pressure drop measurements were not made, so a comparison with Rankin's pressure drop measurements and conclusions therefrom is not possible. However, it is unlikely that liquid-solid contact occurred during Dougall's tests because the temperature differences were greater than 500 degrees F. Most of his tests with the large diameter tube were probably in the film boiling regime because the vaporization rate was always less than five per cent. However, all of his tests with the smaller diameter tube were in dispersed flow. There is some uncertainty with respect to these data since the liquid feed was subcooled and the bulk temperature of the liquid leaving the boiler was not measured. Thus, the distribution of input energy between vapor generation and liquid heating is not known (D-4), but it was estimated that very little

energy went to sensible heat of the bulk liquid. When heat transfer rates are calculated as though all the input energy went to vapor generation and superheating, they are not functionally related to either the degree of subcooling or the liquid feed rate. This fact makes the data appear reliable, and it is believed that they can be used with some confidence to evaluate theoretical models for film boiling.

Lavery (L-2) continued Dougall's work and obtained data with boiling nitrogen inside a 0.32 inch diameter by 4 foot long tube. The total vaporization rate in these tests was enough to cause dispersed flow to occur before the heater exit was reached. In fact, photographs taken of a heated glass tube provide a striking record of the formation of the dispersed flow regime. Film boiling may have occurred in the bottom section of the tube before too much vapor was formed, but this point cannot be evaluated with certainty.

Hendricks et al (H-2) reported data on the forced convection boiling of hydrogen inside vertical electrically heated tubes. Heater dimensions were 0.3 and 0.5 inches in diameter by one foot in length. It is not certain that film boiling occurred during these tests and their own analysis of the data was somewhat inconsistent. They postulated an annular flow model which implies film boiling, but they also assumed that the vapor was at its saturation temperature which implies intimate vapor-liquid mixing and a dispersed flow regime. They calculated the pressure drop along the tube by consider-

ing only the momentum changes that occur as the liquid vaporizes to a low density, high velocity gas. These calculated pressures agreed well with measured values. Since the calculated vapor velocity was based on the density of saturated vapor, it is concluded that the data actually represent dispersed flow heat transfer rather than film boiling.

Some experimental studies of forced convection boiling have been presented where heat transfer rates are large enough to vaporize all of the liquid well before the end of the tube (P-2, S-10). It is unfortunate that the term "film boiling" has been used to describe these processes. As discussed in Chapter I, convective heat transfer to a continuous vapor phase would be more descriptive. Lavin and Young (L-3) and Sachs and Long (S-1) describe the various flow regimes that develop under such circumstances. Lewis et al (L-5) discuss the uncertainties involved in evaluating forced convection boiling processes with high vaporization rates. The apparent confusion in nomenclature has unfortunately resulted in some attempts to apply a single generalized correlation to both types of heat transfer processes (G-2, C-8).

As indicated in this review, much of the data reported in the literature is of limited value with respect to evaluating theoretical developments. End effects reduced the value of some of the data. Other data did not represent the case of stable film boiling being considered here. In many cases, overall average heat transfer rates were reported, but these provide little information about

the local behavior which is needed to reveal mechanisms. Only the data of Dougall and Rohsenow (D-5) are considered generally valid. It is apparent that considerable additional data are required. Of particular value would be more measurements of local heat transfer coefficients versus local Reynolds numbers. This almost requires that the heat source be one of constant heat flux. Other data required are pressure drops in forced convection flows, the general shape of the velocity profiles in the vapor and the liquid, and determination of the conditions at which film instabilities exist. Instabilities include complete breakup of the film boiling regime, bubble release at the interface and liquid-solid contact. The importance of visual observations at this point is clear. In addition, more detailed data about the nature and the effects of interfacial motion are required. These include instantaneous heat flux, surface temperature and film thickness measurements. The objective of the experimental work undertaken in this study was to obtain reliable measurements of this type. This is discussed in Chapter V.

C. SOME ASPECTS OF THE LITERATURE ON WAVES

In two-phase flow situations the nature of the interface between phases exerts a profound effect on the transport processes. For vertical film boiling in particular, the shape and amplitude of the interfacial waves greatly influence the heat transfer rates. However, there is very little theoretical or experimental information about the nature of surface waves. The mathematics of wave action have

been pursued for many years by prominent mathematicians, and this work is well summarized by Lamb (L-1), Ursell (U-1), and Kinsman (K-2). This work has been very useful in terms of defining the nature of the problems and in presenting solutions for very specialized situations. However, very little has been accomplished that can be of direct practical aid to the designer of two-phase flow systems. The primary success of wave analyses has been in determining the onset of instabilities.

In this section, the classic Kelvin-Helmholtz analysis of waves will be reviewed as a means of indicating the general approach of theoretical work in the field. The details of this approach may be found in Lamb (L-1), and an approach more directly related to physical meaning is presented by York et al (Y-1). The general aspects of the problem are discussed here.

Consider a large body of still liquid in the presence of a gas moving parallel to the liquid surface. The conditions under which a small ripple on the surface will grow into larger waves are sought. Worded differently, this is the same as finding the conditions under which energy will be transferred from the gas to the liquid. When there is net energy transfer to the liquid, the waves will grow and the flow situation is called unstable with respect to the initial small disturbance.

The gas moves with a uniform velocity, V , over the deep liquid. Both phases are taken to be inviscid and the motion is assumed irrotational. The equations of motion are linearized. At some instant,

a disturbance within the system causes a small displacement, η , of the liquid surface as follows:

$$\eta = B \sin(nt + kx) \quad 2-1$$

where B , the wave amplitude, may be a function of time and η_0 is the initial value of B . The disturbance is assumed to be initially present at all positions in space since a single point disturbance would greatly complicate the mathematics. Gravity and surface tension forces tend to restore the surface to its original shape, but under the proper conditions, the pressure distribution over the surface that develops because of the flowing gas may lead to a growing wave.

For inviscid fluids, the continuity equation may be expressed in terms of the velocity potential, Φ :

$$\frac{d^2\Phi}{dx^2} + \frac{d^2\Phi}{dy^2} = 0 \quad 2-2$$

where Φ is so defined that:

$$\frac{d\Phi}{dx} = v_x \quad ; \quad \frac{d\Phi}{dy} = v_y \quad 2-3$$

A solution must be found for equation 2-2 that is consistent with the nature of the initial disturbance given by equation 2-1 and with the general kinematic boundary conditions given next. At $y = 0$, the

average interfacial position, the velocity in each phase is set equal to the interfacial velocity given by $d\eta/dt$. As y gets very large, the gas velocity approaches V , and as y gets very large negatively, the liquid velocity approaches zero.

When Φ is found for each phase, the pressure in each phase can be calculated from the equation:

$$\frac{P}{\rho} = F(t) - \frac{d\Phi}{dy} - gy - \frac{1}{2} \left[\left(\frac{d\Phi}{dx} \right)^2 + \left(\frac{d\Phi}{dy} \right)^2 \right] \quad 2-4$$

The pressure on either side of the interface, at $y=0$ for the linearized theory, can then be calculated. These pressures are equated after making allowance for the pressure discontinuity caused by surface tension:

$$P' = P + T \frac{d^2\eta}{dx^2} \quad 2-5$$

where the prime refers to gas properties and T is the surface tension. When P and P' from equation 2-4 are put into equation 2-5, it is seen that certain relationships between the variables must exist if the solution of equation 2-2 is to be consistent with the boundary conditions. These relationships are called the stability criteria and lead to the definition of the critical velocity, V_c :

$$V_c = \left\{ \frac{(\rho + \rho') \cdot [Tk^2 + g(\rho - \rho')]}{\rho\rho'k} \right\}^{1/2} \quad 2-6$$

If the gas velocity, V , is less than V_c , the initial disturbance will be stable and the wave amplitude will remain at η_0 . If V equals V_c the waves will be unstable and will grow linearly with time. If V exceeds V_c , the growth rate will be exponential. For the unstable waves, the relationship between wave length and wave frequency turns out to be:

$$\lambda = \frac{\rho V}{f(\rho + \rho')} \quad 2-7$$

where, by definition, $k = \frac{2\pi}{\lambda}$ and $n = 2\pi f$.

Of course, for an inviscid liquid the waves will never die out, for there is no mechanism postulated whereby energy can be dissipated.

The fastest growing waves will be those with an exponential growth rate. These waves result when the wave length of the initial disturbance is such that the critical velocity is less than the gas velocity. For this case, the wave displacement with time is:

$$\eta = \left[C e^{\theta t} + (\eta_0 - C) e^{-\theta t} \right] \sin(nt + kx) \quad 2-8$$

where one initial condition ($B = \eta_0$ at $t = 0$) has been applied to the solution, C is a constant of integration, and θ is given by:

$$\theta = (\rho + \rho')^{-1} \left[\rho \rho' k^2 V^2 - T k^3 (\rho + \rho') + gk(\rho^2 - \rho'^2) \right]^{1/2} \quad 2-9$$

After a long time, the first exponential in equation 2-8 will dominate. The "most dangerous" wave number is that which leads to the most rapid increase in amplitude. It is found by setting $d\theta/dk$ equal to zero, with the result that:

$$k_{md} = \frac{2\rho\rho'V + g(\rho^2 - \rho'^2)}{3T(\rho + \rho')} \quad 2-10$$

The corresponding "most dangerous" frequency is found from equation 2-7.

The conclusions reached so far have been attained through a formal mathematical approach. The physical meaning of these results is that a net transfer of energy from the gas to the liquid takes place when V equals or exceeds V_c . The energy is transferred by the gas pressure force acting on the moving interface according to:

$$dE' = P' \frac{d\eta}{dt} dx = P' v_i dx \quad 2-11$$

where v_i is the vertical component of the interfacial velocity and dE' is the rate of doing work on a unit area of interface, dx . Equation 2-11 may be evaluated explicitly for the problem at hand, since linearization of the equations and the assumption of irrotational flow have simplified the mathematics. P' is attained from equation 2-4 and is substituted into equation 2-11. The resulting

equation is integrated over a wave length ($2\pi/k$) with the result that the net energy transfer over a cycle is:

$$E' = \frac{\pi\rho'\dot{B}}{k^2} \cdot \left\{ \ddot{B} - B \left[kg - (n + kV)^2 \right] \right\} \quad 2-12$$

where \dot{B} and \ddot{B} represent first and second derivatives with respect to time. For the stable wave, B is constant and \dot{B} is zero, and the net energy transfer by the above equation is zero. For the exponentially growing wave, the rate of energy transfer is positive and increasing with time as follows:

$$E' = \frac{\pi\rho'\theta^2}{k^2} \left[C^2 e^{2\theta t} - (C - \eta_0)^2 e^{-2\theta t} \right] \left[\theta^2 - kg - (n + kV)^2 \right] \quad 2-13$$

Thus, the wave will tend to grow indefinitely, and the final wave size cannot be determined within the framework of the inviscid linearized solution.

The analysis thus far has shown that waves will grow when the critical velocity is exceeded, and that the wave length and frequency are then related by equation 2-7. The amplitude is not known, however, because an initial condition has not been specified and the constant of integration in equation 2-8 cannot be determined. Specifying the missing initial condition would be equivalent to specifying the amount of energy initially added to the original small disturbance. Then, the amplitude would be known as a function of time as long as the linearized theory were valid.

The fact that the amplitude is not known is not too disturbing, for when it becomes large enough to be significant the linearized solution will no longer apply. The usefulness of the linearized solution is primarily to determine the onset of instability. Many writers have attempted to extend its usefulness by assuming that the most dangerous wave length and frequency persist and continue to dominate the surface spectra even after the wave amplitude becomes very large. This has met with apparent success in some cases, as in Zuber's analysis of the minimum heat flux in film boiling (Z-1). However, it would be expected that the non-linear terms in the equations of motion would soon distort the wave lengths and frequencies determined from the linearized equations. This latter view is supported by Concus (C-10) who carried a perturbation solution through the second order equations, and found that the wave shape and frequency were amplitude-dependent for inviscid standing waves.

In addition to the stability criteria that define the flow regime to be expected and the nature of the small growing wave, the shape and amplitude characteristics of the fully developed wave are important to the designer. It was not necessary to determine explicitly the rate of energy addition to the liquid when stability was being evaluated. This must be known for fully developed waves, however, since the equilibrium amplitude is attained when the rate of energy addition is equal to the rate of viscous energy dissipation within the liquid. Several approaches to this problem have been explored in the literature.

Miles (M-3) evaluates the rate of viscous dissipation within a liquid with small amplitude laminar waves. This is done only for the linearized case to establish the criteria of stability, and it does not lead to the wave amplitude. Miles also calculates the rate of energy transfer from the gas to the liquid for "fully developed" waves, but does not determine the viscous dissipation within the liquid for this case. This solution was carried out for a non-uniform velocity profile in the gas and was developed through the Orr-Sommerfeld equation. Although completely similar to the Kelvin-Helmholtz solution in principle, this work is mentioned here since it attacks directly the energy transfer aspect of the problem.

Bradfield's approach to the wave analysis (B-5) is a novel one wherein he considers the wavy interface to be a classical damped oscillator. His theory is based on film boiling around a vertical, cylindrical heater which enters the liquid from the top. He investigates wave formation at the stagnation point of the heater under the rounded tip. As waves develop on the interface, the forces acting on them are gravity, surface tension, the pressure within the gas phase, and a forcing function. The forcing function develops because of the increased boiling rate as the interface approaches the surface of the heater. The mass of the interface that is accelerated by these forces is assumed to be the total weight of fluid supported by the interface, which is essentially the hydrostatic head at the immersion depth of the heater tip. The laminar equations of motion are used to calculate the pressure within the vapor

film as a function of the interfacial motion. Bradfield does not specify the nature of the forcing function, which would have been equivalent to specifying the rate at which energy is added to the interface. As a result, he cannot calculate the wave amplitude. By linearizing his final differential equation, however, he is able to predict the undamped natural frequency of the system. He then postulates that the waves that move up the interface alongside the heater will propagate according to this frequency. His photographic evidence is consistent with this view.

Kapitsa (K-1), whose work is summarized and extended somewhat by Levich (L-4), presents an analysis which contains the first calculation of wave amplitude. Working with a falling liquid film on a vertical wall, he assumes that the velocity profile within the film at any instant is given by the original Nusselt solution for a falling film without waves. By properly averaging the velocity profile and assuming that the interfacial shape is sinusoidal, Kapitsa arrives at an equation that relates the viscous dissipation of energy within the film to the amplitude and propagation velocity of the waves. The rate of dissipation is a constant equal to $g\rho Q$, where Q is the volumetric flow rate per unit width of plate. This is the rate at which gravity adds energy to the fully developed film. Kapitsa then finds the minimum mean film thickness, m_0 , within the restraints that the viscous dissipation is equal to the value stated above and

that the solution be periodic. For a wall height of L , a wall width of one unit, and sinusoidal waves, the total potential energy of the liquid on the wall will be $\frac{1}{2} \rho_L g L^2 m_0$. The minimum potential energy of liquid on the wall then corresponds to the minimum value of m_0 . Kapitsa argues that the most stable flow pattern for the geometry under study is that which has the least potential energy, or the minimum value of m_0 , but he does not present a proof of this assertion. His final results for the wave form, $m = m_0 + a \sin[\omega(t - \frac{x}{c})]$ are:

$$\frac{a}{m_0} = 0.46 ; \quad \frac{c}{v_0} = 2.4 \quad 2-14$$

In this case, 'a' is the wave amplitude, c is its propagation velocity, and v_0 is the average velocity in the liquid film at the time when the film thickness is m_0 , such that $Q = m_0 v_0$. Of course, if a surface structure other than a sinusoidal one had been postulated, the answers would be different. In his original simplification of the equations of motion, Kapitsa had assumed that the amplitude ratio, a/m_0 , was much less than one. Since this ratio turns out to be rather close to one, there is some doubt as to the validity of the final results.

Wicks (W-4) extended Kapitsa's analysis to the case where interfacial shear stress is present due to the flow of a parallel second phase. Massot et al (M-1) have repeated Kapitsa's work but they retained all of the terms in the equations of motion. (Kapitsa and Levich in his extension ignored the term, $\frac{\partial^2 v_x}{\partial x^2}$, and the x-dependency of the instantaneous film thickness.) They found that the Weber number

is the correct parameter for the generalized correlation of the wave length and celerity. They questioned the Kapitsa-approach to amplitude determination, for they assumed that Kapitsa had minimized the viscous dissipation within the liquid film. In reality, the viscous dissipation is constant and predetermined, but the potential energy of the liquid film on the wall was minimized by Kapitsa. It appears, however, that the amplitude determination of Massot et al (M-1) did parallel Kapitsa's approach.

As indicated in this brief review, thoretical studies have advanced very little towards a full knowledge of the structure of stable waves. Several experimental studies have been made of the interfacial structure of thin liquid films with and without shear flow at the interface. This work is reviewed by Wicks (W-4). For the analogous case of the vapor film in film boiling, the only studies of interfacial structure have been visual observations through high-speed photography.

CHAPTER III

THEORETICAL DEVELOPMENT - QUASI STEADY STATE MODEL

In this work, a phenomenological approach is used to calculate velocity and temperature profiles in the vapor film. This requires the development of eddy diffusivity relationships that will properly account for the turbulent transport of heat and momentum within the film. These profiles then lead directly to the relationship between the variable groupings that describe the process, such as the Reynolds number, friction factor and Nusselt number. The first step in this procedure is the conception of a physical model that is reasonably true to nature, yet reasonably responsive to mathematical attack.

A. THE PHYSICAL MODEL

Film boiling along a vertical plate is shown in Figure 3-1, with the vapor moving in a continuous film along a heated wall. The mean thickness of the vapor film increases in the direction of flow because of new vapor generation. The vapor-liquid interface is a "rough" rippled surface possessing a net vertical velocity. In addition to the small scale ripples, relatively large amplitude waves will also exist at the interface as shown in the upper portion of Figure 3-1. This flow situation is evidently too complex for an exact solution of the equations of motion, and the following simplifying assumptions will be made in the

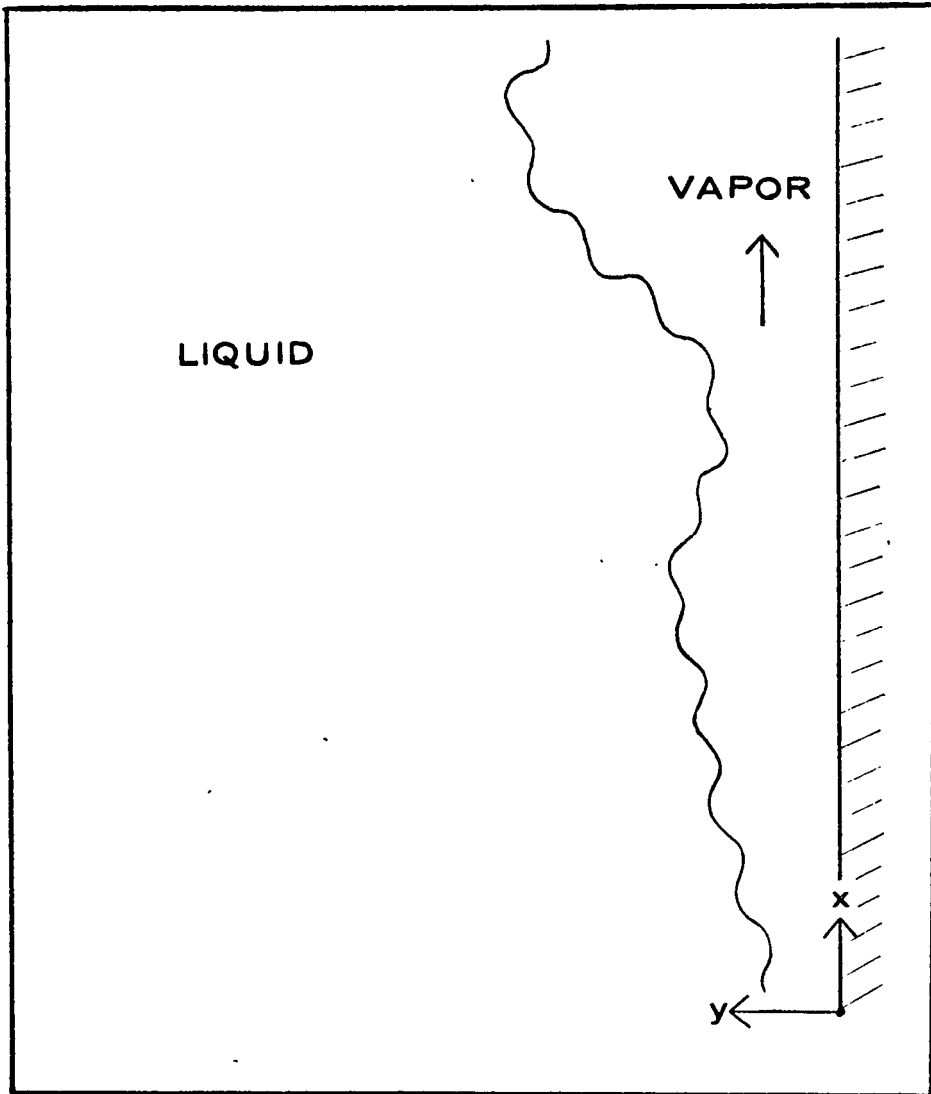


FIGURE 3-1. INTERFACIAL STRUCTURE AND BOUNDARY-LAYER DEVELOPMENT IN VERTICAL FILM BOILING

development of the physical model.

The effect of the wavy interface will be broken down into two parts. The larger oscillatory waves will not be considered at first. The small scale ripples on the interface will be treated as though they were stationary solid roughness elements on a rough surface, as described later in this chapter. Thus, the model will be first developed as if the vapor flow were in steady state. Then in Chapter IV, the effect of the larger waves will be formulated as a correction factor to the quasi-steady state theory. It will be further assumed that x -direction changes in energy and momentum transport are negligible compared to the y -direction changes so that the acceleration terms in the equations of motion may be neglected. This approach parallels the successful derivations of Bromley (B-8) for vertical, non-wavy, laminar film boiling; of Dukler (D-6) for turbulent film condensation; and of Sparrow et al (S-7) for turbulent boundary layer flow. The physical properties of the vapor will be considered constant, and it will be assumed that the results of the theory are applicable to film boiling when the physical properties are evaluated at the mean vapor temperature.

Three types of velocity profile are to be expected as indicated in Figure 3-2. Profile No. 1 would occur in natural convection pool boiling where vapor motion is caused by buoyancy. There will be a net vertical velocity in both phases at the interface, induced by the interfacial vapor shear stress, and this will promote a boundary layer velocity field in the bulk liquid. Note that the profile in the vapor is non-symmetrical because one boundary is smooth and stationary while the other is

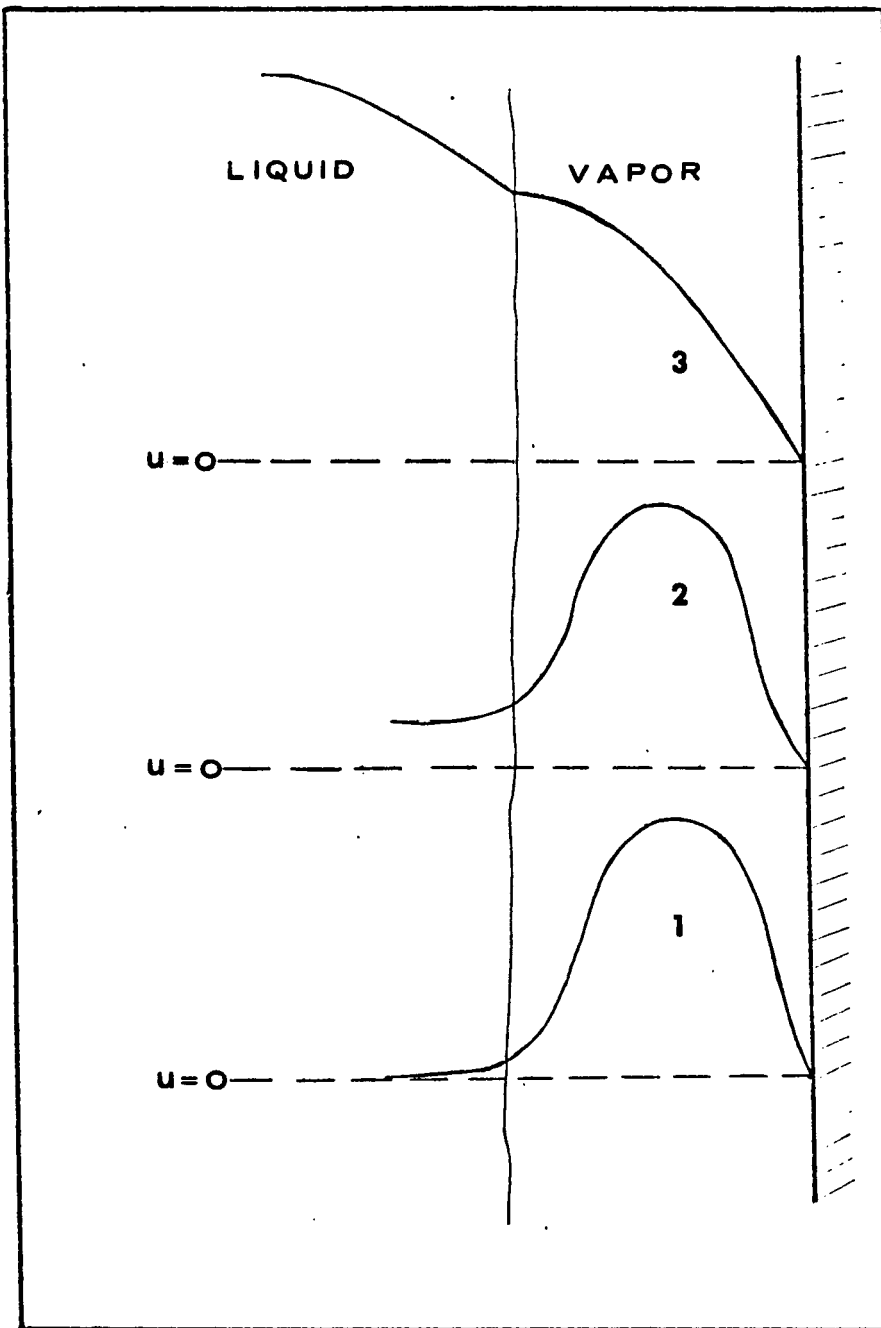


FIGURE 3-2. TYPICAL VELOCITY PROFILES FOR THE VAPOR AND LIQUID PHASES IN VERTICAL FILM BOILING

rough and moving.

Profile No. 2 or 3 would be expected when there is forced convection flow of the liquid in either pool or conduit boiling. Profile 2 is similar to the natural convection profile since the maxima is in the vapor phase and the interfacial velocity is greater than the mean liquid velocity. This occurs when the buoyancy forces promoting vapor motion are much greater than the pressure forces pushing the liquid. Indeed, it is shown later in this chapter that the pressure drop for conduit flow with velocity profile No. 2 should be less than the hydrostatic head of the liquid. If both phases in the conduit are in laminar flow and if the interface is smooth, it can be shown that a profile of type 2 would normally be expected, with type 3 occurring only at relatively large liquid flow rates. (This development is presented in Appendix A.) Qualitatively similar results could be expected for turbulent flow and for vertical forced convection pool boiling. Profile 3 would always be expected in horizontal forced convection flows or with forced convection in a zero-gravity field. In this work, the theory developed for natural convection pool boiling will be considered applicable to forced convection boiling with velocity profiles of type 2.

B. THE TRANSPORT EQUATIONS

Under the assumptions of steady-state, fully developed flow with constant physical properties, the only forces acting on a differential fluid element are shear, pressure and gravity, as shown in Figure 3-3. Application of Newton's second law in rectangular coordinates to this system gives:

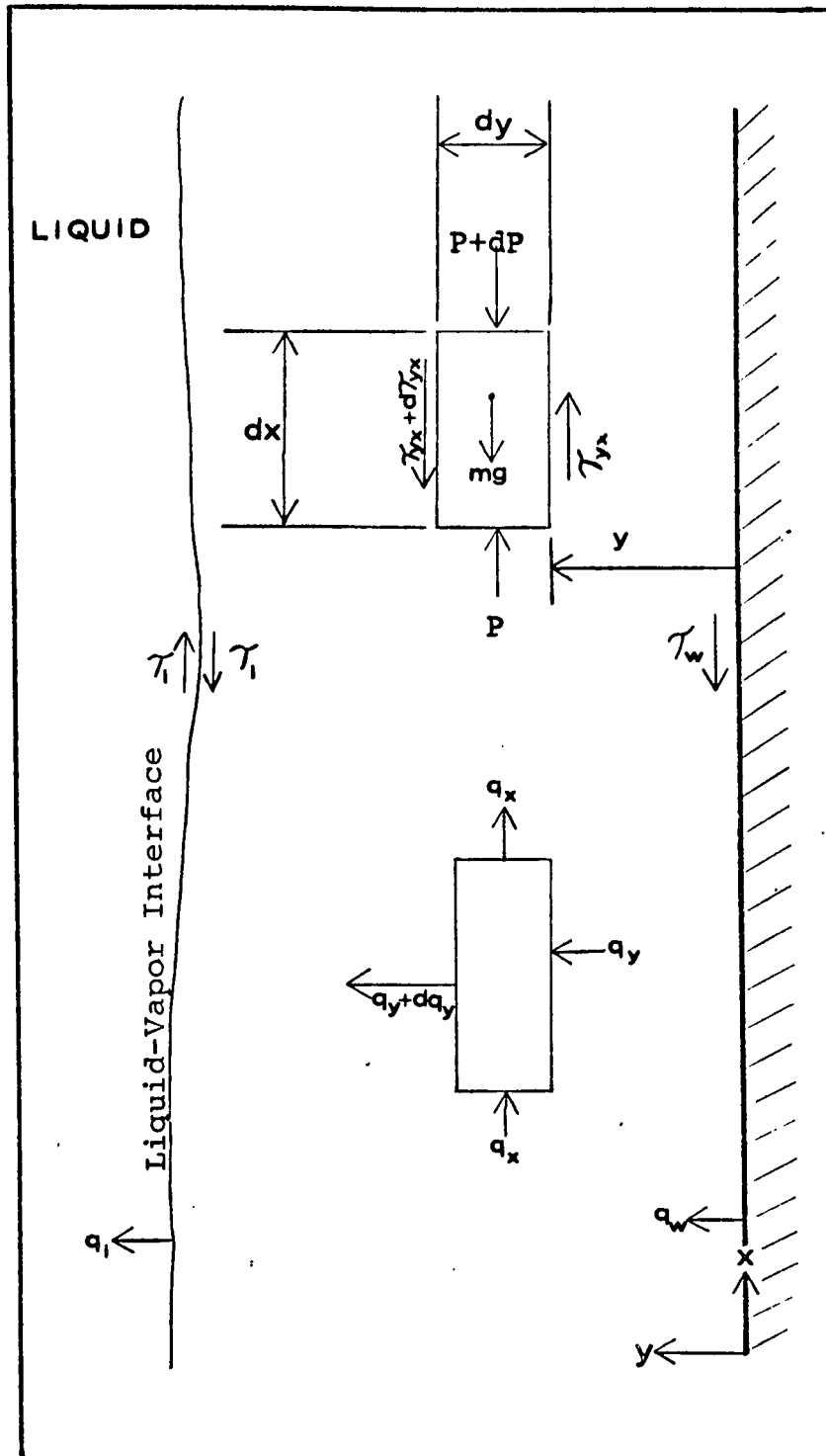


FIGURE 3-3. CONTROL VOLUMES FOR MOMENTUM AND ENERGY BALANCES

$$\left(-\frac{dP}{dx}\right) - \rho g - \frac{d}{dy}(\tau_{yx}) = 0 \quad 3-1$$

The same assumptions applied to the energy equation imply that x-direction transport, q_x , (which includes both conduction and convection) is negligible:

$$\frac{d}{dy}(q_y) = 0 \quad 3-2$$

The assumption that dq_x/dx is much smaller than dq_y/dy might be questioned because of the relatively large amount of energy required to superheat the vapor for many substances with low heats of vaporization. However, the assumption has been used with good results in more extreme cases, such as flow in a round pipe (D-1), or boundary layer flow (D-3). Film boiling should be better suited to this assumption since a large part of the energy crosses the film "intact" to be released at the interface.

The eddy diffusivities, \mathcal{E} and \mathcal{E}_H , are introduced to account for the turbulent transport of momentum and energy as follows:

$$\tau_{yx} = (\mu + \rho\mathcal{E}) \frac{du}{dy}$$

$$q_y = -(\mathcal{K} + \rho C_p \mathcal{E}_H) \frac{dT}{dy}$$

The constant term, $-\left(\frac{dP}{dx} + \rho g\right)$, in equation 3-1 will be represented by K , and equations 3-1 and 3-2 are integrated with respect to y . Then, upon using the above definitions of the eddy diffusivities:

$$\tau_{yx} = Ky + C_1 = (\mu + \rho\mathcal{E}) \frac{du}{dy} \quad 3-3$$

$$q_y = \text{constant} = -(\mathcal{K} + \rho C_p \mathcal{E}_H) \frac{dT}{dy} \quad 3-4$$

Equations 3-3 and 3-4 can be integrated across the vapor film to give the velocity profile as a function of the shear stresses at the boundaries and the temperature profile as a function of the heat flux. The heat transfer coefficient is then found by dividing the heat flux by the temperature difference from the wall to the interface. Integration of the velocity profile gives the mass flow rate, W :

$$W = \int_0^p \rho u f dy \quad 3-5$$

where p and f are the vapor film thickness and the perimeter of the heated wall. With the heat transfer coefficient known as a function of the mass flow rate, the design problem is solved in principle. However, mathematical complications arising from the functional forms of \mathcal{E} and \mathcal{E}_H and the asymmetry of the profiles necessitate a more devious numerical calculation procedure. The mathematical technique used is discussed later in the chapter after the equations for the eddy diffusivities are presented.

C. THE EDDY DIFFUSIVITIES

1. Smooth Tube Eddy Viscosity

For flow along a smooth boundary, several forms of the eddy viscosity distribution have been successfully used to predict rates of turbulent transport. This work will use the relationship suggested by Gill and Scher (G-1):

$$\epsilon_{Gs} = k^2 y^2 (1 - e^{-\phi})^2 \frac{du}{dy} \quad 3-6$$

$$\phi = \frac{y(y_m^+ - a)}{b y_m} \quad 3-7$$

$$y_m^+ = \frac{y_m}{\nu} \left(\frac{\tau_o}{\rho} \right)^{\frac{1}{2}} \quad 3-8$$

where k , a and b are constant parameters, the subscript "o" refers to conditions at the boundary, and the subscript "m" refers to the point at which the local shear stress is zero (which is also the point of maximum velocity).

Simplicity is perhaps the greatest advantage of this formulation of the eddy viscosity in that only one equation applies to the entire flow field, in contrast to other approaches where the flow field must be arbitrarily divided into two or three regions (such as the laminar sublayer, buffer zone and turbulent core). The value of the parameter "a" determines the Reynolds number at which transition from laminar to turbulent flow occurs, since the eddy viscosity becomes zero when "a" equals y_m^+ . For single phase flow in tubes or between parallel plates, Gill and Scher proposed that $a=60$. This predicts transition Reynolds numbers of 1800 and 4800, respectively, for these geometries, and these values are consistent with experimental evidence.

In this work, "a" is taken to be 5 which corresponds to a transition Reynolds number of 33.3. Although no measurements are available,

this value is consistent with the photographic evidence of Hsu (H-5) which indicates that transition occurs at Reynolds numbers of less than 100, and with the stability analysis of Frederking (F-1) which predicts a transition Reynolds number of 5 to 200. In any case, letting "a" be zero or 10, with corresponding transition Re of zero or 133, has little effect on the calculated results. The parameters k and b are here maintained at their values of 0.36 and 22 as normally used for single phase conduit flow.

2. Rough Tube Eddy Viscosity

Experiments have shown that the turbulent momentum transport rate for flow over rough surfaces is greater than that calculated by the equation: $\tau = \rho \epsilon \frac{du}{dy}$. Worley (W-5) has suggested that the transport rate for this case can be given by:

$$\tau = \rho (\epsilon + \epsilon') \frac{du}{dy}$$

where ϵ' is a "wall eddy viscosity" characterized by the nature of the roughness. Worley successfully correlated single phase, rough conduit data in this manner. Here the same approach will be taken under the assumption that the ripples on the liquid interface affect the turbulent transport rates in the same manner as solid roughness elements. The eddy viscosity relation will then be:

$$\epsilon = \epsilon_{GS} + \epsilon'$$

where ϵ_{GS} is the eddy viscosity of Gill and Scher and ϵ' is a constant.

Thus equation 3-3 becomes:

$$\tau_{yx} = Ky + C_1 = (\mu + \rho\epsilon_{GS} + \rho\epsilon') \frac{du}{dy} \quad 3-10$$

A justification for this formulation of the eddy viscosity is presented in Appendix B.

Little has yet been achieved with respect to an a priori prediction of the value of ϵ' to be used for a specified surface. It has been suggested (T-1) that the higher shear stresses experienced in rough tubes occur because of an additive mixing length, l' , induced by the roughness elements. Thus:

$$\epsilon' = l'^2 \frac{du}{dy} \quad 3-11$$

If this mixing length is proportional to the amplitude of the roughness element, η_0 , and if the velocity gradient is taken at the rough surface where ϵ_{GS} is zero, the shear stress at that point is:

$$\tau_0 = (\mu + \rho\epsilon') \left(\frac{du}{dy} \right)_{y=0} \quad 3-12$$

Combining equations 3-12 and 3-11 and solving the resulting equation gives:

$$\epsilon'_{1/2} = -\frac{1}{2} + \frac{1}{2} \left(1 + \frac{4k_1^2 \eta_0^2 \tau_0}{\mu \nu} \right)^{\frac{1}{2}} \quad 3-13$$

where k_e is a proportionality constant. The usefulness of this approach will be discussed in Chapter VI.

3. Eddy Conductivity

The classical approach will be followed in assuming that the eddy conductivity is proportional to the eddy viscosity:

$$\epsilon_H = \gamma \epsilon$$

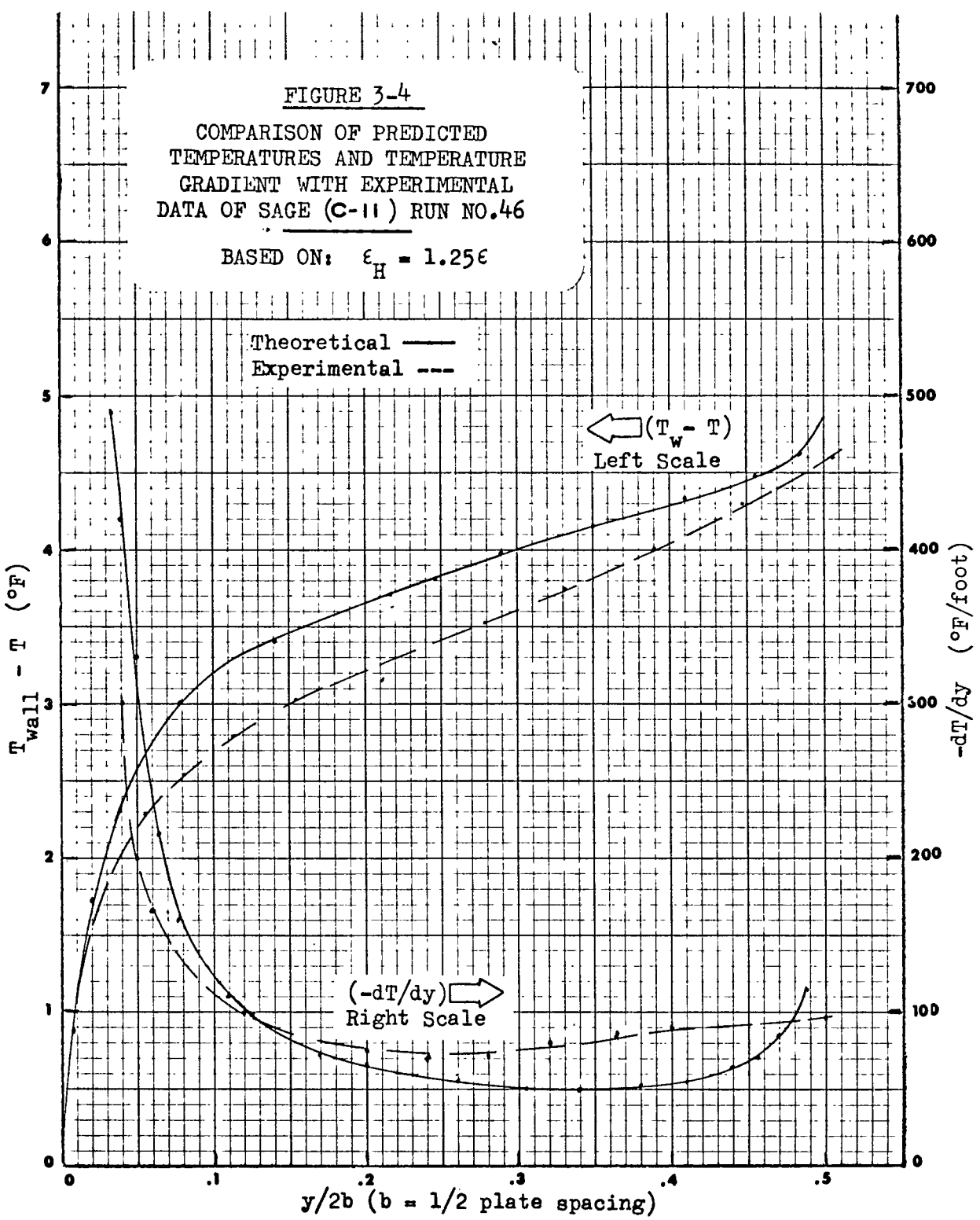
3-14

That this proportionality constant is a function of the position within the flow field and the Reynolds number has been shown by Sage et al (C-11). However, for the sake of simplicity, γ has been given the constant value of 1.25. Temperature profiles for single phase flow between smooth parallel plates have been calculated to determine how closely experimental data can be matched when this value of γ is used. For this calculation, the eddy viscosity of Gill and Scher was used with the constant "a" set at 60. The calculated profiles are compared with the data of Sage (C-11) in Figure 3-4, and reasonably good agreement is shown.

D. INTEGRATION OF THE TRANSPORT EQUATIONS

1. Division of the flow field into a rough and a smooth side

Combining the definitions of the eddy diffusivities given in equations 3-6 through 3-9 and 3-14 with the transport equations (3-3 and 3-4) leads to:



$$T = Ky + C_1 = \left[\mu + \rho \epsilon' + \rho k^2 y^2 (1 - e^{-\phi})^2 \frac{du}{dy} \right] \frac{du}{dy} \quad 3-15$$

$$q_y = q_{y_0} = - \left[k + \gamma \rho c_p \epsilon' + \gamma \rho c_p k^2 y^2 (1 - e^{-\phi})^2 \frac{du}{dy} \right] \frac{dT}{dy} \quad 3-16$$

For symmetrical parallel flows, these equations could be integrated in a straightforward manner from the wall to the plane of zero shear stress, which is the plane of symmetry. However, the velocity and temperature profiles in film boiling are non-symmetrical because the interfacial boundary is rough and moving while the solid boundary is smooth and stationary. Therefore, equations 3-15 and 3-16 must be integrated all the way from one boundary to the other. However, two problems then arise because of the nature of the eddy diffusivities. As shown by its definition in equation 3-6, the eddy viscosity is damped near the boundary where y is close to zero but then begins to increase at positions farther from the wall. When the integration is carried to the second boundary, the eddy viscosity should again approach zero since the eddies will again be under the damping influence of a boundary. Thus, the distance, y , in equation 3-6 should be measured from the "nearest" boundary, where nearest is to be defined. The second problem occurs because one boundary is rough while the other is smooth, and the wall eddy viscosity, ϵ' , would be expected to exist only "near" the rough surface.

The "nearest" boundary to a position in the flow field will be defined as that boundary which is on the same side of the plane of zero

shear stress as the position in question. Thus, in Figure 3-5, the nearest boundary to point M is the interface. This assumption about the region in which the eddy viscosity is effective is equivalent to postulating that there is no momentum transport across the plane of zero shear stress.

Because of the numerical techniques required to integrate equations 3-15 and 3-16, it will be convenient to divide the non-symmetrical flow field into two parts and make the integrations separately for each part. The results from the separate integrations are then combined by properly matching the boundary conditions. The discussion of this procedure will be made clearer by referring to Figure 3-5.

The side of the vapor film between the wall and the point of maximum velocity (or zero shear stress) is called the A-side and the distance between these points is called A. The other side is the B-side, and the distance from the interface to the point of maximum velocity is B. Let p represent the film thickness and let y and y_b be the measures of distances from the wall and from the interface, respectively, into the vapor film. Thus, for any point:

$$y + y_b = p \quad 3-17$$

The velocities on the A- and B- sides are u and u_b , respectively, while the maximum velocity (at $y=A$ or $y_b=B$) is:

$$u_m = u_{mb} \quad 3-18$$

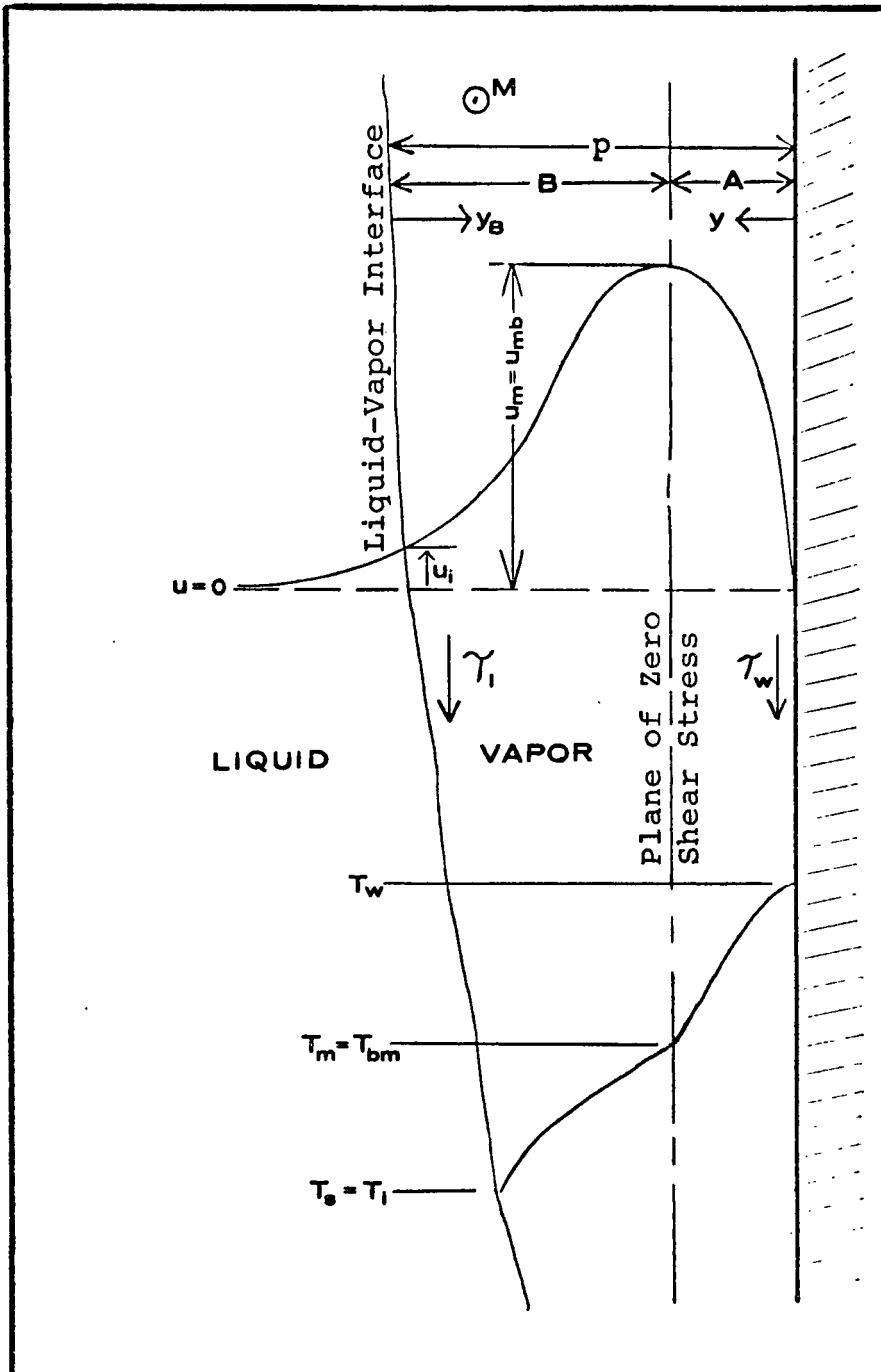


FIGURE 3-5. DIVISION OF THE VAPOR FILM INTO A SMOOTH SIDE AND A ROUGH SIDE

and u_i is the interfacial velocity. Symbols for the shear stresses are τ_w at the wall and τ_i at the interface, while τ_o may represent the shear stress at either boundary i or w . Likewise, q_w , q_i and q_o are the boundary heat fluxes. T and T_b represent the temperatures within the film for the two sides. When $y = A$ or $y_b = B$,

$$T = T_m = T_{mb} \quad 3-19$$

T_w , T_i and T_o are the boundary temperatures.

2. Formulation of the Separate Equations

The transport equations will now be written separately for each side of the flow field, using the suitable definitions of the eddy diffusivities in each case. The integration procedure will be described in this section, and the matching procedure will be discussed in Section E.

For the A-side, equations 3-3, 3-4, 3-14 and 3-6 to 3-8 lead to:

$$T = Ky + C_1 = \left[\mu + \rho k^2 y^2 (1 - e^{-\phi})^2 \frac{du}{dy} \right] \frac{du}{dy} \quad 3-20$$

$$\phi = \frac{y(A^+ - a)}{bA} \quad 3-21$$

$$A^+ = \frac{A}{\nu} \left(\frac{\tau_w}{\rho} \right)^{1/2} \quad 3-22$$

$$q_y = - \left[k + \gamma \rho c_p k^2 y^2 (1 - e^{-\phi})^2 \frac{du}{dy} \right] \frac{dT}{dy} \quad 3-23$$

Considering also equation 3-9, the B-side equations are:

$$T_b = Ky_b + C_{1b} = \left[\mu + \rho \epsilon' + \rho k^2 y_b^2 (1 - e^{-\phi_b})^2 \frac{du_b}{dy_b} \right] \frac{du_b}{dy_b} \quad 3-24$$

$$\phi_b = \frac{y_b (B^+ - a)}{bB} \quad 3-25$$

$$B^+ = \frac{B}{\nu} \left(\frac{\tau_i}{\rho} \right)^{1/2} \quad 3-26$$

$$q_{yb} = - \left[k + \gamma \rho c_p \epsilon' + \gamma \rho c_p k^2 y_b^2 (1 - e^{-\phi_b})^2 \frac{du_b}{dy_b} \right] \frac{dT_b}{dy_b} \quad 3-27$$

To evaluate the constant of integration C_1 , it is seen that at $y=0$, $T = T_w = C_1$. Also, at $y=A$, $T=0$, so that $K = -A/\tau_w$. This leads to:

$$T = \tau_w \left(1 - \frac{y}{A} \right) \quad 3-28$$

Proceeding similarly on the B-side yields:

$$T_b = \tau_i \left(1 - \frac{y_b}{B} \right) \quad 3-29$$

In either case:

$$K = -\rho g + \left(-\frac{dP}{dx}\right) = -\frac{A}{T_w} = -\frac{B}{T_i} \quad 3-30$$

Finally, putting equations 3-20, 3-23, 3-24 and 3-27 into dimensionless form gives for the A-side:

$$\frac{T}{T_w} = 1 - \frac{y^+}{A^+} = \left[1 + k^2 y^{+2} (1 - e^{-\phi})^2 \frac{du^+}{dy^+} \right] \frac{du^+}{dy^+} \quad 3-31$$

$$\frac{q}{q_w} = 1 = \left[\frac{1}{Pr} + \gamma k^2 y^{+2} (1 - e^{-\phi})^2 \frac{du^+}{dy^+} \right] \frac{dT^+}{dy^+} \quad 3-32$$

and for the B-side:

$$\frac{T_b}{T_i} = 1 - \frac{y_b^+}{B^+} = \left[(1 + \frac{\epsilon'}{\nu}) + k^2 y_b^{+2} (1 - e^{-\phi_b})^2 \frac{du_b^+}{dy_b^+} \right] \frac{du_b^+}{dy_b^+} \quad 3-33$$

$$\frac{q_b}{q_i} = 1 = \left[\left(\frac{1}{Pr} + \gamma \frac{\epsilon'}{\nu} \right) + \gamma k^2 y_b^{+2} (1 - e^{-\phi_b})^2 \frac{du_b^+}{dy_b^+} \right] \frac{dT_b^+}{dy_b^+} \quad 3-34$$

Since the integration proceeds similarly for both sides, the details will be presented for one side only. Make the following substitutions:

$$\psi = 1 - \frac{y^+}{A^+} \quad ; \quad \beta = (1 + \frac{\epsilon'}{\nu}) \quad ; \quad \sigma = \left(\frac{1}{Pr} + \gamma \frac{\epsilon'}{\nu} \right) \quad ; \quad \theta = 1 - e^{-\phi} \quad 3-35$$

where β and σ become 1 and $\frac{1}{\rho r}$ for the A-side. Solving the quadratic equation in $\frac{du^+}{dy^+}$ given by equation 3-31 or 3-33 yields:

$$\frac{du^+}{dy^+} = \frac{-\beta + (\beta^2 + 4k^2 y^{+2} \theta^2 \psi)^{\frac{1}{2}}}{2k^2 y^{+2} \theta^2} \quad 3-36$$

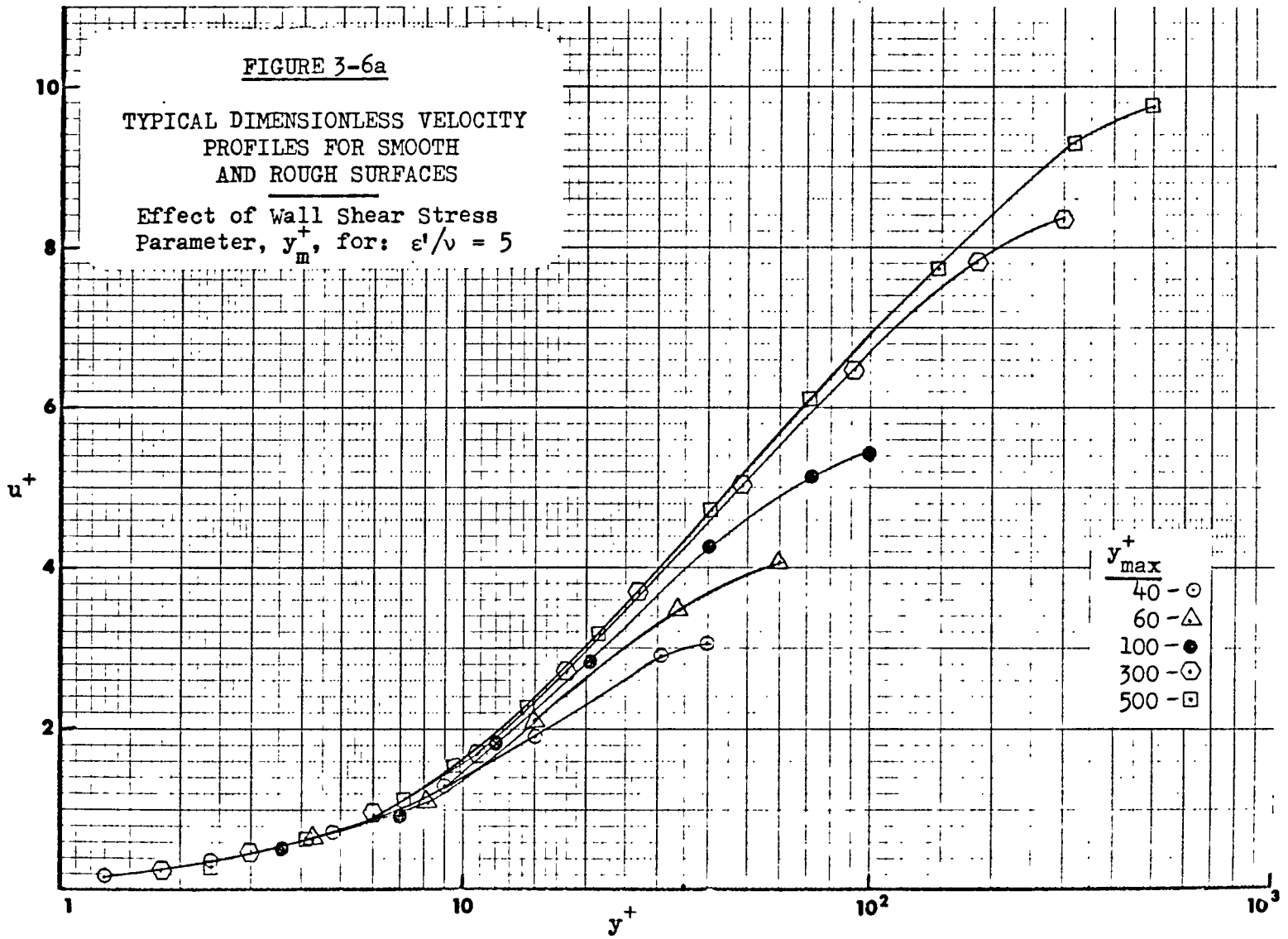
where only the positive square root has physical meaning. The numerator and denominator are both multiplied by $(\beta + (\beta^2 + 4k^2 y^{+2} \theta^2 \psi)^{\frac{1}{2}})$ with the result that:

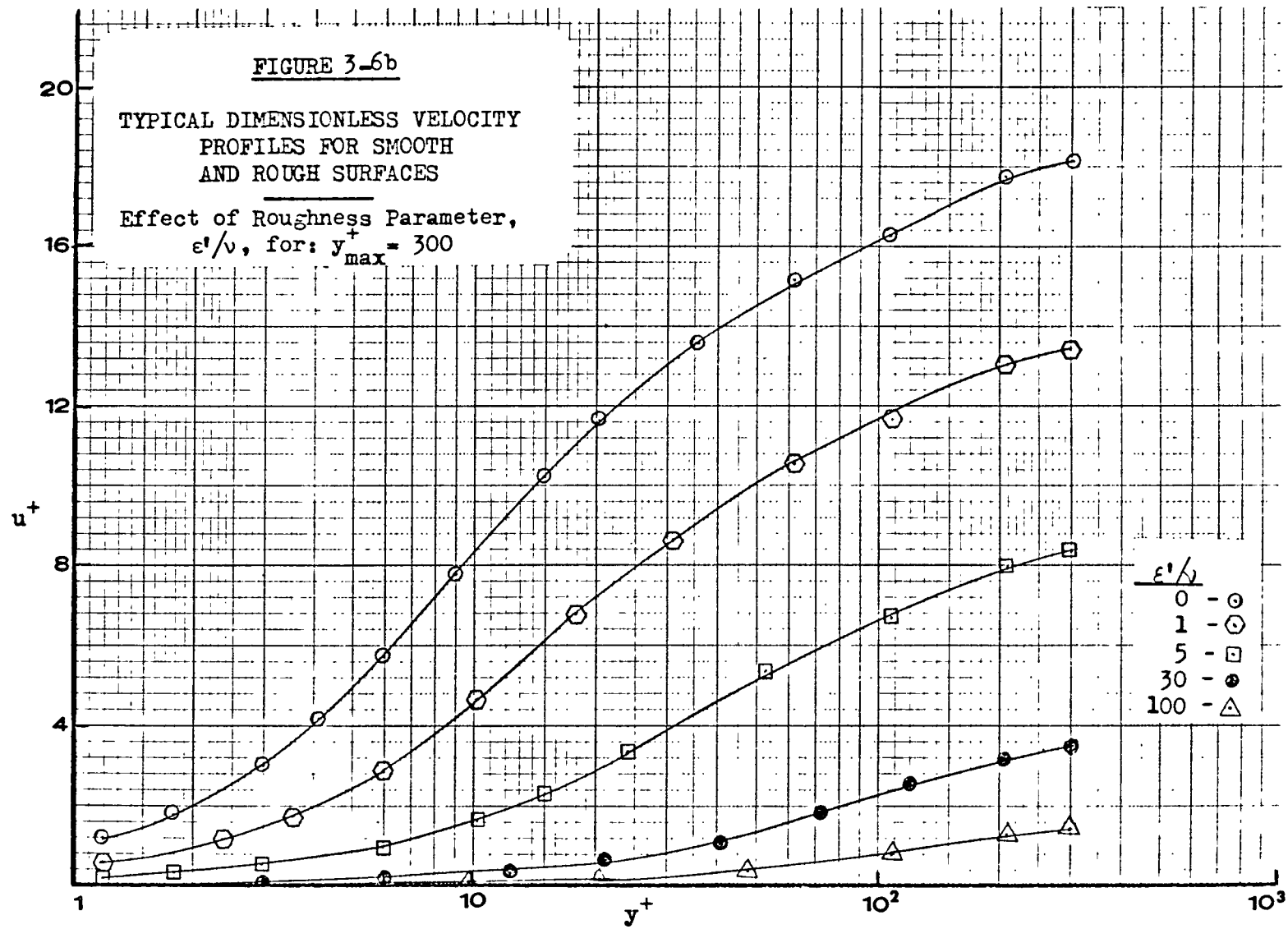
$$\frac{du^+}{dy^+} = \frac{2\psi}{\beta + (\beta^2 + 4k^2 y^{+2} \theta^2 \psi)^{\frac{1}{2}}} \quad 3-37$$

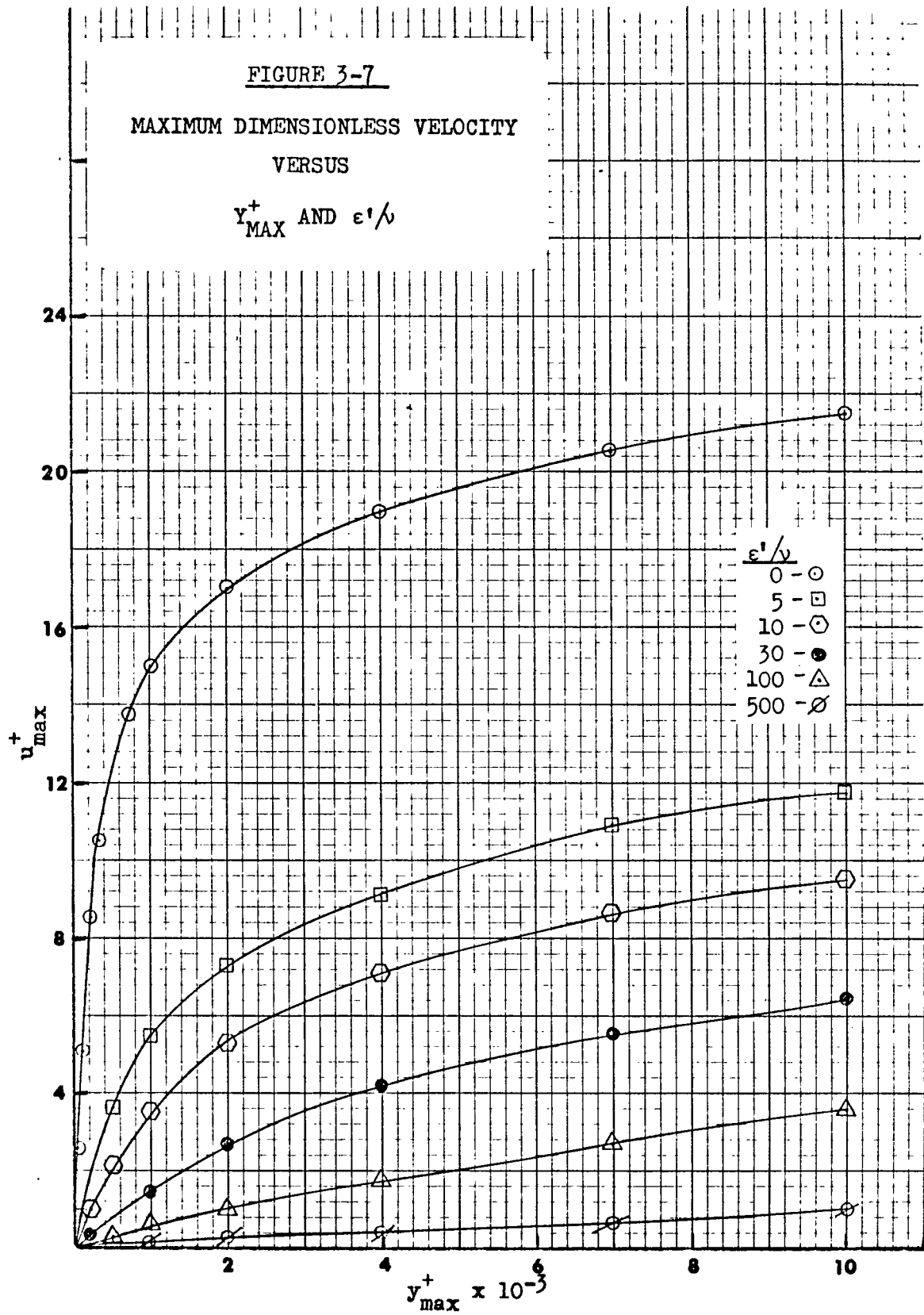
Upon integration:

$$u^+ = u_o^+ + \int_0^{y^+} \frac{2\psi dy^+}{\beta + (\beta^2 + 4k^2 y^{+2} \theta^2 \psi)^{\frac{1}{2}}} \quad 3-38$$

Thus, the parameters involved in the calculation of the velocity profile are u_o^+ (the dimensionless velocity at the boundary), ϵ/ν , and y_m^+ (A^+ or B^+). Both u_o^+ and ϵ/ν are zero for the A-side. Typical dimensionless velocity profile curves for the case of no interfacial velocity are presented in Figures 3-6a and 6b in terms of y_m^+ and ϵ/ν . Two curves are required to fit a flow situation, one each for the A-side and the B-side, as discussed in Section E where the matching procedure is described. Figure 3-7 shows the $u_m^+, y_m^+, \epsilon/\nu$ relationship.







Definition of the local film Reynolds number, based on the hydraulic radius and the assumption that the wall width is much greater than the film thickness, is:

$$Re = \frac{2 \bar{u} \rho}{\nu} \quad 3-39$$

or

$$Re = \frac{2}{\nu} \int_0^b u dy = 2 \int_0^{p^+} u^+ dy^+ \quad 3-40$$

A Reynolds number will be defined for each side of the flow field as though the velocity profile were symmetrical with respect to that side:

$$Re_a = 4 \int_0^{A^+} u^+ dy^+ \quad 3-41$$

$$Re_b = 4 \int_0^{B^+} u_b^+ dy_b^+ \quad 3-42$$

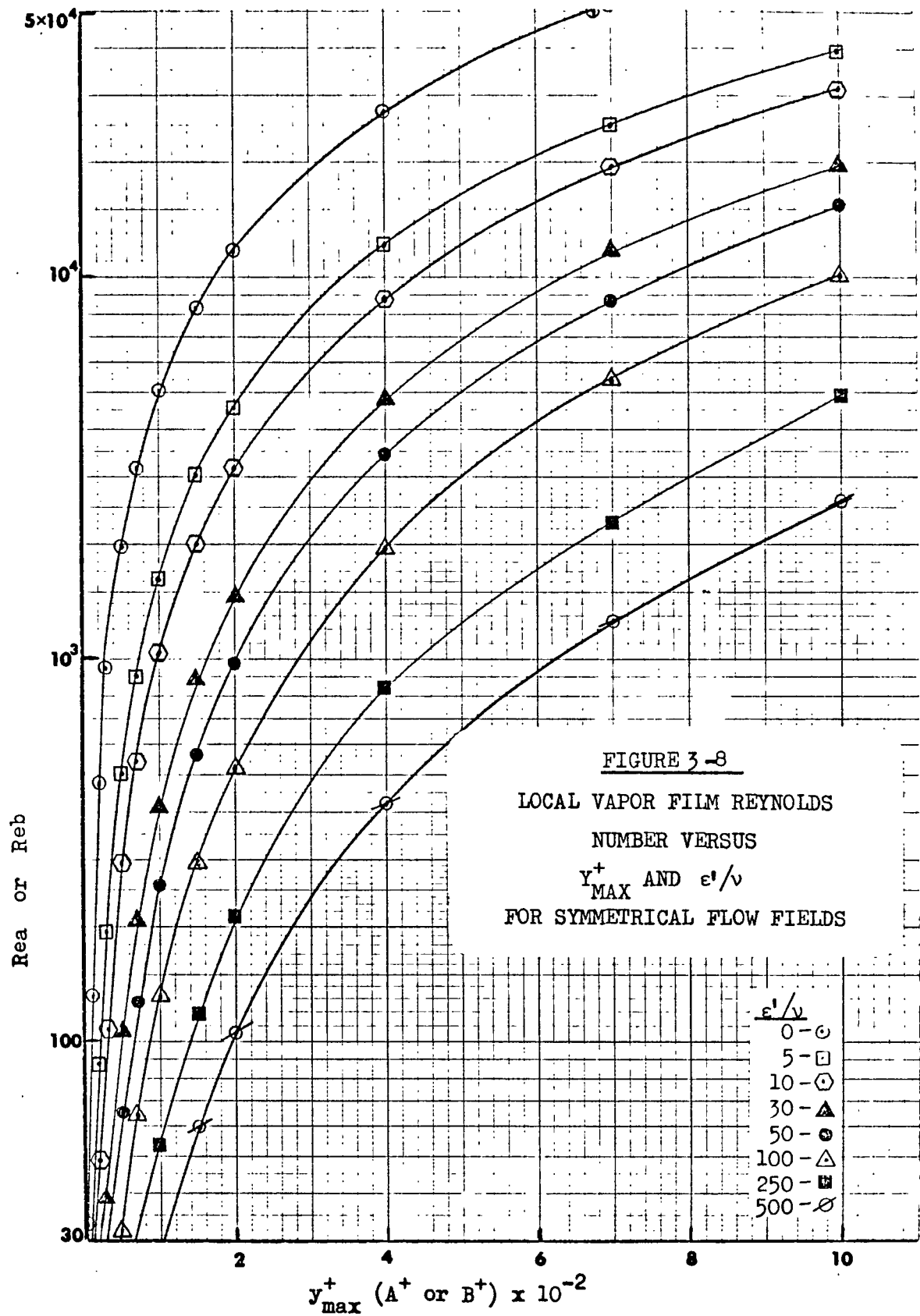
Then, based on equation 3-38:

$$Re_a = 8 \int_0^{A^+} \int_0^{y^+} \frac{(1 - y^+/A^+) dy^+}{1 + \sqrt{1 + 4k^2 y^{+2} (1 - e^{-\phi})^2 (1 - y^+/A^+)}} dy^+ \quad 3-43$$

$$Re_b = 4u_{ib}^+ B^+ + 8 \int_0^{B^+} \int_0^{y_b^+} \frac{(1 - y_b^+/B^+) dy_b^+}{(1 + \xi_b') + \sqrt{(1 + \xi_b')^2 + 4k^2 y_b^{+2} (1 - e^{-\phi_b})^2 (1 - y_b^+/B^+)}} dy_b^+ \quad 3-44$$

Typical curves of Re_a and Re_b with parameters of y_m^+ and ξ_b' are shown in Figure 3-8 for the case of zero interfacial velocity.

The absolute velocity at any point is not involved in the definitions of the eddy diffusivities used in this work. Therefore, the magnitude of the interfacial velocity does not affect the shape of the



velocity profile for a specified value of B^+ . Instead, the contribution of the interfacial velocity is an additive one as shown in equations 3-38 and 3-44 for the B-side velocity profile and Reynolds number. Of course, the absolute value of the interfacial velocity will affect the matching procedure as discussed in the next section. An interesting point that only arises upon consideration of a moving boundary is that the absolute velocity does enter into some equations for eddy viscosity such as that of Diessler (D-1) where $\epsilon = \eta^2 u y$. It seems reasonable to suppose that the relative velocity is controlling with respect to the turbulent transport rates, as is implicit in ϵ_{GS} , so that the term $(u - u_i)$ would replace u in Diessler's equation. However, some experimental evidence with respect to this point would be of interest.

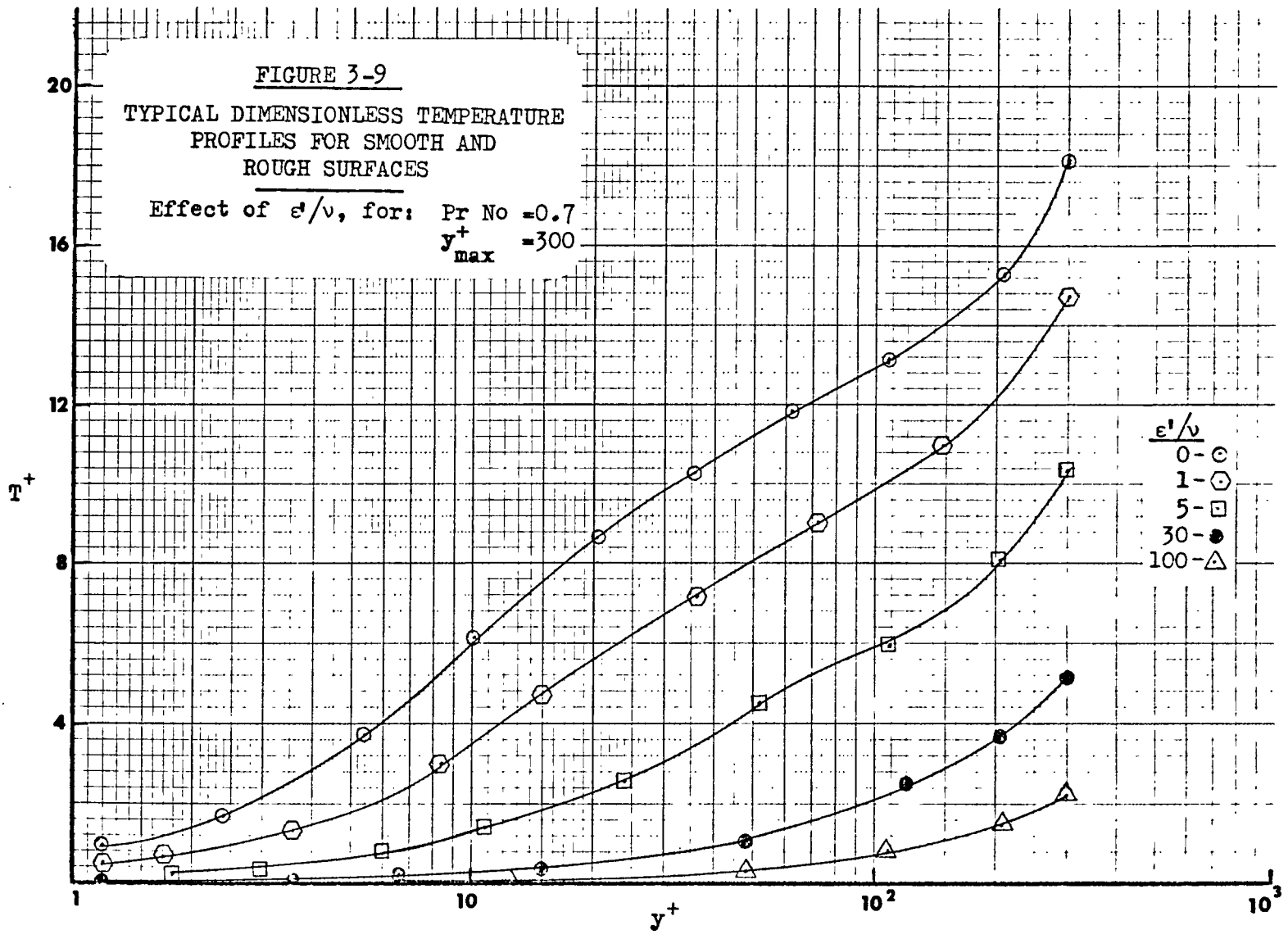
The calculation of the temperature profiles proceeds in a similar way. Thus, equation 3-32 or 3-34 leads to:

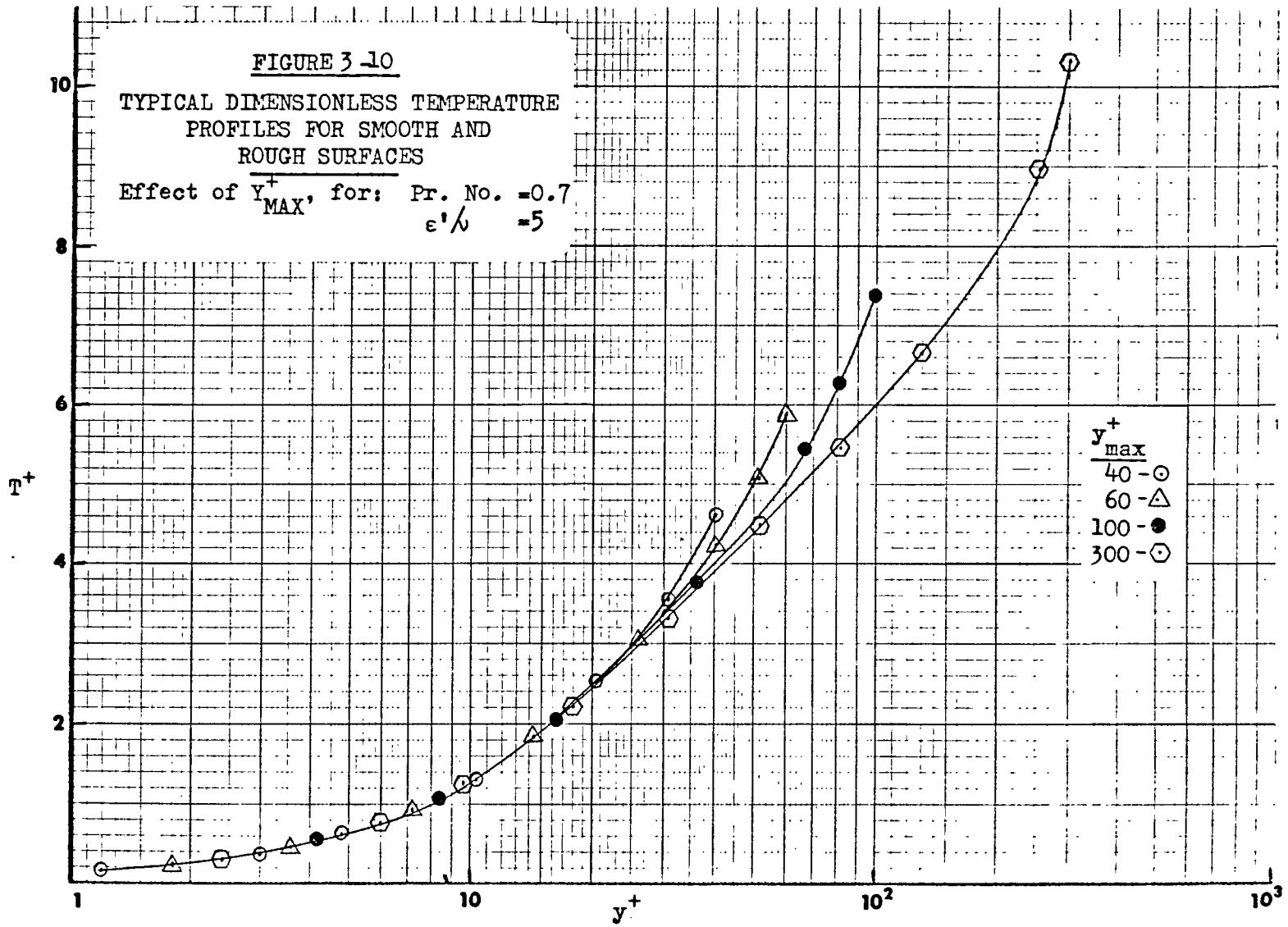
$$\int_0^{T^+} dT^+ = T^+ = \int_0^{y^+} \frac{dy^+}{\sigma + \gamma k^2 y^{+2} \theta^2 \frac{du^+}{dy^+}} \quad 3-45$$

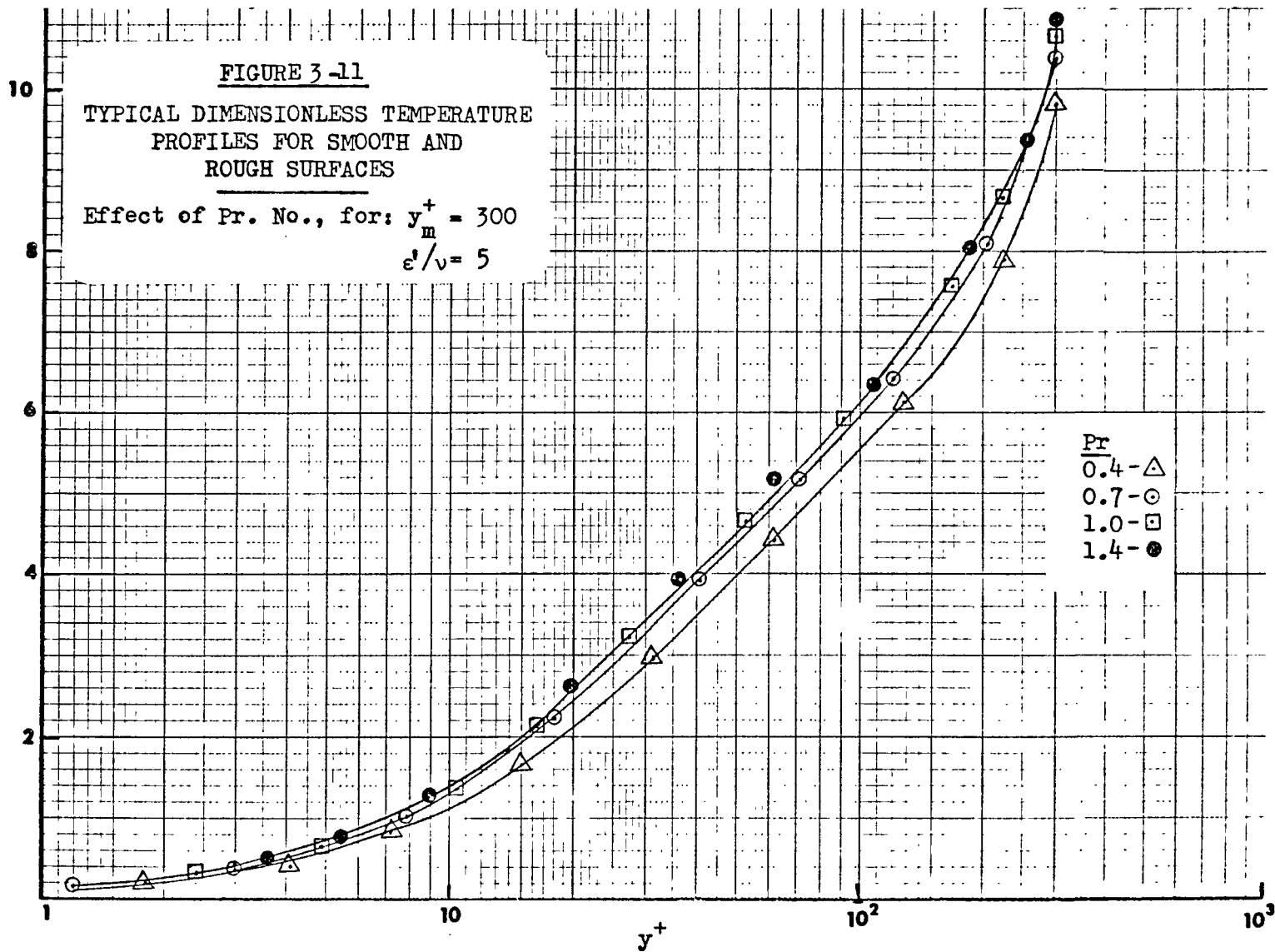
since T^+ at a boundary is zero by definition. Substituting from equation 3-36 gives:

$$T^+ = \int_0^{y^+} \frac{dy^+}{\sigma - \frac{1}{2}\gamma\beta + \frac{1}{2}\gamma\sqrt{\beta^2 + 4k^2 y^{+2} \theta^2 \psi}} \quad 3-46$$

Typical dimensionless temperature profiles are presented in Figures 3-9 to 3-11 in terms of the parameters y_m^+ , Pr and ϵ/ν .







The Nusselt No. for the entire film is defined by:

$$Nu = \frac{hp}{k} \quad 3-47$$

where the heat transfer coefficient, h , is:

$$h = \frac{q_w}{T_w - T_s} \quad 3-48$$

Note that the interfacial temperature is used to define h even though the bulk fluid may be subcooled. This is based on the premise that the liquid at the interface will be at the saturation temperature in any case. Thus, for a given vapor Reynolds number the local heat flux will be independent of the degree of liquid subcooling. Of course, the rate of new vapor generation at this local position will be determined by both the local heat flux and the amount of energy that must go to local heating of the liquid. Based on the definitions for T^+ , Pr , and ρ^+ , equation 3-47 reduces to:

$$Nu = \frac{\rho^+ Pr}{T_i^+} \quad 3-49$$

Note that ρ^+ and T_i^+ , without the subscript b , are defined in terms of the wall shear stress and heat flux:

$$\rho^+ = \frac{\rho}{\nu} \left(\frac{\tau_w}{\rho} \right)^{1/2}$$

$$T_i^+ = \frac{(T_w - T_i) \rho c_p}{q_w} \left(\frac{\tau_w}{\rho} \right)^{1/2} \quad 3-50$$

Of course, T_{ib}^+ would be zero:

$$T_{ib}^+ = \frac{(T_i - T_i) \rho c_p (\frac{\tau_i}{\rho})^{\frac{1}{2}}}{q_i} \equiv 0 \quad 3-51$$

As with the Reynolds number, a Nusselt No. for each side will be defined as though the flow field were symmetrical with respect to that side. For the symmetrical case, $p^+ = 2y_m^+$ and $T_i^+ = 2T_m^+$.

Thus:

$$Nu_a = \frac{A^+ Pr}{T_m^+} \quad 3-52$$

$$Nu_b = \frac{B^+ Pr}{T_{mb}^+} \quad 3-53$$

Both the temperature profile and Nusselt No. are completely independent of the interfacial velocity. However, the Nusselt versus Reynolds No. relationship will be affected by the interfacial velocity because of the latter's effect on the Reynolds No.

The Nusselt number is not a convenient parameter for correlating experimental data because its determination requires a knowledge of the actual vapor film thickness, but the film thickness is usually not known. Therefore, a new dimensionless group, CC, will be defined. From equations 3-50 and 3-47, it follows that:

$$Nu = \frac{h p^+ \nu}{k (\tau_w / \rho)^{\frac{1}{2}}} \quad 3-54$$

$$\tau_w = \frac{A^+ \nu}{(\tau_w/\rho)^{1/2} \left(-\frac{dP}{dx} - \rho g\right)} \quad 3-55$$

Thus:

$$\left(\frac{\tau_w}{\rho}\right)^{1/2} = \left[\frac{A^+ \nu}{\rho \left(-\frac{dP}{dx} - \rho g\right)} \right]^{1/3}$$

$$Nu = \frac{h \rho^+ \nu}{k} \left[\frac{A^+ \nu}{\rho \left(-\frac{dP}{dx} - \rho g\right)} \right]^{1/3}$$

$$\frac{\rho^+}{Nu A^{+1/3}} \stackrel{\text{def.}}{=} CC = \frac{k}{h} \left[\frac{\rho \left(-\frac{dP}{dx} - \rho g\right)}{\mu^2} \right]^{1/3} \quad 3-56$$

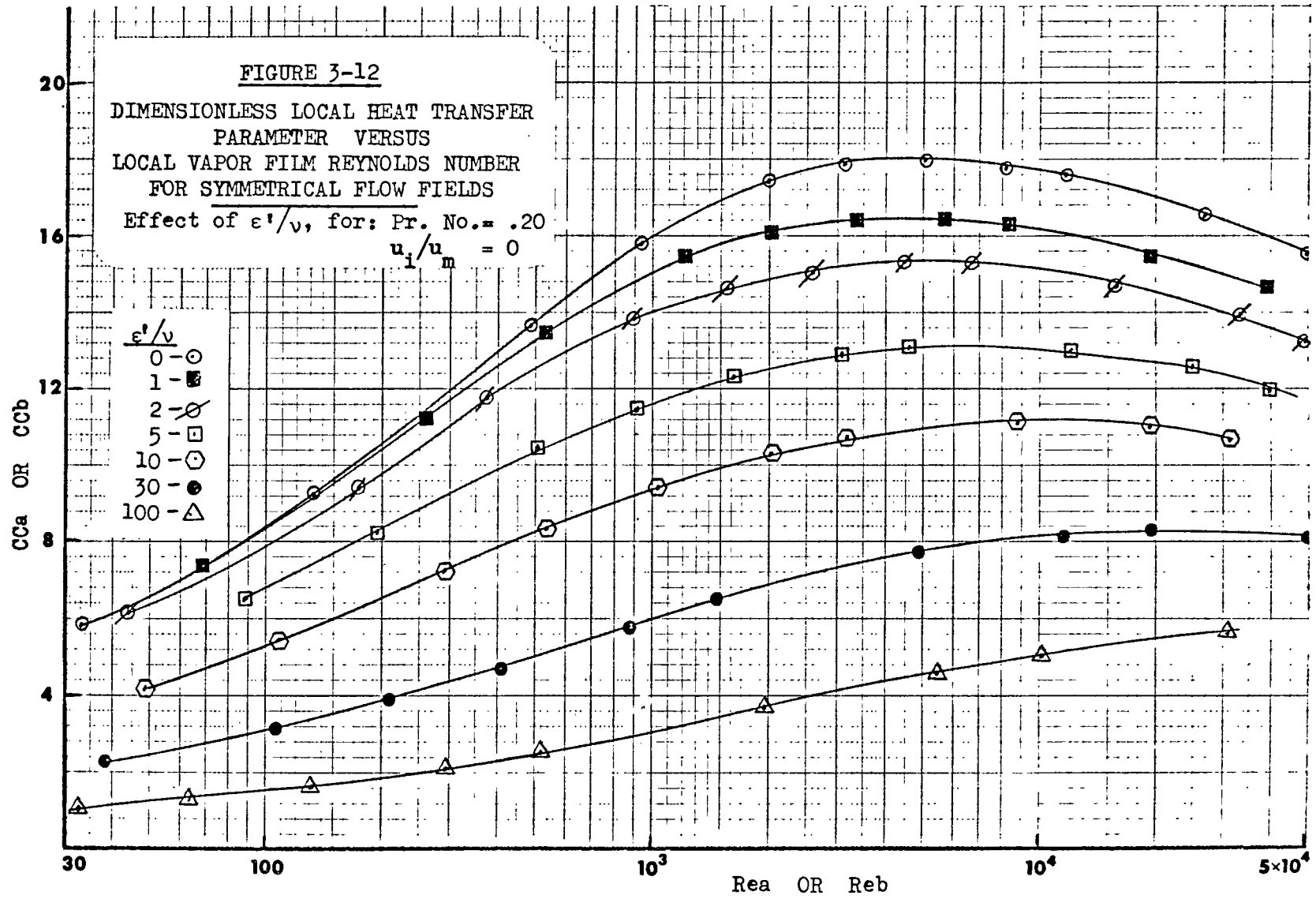
As before, the CC number is also defined for each side as though the entire flow field were symmetrical with respect to that side. In such a case, ρ^+ would be twice A^+ or twice B^+ , and Nu would equal Nu_a or Nu_b .

Therefore:

$$CC_a = \frac{2 A^{+2/3}}{Nu_a} \quad 3-57$$

$$CC_b = \frac{2 B^{+2/3}}{Nu_b} \quad 3-58$$

Typical curves of CC_a and CC_b as functions of ϵ'/ν , Pr and either Re_a or Re_b are presented in Figures 3-12 to 3-18. As with the previous theoretical curves presented, these can be used directly when the roughness on each surface is the same so that the flow field is symmetrical. For non-symmetrical flows, two curves must be used and properly matched.



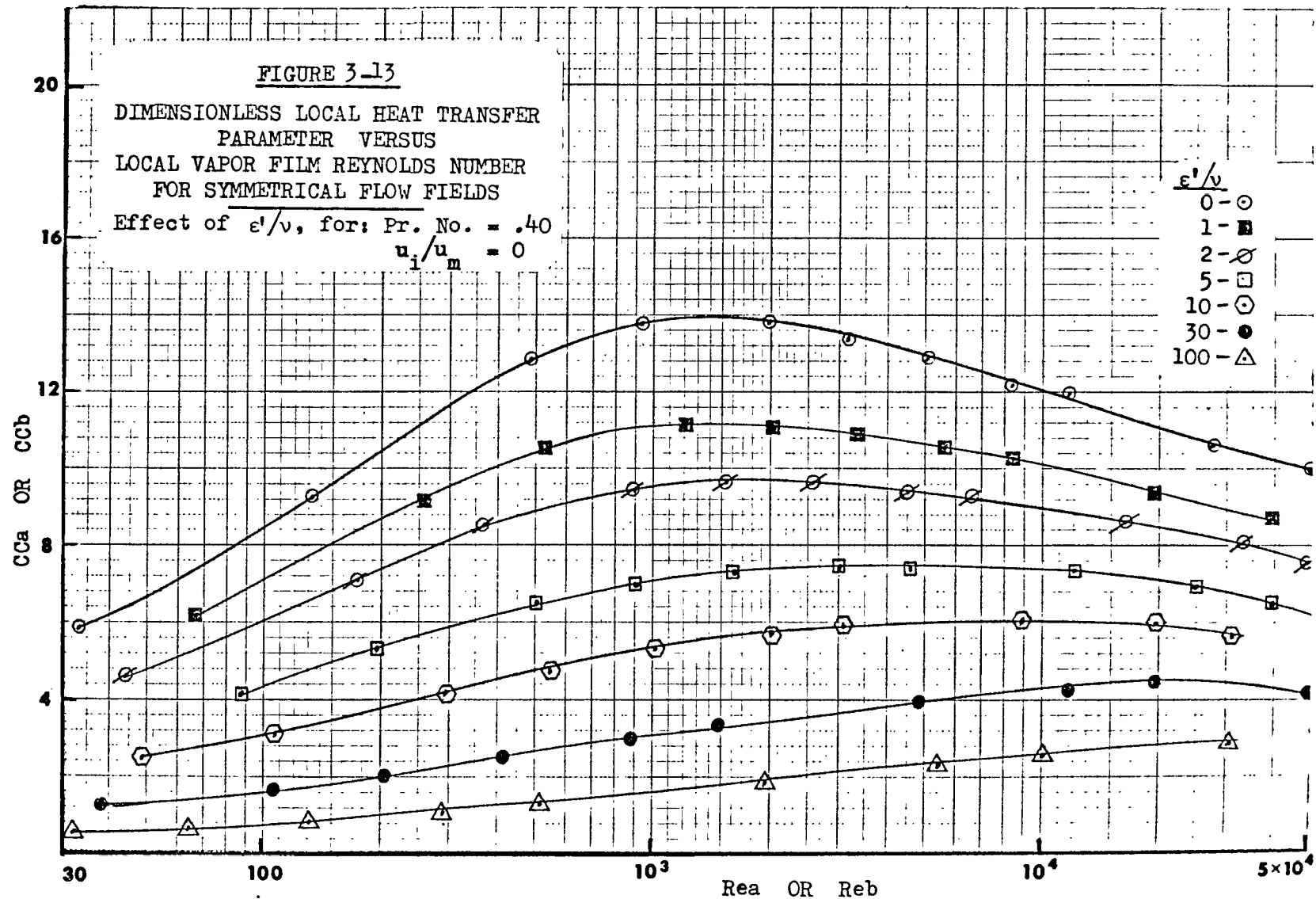
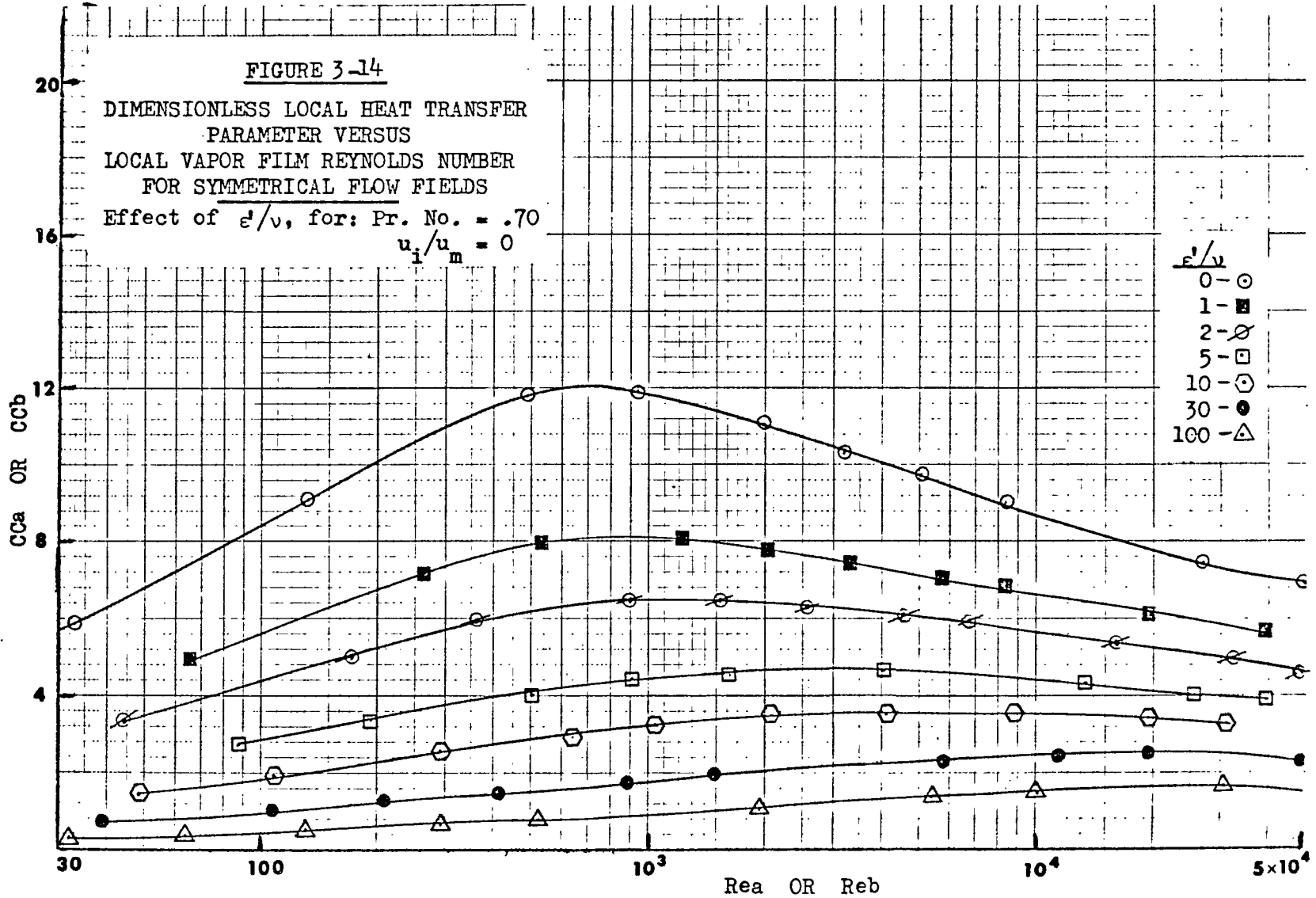
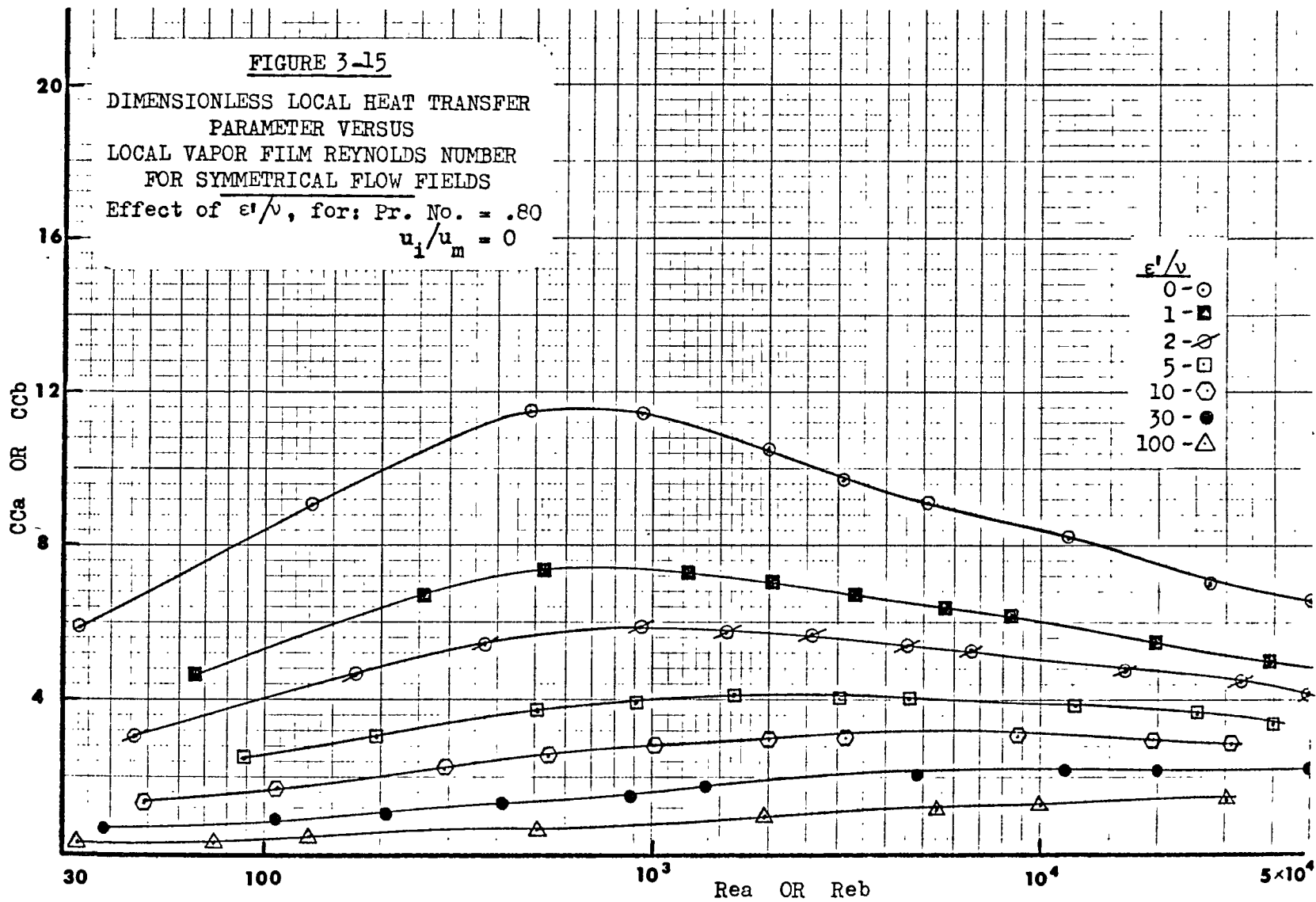


FIGURE 3-14

DIMENSIONLESS LOCAL HEAT TRANSFER
PARAMETER VERSUS
LOCAL VAPOR FILM REYNOLDS NUMBER
FOR SYMMETRICAL FLOW FIELDS

Effect of ϵ'/ν , for: Pr. No. = .70
 $u_i/u_m = 0$





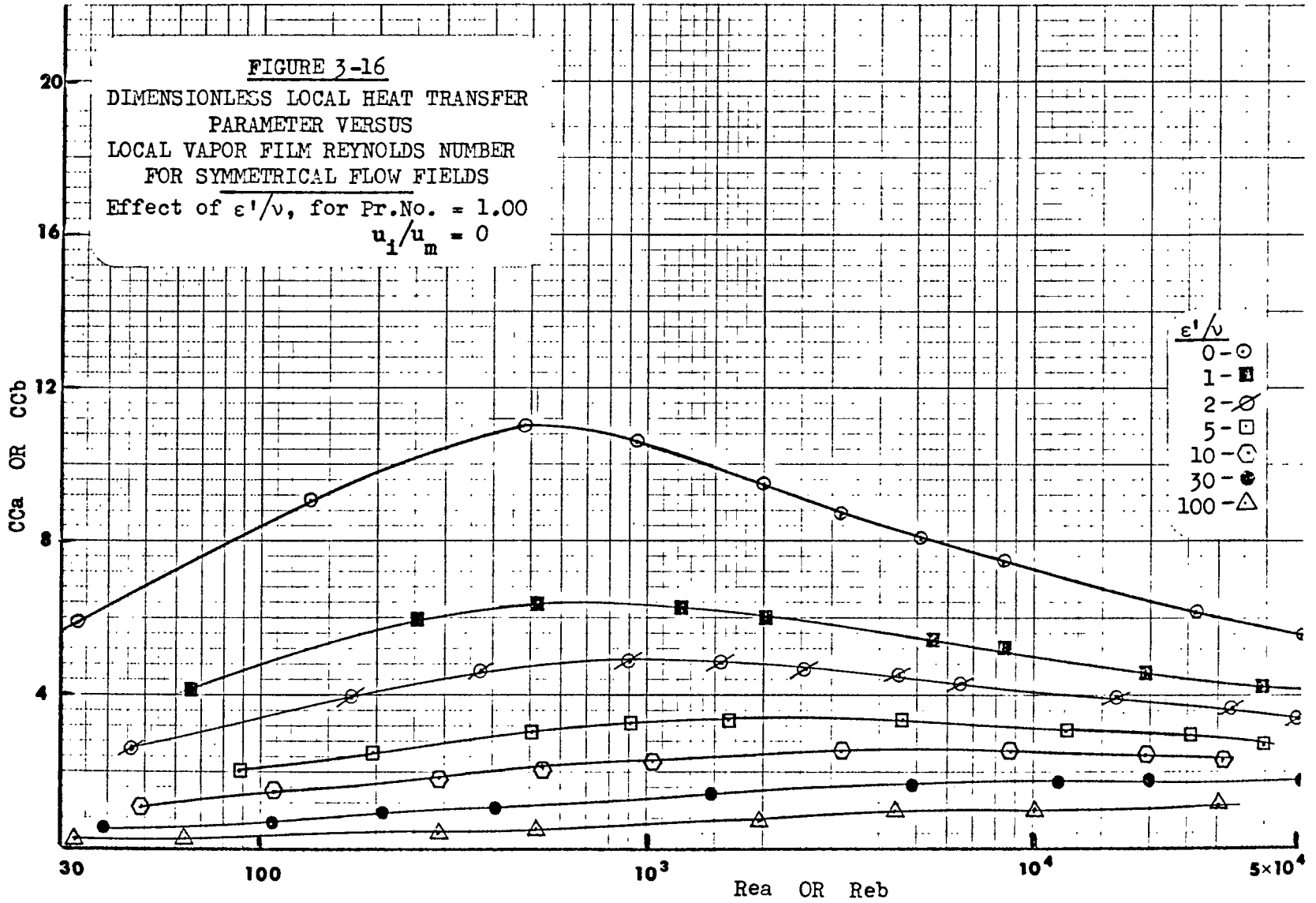
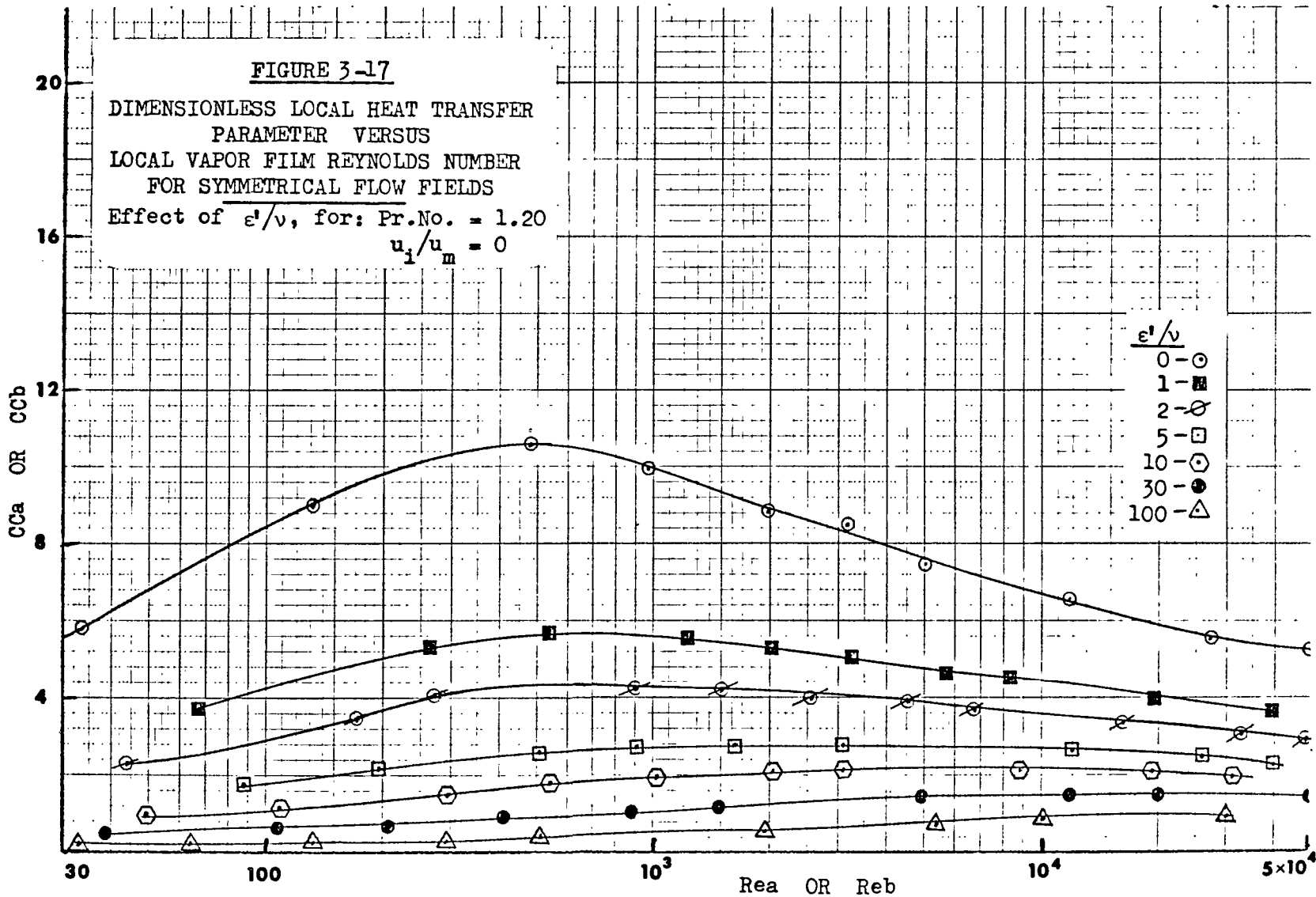
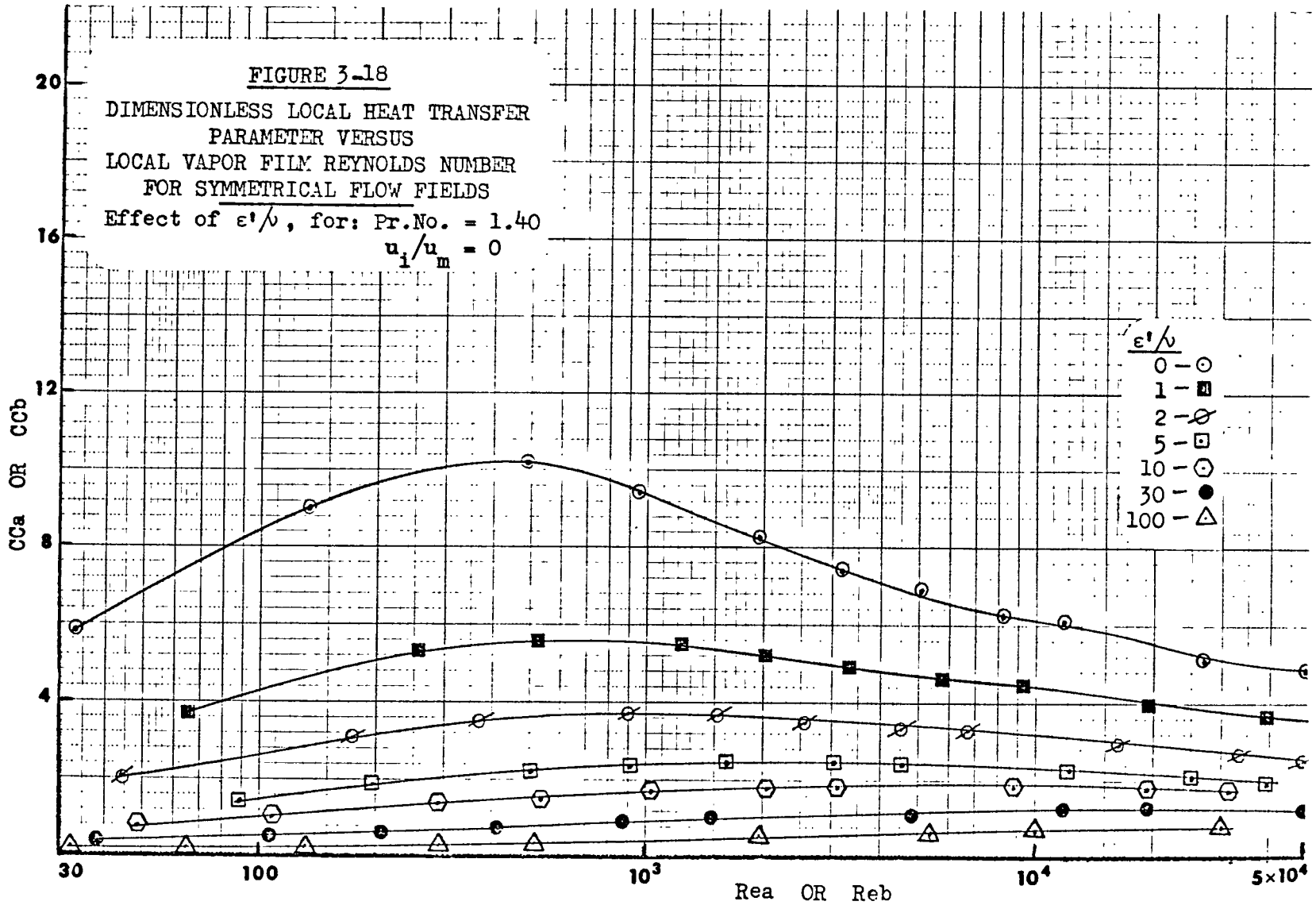


FIGURE 3-17

DIMENSIONLESS LOCAL HEAT TRANSFER
PARAMETER VERSUS
LOCAL VAPOR FILM REYNOLDS NUMBER
FOR SYMMETRICAL FLOW FIELDS

Effect of ϵ'/ν , for: Pr.No. = 1.20
 $u_i/u_m = 0$





E. THE MATCHING PROCEDURE

At this point, relationships have been found on the smooth-walled A-side for u_m^+ and Re_a as a function of A^+ . On the rough-walled B-side, however, u_{mb}^+ and Re_b are functions of three parameters: B^+ , ϵ/ν and u_{ib}^+ . It is now necessary to find the Reynolds number for the entire vapor film as a function of A^+ , ϵ/ν and u_{ib}^+ . It will be shown that B^+ and Re are uniquely determined when these three parameters are specified. First, however, the interfacial velocity parameter, u_{ib}^+ , will be put into the more convenient form of a ratio of the interfacial velocity to the maximum velocity, u_i/u_m . It follows directly from the definitions that $u_i/u_m = u_{ib}^+/u_{mb}^+$.

Let v_{mb}^+ represent the maximum velocity, u_{mb}^+ , that would be calculated for the B-side if the interfacial velocity were zero. For a specified value of B^+ , the shape of the velocity profile is independent of the interfacial velocity. Thus, it follows from equation 3-38 that for any value of u_{ib}^+ :

$$u_{mb}^+ - u_{ib}^+ = v_{mb}^+ \quad 3-59$$

This may be rewritten as:

$$u_{mb}^+ = \left(\frac{u_{ib}^+}{u_{mb}^+} \right) u_{mb}^+ + v_{mb}^+$$

$$u_{mb}^+ = v_{mb}^+ \left(1 - \frac{u_i}{u_m} \right)^{-1} \quad 3-60$$

Combining equations 3-59 and 3-60 leads to:

$$u_{ib}^+ = v_{mb}^+ \left(1 - \frac{u_i}{u_m}\right)^{-1} - v_{mb}^+$$

$$u_{ib}^+ = v_{mb}^+ \frac{(u_i/u_m)}{1 - (u_i/u_m)} \quad 3-61$$

The quantity v_{mb}^+ is the term that has been calculated for the B-side as a function of B^+ and ϵ/ν , for the integration of equation 3-38 has been carried out for u_o^+ equal to zero. The values of u_{mb}^+ in Figure 3-7 are actually values of v_{mb}^+ .

1. Matching for Momentum Transport

The matching procedure involves finding the unique value of B^+ that is consistent with specified values of A^+ , ϵ/ν and u_i/u_m .

That is:

$$B^+ = B^+(A^+, \epsilon/\nu, u_i/u_m) \quad 3-62$$

and this function is monotonic. The matching procedure starts with the obvious physical fact that $u_m = u_{mb}$. That is, the actual value of the velocity at the point of zero shear stress must come out the same, whether the integration is started at the wall or at the interface. Proceeding algebraically:

$$\frac{u_m}{\left(\frac{\tau_w}{\rho}\right)^{1/2}} = \frac{u_m}{\left(\frac{\tau_i}{\rho}\right)^{1/2}} \cdot \left(\frac{\tau_i}{\tau_w}\right)^{1/2}$$

or:

$$u_m^+ = u_{mb}^+ \left(\frac{\tau_i}{\tau_w} \right)^{1/2} \quad 3-63$$

To put the ratio (τ_i/τ_w) in terms of the other parameters, equation 3-30 is put into the following form:

$$\frac{\tau_i}{\tau_w} = \frac{B}{A} = \frac{B^+}{A^+} \left(\frac{\tau_w}{\tau_i} \right)^{1/2}$$

$$\frac{\tau_i}{\tau_w} = \left(\frac{B^+}{A^+} \right)^{2/3} \quad 3-64$$

From equations 3-63 and 3-64, it follows that:

$$u_m^+ A^{+1/3} = u_{mb}^+ B^{+1/3} \quad 3-65$$

By substituting equation 3-60 into 3-65, the basic matching equation is derived.

$$u_m^+ A^{+1/3} = \frac{u_{mb}^+ B^{+1/3}}{(1 - u_i/u_m)} \quad 3-66$$

Now the matching procedure can be completed and the Reynolds number for the entire film can be calculated as a function of the three parameters: A^+ , ϵ/ν , and u_i/u_m . First, values of ϵ/ν and u_i/u_m are specified. Then the following is repeated for each of several values of A^+ .

For the first value of A^+ , the dimensionless velocity profile is calculated from equation 3-38 with u_0^+ set to zero. In particular, u_m^+ is found, being the value of u^+ at $y^+ = A^+$. Then Re_a is calculated from equation 3-43.

The value of B^+ that corresponds to the specified \mathcal{E}'/ν , u_i/u_m and A^+ must be found by trial and error. First u_b^+ is set to zero and \mathcal{E}'/ν is taken as specified. Then, for several values of B^+ , the dimensionless velocity profile and v_{mb}^+ are found from equation 3-38. A table of v_{mb}^+ versus B^+ is made. Now with the value of $\frac{u_i}{u_m}$ specified and with $u_m^+ A^{+1/2}$ already calculated, this table is searched for the value of B^+ that satisfies equation 3-66. Having found B^+ , Re_b can be calculated from equation 3-44 when equation 3-61 is used to provide the value of u_{ib}^+ . Finally, the Reynolds number for the entire film can be calculated from Re_a and Re_b based on definitions implied in equations 3-40 through 3-42:

$$Re = \frac{1}{2} (Re_a + Re_b) \quad 3-67$$

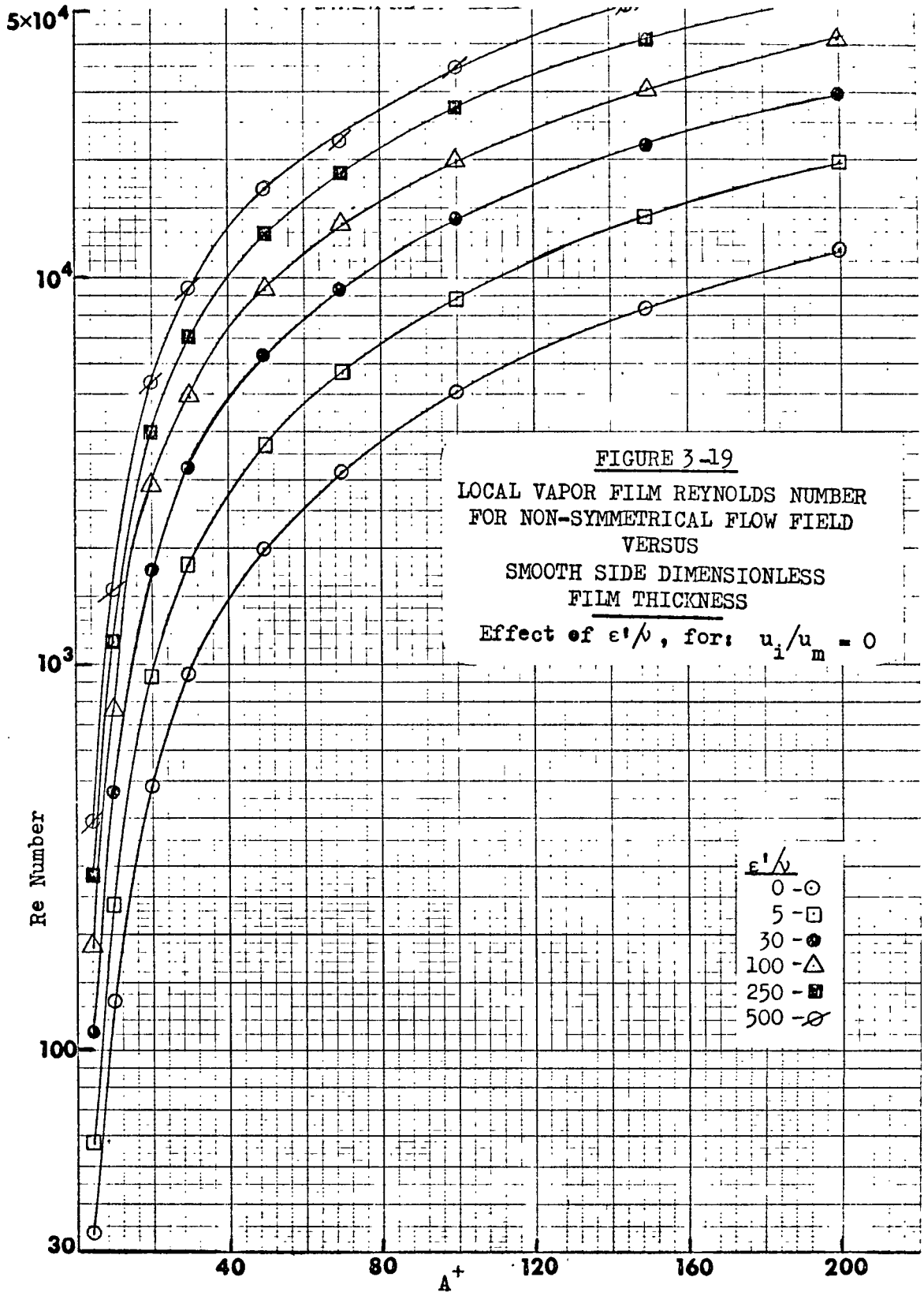
At this point then, the momentum transport theory is complete, summarized by the function:

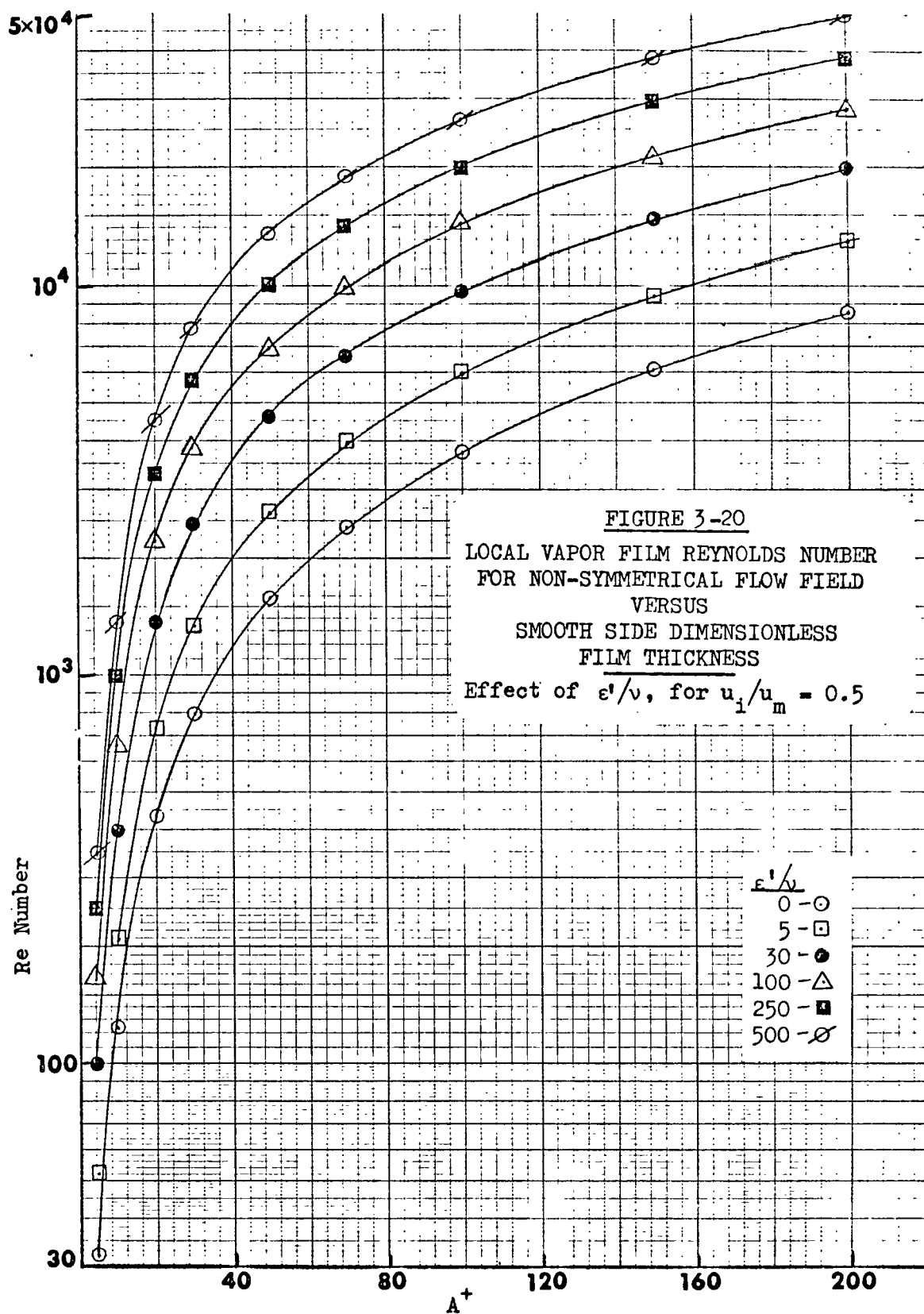
$$Re = Re(A^+, \mathcal{E}'/\nu, u_i/u_m).$$

Typical results are shown in Figures 3-19 and 3-20.

2. Matching for Energy Transport

Now that the Re number has been found, the CC number and the Nu number must be determined as functions of the Prandtl number. T_m^+ and T_{mb}^+ are obtained directly from equation 3-46 when using the A^+ , \mathcal{E}'/ν , and B^+ values specified in the previous section. Equations 3-52, 3-53, 3-57 and 3-58 can then be used directly to calculate Nu_a , Nu_b , CC_a and CC_b . It now remains to find the proper equation for Nu and CC for the entire vapor film. From the definition of the Nusselt number, it follows that:





$$Nu = \frac{hp}{k} = \frac{q_w (A+B)}{(T_w - T_i) k}$$

$$Nu = \frac{q_w Pr}{(T_w - T_i) \rho C_p \left(\frac{\gamma_w}{\rho}\right)^{1/2}} \left[\frac{A}{\nu} \left(\frac{\gamma_w}{\rho}\right)^{1/2} + \frac{B}{\nu} \left(\frac{\gamma_i}{\rho}\right)^{1/2} \left(\frac{\gamma_w}{\gamma_i}\right)^{1/2} \right] \quad 3-68$$

Recalling the definitions of T^+ , y^+ and Pr , and from equation 3-64:

$$Nu = \frac{Pr}{T_i^+} A^{+1/3} (A^{+2/3} + B^{+2/3}) \quad 3-69$$

Now T_i^+ may be algebraically revised with the aid of the assumption that

q_y is constant, so that $q_i = -q_w$:

$$T_i^+ = \frac{\rho C_p (T_w - T_m)}{q_w} \left(\frac{\gamma_w}{\rho}\right)^{1/2} + \frac{\rho C_p (T_i - T_m)}{q_i} \left(\frac{\gamma_i}{\rho}\right)^{1/2} \left(\frac{\gamma_w}{\gamma_i}\right)^{1/2}$$

$$T_i^+ = T_m^+ + T_{mh}^+ \left(\frac{A^+}{B^+}\right)^{1/3}$$

3-70

Substituting equation 3-70 into 3-69 soon yields:

$$Nu = (A^{+2/3} + B^{+2/3}) \cdot \left(\frac{A^{+2/3}}{Nu_a} + \frac{B^{+2/3}}{Nu_b} \right)^{-1} \quad 3-71$$

With respect to CC , from its definition in equation 3-56 and recalling:

$$\rho^+ = \frac{A+B}{\nu} \left(\frac{\gamma_w}{\rho}\right)^{1/2} = A^+ + B^+ \left(\frac{A^+}{B^+}\right)^{1/3} \quad 3-72$$

it follows that:

$$CC = \frac{\rho^+}{Nu A^{+1/3}} = \frac{A^{+2/3} + B^{+2/3}}{Nu} \quad 3-73$$

Finally, utilizing equations 3-71, 3-57 and 3-58:

$$CC = \frac{A^{+2/3}}{Nu_a} + \frac{B^{+2/3}}{Nu_b} = \frac{1}{2} (CC_a + CC_b) \quad 3-74$$

The energy transport theory is now complete with results in the form of:

$$Nu = Nu(Re, Pr, \epsilon/\nu, u_i/u_m)$$

$$CC = CC(Re, Pr, \epsilon/\nu, u_i/u_m)$$

Typical results for the CC number are summarized in Figures 3-21 through 3-24. The effect of the interfacial velocity is seen to be small for ϵ/ν values greater than zero, and too small to be significant for the ϵ/ν values of 30 and 100. In fact, only when the u_i/u_m ratio exceeds about 0.9 does the CC number change appreciably as is shown by a typical set of curves in Figure 3-24b. As pointed out in Appendix A, however, such high ratios can be achieved only during forced convection film boiling with very high liquid flow rates. With natural convection boilers, the theoretical value of u_i/u_m (calculated by the method presented in the next section) is usually less than 0.5. This will be illustrated in Section G of Chapter VI.

F. THE INTERFACIAL VELOCITY

The vapor velocity at the vapor-liquid interface must equal the liquid velocity on the other side of the interface, and the shear stress across the interface must also be continuous. These two conditions are sufficient to uniquely relate the interfacial velocity parameter, u_i/u_m , to the other system parameters ($Re, A^+, \epsilon/\nu$). It has been shown that:

$$u_i = v_{mb} \frac{(u_i/u_m)}{1 - u_i/u_m} \quad 3-61$$

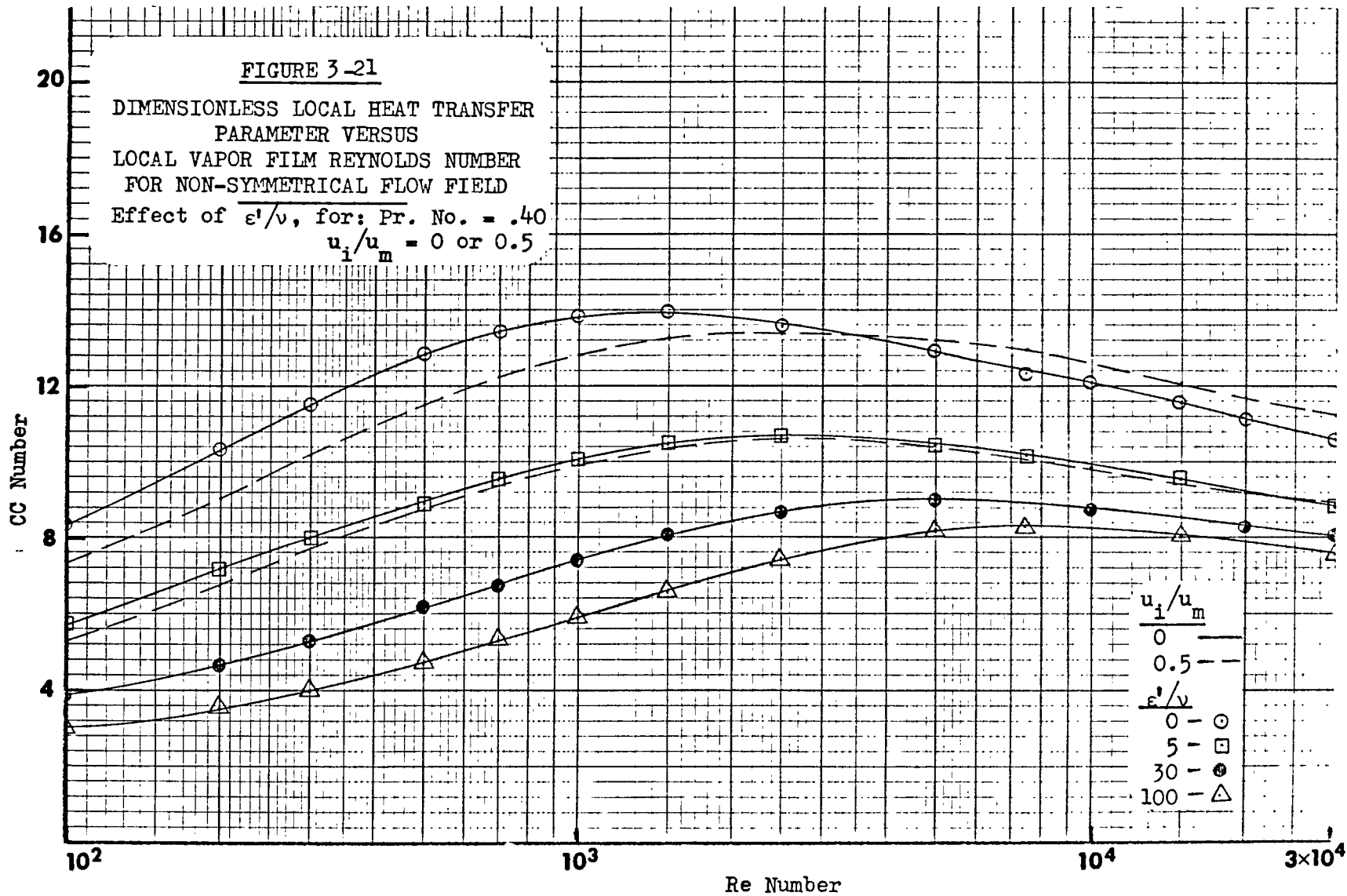
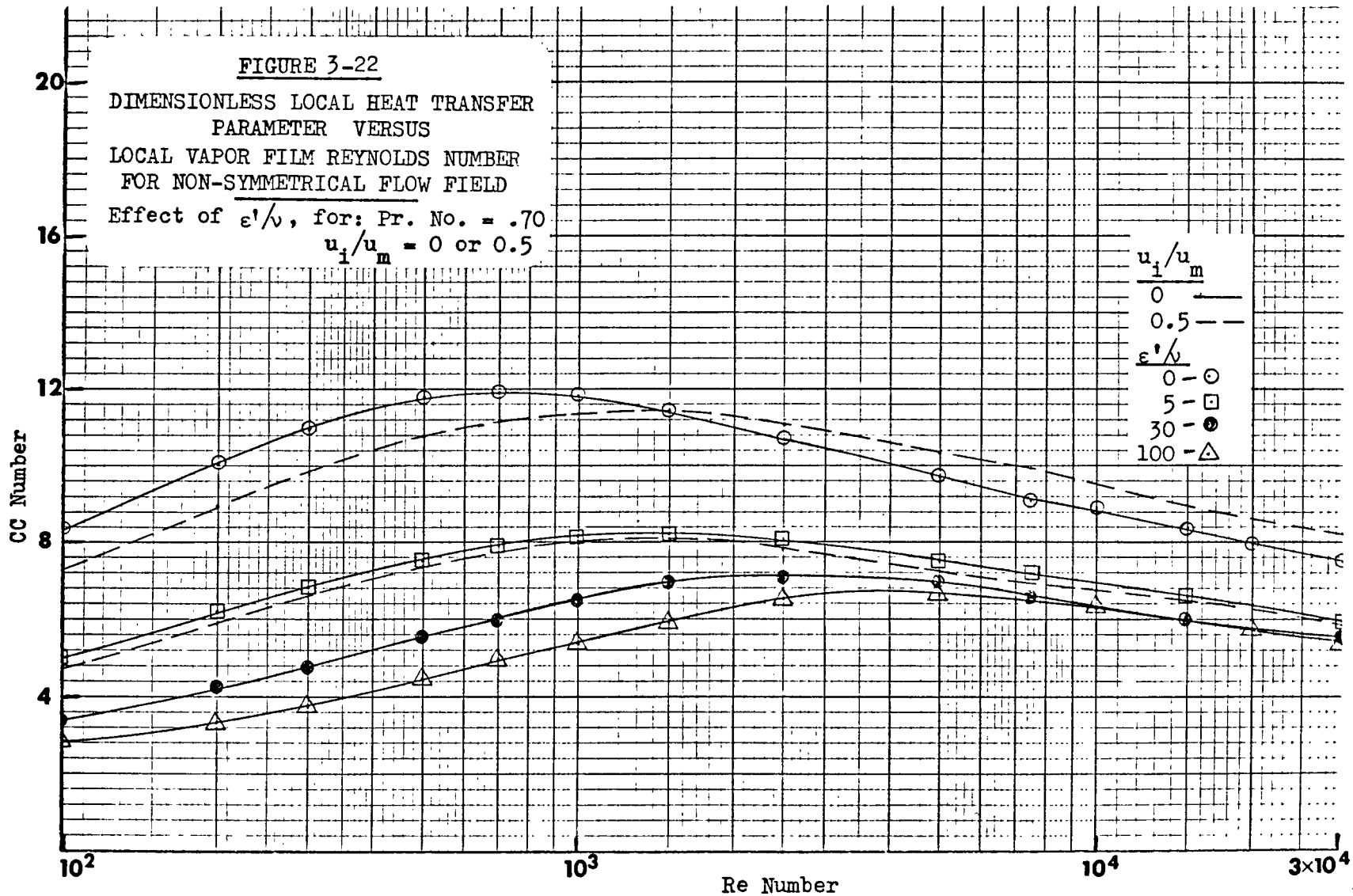


FIGURE 3-22

DIMENSIONLESS LOCAL HEAT TRANSFER
PARAMETER VERSUS
LOCAL VAPOR FILM REYNOLDS NUMBER
FOR NON-SYMMETRICAL FLOW FIELD

Effect of ϵ'/ν , for: Pr. No. = .70
 $u_i/u_m = 0$ or 0.5



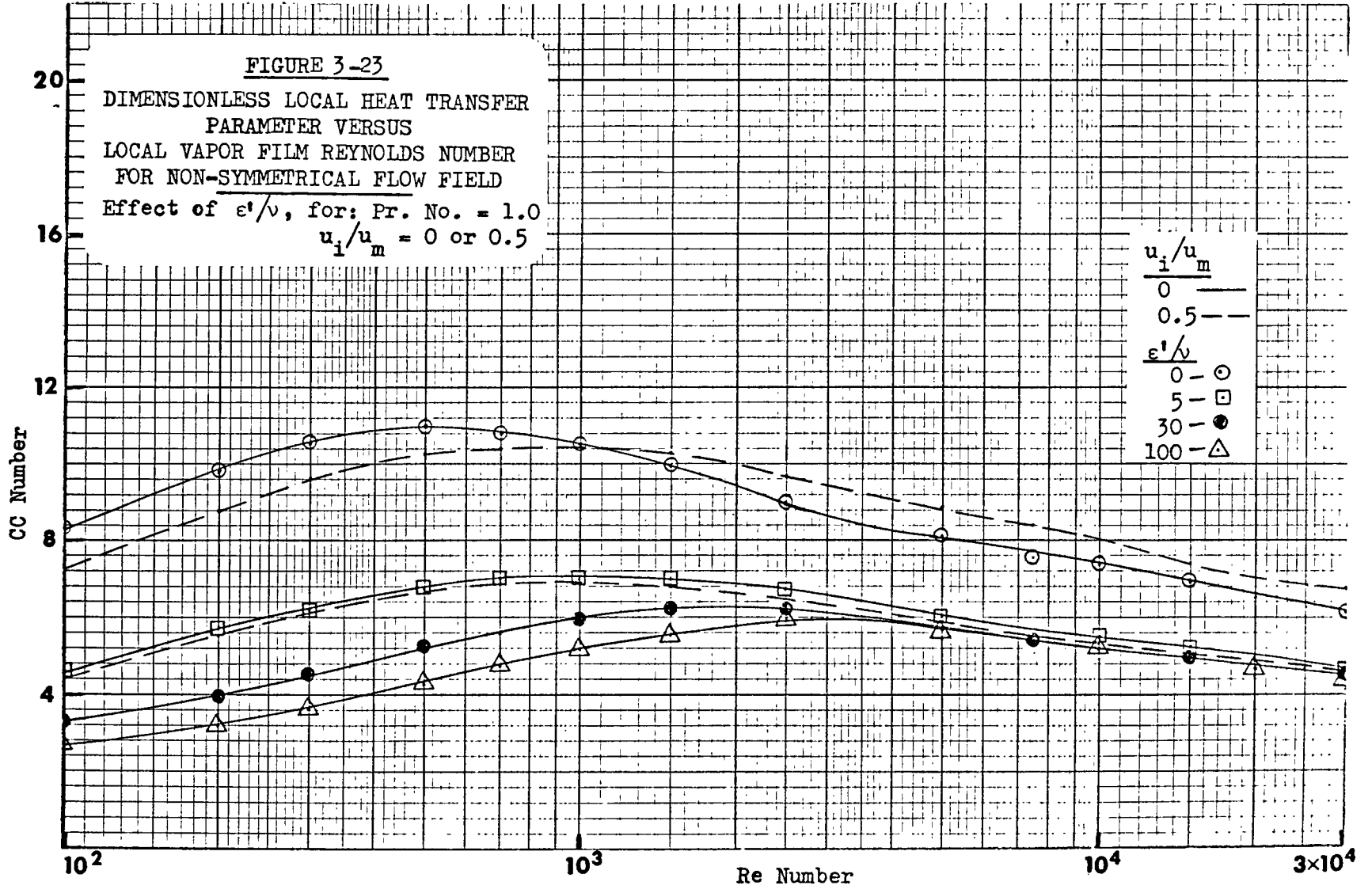


FIGURE 3-24

DIMENSIONLESS LOCAL HEAT TRANSFER
PARAMETER VERSUS
LOCAL VAPOR FILM REYNOLDS NUMBER
FOR NON-SYMMETRICAL FLOW FIELD

Effect of ϵ'/ν , for: Pr. No. = 1.4
 $u_i/u_m = 0$ or 0.5

u_i/u_m	0	○
	0.5	□
ϵ'/ν	0	○
	5	□
	30	●
	100	△

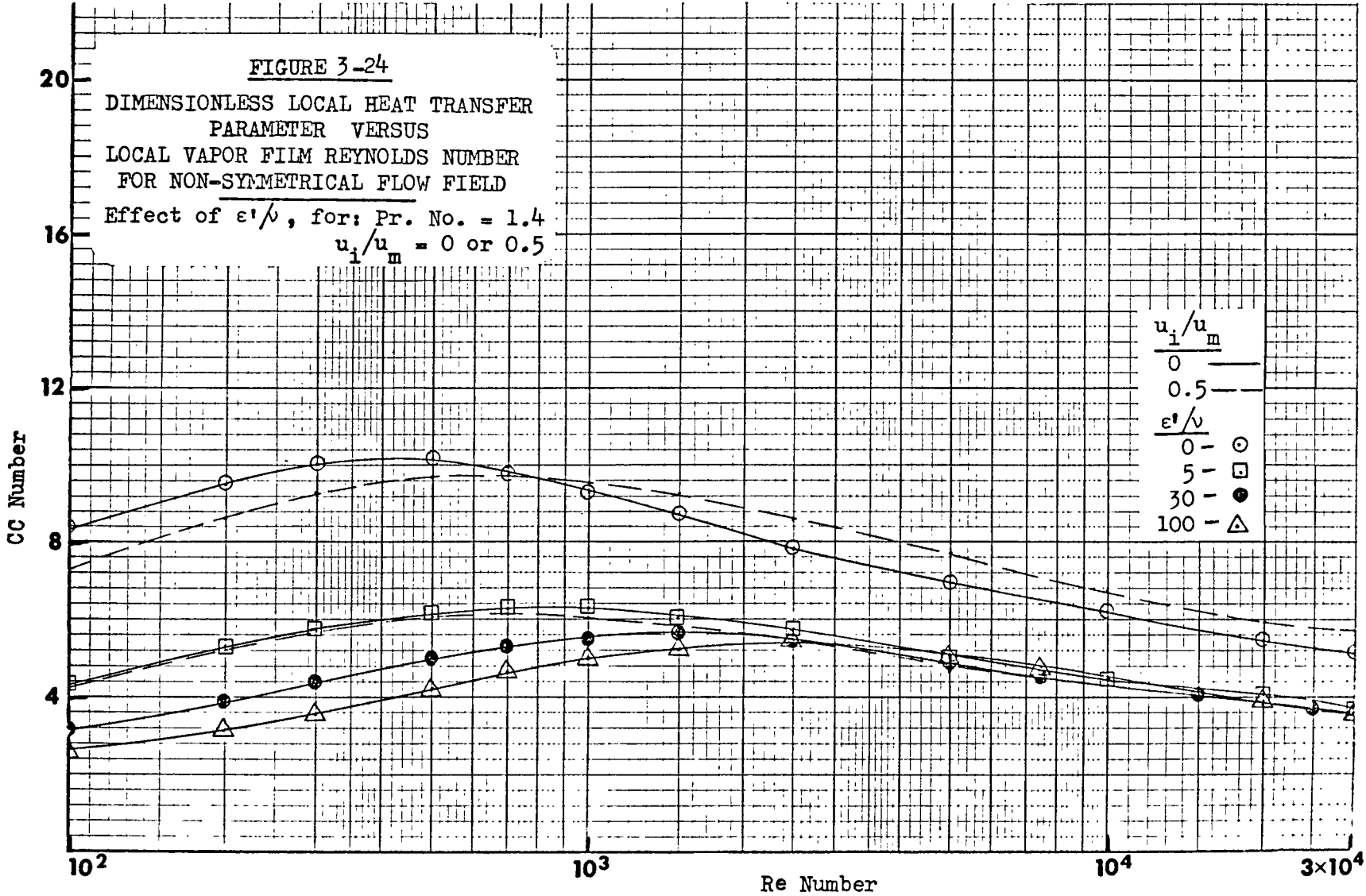
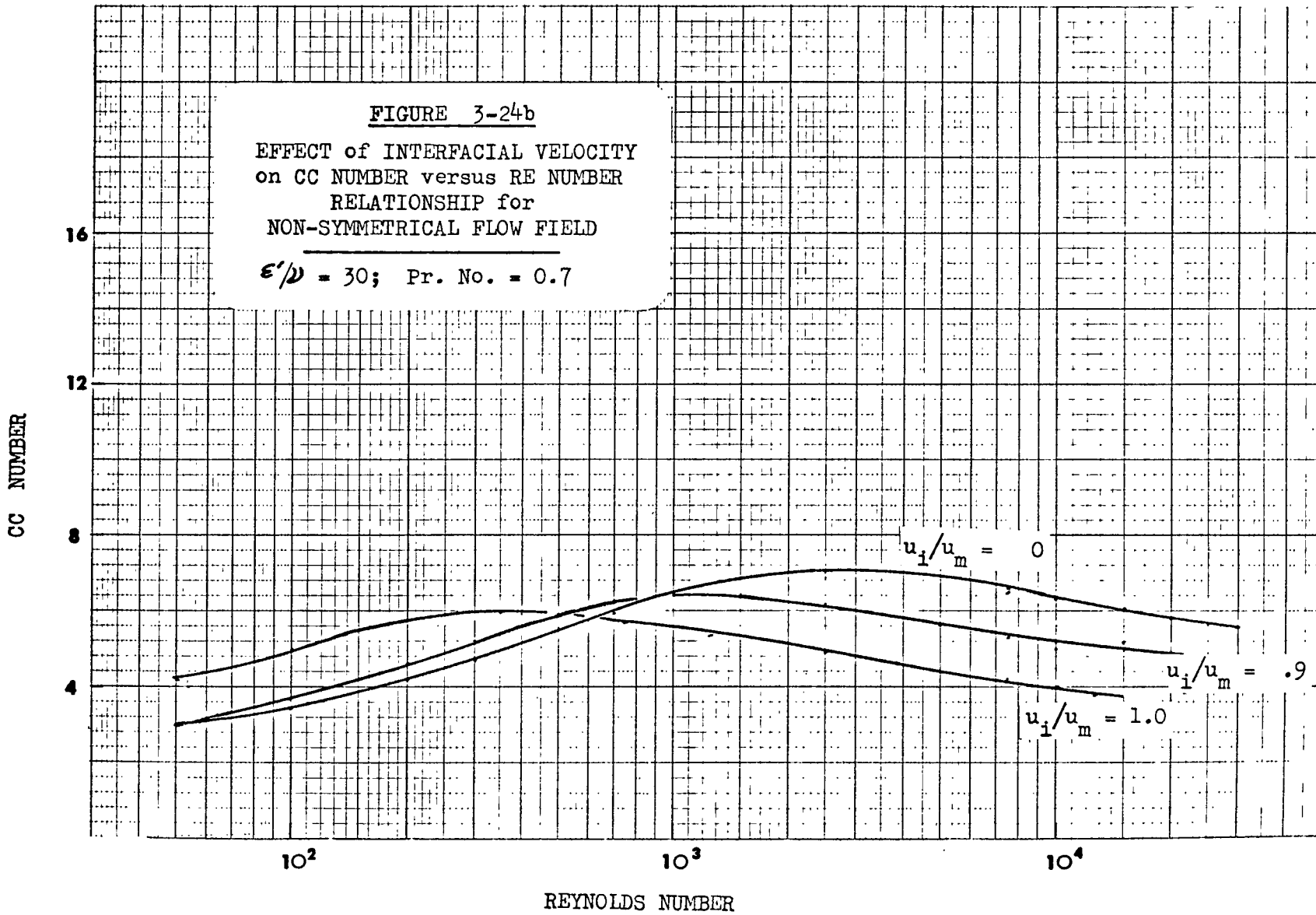


FIGURE 3-24b

EFFECT of INTERFACIAL VELOCITY
on CC NUMBER versus RE NUMBER
RELATIONSHIP for
NON-SYMMETRICAL FLOW FIELD

$\epsilon'/\nu = 30$; Pr. No. = 0.7



Since $v_{mb} = \nu v_{mb}^+ (\tau_i / \rho)^{-1/2}$ by definition and $\tau_i = (-\frac{d\rho}{dx} - \rho g) B$
 by equation 3-30, where $B = B^+ \nu (\tau_i / \rho)^{-1/2}$,
 then: $\tau_i = \rho^{1/3} [B^+ \nu (-\frac{d\rho}{dx} - \rho g)]^{2/3}$ 3-75

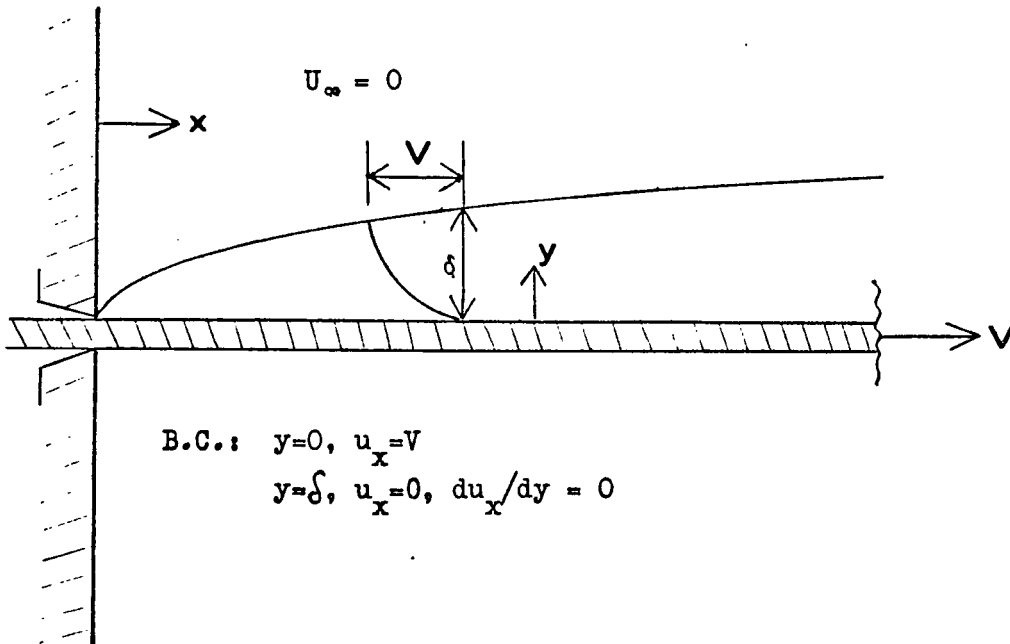
and:
 $u_i = v_{mb}^+ (u_i / u_m) (1 - u_i / u_m)^{-1} [B^+ \nu \rho^{-1} (-\frac{d\rho}{dx} - \rho g)]^{1/2}$ 3-76

Equations 3-75 and 3-76 represent the relationship between the interfacial velocity and shear stress based on the rate of momentum transport in the vapor phase. It is now necessary to derive an equivalent relationship for the liquid side.

The liquid interfacial velocity induced by the vapor shear stress causes a boundary-layer type velocity profile to develop in the liquid. This boundary layer will be similar to that which results when a continuous surface is pulled through a fluid, as discussed by Sakiadis (S-2). Under these circumstances, the boundary layer has a zero thickness at the point where the surface enters the fluid and grows in the direction of motion of the surface. On the other hand, if a surface of finite length is pulled through the fluid, the boundary layer has a zero thickness at the leading edge and grows in the direction opposite to that of the surface's motion. These cases are shown in Figure 3-25. Since the boundary conditions are reversed, different solutions to the boundary layer equations will be attained for these two situations. The relationship between surface shear stress and surface velocity for the continuous surface is given by Sakiadis. For the laminar boundary layer, this is:

$$\tau_i = 0.444 \rho_L u_i^2 \left(\frac{\nu_L}{x u_i} \right)^{1/2}$$
 3-77

A. CONTINUOUS SURFACE PULLED THROUGH A FLUID



B. FINITE SURFACE PULLED THROUGH A FLUID
 (Same as fluid moving past a stationary surface.)

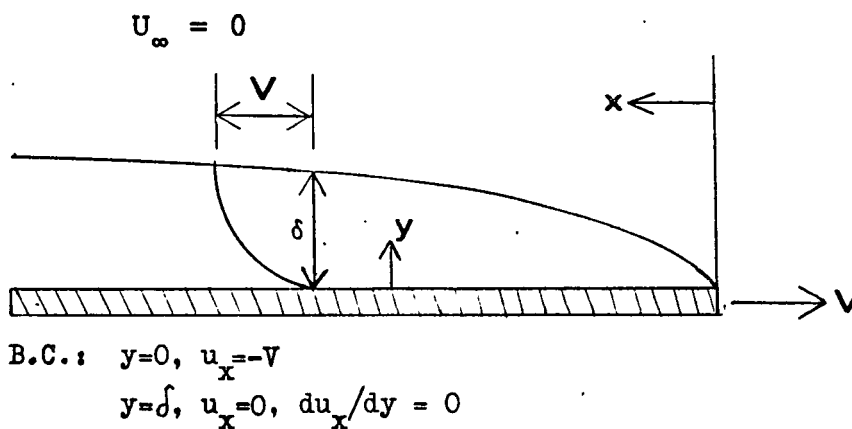


FIGURE 3-25. BOUNDARY LAYER DEVELOPMENT OVER CONTINUOUS AND FINITE SURFACES

while for the turbulent boundary-layer, it is:

$$\tau_i = 0.0225 \rho_L u_i^2 \left(\frac{\nu_L}{x u_i} \right)^{0.2}$$

3-78

where x is the distance along the surface from the point at which it emerges into the fluid.

To the liquid interface in vertical film boiling, the drag imposed by the vapor is similar in effect to that which would be caused by a continuous surface originating at the leading edge of the boiler. Thus, the interfacial shear stress and velocity from equations 3-75 and 3-76 based on the vapor phase conditions, must satisfy either equation 3-77 or 3-78, depending upon whether the liquid boundary layer is laminar or turbulent. Since a complex relationship between u_i , B^+ , Re and ϵ/ν is implicit in equation 3-76, a trial and error solution is necessary to find the proper value of u_i/u_m for a specific design problem.

G. EVALUATION OF THE PRESSURE DROP

Before the theory can be used in design, a means of predicting the pressure drop must be developed. This is needed so that the heat transfer coefficient can be calculated from the theoretical value of CC , according to equation 3-56. The prediction of the pressure drop will proceed from the normal boundary layer assumption that $dP/dy = 0$. For pool boiling then, the pressure gradient is just the hydrostatic head of the bulk liquid, $g\rho_L$, and the constant K from equation 3-3 becomes:

$$K = K_p = - \frac{dP}{dx} - \rho g = g(\rho_L - \rho)$$

3-79

Of course, if a large amount of vapor escapes into the bulk liquid, the liquid density must be modified accordingly.

For film boiling in a vertical conduit with forced convection, the pressure gradient will be the sum of the frictional pressure drop and the hydrostatic head of the liquid:

$$\left(-\frac{dP}{dx}\right) = \left(-\frac{dP}{dx}\right)_f + g\rho_L = \eta_f g\rho_L \quad 3-80$$

where, by definition:

$$\eta_f = 1 + \frac{\left(-\frac{dP}{dx}\right)_f}{g\rho_L} \quad 3-81$$

In this case,

$$K = K_f = g(\eta_f \rho_L - \rho) \quad 3-82$$

with K_f approaching K_p as the frictional pressure drop approaches zero and η_f approaches unity.

The normal velocity profile to be expected in vertical film boiling in a conduit will have a maxima in the vapor phase, as shown by profile 2 in Figure 3-2. This will occur unless relatively large liquid flow rates are encountered as discussed in Section A of this Chapter and in Appendix A. For velocity profiles of type 2, the frictional pressure drop, $\left(-\frac{dP}{dx}\right)_f$, will be negative, because the interfacial shear stress will cause some liquid to be pulled through the conduit. Therefore, η_f will be less than one. An exact calculation of the value of η_f for laminar flows is included in Appendix A. Calculating η_f for turbulent flows is more involved because analytic solutions cannot be obtained, but the procedure would be the same.

There is little experimental evidence available to show whether the negative frictional pressure gradient actually exists. Rankin's measure-

ments (R-1) showed the negative gradient but he felt that this was caused by excessive vapor entrainment in the bulk liquid core. If this were the case, the small pressure gradient may have reflected a low average density of the core fluid. The pressure gradient was not measured by Dougall and Rohsenow (D-5). In Chapter VI where data are compared with the theory, η_f is taken to be one if pressure gradient measurements were not reported.

H. THE EFFECTS OF RADIANT HEAT TRANSFER

Because of the large temperature differences in film boiling, radiant heat transfer from the wall may be a significant fraction of the total heat transfer. A rigorous treatment of this effect would be quite complicated since most organic vapors are not transparent to thermal radiation, but will exchange energy with the wall, the liquid interface, and with the rest of the vapor in the film. The error introduced by neglecting the non-zero emissivity of the vapor was estimated by the technique of Hottel (H-3). Because the vapor film is so thin (about 0.05 inches) this error was found to be negligible. The same conclusion was reached by Sparrow (S-8).

Thus, the radiation effect will be considered as simply a wall-liquid interchange with no radiant energy being received directly by the vapor. For this case, radiation and convection are parallel heat transfer mechanisms. At any local position on the surface the two heat transfer rates may be computed separately and the results added together to give the total heat transfer rate. The convection and radiation processes are indirectly coupled, however, in that any vapor generation due to radiation will change the vapor flow rate and the velocity distribution in the

film. This then affects the convective heat transfer coefficient.

To determine the local radiant heat flux, the process is considered to be one of energy transfer between two large, closely spaced parallel plates. The liquid is assumed to be a black body (J-1) and all radiant energy reaching the liquid will be absorbed there. The local radiant heat flux is then given by the following equation:

$$q_r = \epsilon_w \sigma_r (T_{wa}^4 - T_{ia}^4) \quad 3-83$$

The subscript "a" refers to the absolute temperature scale, σ_r is the Stefan - Boltzmann constant, and ϵ_w is the wall emissivity.

I. APPLICATION OF THE THEORY TO DESIGN

The theory developed here provides for the calculation of local heat transfer coefficients. Applying this theory to the design of a film boiling system involves an integration of the local coefficients over the entire surface. The differential equation governing this integration is simply:

$$dW = \frac{fQ}{\lambda'} dx = \frac{fh\Delta T}{\lambda'} dx \quad 3-84$$

where Q is the total local heat flux (including radiation) to the fluid, f is the perimeter of the heated wall, dx is the differential height of heated wall, and dW is the rate of vaporization over dx . The effective heat of vaporization is given by:

$$\lambda' = \bar{c}_{pL} (T_s - T_{sc}) + \Delta H_v + \bar{c}_p (\bar{T} - T_s) \quad 3-85$$

which includes the energy required to heat subcooled liquid at T_{sc} to the

boiling point, vaporize the liquid, and heat the new vapor to the average vapor temperature, \bar{T} . As will be shown later in this Chapter, this average should be the arithmetic average of the wall and interfacial temperatures:

$$\bar{T} = \frac{1}{2} (T_w + T_s) = \frac{1}{2} (T_w + T_i) \quad 3-86$$

The definition of λ' implies that all sensible heating of the liquid is accomplished locally at the point of vaporization and that sensible heating of the bulk liquid is negligible.

Integration of equation 3-84 requires the specification of either the heat flux distribution or the temperature distribution along the length of the wall. The two extreme cases to be considered here are those of constant wall temperature and constant heat flux.

1. Constant Wall Temperature

The total heat flux can be expressed as a multiple of the convective heat flux:

$$Q = \phi_r h \Delta T = h \Delta T \left(1 + \frac{q_r}{h \Delta T} \right) \quad 3-87$$

where ϕ_r is a radiation factor defined by the above equation, q_r is given by equation 3-83, and $h \Delta T$ is the convective heat flux. Practically all of the data reported in the literature for a constant wall temperature have been obtained from systems with either low temperature differences or with low boiling point cryogenic liquids, so that the radiant heat flux was less than 5% of the convective heat flux. Thus, the radiation factor will be set equal to one in what follows without

significantly affecting the comparison of the resulting theory to the available data. It is not expected that ϕ_r would be significant unless temperature differences of 600 degrees F. or more and wall temperatures of 800 degrees F. or more were attained.

With the mass flow rate, W , equal to $\rho \bar{u} p f$, where f is the perimeter of the heater, the Reynolds number of equation 3-39 may be expressed in terms of W :

$$Re = \frac{2W}{f\mu} \quad 3-88$$

Using also the definition for the CC group from equation 3-56, equation 3-84 becomes:

$$\left(\frac{2k\Delta T}{\mu\lambda'} \right) \left[\frac{L^3 g \rho (\eta_f \rho_L - \rho)}{\mu^2} \right]^{1/3} = \int_0^{Re_L} CC dRe \quad 3-89$$

where Re_L is the local Reynolds number, defined in terms of the local vapor film thickness, at a distance L from the start of the heater block.

An overall Nusselt number is now defined as follows:

$$\overline{Nu} \equiv \frac{\bar{h}L}{k} = \frac{Q_{TOT}}{f k \Delta T} = \frac{W_L \lambda'}{f k \Delta T} \quad 3-90$$

where W_L is the total mass flow rate in the vapor film at the distance L . Substituting the definition of the Reynolds number into equation 3-90 allows the overall Nusselt number to be expressed as follows:

$$\overline{Nu} \left(\frac{2k\Delta T}{\mu\lambda'} \right) = Re_L \quad 3-91$$

Each term in equation 3-89 is raised to the 3/4 power and the result is divided into equation 3-91. After some algebraic rearrangement:

$$\overline{Nu} \left[\frac{\frac{2k\Delta T}{\mu\lambda'}}{\frac{L^3 g \rho (\eta_f \rho_L - \rho)}{\mu^2}} \right]^{1/4} = Re_L \left[\int_0^{Re_L} CC dRe \right]^{-3/4} \quad 3-92$$

The left hand side of equation 3-92 can be considered a "dimensionless Nusselt number". This grouping of variables appears in the theoretical equations for laminar film boiling where it can be shown to have a constant value, independent of the Reynolds number, determined only by the interfacial boundary conditions that are specified. For a zero interfacial velocity, this constant is 0.8. The right hand side of equation 3-92 shows how the Nusselt grouping depends on the Reynolds number for turbulent flows.

The integration of equation 3-92 can now be performed numerically according to the results of the steady state theory:

$$CC = CC(Re, Pr, \epsilon/\nu, u_i/u_m)$$

as presented in Figures 3-21 through 3-24. For the laminar region near the leading edge of the hot surface, the laminar relationship between the CC and Re numbers must be used. The integral then becomes:

$$\int_0^{Re_L} CC dRe = \int_0^{Re_t} CC_{lam.} dRe + \int_{Re_t}^{Re_L} CC dRe \quad 3-93$$

where Re_t is the Reynolds number at which transition from laminar to turbulent flow occurs. The value of the laminar integral is a function of the interfacial boundary condition. For the case of zero interfacial velocity:

$$\int_0^{Re_t} C C_{lam.} dRe = 1.36 (Re_t)^{4/3} \quad 3-94$$

The laminar term has little effect on the calculated heater area for most situations, but it was included here so that the turbulent solution would reduce exactly to the laminar solution. Typical results of the integration of equation 3-92 for constant values of Pr , ϵ/ν and u_i/u_m are presented in Figures 3-26 through 3-28.

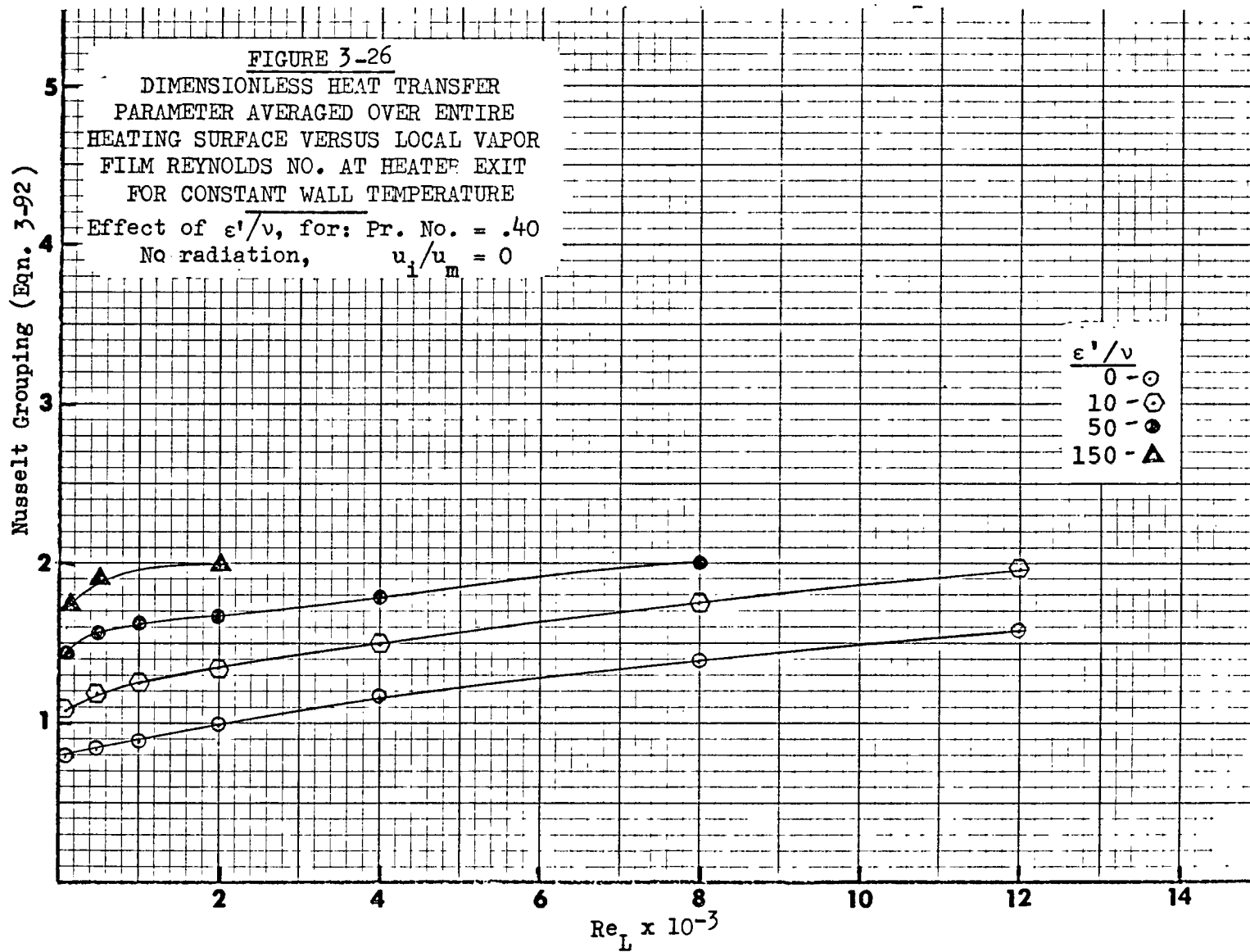
The use of these curves will be illustrated for a typical design problem. The surface area of the heater may be required when the wall and liquid temperatures and the total mass to be vaporized are given as design parameters. The physical properties of the vapor can be calculated based on the known temperatures. Then, Re_L , Pr and \overline{Nu} can be determined in terms of a specified value for f , the perimeter of the heating surface:

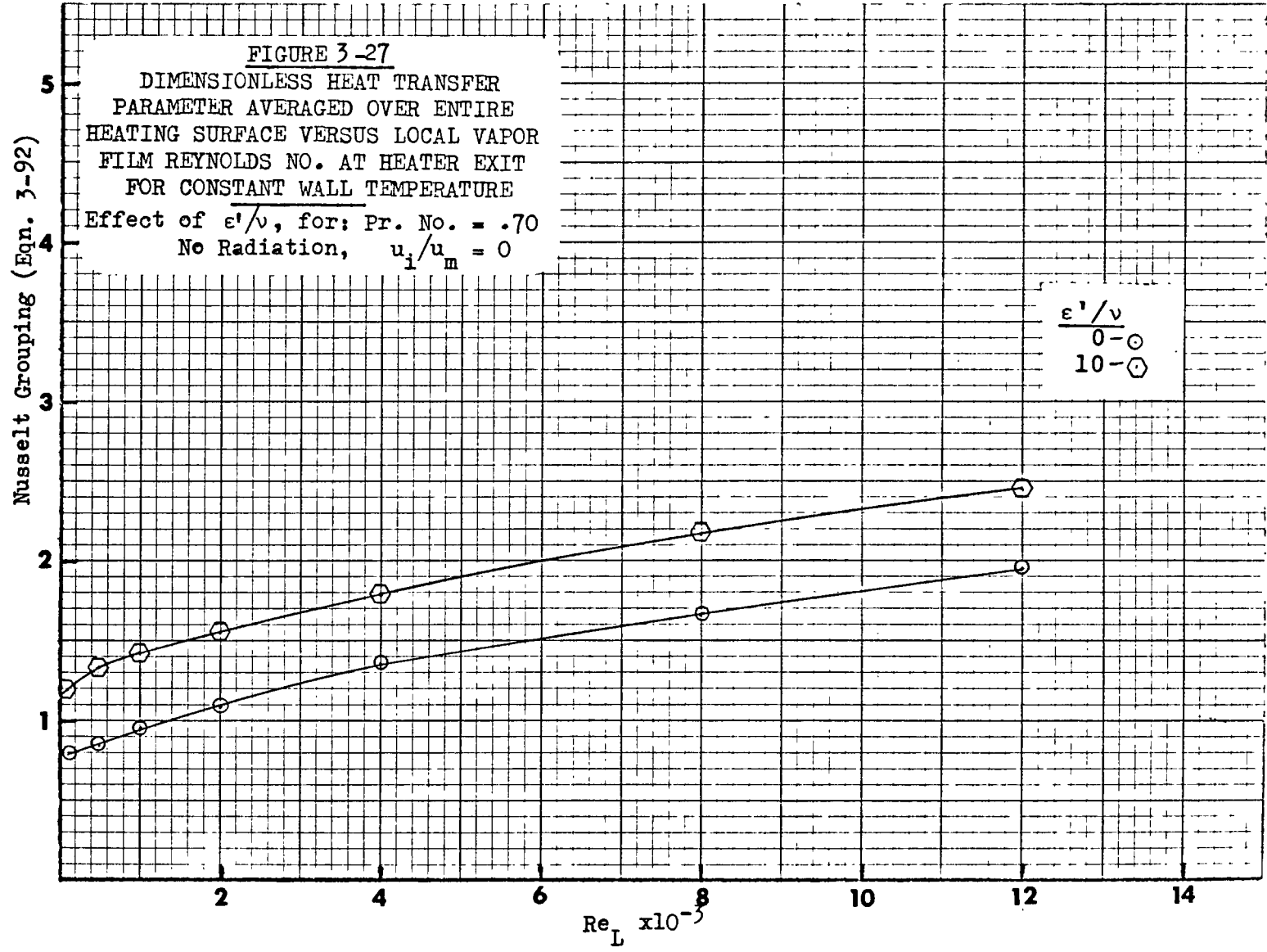
$$Re_L = \frac{2W_L}{f\mu}$$

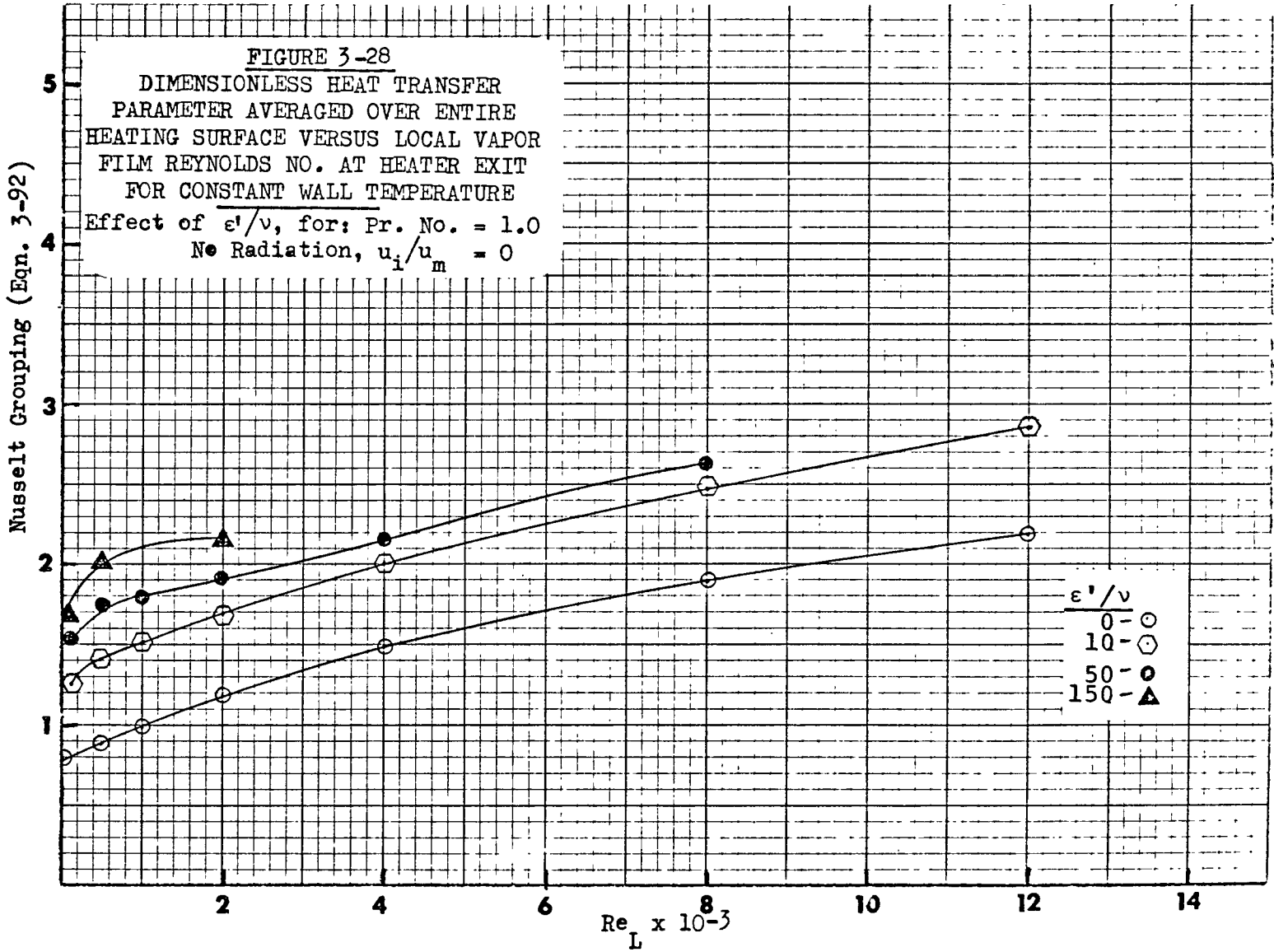
$$Pr = \frac{c_p\mu}{k}$$

$$\overline{Nu} = \frac{W\lambda'}{k f \Delta T}$$

Values of the interfacial parameters, u_i/u_m and ϵ/ν , will have to be specified. Then the design curves, such as those in Figure 3-26, give the value of the Nusselt grouping of equation 3-92. The desired heater length, L , can now be calculated directly:







$$L = \left\{ \overline{Nu} \cdot \left[\frac{\frac{2k\Delta T}{\mu\lambda'}}{\frac{g\rho(\eta_f\mu - \rho)}{\mu^2}} \right]^{1/4} \right\}^{4/3}$$

(Value of the Nusselt Grouping)

2. Constant heat flux

For the case of a constant heat flux boiler, the total amount of energy added to the fluid is known once the area of the heater is specified. The theory thus serves a somewhat different purpose. First, the theory leads to the wall temperature of the boiler at every position. This must be known to satisfy safety requirements and to properly define the physical properties of the materials of construction. Secondly, the theory leads to the amount of superheat in the vapor leaving the heated surface. If the design criterion is that a certain amount of energy be added to the fluid, then this knowledge of the superheat temperature is needed only to evaluate the operation of downstream equipment. On the other hand, if maximum vaporization of liquid is the design objective, then mixing devices could be used to recover the sensible heat as new vapor. The technique of using the theory for design in this way is discussed below.

Equation 3-84 serves as the starting point for design calculations in constant heat flux boiling, but the procedure is quite different from that for the case of a constant wall temperature. For any length of tube, L , the total energy added to the fluid by radiation plus convection, Q_{TOT} is known:

$$Q_{TOT} = QfL = (q_r + q_c) fL \quad 3-95$$

where Q is the local heat flux. The mass flow rate past that point,

W_{TOT} , is:

$$W_{TOT} = \frac{Q_{TOT}}{\lambda'} \quad 3-96$$

where λ' , given by equation 3-85, depends only on the local wall temperature, since

$$\bar{T} = \frac{1}{2} (T_w + T_s)$$

Then, equations 3-95 and 3-96 lead to:

$$QfL = W_{TOT} * \left[\bar{c}_{pL} (T_s - T_{sc}) + \Delta H_v + \frac{1}{2} \bar{c}_p (T_w - T_s) \right] \quad 3-97$$

But the local wall temperature is also a function of the local heat flux:

$$Q = q_r + q_c = \epsilon \sigma_r (T_{wa}^4 - T_{sa}^4) + h (T_w - T_s) \quad 3-98$$

Replacing h by the dimensionless group, CC , and W_{TOT} by the local Reynolds number, the last two equations become:

$$QfL = \frac{1}{2} f \mu Re_L \left[\bar{c}_{pL} (T_s - T_{sc}) + \Delta H_v + \frac{1}{2} \bar{c}_p (T_w - T_s) \right] \quad 3-99$$

$$Q = \epsilon \sigma_r (T_{wa}^4 - T_{sa}^4) + \frac{\bar{k}}{CC} (T_w - T_s) \left[\frac{9\rho(\eta_f \rho_L - \rho)}{\mu^2} \right]^{1/3} \quad 3-100$$

All quantities in these two equations are known except for T_w , Re , CC , and the physical properties of the vapor: μ , \bar{c}_p , ρ , and \bar{k} . The physical properties can be specified in terms of the unknown wall temperature since they are evaluated at the average vapor film temperature:

$$\bar{T} = \frac{1}{2} (T_w + T_s)$$

Two more equations are then required to make the system algebraically complete. They are:

$$Re_L = \frac{2 Q_{TOT} \lambda'}{f \mu}$$

$$CC = CC(Pr, Re_L, \epsilon'/\nu, u_i/u_m)$$

The latter equation is the result of the theory developed in this work. In the evaluation of CC , of course, ϵ'/ν and u_i/u_m must be specified.

J. THE AVERAGE VAPOR TEMPERATURE

The average vapor temperature is needed for two purposes. First, it will be assumed that this is the temperature at which physical properties must be evaluated. Secondly, the average vapor temperature is needed for

the calculation of the total mass of liquid vaporized by a given amount of energy, according to equations 3-84 and 3-85. The average temperature is defined as:

$$\bar{T} = T_s + \frac{\int_0^p u (T - T_s) dy}{\int_0^p u dy} \quad 3-101$$

That is, if all the mass flowing past a local position on the heater surface were at the temperature, \bar{T} , the energy within the vapor would equal that determined according to the actual velocity and temperature profiles.

Solutions of equation 3-101 using velocity and temperature profiles from the theory presented in this work show that \bar{T} can be closely approximated by the arithmetic mean of the wall and interfacial temperatures. The details of this integration are presented in Appendix C.

For laminar flows, Bromley (B-9) has suggested that defining the effective heat of vaporization as in equation 3-102 will compensate for the neglected convective acceleration terms in the equations of motion.

$$\lambda'_{Brom.} = \Delta H_v \left[1 + \frac{0.34 c_v (T_w - T_s)}{\Delta H_v} \right]^2 \quad 3-102$$

Other writers have used the same expression for turbulent flows. It was felt here that such a correction would probably not suitably describe the acceleration terms for turbulent flow, and λ' was defined to simply account for the energy going to the vapor.

K. SUMMARY OF THE QUASI-STEADY STATE MODEL

Velocity and temperature profiles have been calculated for the vapor film as a function of the interfacial parameters, ϵ/ν and u_i/u_m . These profiles lead directly to the parameters, the Re and CC numbers, that express the local heat transfer coefficient as a function of the local mass flow rate. Utilization of these correlations in design requires an integration over the entire heater surface, and this integration was discussed for the two wall conditions of constant temperature and constant heat flux. Finally, for design purposes, it is necessary to predict a priori the values of the interfacial parameters. A boundary layer approach to the liquid has been shown to lead to the interfacial velocity. No completely satisfactory method has been developed for predicting the roughness parameter, ϵ/ν , so its value must be estimated by correlating experimental data.

The steady state theory has ignored the possibility that relatively large amplitude waves may be present. The effect of such waves is discussed in the next chapter.

CHAPTER IV

THEORETICAL DEVELOPMENT - THE EFFECT OF LARGE AMPLITUDE WAVES

In the presence of large amplitude waves the vapor flow will be neither steady state nor fully developed. The acceleration terms will remain in the equations of motion and some modifications to the shear stress distribution given by equation 3-3 would appear necessary. In this chapter, the differential equation governing the shear stress distribution will be developed more exactly. Of course, an exact solution to the equations of motion will not be possible, but presentation in this manner will indicate the magnitude of the errors inherent to the assumptions and will point the way to a means of correcting for these errors.

A. THE COMPLETE EQUATIONS OF MOTION

The system to be considered is the vapor film shown in Figure 3-1.

The equation of motion for the x-direction can be written:

$$\frac{du}{dt} + u \frac{du}{dx} + v \frac{du}{dy} = -\frac{1}{\rho} \frac{dP}{dx} - g - \frac{1}{\rho} \left(\frac{d\tau_{xx}}{dx} + \frac{d\tau_{yx}}{dy} \right) \quad 4-1$$

As before, the pressure gradient will be divided into two parts:

$$-\frac{dP}{dx} = \left(-\frac{dP}{dx} \right)_f + \rho \cdot g \quad 4-2$$

So that

$$-\frac{1}{\rho} \frac{dP}{dx} - g = \frac{g \Delta \rho}{\rho} \quad 4-3$$

where

$$\Delta \rho = \eta_f \rho_L - \rho \quad 4-4$$

and

$$\eta_f = 1 - \frac{\left(\frac{dP}{dx}\right)_f}{g \rho_L} \quad 4-5$$

It will be assumed that $d\tau_{xy}/dx$ is much smaller than $d\tau_{yx}/dy$, and τ will mean τ_{yx} . Then:

$$\frac{d\tau}{dy} = g \Delta \rho - \rho \frac{du}{dt} - \rho \left(u \frac{du}{dx} + v \frac{du}{dy} \right) \quad 4-6$$

Adding and subtracting $\rho u \frac{dv}{dy}$ to the above equation, and recalling from the continuity equation that:

$$dv/dy = - du/dx \quad 4-7$$

equation 4-6 can be rewritten:

$$\frac{d\tau}{dy} = g \Delta \rho - \rho \frac{du}{dt} - \rho \left[\frac{d}{dx}(u^2) + \frac{d}{dy}(uv) \right] \quad 4-8$$

Integrating the above equation from $y = 0$ to $y = y$, and utilizing the condition that u and v are zero at $y = 0$:

$$\tau = \tau_0 + gy \Delta \rho - \rho \int_0^y \left(\frac{du}{dt} \right) dy - \rho \int_0^y \frac{d(u^2)}{dx} dy - \rho u_y v_y \quad 4-9$$

The subscripts, y , on the velocity terms indicate that they are to be evaluated at a specific position. From the continuity equation again:

$$v_y = - \int_0^y \left(\frac{du}{dx} \right) dy \quad 4-10$$

Substituting equation 4-10 into 4-9 yields:⁽¹⁾

$$\tau = \tau_0 + gy\Delta\rho - \rho \int_0^y \left(\frac{du}{dt}\right) dy + \rho \int_0^y \frac{d}{dx} (uu_y - u^2) dy \quad 4-11$$

At $y = y_m$ the shear stress is zero and:

$$\tau_0 = -gy_m\Delta\rho + \rho \int_0^{y_m} \left(\frac{du}{dt}\right) dy - \rho \int_0^{y_m} \frac{d}{dx} (uu_m - u^2) dy \quad 4-12$$

Upon dividing equation 4-11 by τ_0 , and then using equation 4-12:

$$\frac{\tau}{\tau_0} = 1 - \frac{gy\Delta\rho - \rho \int_0^y \left(\frac{du}{dt}\right) dy + \rho \int_0^y \frac{d}{dx} (uu_y - u^2) dy}{gy_m\Delta\rho - \rho \int_0^{y_m} \left(\frac{du}{dt}\right) dy + \rho \int_0^{y_m} \frac{d}{dx} (uu_m - u^2) dy} \quad 4-13$$

Within the limits of the boundary layer theory, equation 4-13 is a completely general expression for the shear stress distribution. The shear stress distribution may also be expressed in terms of the eddy viscosity according to equation 3-3, which can be put into the following dimensionless form:

$$\frac{\tau}{\tau_0} = \left(1 + \frac{\epsilon}{\nu}\right) \frac{du^+}{dy^+} \quad 4-14$$

Then once the eddy viscosity is known, the velocity profile can be calculated by integration of equation 4-14. However, equation 4-13 is too complex to be integrated in this manner and many liberties have been taken with this equation. Some typical examples will be summarized here. For the least complex case of steady state, fully developed flow, equation 4-13 reduces to:

$$\frac{\tau}{\tau_0} = 1 - \frac{y}{y_m}$$

However, many derivations, such as Deissler's work on turbulent flow in a round pipe (D-1) or the development of the universal velocity profile,

(1) It has been pointed out that u_y , being a function of x , has been erroneously placed inside the operator " $\frac{d}{dx}$ " in equation 4-11 and thereafter. The effects of this are discussed in the footnote on page 108.

have assumed that $\tau/\tau_0 = 1$ with satisfactory results. For steady state boundary layer flow, equation 4-13 reduces to:

$$\frac{\tau}{\tau_0} = 1 - \frac{gy\Delta\rho + \rho \int_0^y \frac{d}{dx} (uu_y - u^2) dy}{gy_m\Delta\rho + \rho \int_0^{y_m} \frac{d}{dx} (uu_m - u^2) dy} \quad 4-16$$

Even in this case, however, drastic simplifications have proven useful. For turbulent flow in an entrance region (D-2) and for turbulent boundary layer flow over a flat plate, (D-3), Deissler assumed $\tau/\tau_0 = 1$. For turbulent boundary layer flow longitudinally over a cylinder, Sparrow et al (S-7) assumed $\tau/\tau_0 = \frac{R_0}{R_0 + y}$, where R_0 is the radius of the cylinder. Upon consideration of the variation of area with radius for the cylindrical geometry, this is about equivalent to the assumption of a constant shear stress across the boundary layer of a flat plate.

In view of the complexities of equation 4-13, it would be expeditious to this work to make the assumption that $\tau/\tau_0 = 1 - y/y_m$, even for the case where relatively large amplitude waves are present. Before proceeding on this basis, however, it would seem worthwhile to estimate the order of magnitude of the errors so introduced. For this purpose, equation 4-13 will be rewritten as follows, where equations 4-18 and 4-19 define θ_1 and θ_2 .

$$\tau/\tau_0 = 1 - \theta \frac{y}{y_m} \quad 4-17$$

$$\theta = \frac{1 - \frac{\rho}{gy\Delta\rho} \int_0^y \left(\frac{du}{dt}\right) dy + \frac{\rho}{gy\Delta\rho} \int_0^y \frac{d}{dx} (uu_y - u^2) dy}{1 - \frac{\rho}{gy_m\Delta\rho} \int_0^{y_m} \left(\frac{du}{dt}\right) dy + \frac{\rho}{gy_m\Delta\rho} \int_0^{y_m} \frac{d}{dx} (uu_m - u^2) dy} \quad 4-18$$

$$\theta = \frac{1 - \theta_1}{1 - \theta_2} \quad 4-19$$

The deviation of θ from unity will be investigated. The value of θ_2 at any instant is fixed by the value of y_m , while θ_1 has a non-constant value varying from zero at $y = 0$ to θ_2 at $y = y_m$. Thus, θ varies from a maximum value of $(1 - \theta_2)^{-1}$ at the interface ($y = 0$) to a value of one at $y = y_m$. To estimate the maximum error incurred by the assumption that θ is identically equal to one, the value of θ_{max} will be determined from an estimate of the maximum size of θ_2 .

These calculations will be made for Freon - 113 for which the value of $(\rho/g\Delta\rho)$ is about 6×10^{-5} sec²/foot. The first term of θ_2 will be approximated by using an average value of the argument of the integral, as follows:

$$\frac{1}{y_m} \int_0^{y_m} \left(\frac{du}{dt} \right) dy = \overline{\left(\frac{du}{dt} \right)} y_m \quad 4-20$$

This will then be evaluated by assuming that the velocity changes inversely as the area of flow (which is proportional to the vapor film thickness), and that this change in velocity occurs over a time interval of 1/4 of the period of the oscillation. Typical circumstances will include a wave frequency of 10 cps, a wave amplitude of about one-half the mean film thickness, and a maximum velocity within the vapor film of about 40 feet per second for the steady state case with no waves. Thus, the maximum velocity would increase to 80 feet per second when the interface moves closest to the wall and would decrease to 27 feet per second when it moves farthest away. These changes of 40 and 13 feet per second, respectively, from the steady state value of the maximum velocity

will occur in about 1/40 of a second. The maximum value of $\overline{(du/dt)}^{y_m}$ will then range from about 1600 to 500 feet/sec², with an average on the order of 1100 feet/sec². Multiplying this by $(\rho/g\Delta\rho)$ gives 0.07 for the first term of θ_2 .

The integral within the second term of θ_2 , to be called I_2 , will be evaluated by applying the frequently used one-seventh power velocity profile to the turbulent vapor film. Thus:

$$u = u_m \left(\frac{y}{y_m} \right)^{1/7} \quad 4-21$$

$$u(u_m - u) = u_m^2 \left[\left(\frac{y}{y_m} \right)^{1/7} - \left(\frac{y}{y_m} \right)^{2/7} \right] \quad 4-22$$

Since the term, $u(u_m - u)$, is zero when evaluated at $y = y_m$, it follows from Leibnitz' rule:

$$I_2 = \frac{1}{y_m} \int_0^{y_m} \frac{d}{dx} (u u_m - u^2) dy = \frac{1}{y_m} \frac{d}{dx} \int_0^{y_m} u(u_m - u) dy \quad 4-23$$

Using equation 4-22, this integral becomes:

$$I_2 = \frac{1}{y_m} \frac{d}{dx} \left(\frac{7}{72} y_m u_m^2 \right) \quad 4-24$$

A sinusoidal interface will be assumed, so that:

$$y_m = y_{m0} \left[1 + \mathcal{N}_0 \sin \left(2\pi ft + \frac{2\pi x}{\lambda} \right) \right] \quad 4-25$$

Since the velocity is considered inversely proportional to the film thickness:

$$u_m = u_{m_0} \left(\frac{y_{m_0}}{y_m} \right) \quad 4-26$$

where u_{m_0} and y_{m_0} refer to values for the steady state situation. Equation 4-24 may be evaluated by considering equations 4-25 and 4-26:

$$I_2 = -\frac{7}{72} \frac{2\pi N_0 u_{m_0}^2 \cos\left(2\pi ft + \frac{2\pi x}{\lambda}\right)}{\lambda \left[1 + N_0 \sin\left(2\pi ft + \frac{2\pi x}{\lambda}\right)\right]^3} \quad 4-27$$

The maximum value of I_2 is attained when the cosine and sine terms are one and zero, respectively:

$$I_{2 \max} = -\frac{7}{36} \frac{\pi N_0 u_{m_0}^2}{\lambda} \quad 4-28$$

As already discussed, u_{m_0} and N_0 are 40 feet per second and 0.5 respectively. The wave length, λ , will be about 0.1 feet as indicated by measurements of Hsu (H-6). Then $I_{2 \max} = 4900 \text{ feet/sec}^2$. Multiplying this by $(\rho/g\Delta\rho)$ gives 0.29 for the second term in θ_2 .

Thus, the maximum value of θ_2 will be about 0.36 (0.07 + 0.29). This leads to a maximum value for θ of about 1.55, from $1/(1 - \theta_2)$, at the interface, but θ will decrease to unity at y_m , the position of zero shear stress.⁽¹⁾ Thus, the assumption that θ is everywhere one seems reasonable enough. It should be reemphasized here that the basic assumptions are a large wave length to amplitude ratio and a low frequency.

B. CORRECTION OF THE STEADY-STATE THEORY

It has just been shown that a reasonably good approximation for the shear stress distribution at any moment in time is given by equation 3-3. This means that the momentum transport equations 3-38 to 3-44, and

(1) See footnote, page 104. θ_2 has been recalculated by the procedure described above but with u_m remaining outside of the operator " $\frac{d}{dx}$ ". The conclusion reached was not changed, however. θ remains unity at y_m , but its value changes by a factor of 3.1 (instead of the 1.55 stated above) in the region between y_m and the interface.

the energy transport equations 3-46 to 3-58, are instantaneously applicable to wavy flow. The graphs for Re versus A^+ , ϵ/D and u_i/u_m in Figures 3-19 and 3-20, and the graphs for CC vs Re , Pr , ϵ/D and u_i/u_m in Figures 3-21 to 3-24 apply at any instant. It then becomes necessary to establish the time dependency of the local Reynolds number so that the quasi-steady state relations may be integrated over time to give the proper average value of the local heat transfer rate.

It will be assumed here that the local Reynolds number remains constant with time. According to the Reynolds number formulation given by equation 3-88 ($Re = \frac{2W}{f\mu}$), this implies that the mass flow rate past any point on the heated wall will be constant. As the vapor film thickness gets smaller because of the approaching interface, there will be a tendency for the flow rate to decrease. However, the local vapor generation rate will also increase at this time and tend to keep the flow rate constant.

According to the quasi-steady state theory, a constant Reynolds number implies a constant Nusselt number. Thus:

$$Nu = Nu(Re) = h_s \rho_s / k_e = h \rho / k_e \quad 4-29$$

where the subscript "s" refers to the steady state situation without waves and the absence of the subscript refers to instantaneous values in the presence of waves. It follows that:

$$h/h_s = \rho_s/\rho \quad 4-30$$

The time average local heat transfer coefficient is defined as:

$$\bar{h} = \text{Limit}_{T \rightarrow \infty} \frac{1}{T} \int_0^T h dt \quad 4-31$$

The instantaneous film thickness will be written in the following form:

$$\rho = \rho_s (1 + \eta) \quad 4-32$$

where η is a function of time and represents the wave shape. Then for periodic interfacial motion with a period, T:

$$\bar{h}/h_s = \frac{1}{T} \int_0^T (1 + \eta)^{-1} dt \quad 4-33$$

To summarize briefly, it has been first assumed that both the wave frequency and the amplitude to wavelength ratio of the interfacial waves are small so that the steady state theory applies at any instant. Then it has been assumed that the mass flow rate past a point on the heated wall is constant. This leads directly to equation 4-33. Now, only the wave shape must be known to calculate the local time average heat transfer coefficient.

C. THE EFFECT OF WAVE SHAPE

From equation 4-33, the only parameter left to be considered is the wave shape as represented by $\eta(t)$. There is very little guidance in the literature with respect to this point. Most theoretical studies assume a sinusoidal wave form because of the mathematical advantages involved. Experimental work on falling liquid films, such as that of Wicks (W-4) or Telles (T-2), show that the wave front is very definitely non-sinusoidal. Movies of film boiling by Westwater and Hsu (W-3) and by Simoneaux and Simon (S-6) of film boiling suggest a random rather than sinusoidal interface, but this is somewhat indefinite because three-dimensional effects can distort the observations. In any case, a complex almost periodic wave form would be difficult to discern visually.

Experimental power spectrum data taken in this work indicate that the waves frequently exhibit preferred frequencies, but the frequency band is usually quite broad.

The movies of pool boiling suggest that the film thickness is normally thin with occasional large bursts of vapor penetrating into the liquid. In particular, the movies of Westwater show a very interesting behavior of this vapor burst, as is shown in Figure 4-1 for various stages of the activity. The pocket of vapor will sometimes become extremely elongated and string out far into the liquid. Then the liquid at the interface near the base of the vapor pocket will begin to fall by gravity, until it appears that the liquid will pinch off the vapor pocket to produce a bubble. Yet the vapor from the pocket practically always flows back into the main vapor film before the "pinching-off" process can be completed, and the vapor pocket disappears. For this to take place, a pressure differential must exist between the vapor in the pocket and the vapor in the continuous film. This pressure is not likely to have its origin in surface tension because of the relatively large curvatures involved. A possible source of this driving force is discussed in Section F, Chapter VI.

Two wave shapes will be considered here: a sinusoid for mathematical convenience and a periodic pulse type shape. For the first case, if $\eta = \eta_0 \sin(\omega t - \eta x)$ so that η_0 is the relative amplitude of the wave and $\eta_0 \rho_s$ is the absolute amplitude, then from equation 4-33:

$$\frac{\bar{h}}{h_s} = \frac{\omega}{2\pi} \int_0^{\frac{2\pi}{\omega}} \frac{dt}{1 + \eta_0 \sin(\omega t - \eta x)} = \frac{1}{2\pi} \int_{-\eta x}^{2\pi - \eta x} \frac{d\theta}{1 + \eta_0 \sin \theta}$$

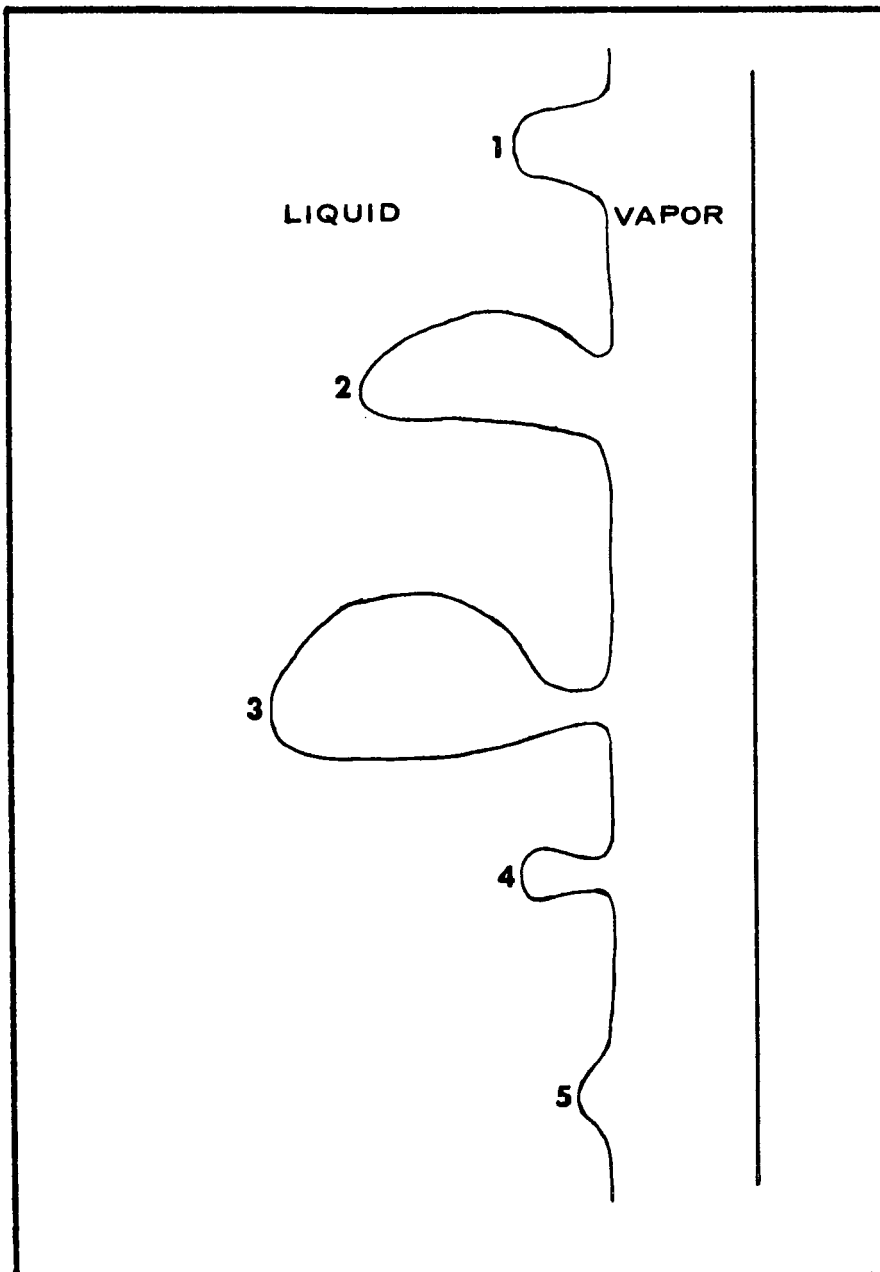


FIGURE 4-1. THE FORMATION AND DISAPPEARANCE OF VAPOR CAVITIES WITHIN THE LIQUID AT THE INTERFACE

This integral can best be evaluated by the theory of residues (B-7), with the result that:

$$\frac{\bar{h}}{h_s} = (1 - \eta_o^2)^{-\frac{1}{2}} \quad 4-35$$

Two interesting points are made clear by this result. First, the waves affect the heat transfer rate only through the amplitude while the effects of wave length and frequency cancel out during the averaging procedure. Second, the presence of waves causes an increase in the time average heat transfer coefficient over that calculated by the steady state theory, since η_o is always less than one. The physical explanation of this result is that the heat transfer rate is enhanced as the interface approaches the wall to a greater extent than it is reduced as the interface moves away. Since the wave is sinusoidal, the interface is near the wall just as often as it is far away.

There are several ways in which the information expressed in equation 4-35 can be used. In an experimental study where \bar{h} and η_o are measured, equation 4-35 leads directly to h_s . This, then, leads to the value of ϵ/ρ required to predict h_s by the quasi-steady state theory, and allows an experimental correlation for ϵ/ρ to be developed. In design, if the wave amplitude and ϵ/ρ could be predicted in advance, equation 4-35 allows calculation of the heat transfer coefficient, \bar{h} , since the quasi-steady state theory will establish h_s . Finally, equation 4-35 can lead to an indirect experimental measurement of the wave amplitude as discussed later in this chapter.

The second wave shape to be discussed is the modified pulse type

shown in Figure 4-2. Since a travelling wave is assumed, this figure represents either a time record at a given position or a space record at a given time. The wave length, λ , and the lengths of the substrate and the pulse, λ_1 and λ_2 , are defined in the figure. The fractional wave lengths of the pulse and the substrate, λ_p and λ_b , are:

$$\lambda_b = \frac{\lambda_1}{\lambda} ; \quad \lambda_p = \frac{\lambda_2}{\lambda} ; \quad \lambda_b + \lambda_p = 1 \quad 4-36$$

The film thickness at the substrate and at the peak of the pulse are ρ_b and ρ_p , while ρ_s represents the average film thickness that would be calculated by the steady-state theory. The function, $\rho_p(x)$, defines the shape of the pulse. The relation between ρ_s and the pulse parameters is then:

$$\rho_s = \frac{1}{\lambda} \int_0^{\lambda_1} \rho_b dx + \frac{1}{\lambda} \int_{\lambda_1}^{\lambda} \rho_p(x) dx \quad 4-37$$

From equations 4-30 and 4-31, it follows that:

$$\frac{\bar{h}}{h_s} = \frac{1}{\lambda} \int_0^{\lambda} \frac{\rho_s}{\rho} dx = \frac{1}{\lambda} \int_0^{\lambda_1} \frac{\rho_s}{\rho_b} dx + \frac{1}{\lambda} \int_{\lambda_1}^{\lambda} \frac{\rho_s}{\rho_p(x)} dx \quad 4-38$$

A simplified square pulse wave will be discussed from this point, defined by:

$$\rho_p(x) = \text{constant} = \rho_p \quad 4-39$$

Then, from equations 4-37 and 4-38:

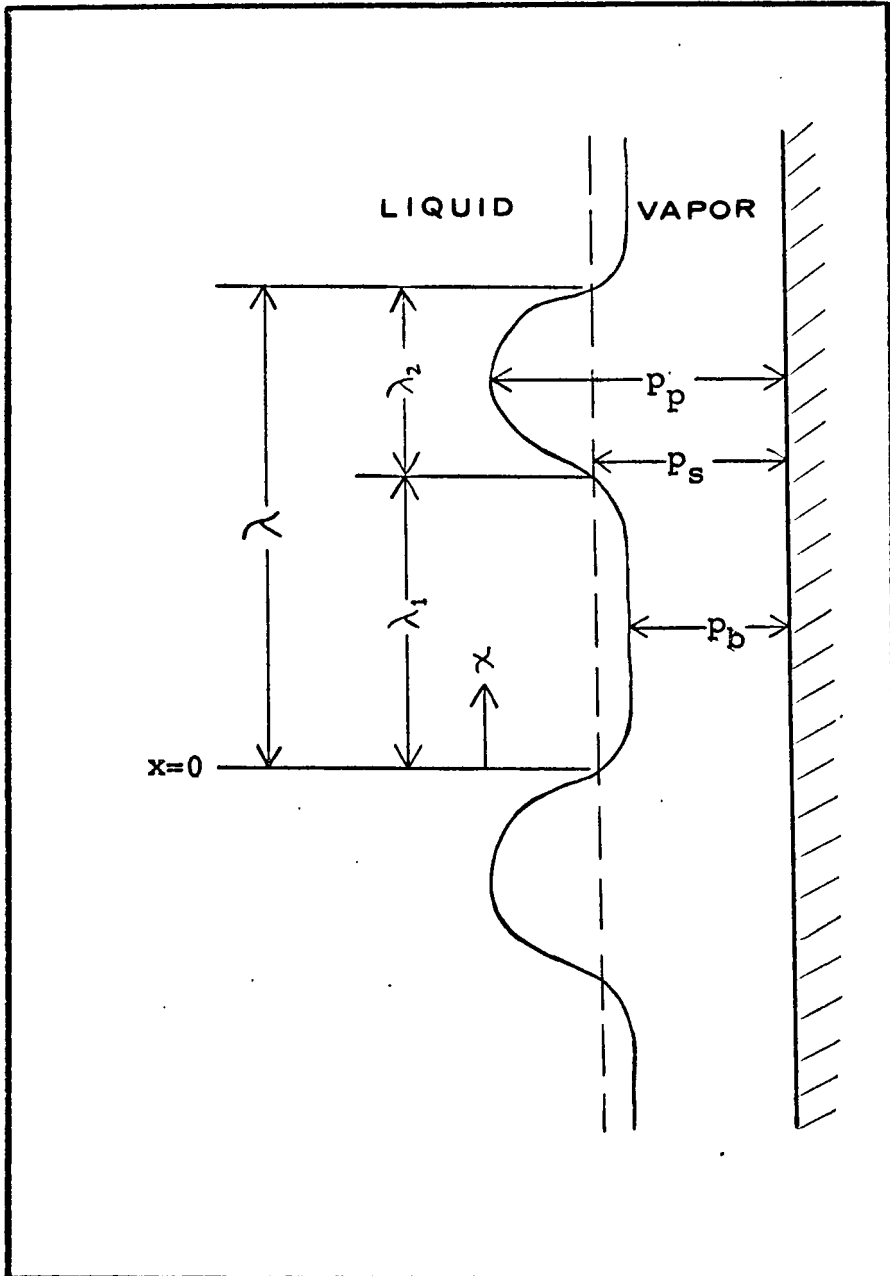


FIGURE 4-2. GEOMETRY OF A PERIODIC PULSE TYPE WAVE

$$\rho_s = \lambda_b \rho_b + (1 - \lambda_b) \rho_p \quad 4-40$$

$$\frac{\bar{h}}{h_s} = \lambda_b \left(\frac{\rho_s}{\rho_b} \right) + (1 - \lambda_b) \left(\frac{\rho_s}{\rho_p} \right) \quad 4-41$$

Equation 4-40 can be solved for (ρ_s/ρ_b) to give:

$$\frac{\rho_s}{\rho_b} = \frac{\lambda_b \left(\frac{\rho_s}{\rho_p} \right)}{\left(\frac{\rho_s}{\rho_p} \right) - (1 - \lambda_b)} \quad 4-42$$

When this is substituted into equation 4-41:

$$\frac{\bar{h}}{h_s} = \frac{2\lambda_b - 1 + (1 - \lambda_b) \left(\frac{\rho_s}{\rho_p} \right)}{1 - (1 - \lambda_b) \left(\frac{\rho_s}{\rho_p} \right)^{-1}} \quad 4-43$$

Thus, for the square pulse wave, \bar{h}/h_s depends on two parameters: λ_b and ρ_s/ρ_p . Equation 4-43 serves the same purposes as did equation 4-35.

D. EVALUATION OF THE UNSTEADY STATE MODEL

As a matter of review, the quasi-steady state theory predicts the local time average heat transfer coefficient, h_s , that would exist in the absence of large waves. When waves are present, the local coefficient, \bar{h} , can be determined if the wave shape parameters are known, as indicated by equations 4-35 and 4-43 for two types of waves. Complete evaluation of the unsteady state model would require experimental measurements of

\bar{h} , h_s and the wave shape parameters. Although \bar{h} is measured, h_s cannot be directly measured because it does not exist when waves are present. Measurements of the wave shape parameters are not usually available. In this section, an indirect method of determining h_s and the wave amplitude will be presented, based on a postulated wave shape.

To this end, a root-mean-square (rms) heat transfer coefficient must be defined. For a system with period T, this will be:

$$h_{rms} = \left[\frac{1}{T} \int_0^T h^2 dt \right]^{1/2} \quad 4-44$$

When this definition is applied to the sinusoidal wave, it follows from equations 4-30 and 4-32 that:

$$h_{rms} = h_s \left[\frac{1}{2\pi} \int_{-n\pi}^{2\pi - n\pi} \frac{d\theta}{(1 + \eta_o \sin \theta)^2} \right]^{1/2} \quad 4-45$$

Evaluation of this integral by the method of residues gives:

$$\frac{h_{rms}}{h_s} = (1 - \eta_o^2)^{-3/4} \quad 4-46$$

Combining this with equation 4-35 leads to:

$$\frac{\bar{h}}{h_{rms}} = (1 - \eta_o^2)^{1/4} \quad 4-47$$

Thus, an experimental measurement of both \bar{h} and h_{rms} will allow the calculation of the amplitude of a sinusoidal wave and the quasi-steady state heat transfer coefficient, h_s .

Because of the nature of the electronic equipment used in the experiment, h_{rms} itself was not measured. Rather, the voltage equivalent to the

heat transfer coefficient was first A.C.-coupled, to remove the D.C. component of the voltage, and the rms voltage of the remaining fluctuations was then measured. If the heat transfer coefficient, $h(t)$, is expanded in a Fourier series, it is easily seen that the magnitude of the D.C. component is simply the time-average coefficient, \bar{h} .

Then, an A.C.-coupled heat transfer coefficient, $H(t)$ can be defined:

$$H(t) = h(t) - \bar{h} \quad 4-48$$

The rms measurement that is made then becomes:

$$H_{rms} = \left(\frac{1}{T} \int_0^T H^2 dt \right)^{1/2}$$

or

$$H_{rms} = \left\{ \frac{1}{T} \int_0^T h^2 dt - \frac{2\bar{h}}{T} \int_0^T h dt + \frac{\bar{h}^2}{T} \int_0^T dt \right\}^{1/2} \quad 4-49$$

The first integral within the brackets is the square of the rms value of the actual signal before the A.C.-coupling, while the second integral is simply \bar{h} . Then, the above equation becomes:

$$H_{rms} = (h_{rms}^2 - \bar{h}^2)^{1/2} \quad 4-50$$

Since H_{rms} and \bar{h} are measured experimentally, h_{rms} may be calculated.

Thus, equation 4-50 is equivalent to equation 4-47.

Following the same procedure for the square pulse wave, h_{rms} is first calculated:

$$h_{rms}^2 = \frac{1}{\lambda} \int_0^\lambda \left(\frac{h_s \rho_s}{\rho} \right)^2 dx$$

$$\left(\frac{h_{rms}}{h_s}\right)^2 = \lambda_b \left(\frac{\rho_s}{\rho_b}\right)^2 + (1-\lambda_b) \left(\frac{\rho_s}{\rho_p}\right)^2 \quad 4-51$$

Equations 4-42, 43, 50 and 51 then provide a system of 4 equations with seven variables. Three variables (\bar{h} , H_{rms} and, as will be shown later, λ_b) are measured experimentally. Therefore, the other four (h_s , ρ_s/ρ_p , ρ_s/ρ_b and h_{rms}) can be calculated. Since ρ_s can be calculated from the quasi-steady state theory, ρ_p and ρ_b can also be determined.

It should be emphasized that this indirect method of determining the experimental wave amplitudes and the equivalent steady state heat transfer coefficient, h_s , depends upon a postulated wave shape, as shown in more detail in Chapter VI. The value of \bar{h}_s so determined then leads to the value of the roughness parameter, ϵ'/λ , required to fit the data.

E. THEORETICAL CALCULATION OF THE WAVE AMPLITUDE

The problems associated with predicting wave amplitude and the previous work conducted along these lines were discussed in Chapter II. Kapitsa (K-1) calculated the amplitude of the waves on a falling laminar liquid film by assuming that the stable mode of flow is attained when the potential energy of the liquid on the wall is at a minimum. Though this assumption appears quite plausible, it has not been proven. In any case, it does not seem reasonable that the potential energy of the vapor in film boiling will be minimized when the film is in the presence of a large, dense liquid mass. Therefore, no attempt will be made to apply Kapitsa's method to the present problem. An approach similar to that of Bradfield (B-5) seems most promising for the prediction of amplitude. Further work in this area would be of great value.

F. STABILITY OF FILM BOILING

The word "stability" has several meanings when used in connection with film boiling. These include: (1) The transition from laminar to turbulent flow within the film; (2) The occlusion of vapor bubbles within the bulk liquid; (3) The complete breakup of the vapor film and transition to a dispersed flow regime; and (4) The occurrence of liquid-solid contact. With respect to the first matter, Frederking (F-1) demonstrated that transition to turbulent flow occurs at very low Reynolds numbers. In this work, transition was assumed to take place at $Re = 33$, as discussed in Chapter III. With respect to the second kind of stability, it has been mentioned already that vapor release as bubbles rarely occurs, as shown by the movies of Westwater (W-3). No theoretical examination of this phenomena has been found in the literature.

For forced convection flow within a conduit, Lavery (L-2) made qualitative observations of the transition from the film boiling regime to the dispersed two-phase flow regime which is characterized by a continuous vapor phase. He provided no quantitative data or theory. Dougall (D-5) proposed an empirical theory for prediction of the point of breakup, as mentioned in Chapter II. The evidence indicates that dispersed flow occurs when the vapor bursts into the bulk liquid are large enough to penetrate the liquid core. Thus, for pool boiling, the large amount of liquid available would seem to preclude the development of the dispersed phase regime even for very large vapor phase Reynolds numbers. This point is substantiated by the data taken in this work and by the data of Hsu (H-5) and Morgan (M-6). With respect to predicting the inception

of the dispersed flow regime for conduit flow, a promising approach would be a theoretical development paralleling the work of York et al (Y-1) which considered the breakup of a falling liquid sheet.

The mechanism by which liquid-solid contact occurs in vertical film boiling is not completely known. As the liquid interface nears the wall, the heat transfer rate should increase to provide faster vapor generation and a localized increase in pressure. This pressure buildup together with the shear forces caused by vapor flowing past the wave will tend to repel the liquid from the wall. Experimental measurements taken during this work indicate that liquid-solid contact occurs only at low wall temperatures and low vapor Reynolds numbers, conditions at which these repulsion forces would be expected to be small.

The consequences of liquid-solid contact are strongly influenced by the nature of the wall and the heat source. It would be expected that local nucleate boiling would occur immediately after such contact. Thus, the local heat transfer coefficient would suddenly increase from about $50 \text{ Btu/hour} - \text{ft}^2 - \text{deg. F.}$, which is characteristic of film boiling, to several hundred for the nucleate boiling regime. Local wall temperatures would then tend to fall very rapidly. Dougall (D-5) observed that once nucleate boiling occurred anywhere on his heater, as evidenced by very low local temperatures, the entire heating surface would gradually revert from film boiling to nucleate boiling. Indeed, Dougall's boiler could sustain film boiling only with very high temperature differences of 500 degrees F. or more. The boiler used in the work reported here, however, could support film boiling with wall to liquid temperature

differences as low as 200 degrees F., and could tolerate local liquid-solid contact without reverting to a permanent nucleate boiling regime.

This apparent anomaly may be explained by examining the nature of the heating systems. The drop in the local wall temperature that occurs right after contact will induce conduction of heat from the warmer adjacent sections of the wall to the cool spot. If this energy can be supplied fast enough to prevent the local wall temperature from falling below the Leidenfrost temperature (point B in Figure 1-1), enough vaporization will occur to re-establish a blanket of vapor at the surface and film boiling will be restored. Such a large heat transfer rate by conduction without a large temperature driving force requires that the cross-sectional area and the thermal conductivity be relatively large. Also, the ability of the heater to supply large amounts of energy rapidly without large temperature reductions implies that either the heater walls have a large heat capacity or that the heat source has a fast response time.

The massive nickel block used as the heater wall in this work apparently satisfied these conditions, and this boiler was quite stable in the film boiling regime as has been mentioned. The boiler used by Dougall (D-5) was considerably different, however, and its relative instability to liquid-solid contact is not surprising. This heater was a thin-walled (0.046 inches) stainless steel tube with a low heat capacity, a small cross-sectional area for heat flow by conduction, and a relatively low thermal conductivity. The heat source, which was an electric current passing through the tube wall, would not provide a rapid

response to changing local temperatures because the tube resistivity is not a strong function of temperature.

Rankin (R-1) considered the general question of film boiling stability in the presence of rapidly changing heat transfer rates. However, he classified heat sources as being stable or unstable in this sense simply according to whether they were steam or electrical heaters. The discussion above indicates that this is erroneous with respect to electrical heaters which will be stable under certain circumstances. In general, steam heaters would be expected to be stable to liquid-solid contact as suggested by Rankin, because condensing steam can rapidly supply additional energy as the wall temperature falls. However, this conclusion cannot be generalized to apply to all steam heating systems, for if the tube wall were thick or of a low thermal conductivity, or if the local condensate film on the steam side were thick, the response time might be too slow to prevent nucleate boiling from developing.

In summary, much work remains with respect to stability aspects of vertical film boiling. In particular, the system must be evaluated as a whole to determine the conditions under which film boiling can even exist.

CHAPTER V

EXPERIMENTAL EQUIPMENT AND PROCEDURE

The experimental equipment used in the research is described in this chapter. The boiler was used for pool boiling studies, but it was designed for ready conversion to a forced convection situation. The energy source provided a constant heat flux, while glass walls and windows permitted visual observations. Both saturated and subcooled liquid feed could be provided. Thermocouples allowed local measurements of instantaneous as well as time-average surface temperatures. Facilities were included for measurements of interfacial motion. A photograph of the overall experimental system is presented in Figure 5-1.¹

A. THE BOILER CONSTRUCTION

The boiler was a rectangular vessel with overall inside dimensions of about 3 feet high by 3 inches by 3 3/4 inches. Two vertical walls were Pyrex glass, one vertical wall and the top and bottom walls were brass, and the fourth vertical wall consisted of a nickel heating block between two short vertical brass sections. Photographs of the installed boiler without the glass walls and of the boiler components are presented in Figures 5-2 and 5-3, and a cross-sectional view of the test section is shown in Figure 5-9a.

The heater block was machined from forging quality Nickel-200² with a specified purity of at least 99.0% nickel. The heating surface was about 1/2

¹ Figures associated with Chapter V are located at the end of the chapter.

² International Nickel Co. designation

square feet in area (2 feet by 3 inches) and the nickel block was $2\frac{1}{2}$ inches thick. Energy was provided by two Redhead¹ electric cartridge heaters, each 2 feet long by $\frac{3}{4}$ inches in diameter and rated at 4600 watts, which were installed lengthwise in the nickel block. The heating elements were insulated from the sheath of the heaters, so that no electric current passed through the nickel wall. One heater is shown in Figure 5-3, and the electrical leads from the heaters can be seen in the upper right hand corner of Figure 5-2.

The thickness of the nickel block and the position of the heaters were designed so that heat conduction through the block would be one-dimensional at the heater surface. This objective was achieved by making use of the analogy between electrical conduction and heat conduction. Each process obeys similar differential equations for steady state systems:

$$\frac{d^2v}{dx^2} + \frac{d^2v}{dy^2} = 0 \quad ; \quad i_x = -\frac{1}{R} \frac{dE}{dx} \quad 5-1$$

$$\frac{d^2T}{dx^2} + \frac{d^2T}{dy^2} = 0 \quad ; \quad q_x = -k \frac{dT}{dx} \quad 5-2$$

Finding the lines of constant voltage in a system of constant resistivity is then equivalent to finding lines of constant temperature in a geometrically similar system of constant thermal conductivity. When these lines are parallel, the current, or the heat flux, will be uniform and one-dimensional. A piece of electrical conducting paper was cut to the shape of half of the

¹ Chromalox, Inc. trademark

nickel wall as shown in Figure 5-8. Only half of the wall had to be tested because of symmetry. Areas of constant voltage (E_0 and E_1 on the Figure) were created to correspond to the areas of constant temperature that would exist in the nickel block; that is, at the surface of the block and at the surface of the cartridge heater. These areas were formed on the paper with a silver paint of relatively low electrical resistance. A voltage drop was imposed across the two areas and lines of constant voltage were then determined with a potentiometer. Several geometric configurations were tested and the design finally used is shown in Figure 5-8. The constant voltage lines indicate that one-dimensional current flow existed for a depth of about one inch from the surface (E_0) except in the vicinity of the shoulders which are required for attaching the glass side walls. Of course, the actual heat transfer system would have some heat loss from the side and back walls that are not duplicated in the electric analog, but these losses were found to be negligibly small. Over most of the cross section of the heater block, and in particular in the center region where the measuring instruments were located, the heat flux would be quite uniform.

The top and bottom brass plates were connected to the nickel heater block by nickel studs extending the length of the brass plates. To reduce the heat loss from the ends of the heater block, these studs were surrounded by a two-inch long asbestos tube with a $\frac{1}{4}$ inch thick wall. These details can be seen in Figure 5-3. The gasket used to provide a seal between the brass and nickel was fabricated of asbestos fibers coated with a nitrile-butadiene rubber¹. These gaskets were rated usable to only 800 degrees F.

¹ Armstrong gasket No. AN-859

and the rubber coating seemed to decompose at still lower temperatures. However, once in place these gaskets were suitable for temperatures above 900 degrees F. Four 1/16 inch thick gasket layers were used to minimize the heat loss to the brass sections. This seal can be seen in Figure 5-5. The transition from brass to nickel across the gasket surface was quite smooth and probably caused only minor hydrodynamic disturbances.

The mechanical design of the boiler anticipated nickel temperatures up to 1200 degrees F. To maintain a tight gasket seal between the brass and the nickel even when the boiler is heated and the nickel studs have expanded, compression washers of the Belleville spring type were used. As shown in Figure 5-9, three spring washers in a parallel arrangement were used to compensate for the expected expansion. Thus, the force on the gaskets was kept fairly constant as high temperatures were attained. In addition to the nickel studs, the entire heater wall would expand up to 0.2 inches in length at the maximum temperatures. To allow this wall to move freely, the top brass plate was slotted as shown in Figure 5-4. To prevent leakage at this point, a segment of a rubber O-ring seal was installed in a groove cut into the side wall of the slot.

The $\frac{1}{4}$ inch thick glass walls were clamped to the metal walls as shown in Figure 5-10. Valuable information on techniques of construction with glass was provided by Shand (S-5) and Avitts (A-1). Clamping bars were screwed onto the shoulders on the side walls while small lips on the shoulders served as fulcrums for the clamps. The rubber coated gasket material was used on either side of the glass to prevent fluid leakage, reduce heat losses, and prevent scratching of the glass. The gasket was

1/16 inch thick by $\frac{1}{4}$ inch wide and cut into the shape of a continuous rectangle so that one piece would fit all around the glass. The shoulder and lip dimensions were such that the clamping bars would be parallel to the glass after compression of the gaskets. The clamping screws were placed on one-inch centers and were uniformly tightened to a torque of 15 to 20 inch-pounds. In order to hold the inner gasket in position while the glass was being installed, small dabs of Vaseline were applied at several points along the gasket to serve as a semi-adhesive. The Vaseline had the desirable property of sticking while cool, but vaporizing with no residual adhesiveness when heated. A potential problem with the glass construction is that friction on the gasket can cause local stresses and breakage as the boiler is heated. This was avoided by lubricating the gasket and metal sealing surfaces with a very fine graphite dust¹ before assembly. Visual observations could also be made through six round sight glasses of 1 3/4 inch diameter. These were installed in the long vertical brass wall and are shown in Figure 5-6.

The boiler was insulated with strips of a two-inch thick mineral wool blanket. The top of the boiler and the areas around the hot nickel were built up to a six-inch thickness while a single two-inch thick layer was used everywhere else. Small pieces were hand cut to fit all irregularities. The insulated boiler is shown in Figure 5-7. The mineral wool was covered with a thin layer of high temperature insulating cement. Seven windows, each 1 by 3 inches in size, were cut out of the insulation and then sealed with removable asbestos plugs. Tests showed that the heat loss through the

¹ Dixon "Microfyne" Graphite

insulation was less than 3% of the heat transferred to the fluid.

B. THE OVERALL FLOW SYSTEM

A schematic drawing of the flow system is presented in Figure 5-11. Liquid was fed to the boiler from an overhead gravity feed tank. Dissolved air was first removed from the feed by preheating with an electric cartridge heater installed in the feed line. The feed could then be directed to a refrigerated cooler if the effects of subcooled liquid were to be studied. The feed then passed through a trim heater that contained a small electric cartridge heater where a final temperature adjustment was made. As the feed entered the bottom of the boiler, visual observations through a window in the insulation were made to determine whether any vaporization had occurred in the preheating system.

The liquid level within the boiler was maintained at the top of the heated nickel block. Vapor leaving the boiler was condensed and subcooled in two tube-in-shell heat exchangers with cooling water on the shell side. Condensate dropped into a graduated cylinder from which it could be pumped directly back to the feed tank or retained while the rate of condensate collection was measured. A standard refrigeration type filter-drier¹ installed in the discharge line of the pump served to remove water and acid decomposition products from the condensate. This was installed specifically because Freon-113² was used as the test liquid, and Dougall and Rohsenow (D-5) had

¹ "Dri-Cor" filter-drier of Henry Valve Co.

² Product of E. I. du Pont de Nemours and Co.

experienced considerable decomposition with this material at high temperatures. Manual cleaning of a black deposit from their heater surface was required on several occasions. No significant deposit was noticed in the work reported here, apparently because of the filter-drier, but thermocouple problems to be described later may have had their origin in a small deposit of this kind.

To achieve film boiling in the boiler without passing through the point of critical heat flux, a quick feed technique was used similar to the approach taken by Dougall and Rohsenow (D-5). The boiler was filled to just below the bottom of the nickel block and the nickel wall was heated to between 350 and 450 degrees F. In the meantime, a quick feed tank was filled with enough liquid to charge the boiler. When the heater wall reached the desired temperature, a two-inch ball valve was opened and liquid from the quick feed tank rapidly drained into the boiler by gravity flow. The filling time was less than two seconds, and film boiling was immediately initiated.

About two hours were required to reach steady state conditions. This condition was assumed to exist when the surface temperature of the heater changed by less than two degrees F. per hour. Usually though, no temperature change could be discerned over a period of several hours. While steady conditions were maintained, several sets of measurements would be taken at 20 to 30 minute intervals. These measurements and the equipment used for data gathering and data analysis are described in the following sections.

C. TIME AVERAGE MEASUREMENTS

The locations at which time average measurements of flow, power,

pressure and temperature were made are indicated on Figure 5-11. The average boiling rate was determined by the rate at which condensate was collected. Instantaneous flow indications of the feed rotometer were within 5% of this value. The total energy received by the fluid was calculated from the enthalpy change from inlet liquid to outlet vapor. The power was independently determined with a wattmeter on the input power line and also from the energy gained by the cooling water. These three measurements agreed within 5%. Pressure measurements in the boiler were made with calibrated pressure gauges, while the vapor space and atmospheric pressures were measured with mercury manometers.

Liquid temperatures were measured at three elevations within the boiler to determine the amount of subcooling that existed. The temperatures of the upper and lower vertical brass walls were measured as an aid to determining the heat losses from the ends of the nickel.

Seven iron-Constantan thermocouples were used to measure the time average temperatures at the surface of the heater. These thermocouples were enclosed within thin walled stainless steel sheathes with a 1/16 inch outside diameter. Tightly packed magnesium oxide powder insulated the thermocouple wires within the sheath, and the wires were welded together and to the sheath at the tip. The units were then installed into tight fitting holes that originated in the back of the nickel block and terminated near the front surface. The exact location of these thermocouples is shown in Table 5-1 and the arrangement can be seen in Figure 5-11. By correcting the thermocouple readings for the temperature drop between their tips and the heater surface, the actual surface temperature could be calculated.

TABLE 5-1

Location of Thermocouples in Heater Wall

<u>Thermocouple Position No.</u>	<u>Thermocouple Type *</u>	<u>Vertical Distance From Bottom Edge of Heater (inches)</u>	<u>Horizontal Distance From Heater Surface (inches)</u>
1	F C	0.25	0.25
2	No. 1 Sur TC	1.02	0
3	F C	4.0	0.188
4	No. 2 Sur TC	5.92	0
5	F C	9.0	0.156
6	No. 3 Sur TC	12.0	0
7	F C	15.0	0.25
8	F C	18.0	0.125
9	F C	22.0	0.125
10	F C	23.0	0.125

* FC refers to iron-constantan thermocouple that terminates within heater wall.

Sur TC refers to low mass surface thermocouple that terminates at the surface of the heater wall.

Those thermocouples designated 'TR' on Figure 5-11 were connected to a 16 point temperature recorder which operated on a 32 second cycle. These thermocouples and the recorder were calibrated as a unit. The primary temperature standards were melting point samples of lead, tin and aluminum supplied by the National Bureau of Standards and boiling distilled water. The system as a whole was thus determined to be accurate within the 2 degrees F. that represents the repeatability and chart reading limitations of the recorder.

D. INSTANTANEOUS SURFACE TEMPERATURE MEASUREMENTS

Three chromel-Constantan thermocouples¹ with very low mass sensing tips were placed in the nickel wall to measure the instantaneous surface temperature. Their locations are indicated on Figure 5-11 by an asterisk and on Table 5-1. These thermocouples were embedded in a $\frac{1}{2}$ inch diameter by 3 inch long nickel screw to facilitate installation. Figure 5-14 is a schematic sketch of one of these units, while Figure 5-3 includes a photograph of one of them. For most of their length, the two thermocouple wires are contained within a $\frac{1}{8}$ inch diameter stainless steel sheath to electrically insulate the wires from one another. The sheath enters the nickel screw from the back (where it was silver soldered in place) and penetrates about $1 \frac{3}{4}$ inches. The last $1 \frac{1}{4}$ inches of the thermocouple wires are free of the sheath and are contained within the body of the screw itself. These free sections of wire were flattened to rectangular shapes of 0.001 by 0.063 inches in size. The two flattened wire sections are separated from each other and from the body of the nickel screw by 0.0002 inch thick sheets

¹ Product of Nanmac Corporation

of mica insulation arranged in a sandwich fashion. The tips of the wires and the mica layers terminate flush with the surface of the screw. At this stage, no thermocouple exists because the chromel and Constantan wires are still insulated from each other. However, gentle rubbing of the surface of the screw with a fine emory paper (about 100 grit) will scratch the surface and carry tiny slivers of metal across the insulation to complete the electrical circuit. This can be seen in Figure 5-12 which is a photomicrograph of the surface magnified 50 times. These slivers constitute the thermocouple junction. Because of its very low mass, the junction will respond very rapidly to changes in the surface temperature and can accurately measure temperature fluctuations at frequencies up to several thousand cps. Since only a small part of the system (the thermocouple wire and mica sandwich) differs in composition from the nickel heater block, there will be practically no distortion of the heat transfer process as a result of the thermocouple's presence. Excellent discussions of the design and usage of similar low mass surface thermocouples are given by Bendersky (B-2), Moore and Mesler (M-4), and Sellers (S-4).

The surface thermocouples were calibrated in a specially constructed furnace, using as standards iron-Constantan thermocouples that had been calibrated with pure metals from the Bureau of Standards. Voltage measurements were made with a precision potentiometer that was accurate to about one microvolt. Before installing the surface thermocouples in the nickel block, the threads were covered with 'Silver Goop'¹ which prevented leakage of fluid

¹ A product of Crawford Fitting Co.

through the threads. A 1/8 inch deep shoulder cut into the front of the screw was fit tight against a mating surface that had been cut into the nickel block. This detail is shown in Figure 5-14. The tip of the nickel screw protruded slightly out of the wall and it was hand ground with a fine grinding stone to be flush with the heater surface. Then 100 grit emory paper was used to scratch the tip and reestablish the thermocouple junction that had been ground away with the fine stone. The nickel was then heated to a temperature of about 900 degrees F. to boil off solvents and decomposition products from the 'Silver Goop'.

Some problems were encountered with the surface thermocouples. The junctions at the tips were occasionally destroyed and rescratching with emory paper was required. The cause of this was not determined, but it was suspected that decomposition products of Freon-113 that form when the vapors contact a hot surface were involved. In addition, breakage of the thermocouple wires within the body of the nickel screw occurred in two instances. It was suspected that differential thermal expansion was the cause of this problem.

During the film boiling experiments with wall temperatures as high as 800 degrees F., instantaneous temperature variations of the order of $\frac{1}{2}$ degree F. from the mean temperature were encountered. This corresponded to a fluctuation in the surface thermocouple output signal of about 20 microvolts from a mean value of as much as 30 millivolts. To accurately analyze the small voltage fluctuations, the signal had to be amplified by a factor of 1000 to 6000. Such an amplification of the large time-average component of the signal would have greatly overloaded the electronic equipment. Thus, a simple bucking circuit as shown in Figure 5-15 was used to remove the DC component

from the signal.

The thermocouple signal could be switched to either the precision potentiometer for time average measurements of the signal or to the instantaneous measuring system. In the latter case, the DC component was first removed and the remaining signal was then amplified 1000 times by a Dana Model 3520 DC data amplifier. This amplifier was quite stable and noise free. The drift in gain would not exceed one per cent over a several day period. Noise developed in the amplifier was less than one microvolt rms based on the input. When the input signal was properly grounded and balanced, the amplifier's common mode rejection was rated at 120 decibels. To insure that the input signal to the amplifier was nearly balanced, the variable resistor in the bucking circuit of Figure 5-15 was kept at the low value of 20 ohms. With this system, only a negligible amount of 60 cps noise passed through the amplifier. The output signal from the amplifier passed through a built-in low pass filter which was set at 1000 cps for this work. Signals of this frequency or higher were attenuated by about 30% or more, while signals with a frequency of less than 200 cps were attenuated by less than 3%. It will be seen in Chapter VI that practically no temperature fluctuation existed in the frequency range affected by the filter.

Using three circuits in parallel similar to that of Figure 5-15, the outputs from the three surface thermocouples were recorded simultaneously on a seven channel Ampex Tape Recorder. The tape recorder gain was set at values between one and six for the various runs. The recording speed was $7\frac{1}{2}$ inches per second while playback speeds of $1\frac{3}{4}$ and $7\frac{1}{2}$ inches per second were used. These records of the surface temperature fluctuations were subsequently analyzed with a strip chart recorder, a heat meter, and a wave

form analyzer. These procedures will be more fully described in later sections.

E. THE HEAT METER

With the temperature fluctuations at the surface of the heater known as a function of time, the instantaneous heat flux at the surface can be determined. Then, the effect of interfacial waves on the heat transfer rates in film boiling can be studied. Surface thermocouples were used in this manner by Bendersky (B-2) and Myers (M-7). The procedure is discussed in this section.

One-dimensional heat conduction is governed by the differential equation:

$$\frac{d^2T}{dx^2} = \frac{1}{\alpha} \frac{dT}{dt} \quad 5-3$$

with the local heat flux given by:

$$q = -k \frac{dT}{dx} \quad 5-4$$

The instantaneous temperature history that was recorded on tape can serve as a boundary condition in the solution of equation 5-3. If the heater block is assumed to be infinite in depth, the temperature profile within the nickel block could then be determined and equation 5-4 could be solved for the local heat flux. For example, let the surface temperature, T_0 , fluctuate periodically:

$$x=0, \quad T_0 = \bar{T}_0 + \gamma \sin \omega t \quad 5-5$$

where \bar{T}_0 is the time average surface temperature. Then, from Carslaw and Jaeger (C-1), the solution to equation 5-3 is:

$$T = \bar{T}_0 + \gamma e^{-x(\omega/2\alpha)^{1/2}} \sin \left(\omega t - x \sqrt{\frac{\omega}{2\alpha}} \right) \quad 5-6$$

where the transient solution has not been considered. By equation 5-4, the heat flux is:

$$q = k \gamma \left(\frac{\omega}{\alpha}\right)^{1/2} e^{-x\left(\frac{\omega}{2\alpha}\right)^{1/2}} \sin\left(\omega t - x\sqrt{\frac{\omega}{2\alpha}} + \frac{\pi}{4}\right) \quad 5-7$$

In particular, the heat flux at the surface to the fluid is:

$$q_{x=0} = k \gamma \left(\frac{\omega}{\alpha}\right)^{1/2} \sin\left(\omega t + \frac{\pi}{4}\right) \quad 5-8$$

Thus, measuring the frequency and amplitude of a sinusoidal surface temperature fluctuation ($\omega/2\pi$ and γ) would lead directly to the amplitude ($k\gamma\sqrt{\frac{\omega}{\alpha}}$) of the corresponding heat flux changes.

In reality, the nickel block is not infinite in depth and the procedure described will only provide an approximate solution. However, it is shown in Appendix D that the temperature disturbances at the surface do not penetrate very deeply into the nickel wall, so that the assumption of an infinite thickness is accurate enough.

A greater problem is presented by the fact that the surface temperature fluctuations are random rather than periodic, so that solving equation 5-3 becomes very difficult. A numerical solution of the equivalent difference equation could be attained as was done by Bendersky (B-2). In this work, however, a specialized analog computer, called the heat meter, was used to solve equation 5-3. The principle of the heat meter was discussed by Meyer (M-2), and Myers (M-7) used such a system to measure the instantaneous heat flux during film condensation of acetone and methanol inside a horizontal tube.

The basis for the heat meter is the mathematical analogy between one-dimensional heat conduction and one-dimensional current flow in an electrical

system containing distributed capacitance and resistance (such as a coaxial cable). The differential equations governing the electrical system are:

$$\frac{d^2 v}{dx^2} = RC \frac{dv}{dt} \quad 5-9$$

$$i = -\frac{1}{R} \frac{dv}{dx} \quad 5-10$$

where R and C are the resistance and capacitance per unit length of cable. Equations 5-9 and 5-10 are clearly analogous to equations 5-3 and 5-4 that apply to heat conduction, so that similar boundary conditions for the two sets of equations will lead to similar solutions. The mathematical analogy among these and other physical processes is excellently described by Moore (M-5). In Appendix D the mathematics of the heat meter are presented in detail but the results will be anticipated here.

A coaxial cable could be used as a heat meter, but typical values of resistance and capacitance would lead to a prohibitively long cable of several miles. Instead, the cable is approximated by a lumped parameter system containing discrete resistors and capacitors as shown in Figure 5-16. To further reduce the size of the circuit, the resistors and capacitors are increased in size according to an arithmetic progression. These details are discussed in Appendix D. The surface temperature of the heater block is transformed into a voltage by the surface thermocouple:

$$T = a_0 + a_1 v \quad 5-11$$

where 'a₀' and 'a₁' are constants. This linear relationship is quite accurate for the small range of temperature fluctuations encountered, though the

constants are dependent upon the time average temperature. When this voltage is applied to the input of the heat meter, the resulting voltage drop, ΔE , across the first resistor (r_1) corresponds uniquely to the temperature change ($\Delta T = a_1 \Delta E$) across a small thickness of the nickel block at the surface of the heater. This thickness is shown in Appendix D to be:

$$\Delta x = \left(\frac{1}{2} \propto r_1 C_1 \right)^{1/2} \quad 5-12$$

Thus, the instantaneous heat flux at the surface can be approximated from equation 5-4:

$$\bar{q}^{\Delta x} = -k \frac{a_1 \Delta E}{\left(\frac{1}{2} \propto r_1 C_1 \right)^{1/2}} \quad 5-13$$

The bar above 'q' indicates that this is the instantaneous local heat flux averaged over the distance Δx . As Δx becomes sufficiently small, $\bar{q}^{\Delta x}$ approaches the surface heat flux, which is also the instantaneous rate of heat transfer from the wall to the fluid. An advantage of the heat meter over an analytical solution is observed by comparing equation 5-13 to equation 5-8. It is seen that the heat meter output can be converted to heat flux without a knowledge of the frequency of the disturbance.

The tape recording of the surface temperature fluctuations was played back through the heat meter. The heat meter output signal as well as the temperature signal itself were recorded simultaneously on a two-channel Sanborn strip chart recorder. The voltage indications on these records could then be converted to peak values of the heat flux according to equation 5-13. These charts and calculations are presented in Chapter VI. The signals were also studied on the wave form analyzer to be described next.

F. THE WAVE FORM ANALYZER

The spectral densities and mean-square averages of the fluctuating surface temperature and heat flux signals were measured as a means of further characterizing the film boiling system. For this purpose, a Weston-Boonshaft and Fuchs Wave Form Analyzer, Model 711C, was used. This machine will analyze two input signals, $x(t)$ and $y(t)$, simultaneously and provide as output signals:

- (1) the spectral density of each signal, $\bar{\Phi}_{xx}(f)$ and $\bar{\Phi}_{yy}(f)$;
- (2) the cross-spectral density or amplitude spectrum of the two signals, $\bar{\Phi}_{xy}(f)$; and
- (3) the phase angle between the two signals, or the phase spectra, $\theta(f)$.

This analysis is performed as a function of the frequency, f , which can be specified with three significant figures within a range from 0.010 to 3000 cps. In addition, the mean square average of the signals can be measured over the frequency range between DC and 3000 cps.

A window size about the selected frequency could be chosen from the values: ± 0.1 , 0.33, 1., 3.3, 10., 33., or 100. cps. The integration time could be set at any integer value between 1 and 1000 seconds. When analyzing a random signal, the accuracy of the spectral density function determined by the wave form analyzer must be stated in statistical terms. As pointed out by Schiesser (S-3), this statistical accuracy is a function of both the window size and the time length of the record being analyzed.

In this work, the DC levels of the temperature and heat flux signals were not required at this stage of the analysis. The input signals to the wave form analyzer were accordingly routed through an internal high pass

filter set at 0.01 cps to remove any residual DC voltage component that had not been removed by the bucking circuit of Figure 5-15. Integration times and window sizes were always set to provide a 90% confidence level that the measured spectral density values agreed within 10% of actual values. The results of these analyses are presented in Chapter VI.

G. MEASUREMENTS OF THE INTERFACIAL STRUCTURE

A special pressure measuring probe¹ was used in an attempt to determine the nature of the interfacial motion and the average vapor film thickness. The probe and associated equipment are shown in Figure 5-17. With the tip of the probe positioned at a known distance from the heater wall, pressure changes due to interfacial motion were detected. The resulting voltage signal was recorded both on tape and on the strip chart recorder.

The probe was essentially a long, small bore tube through which nitrogen gas flowed at very low rates of less than 0.01 standard cubic feet per hour. The nitrogen source was a very large reservoir with a volume of about 1.5 cubic feet that maintained a constant upstream pressure. Because of the low flow rates, standard pressure regulating devices were not suitable for this purpose. The downstream pressure at the orifice in the tip of the probe depended upon the conditions within the boiler. Depending upon its orientation, the orifice sensed either the static pressure or the total pressure including the velocity head of the fluid.

Since the upstream pressure was constant, the nitrogen flow rate depended only upon the pressure at the tip of the probe. Furthermore, the flow was

¹ Manufactured by Thermo-Systems, Inc.

laminar, so the flow rate was directly proportional to the downstream pressure. This flow rate was detected by a standard 0.001 inch diameter hot film sensor that had been installed across the diameter of the probe within a venturi section. The sensor was controlled by a constant temperature anemometer¹ that provided an output voltage with both DC and fluctuating components. The DC voltage represented the average flow rate past the sensor, or the time average pressure at the tip of the probe. The fluctuating component of the anemometer signal was directly proportional to the pressure fluctuations at the orifice. The DC voltage had to be removed before amplifying the signal to avoid overloading of the electronic equipment. The bucking circuit shown in Figure 5-18 was used for this purpose. Two DC amplifiers were required to overcome ground loop problems that occurred when the bucking circuit was connected directly to the anemometer output. The entire system was statically calibrated with no liquid in the boiler. The reservoir and the boiler were filled with nitrogen gas to attain the desired pressure differential. The voltage output from the anemometer was then a measure of the resulting nitrogen flow rate and of the pressure drop across the probe.

The position of the probe with respect to the heater wall was fixed with the micrometer-driven traversing mechanism shown in Figure 5-13. This distance could be set with an accuracy of 0.1 mils. The traversing mechanism was mounted on the vertical rod shown in Figure 5-7 and could be stationed at various elevations corresponding to the elevations of the surface thermocouples. The zero position, at which the probe tip contacted the

¹ Thermo-Systems, Inc. Model 1010

wall, had to be determined while the boiler was at its operating temperature. It could not be determined visually because interfacial activity obscured the field of view. Therefore, electrical continuity between the body of the probe and the heater wall was determined with an ohmmeter to indicate when the probe tip touched the wall. With this technique, the zero position could be determined with a repeatability of 0.4 mils.

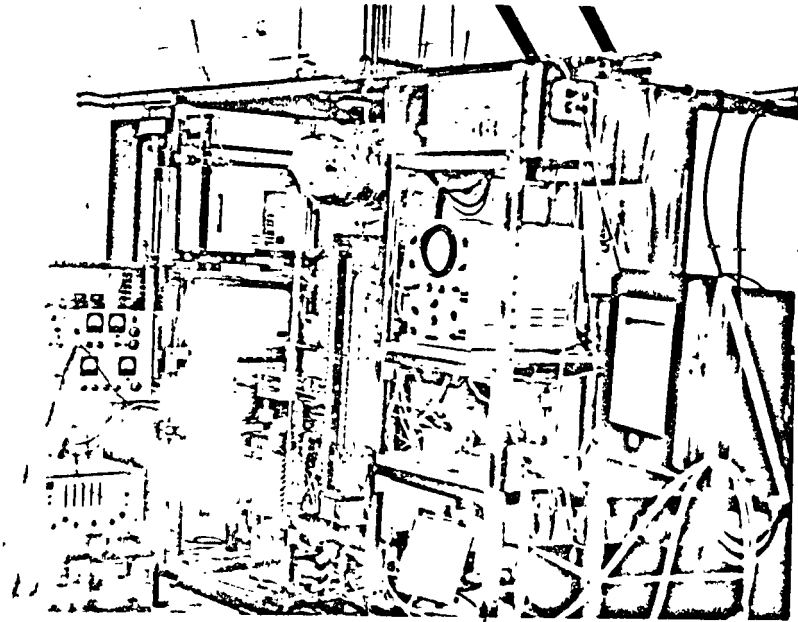


FIGURE 5-1
EXPERIMENTAL EQUIPMENT FOR FILM
BOILING MEASUREMENTS

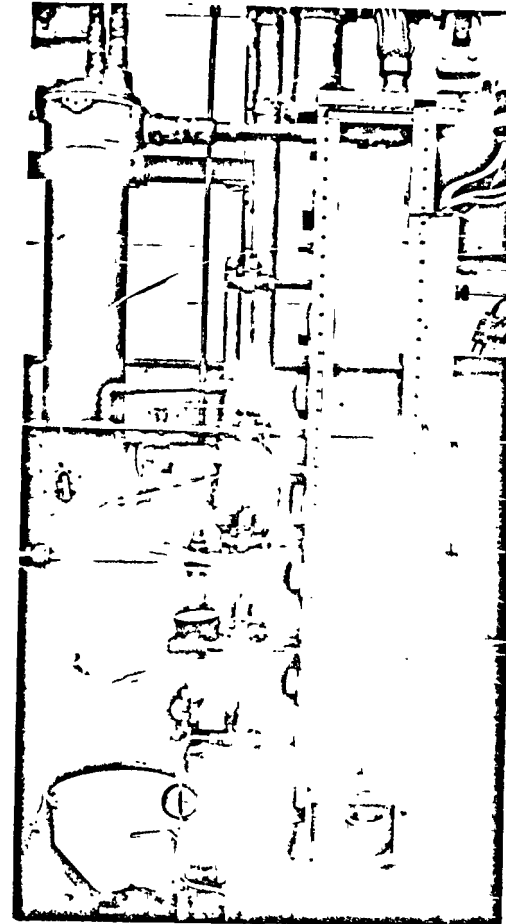


FIGURE 5-2
BOILER IN PLACE BEFORE
INSTALLATION OF GLASS

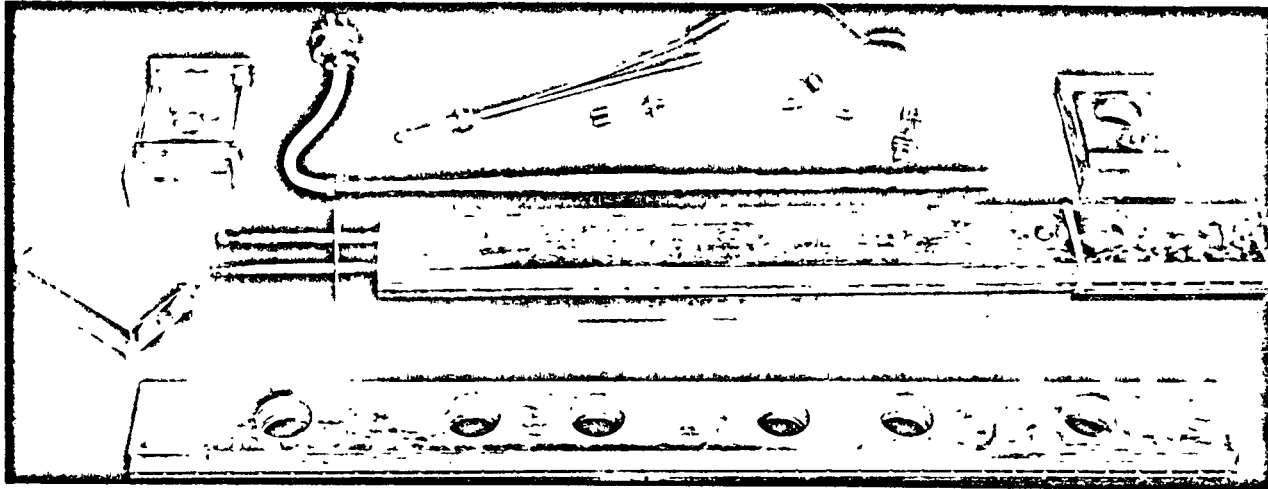


FIGURE 5-3. COMPONENTS OF BOILER BEFORE ASSEMBLY

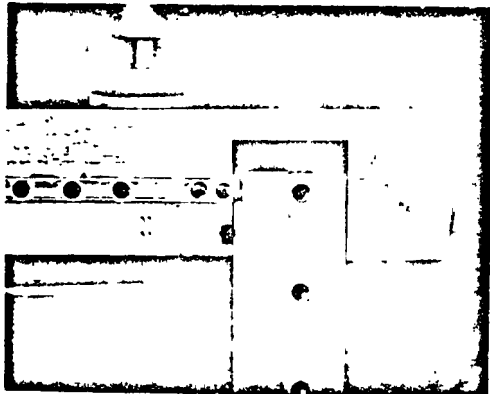


FIGURE 5-4
SLIDING SEAL IN TOP
WALL OF BOILER



FIGURE 5-5
GASKET SEPARATING NICKEL
AND BRASS

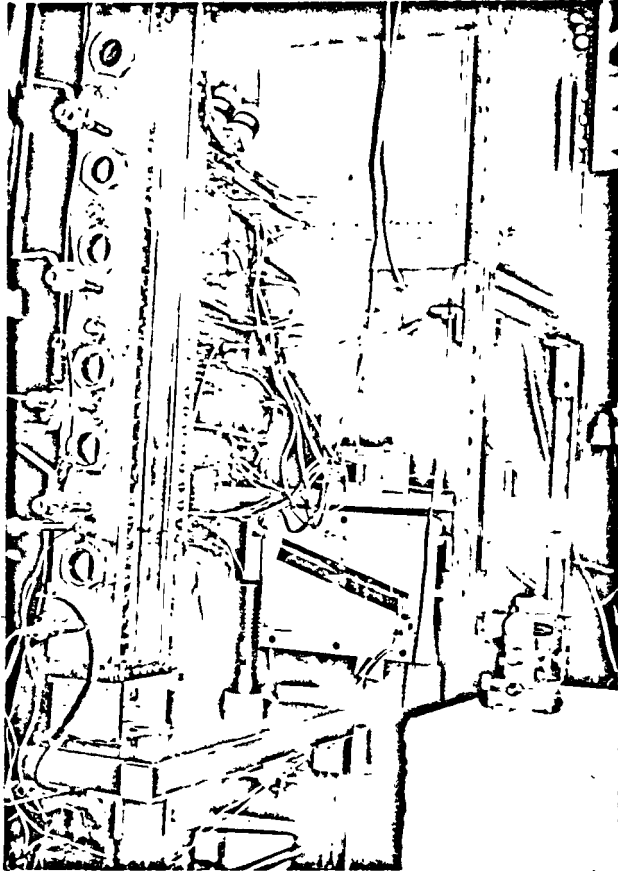


FIGURE 5-6
ASSEMBLED BOILER WITH GLASS
IN PLACE

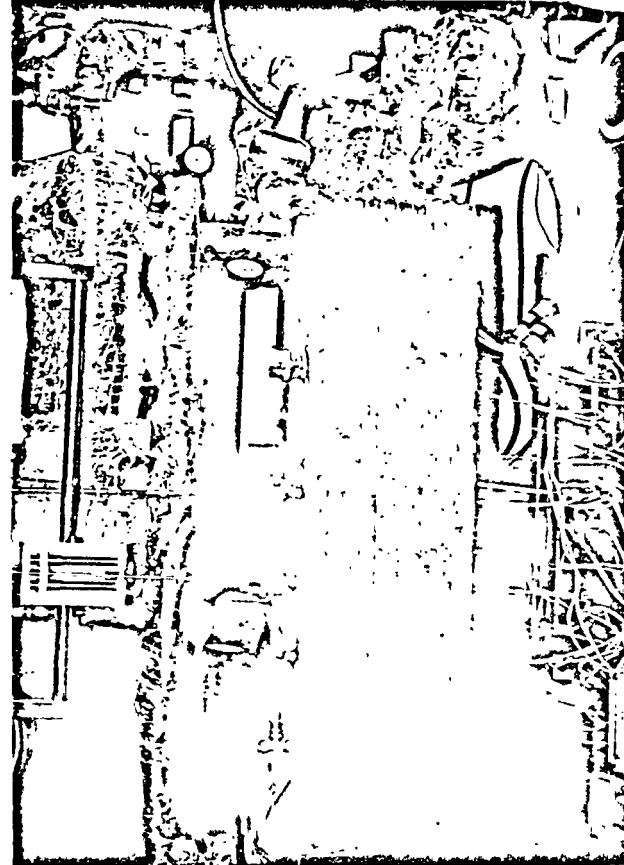
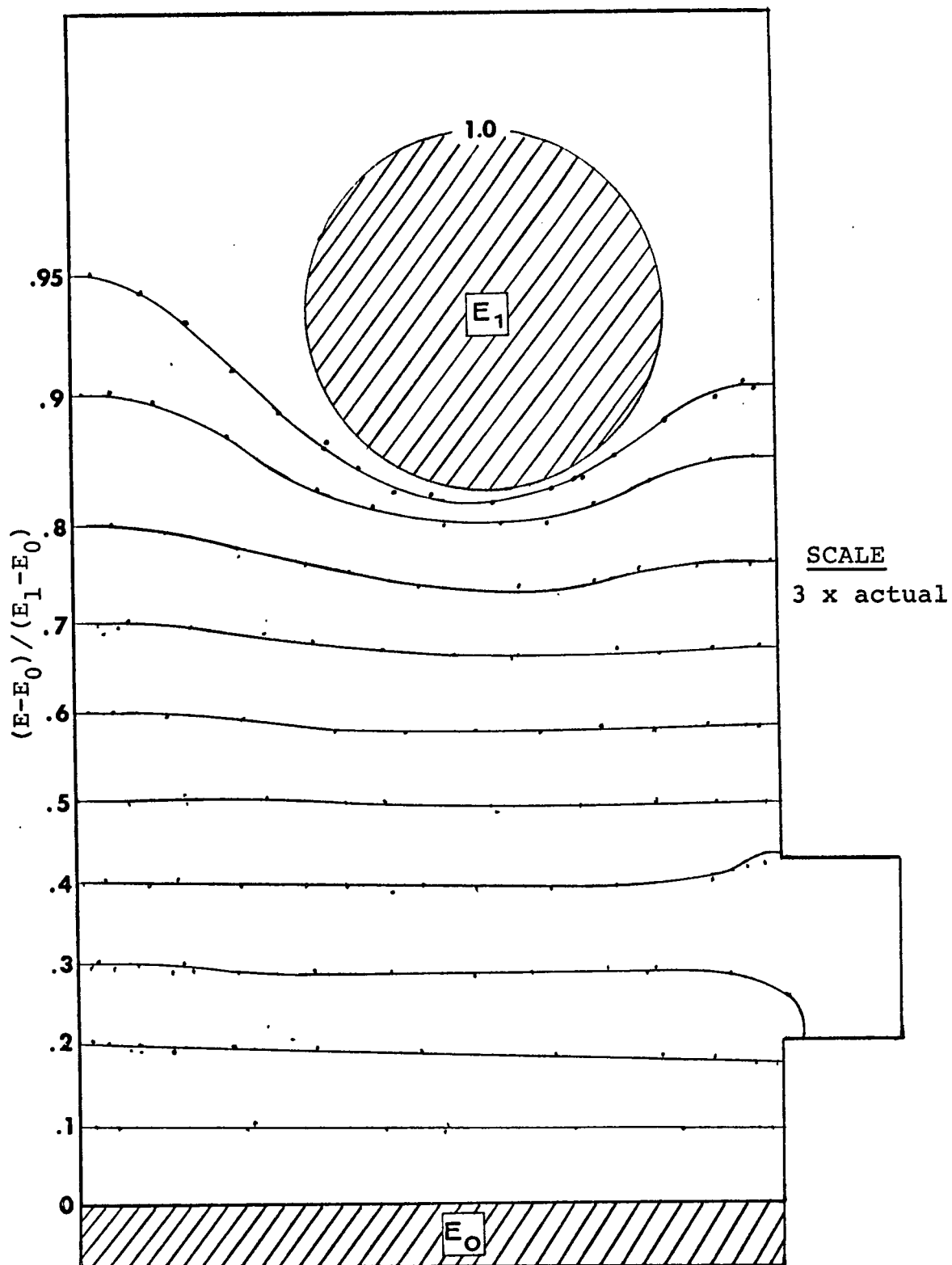


FIGURE 5-7
BOILER WITH MINERAL WOOL
INSULATION IN PLACE

FIGURE 5-8: LINES OF CONSTANT POTENTIAL BETWEEN SURFACES AT E_0 AND E_1 , FOR TWO-DIMENSIONAL ELECTRICAL CONDUCTOR WITH SAME SHAPE AS BOILER



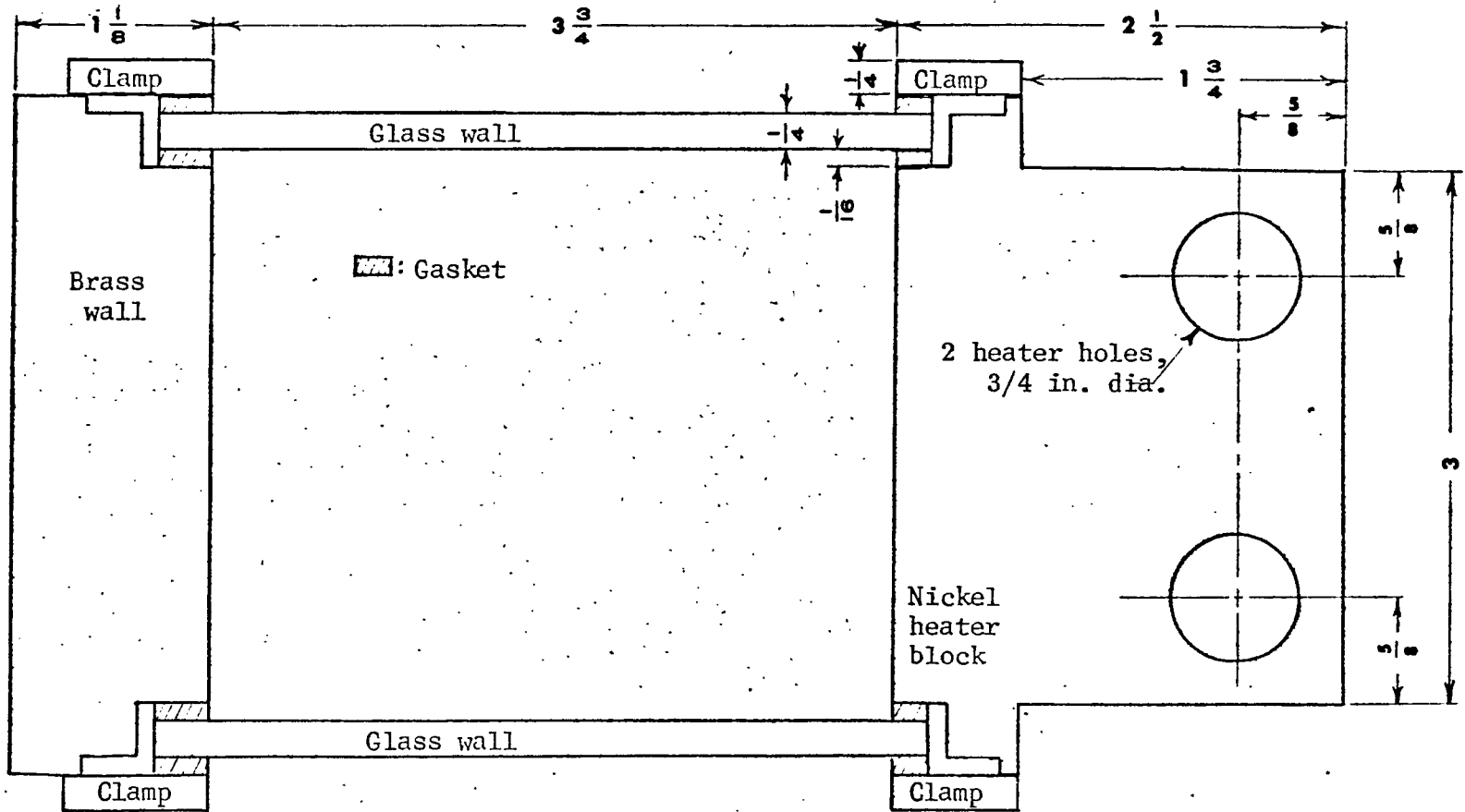


FIGURE 5-9a
 CROSS-SECTIONAL VIEW of BOILER

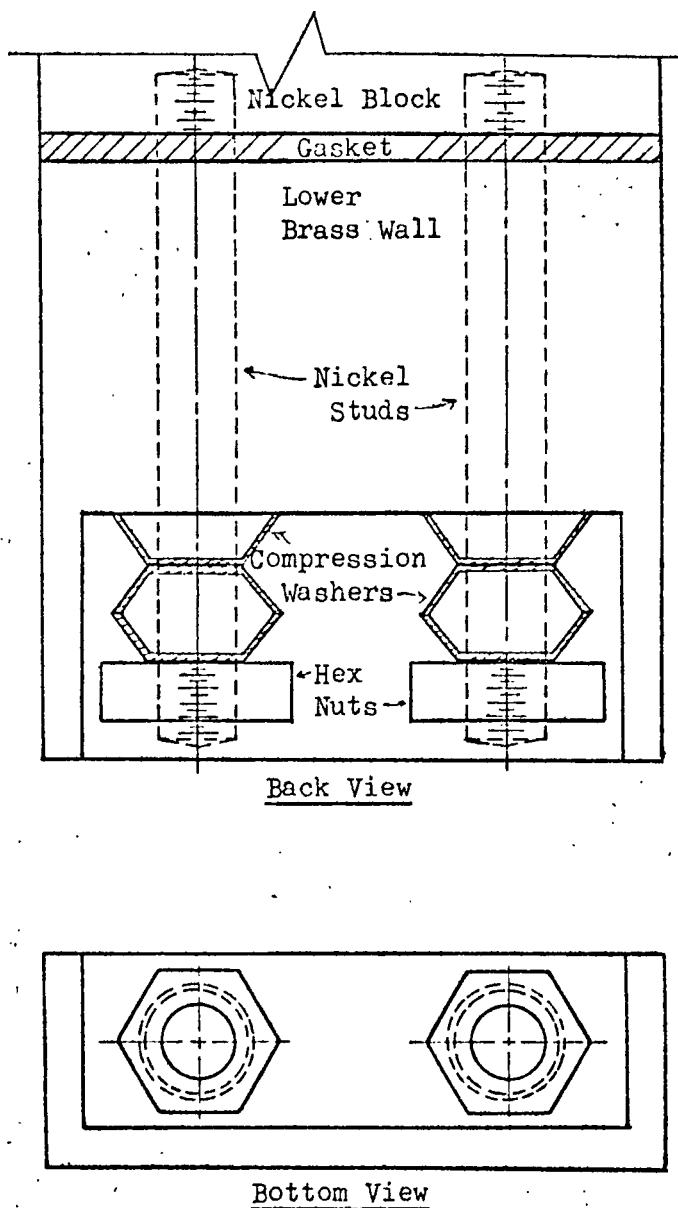


FIGURE 5-9

Details of Fastening Brass Section
to Nickel Heater Block

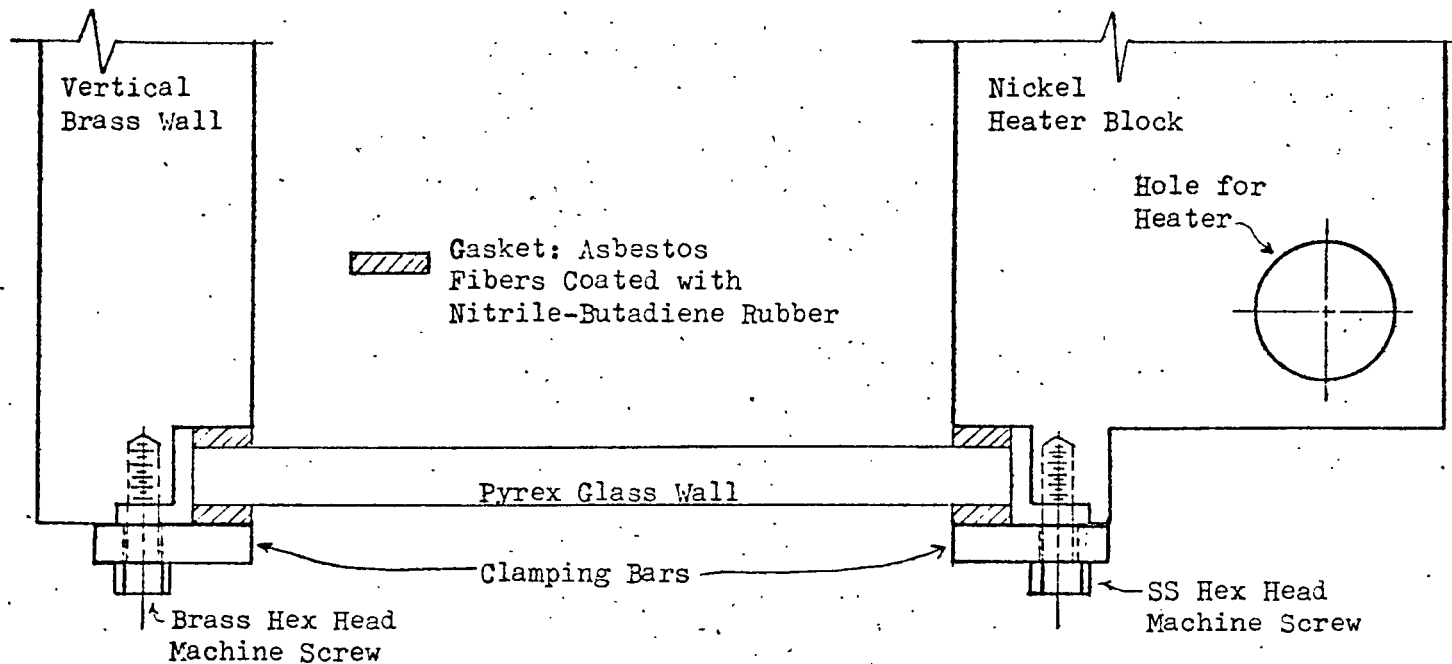


FIGURE 5-10

Details of Clamping Glass Side Walls to Boiler

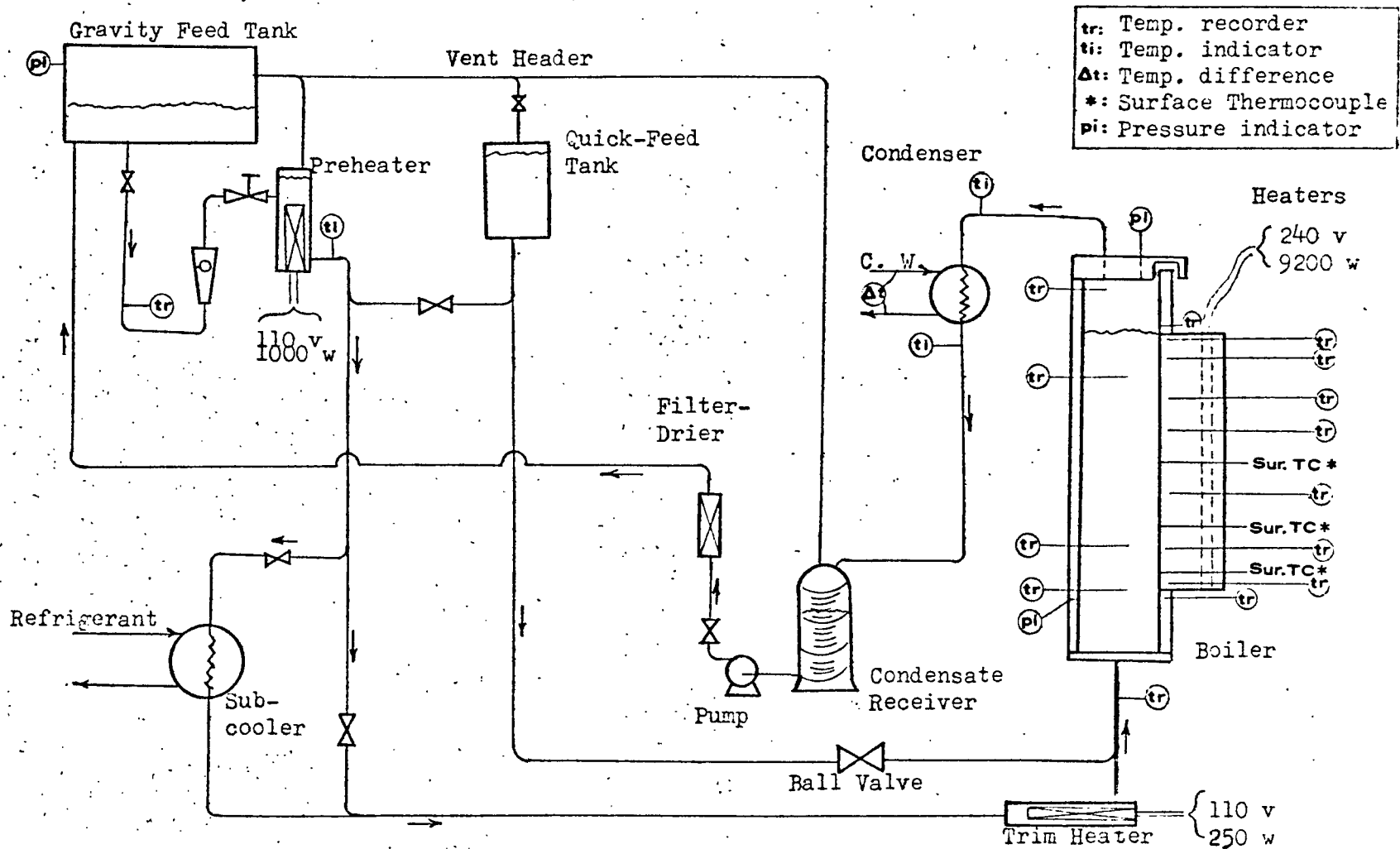


FIGURE 5-11

Schematic View of Flow System,
Showing Measuring Stations

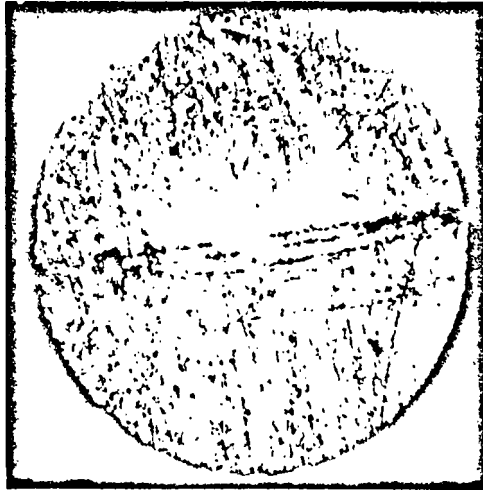


FIGURE 5-12
X 50 PHOTOMICROGRAPH OF TIP
OF SURFACE THERMOCOUPLE

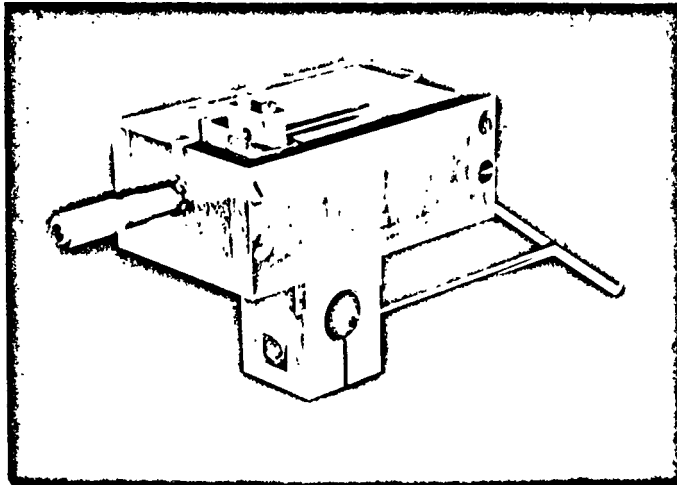


FIGURE 5-13
MICROMETER DRIVE MECHANISM FOR
FILM THICKNESS PROBE

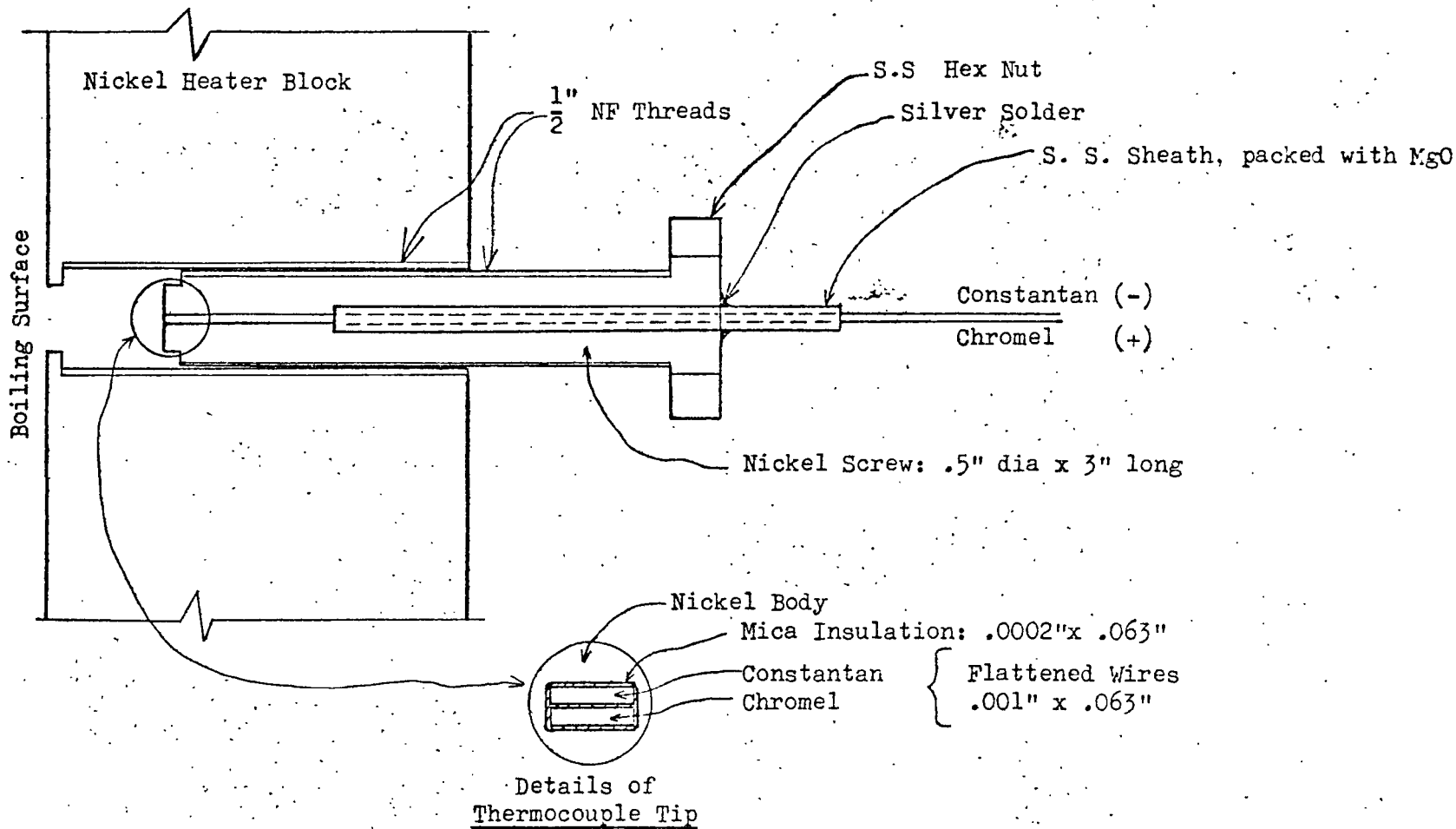


FIGURE 5-14

Cut-away View of Screw Containing Surface Thermocouple

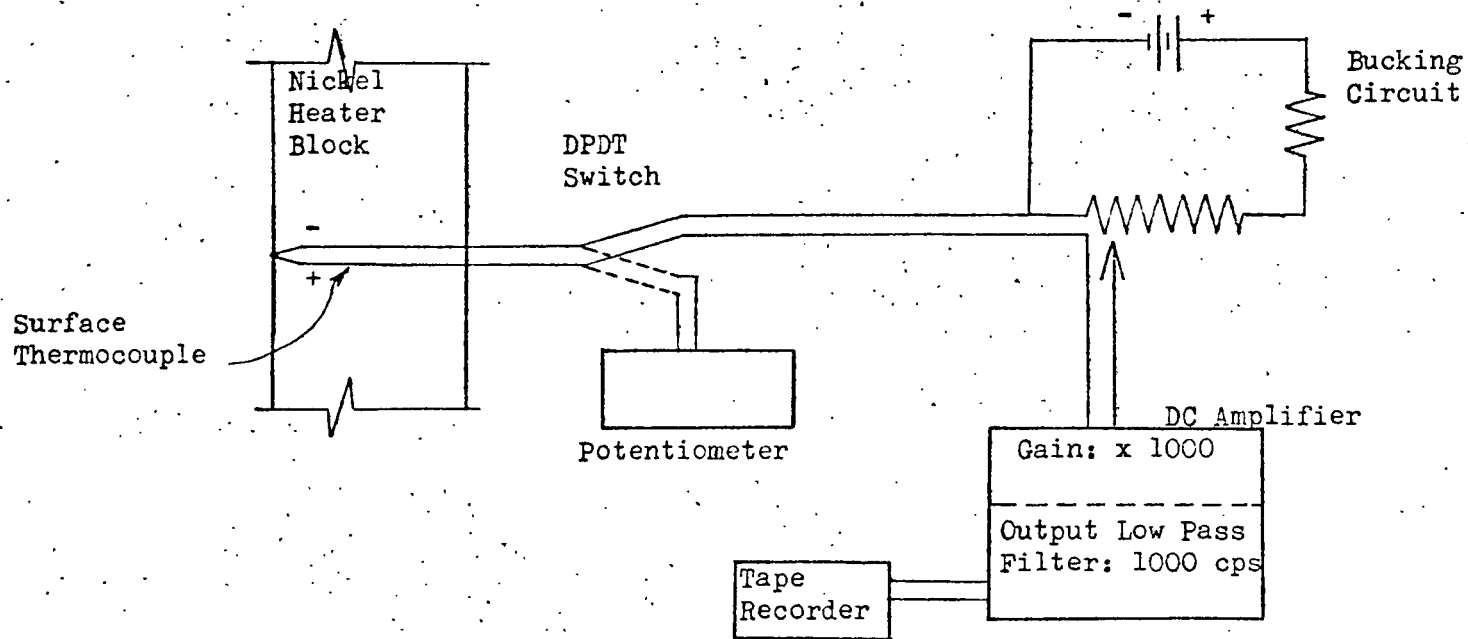
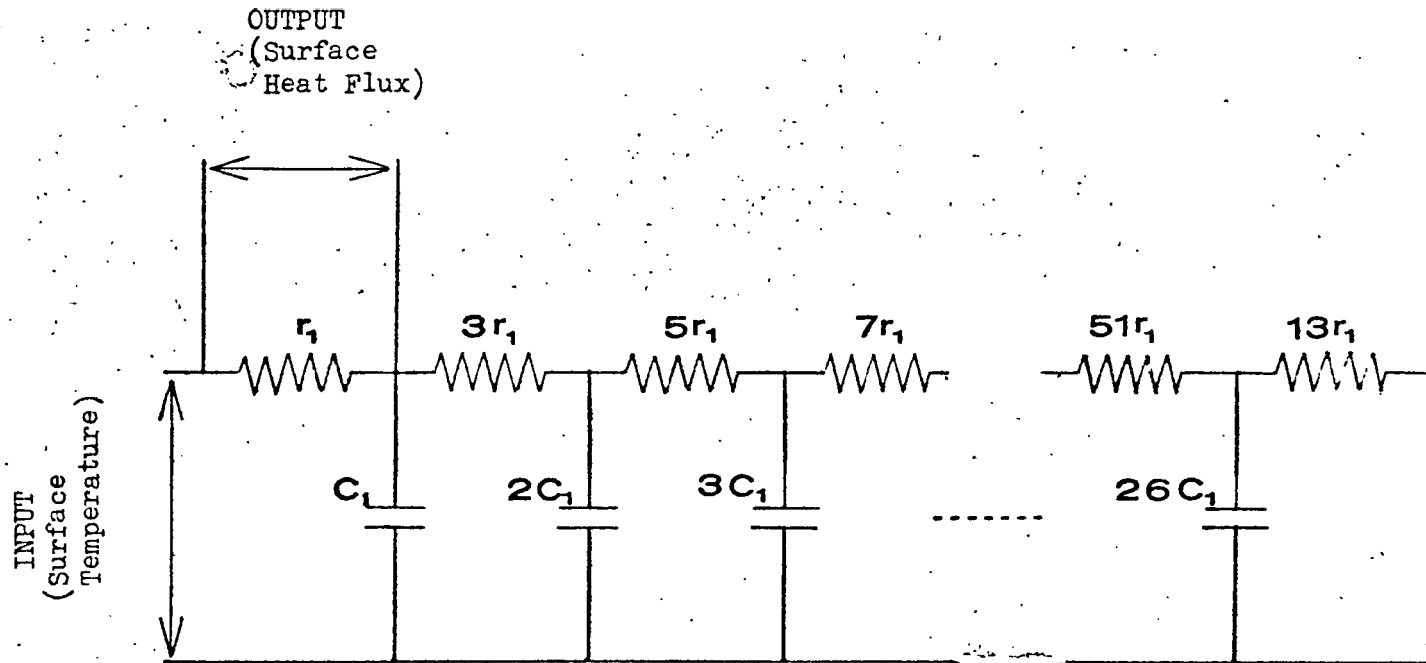


FIGURE 5-15

Circuit for Monitoring Signal
from Surface Thermocouple



$r_1 = 14,240$ ohms
 $C_1 = 0.0102$ farads $\times 10^{-6}$

FIGURE 5-16
 Heat Meter Design

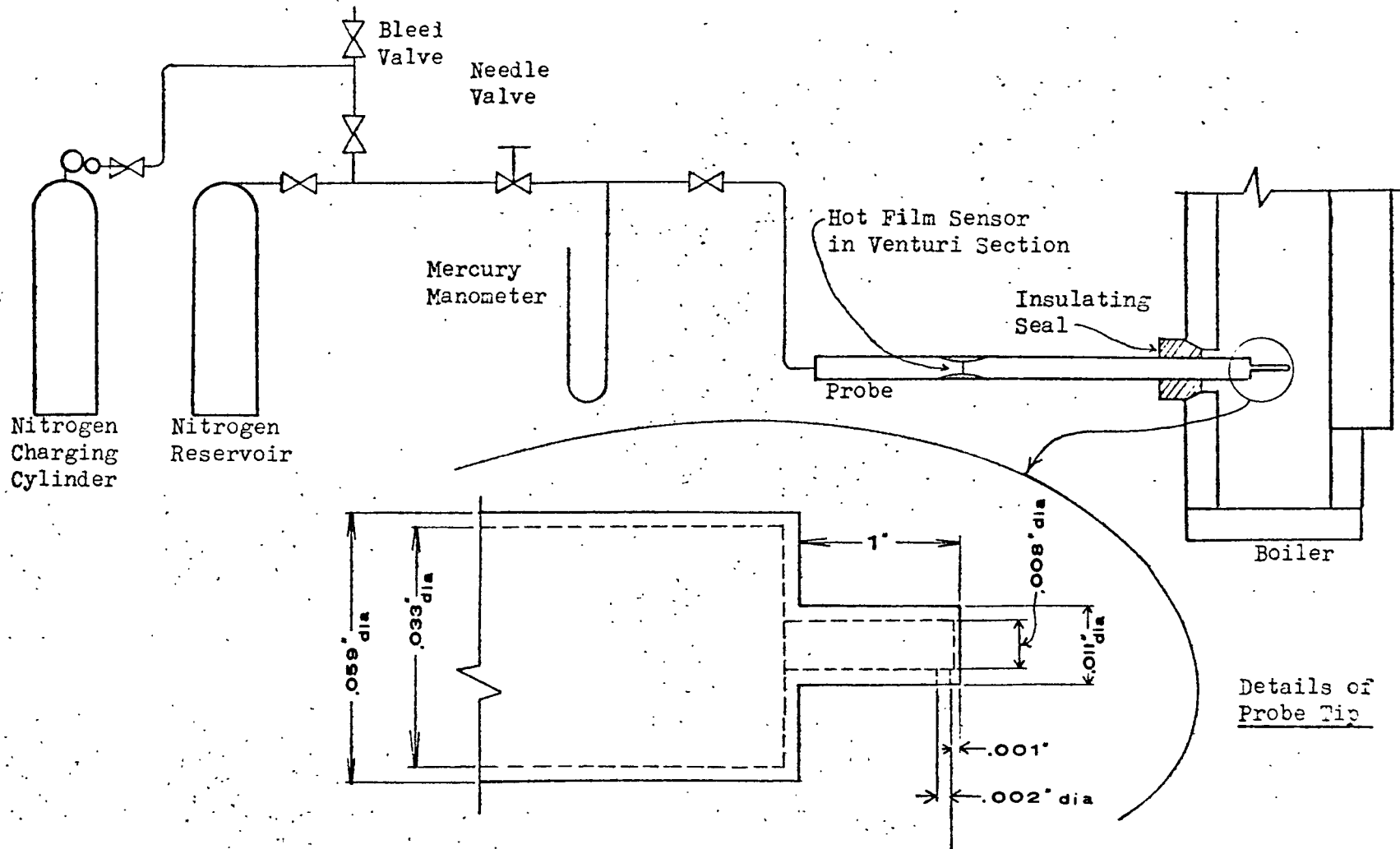


FIGURE 5-17

Pressure Sensing Probe and
Auxiliary Equipment

Input Signal from
Pressure Sensing
Probe

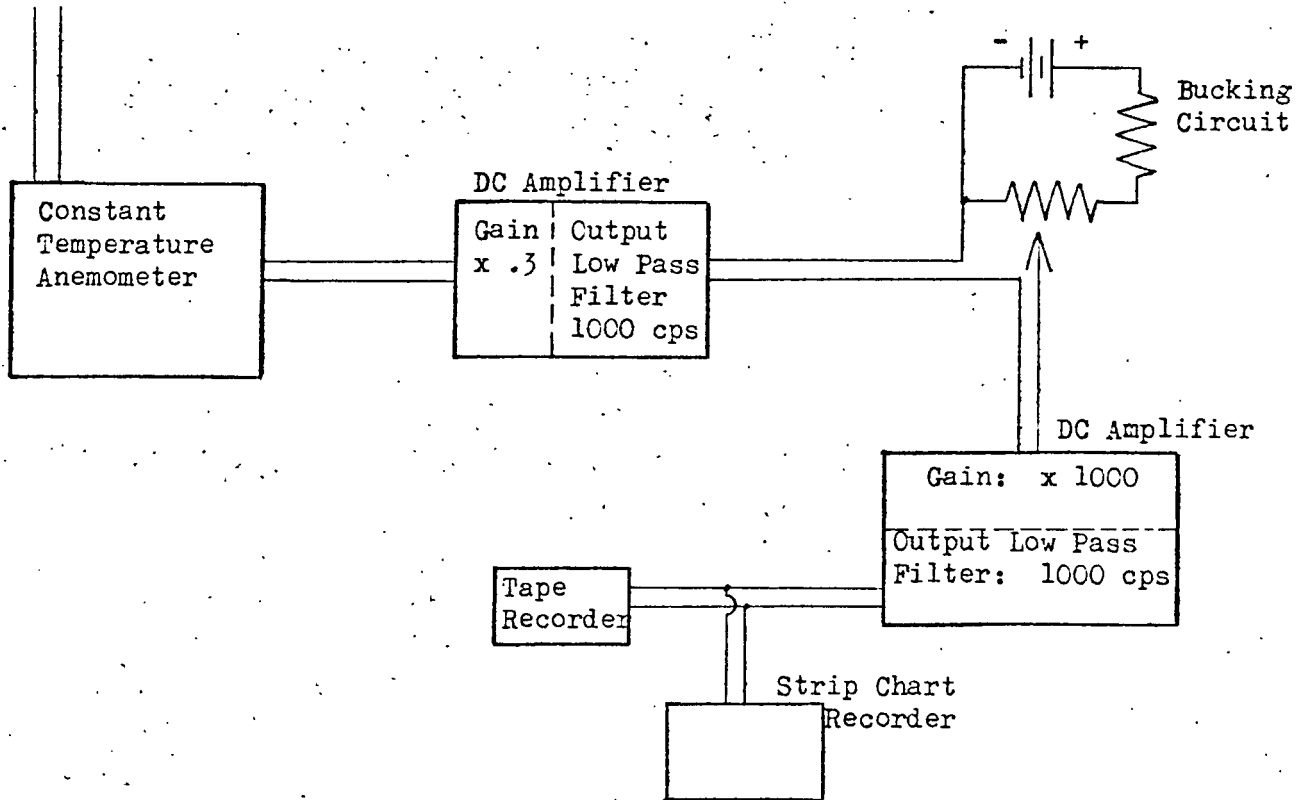


FIGURE 5-18

Circuit for Monitoring Signal from
Pressure Sensing Probe

CHAPTER VI

EVALUATION OF THE DATA AND THE THEORIES

The data collected for this dissertation will be examined in detail in this chapter. The experimental time-average local heat transfer coefficients will first be compared to the predictions of the quasi-steady state theory. The instantaneous measurements of the fluctuating surface temperature and heat flux will then be presented and the implications of these fluctuations will be determined according to the unsteady state theory. Evidences of liquid-solid contact will be discussed. Later in the chapter, some of the theories and data presented in the literature will be compared with those of this work.

A. TIME-AVERAGE LOCAL MEASUREMENTS

Evaluation of the quasi-steady state theory requires an experimental determination of the local CC, Reynolds and Prandtl numbers. These dimensionless terms can be calculated when the surface temperature of the heater, the liquid saturation temperature, and the local heat flux are known. The total heat transferred to the liquid was determined by:

$$Q_{\text{total}} = W_{\text{con}} \times \Delta H_b \quad 6-1$$

where W_{con} is the measured collection rate of liquid condensate and ΔH_b is the change of enthalpy of the fluid from the boiler entrance to exit. Some of this energy is transferred to the fluid by conduction through the top and bottom brass walls and the side glass walls. The vapor generated in this manner will not be in the vapor film next to the heated

wall. Therefore, this heat flow is subtracted from Q_{total} before 'h' or the vapor film Reynolds number is calculated. The remaining heat flow was assumed to be uniformly distributed over the heater surface.

$$Q = (Q_{\text{total}} - Q_{\text{end losses}})/(\text{Boiler Area}) \quad 6-2$$

where the heat flux, Q , includes the energy transferred by radiation. Local wall temperatures were measured at the ten locations shown in Table 5-1. At positions 2, 4 and 6, the surface thermocouples gave a direct measure of this temperature. At the other positions, the temperature was measured within the solid just below the surface and converted to a surface temperature by assuming one-dimensional heat conduction:

$$T_w = T_{\text{buried}} - \frac{Q \cdot \Delta x}{k_{Ni}} \quad 6-3$$

The local radiant heat flux was then determined by equation 3-83 with the nickel emissivity assumed to be 0.7. The local convective heat transfer coefficient was then calculated:

$$h = \frac{Q - q_r}{T_w - T_s} \quad 6-4$$

With physical properties determined at the average vapor temperature, the CC number was determined from equation 3-56. The local Reynolds number was calculated from equations 3-88, 3-95 and 3-96, with Q given by equation 6-2 since the vapor generated by radiation remains in the film. The physical properties of Freon-113, the nickel heater wall and the glass side walls were taken from publications of the manufacturers .

(E -1, E-2, H-4, C-12). These values are summarized in Appendix F.

The test runs that were used to evaluate the theory are listed in Table 6-1 in order of increasing heat flux. Table 6-2 at the end of this section contains a detailed summary of the time-average data from these runs, while the nomenclature used for this tabulation is presented as the first entry in the table. The lack of an entry for thermocouple positions 2, 4 and 6 in several sections of the table indicates that surface-thermocouple measurements were not made for those runs.

Graphs of the vertical temperature profile at the nickel surface are presented in Figures 6-1 and 6-2 for several typical runs. These indicate the presence of some vertical heat flow within the heater wall. These curves are nearly linear in the center regions, indicating that the net vertical heat flux was small over most of the heater surface. The primary cause of the vertical heat flux was the end losses of energy from the nickel block to the brass sections. In some cases where liquid-solid contact occurred near the bottom of the nickel wall (see Section E), the large local heat transfer coefficients in the regions of contact also led to vertical transfer of energy. An exact calculation of the vertical flux could not be made without extensive measurements of the temperature distribution within the heater block. Therefore, the heat flux was assumed to be uniformly distributed over the entire heating surface. To evaluate the accuracy of this assumption, the differential equation for two-dimensional heat conduction:

$$\frac{d^2 T}{dx^2} + \frac{d^2 T}{dy^2} = 0$$

TABLE 6-1

Summary of Test Runs Arranged in Order of Increasing Heat Flux

<u>Run No.</u>	<u>Heat Flux (Btu/hr-ft²)</u>
22D	8600
16D	9260
23C	9370
17D	9460
18C	9520
24C	10900
3B	11600
11C	12000
5C	12000
9B	12100
13C	12300
1D	12300
12D	12300
25D	12500
19C	14900
7B	17800
20B	18000
14D	18200
2B	20900
6B	21800
15C	22300
21A	24000

FIGURE 6-1

TEMPERATURE PROFILES AT SURFACE
OF NICKEL HEATER

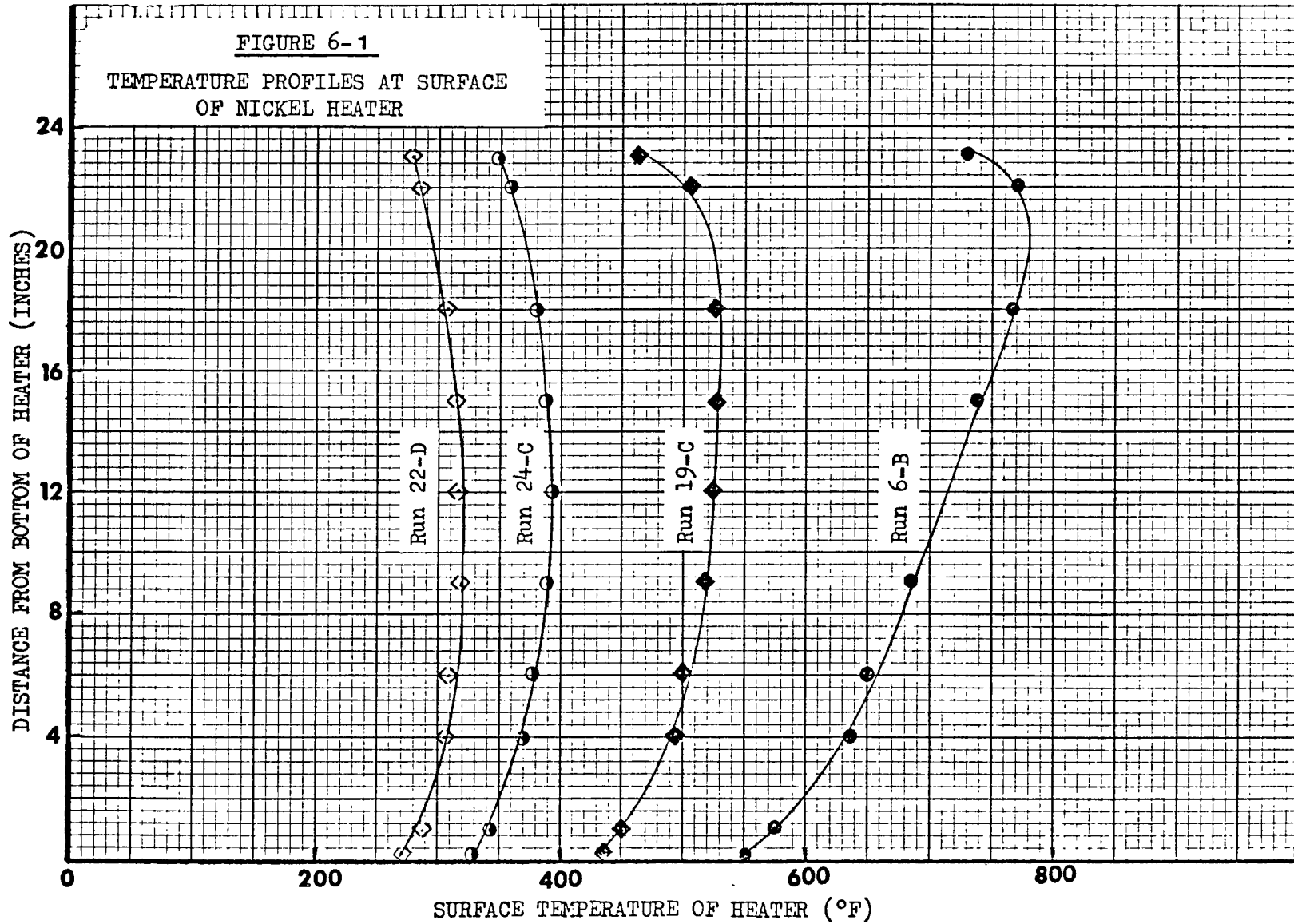


FIGURE 6-2

TEMPERATURE PROFILES AT SURFACE
OF NICKEL HEATER

DISTANCE FROM BOTTOM OF HEATER (INCHES)

SURFACE TEMPERATURE OF HEATER (°F)

24
20
16
12
8
4
0

200

400

600

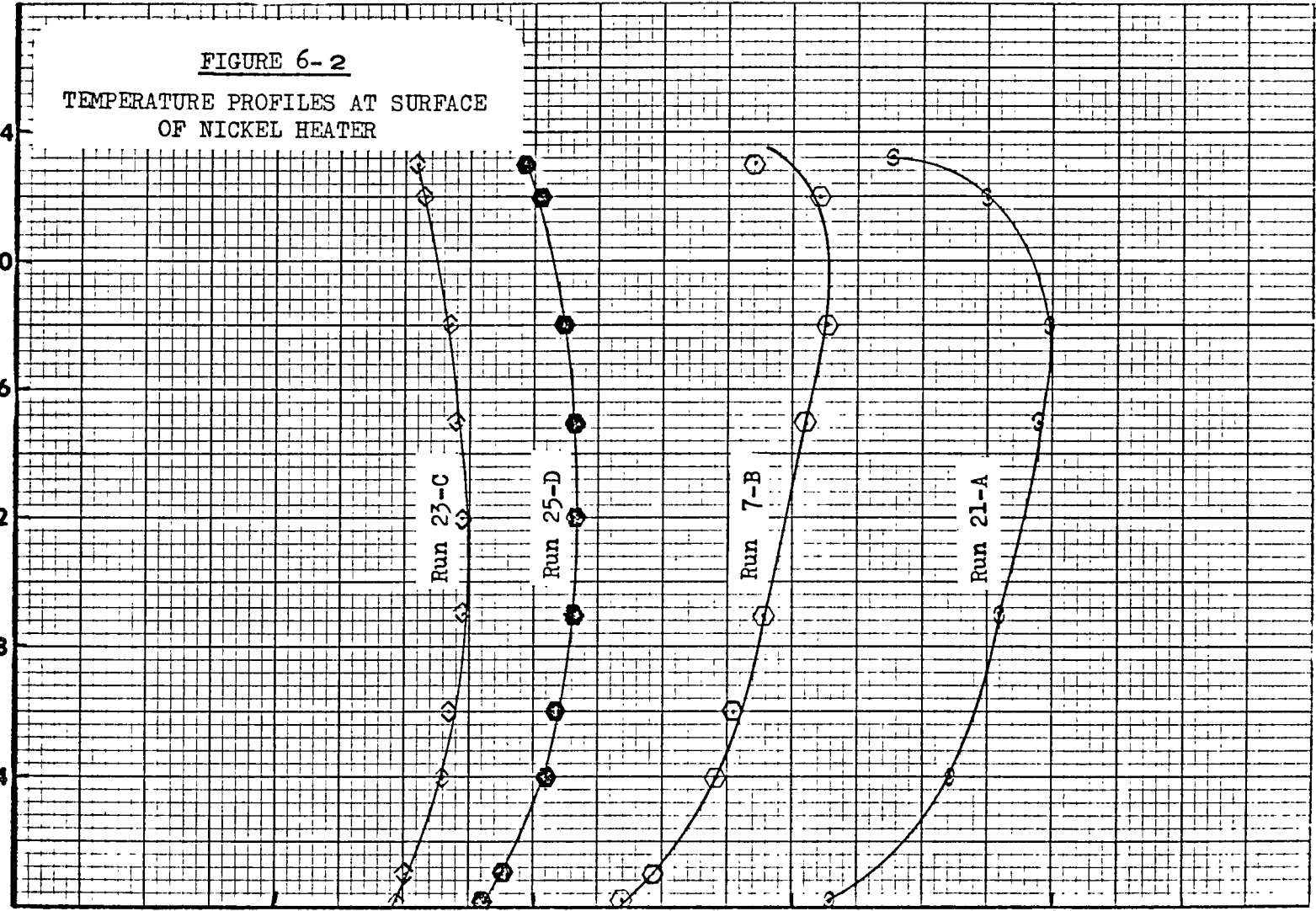
800

Run 23-C

Run 25-D

Run 7-B

Run 21-A



was solved numerically on an electronic digital computer. The boundary conditions used in the solution of this equation were the known heat loss from the ends and the measured heat transfer coefficient to the fluid. These calculations indicated that the assumption of a uniformly distributed surface heat flux was accurate to within 5% over about 80% of the heater surface, and did not exceed 15% at the ends where the greatest deviation from uniformity was noted. These calculations were not exact because the geometry was more complex than indicated and the boundary conditions were not known exactly, but the calculations showed that the assumption of a uniform heat flux was reasonable.

Since all data are subject to experimental error, it is important to discover and discard all faulty data points before the data is used to provide insight into physical mechanisms and to evaluate theoretical studies. In particular, the sensitive thermocouples and electronic equipment used in this work were potential sources of error. In order to detect large experimental errors, the following assumption was made : this physical process would not exhibit large or erratic changes in its output as a result of small changes in its input. Thus, if the measured values of the dependent variables are plotted as functions of the independent, externally controlled variables, an examination of the trend of the data should reveal those points that are significantly out of line. In the case of the present work, the only dependent variable is the local heat transfer coefficient which is expressed as the CC number, and the only effective independent variable is the heat flux which was externally controlled. Accordingly, curves of the experimental CC number at each thermocouple position versus the local heat flux (as defined in equation 6-2) are presented in Figures 6-3 through 6-6.

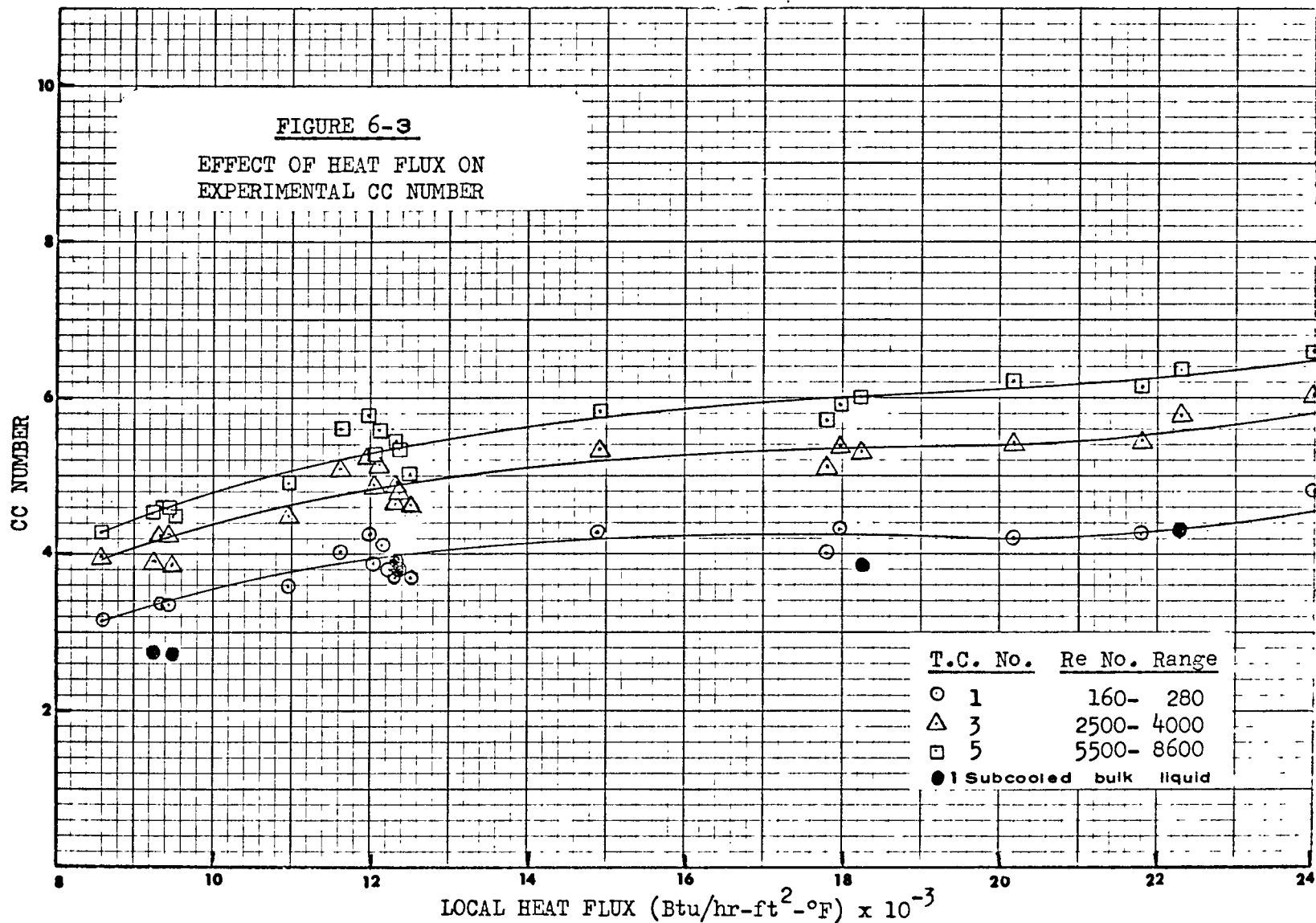


FIGURE 6-4

EFFECT OF HEAT FLUX ON
EXPERIMENTAL CC NUMBER

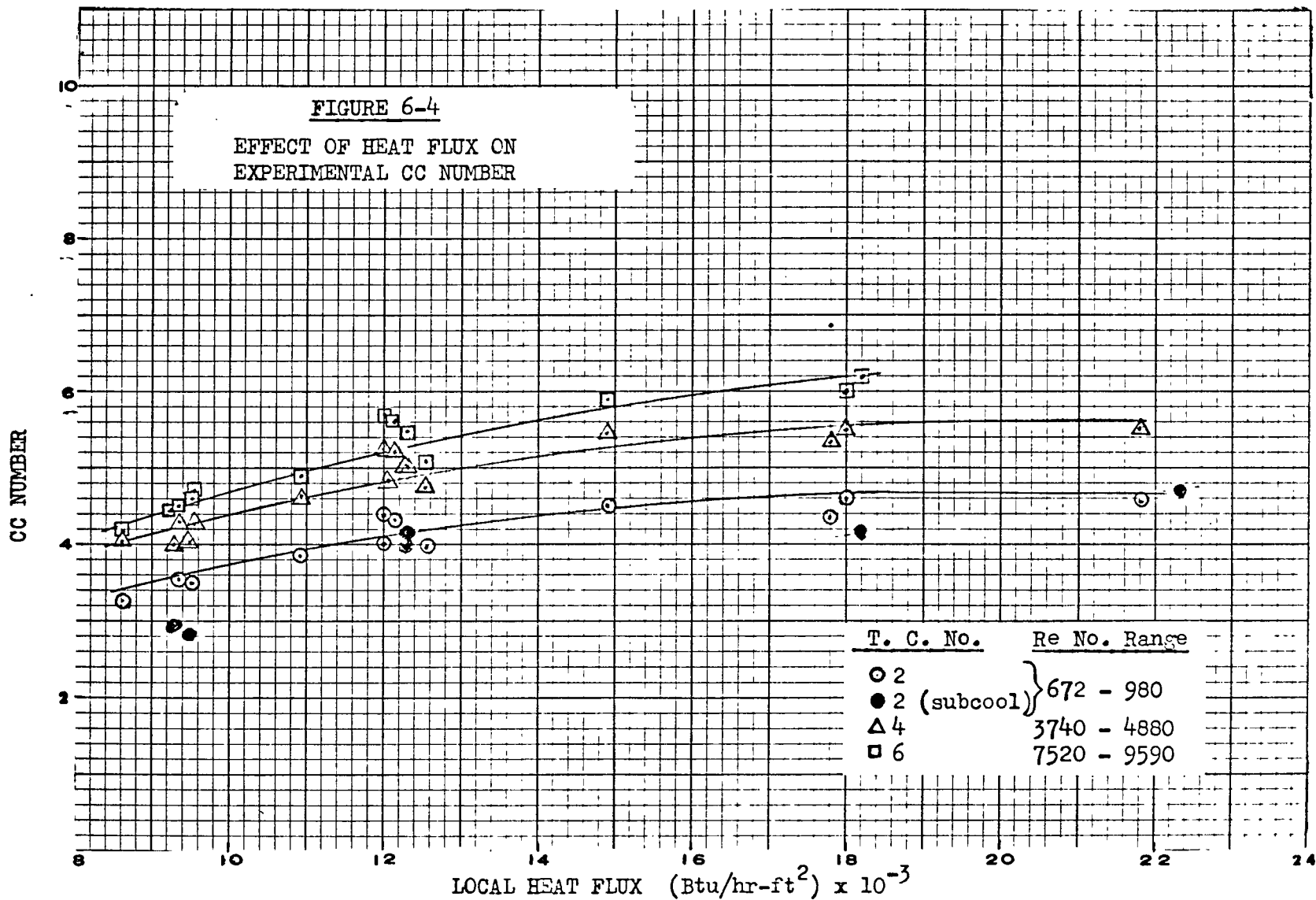
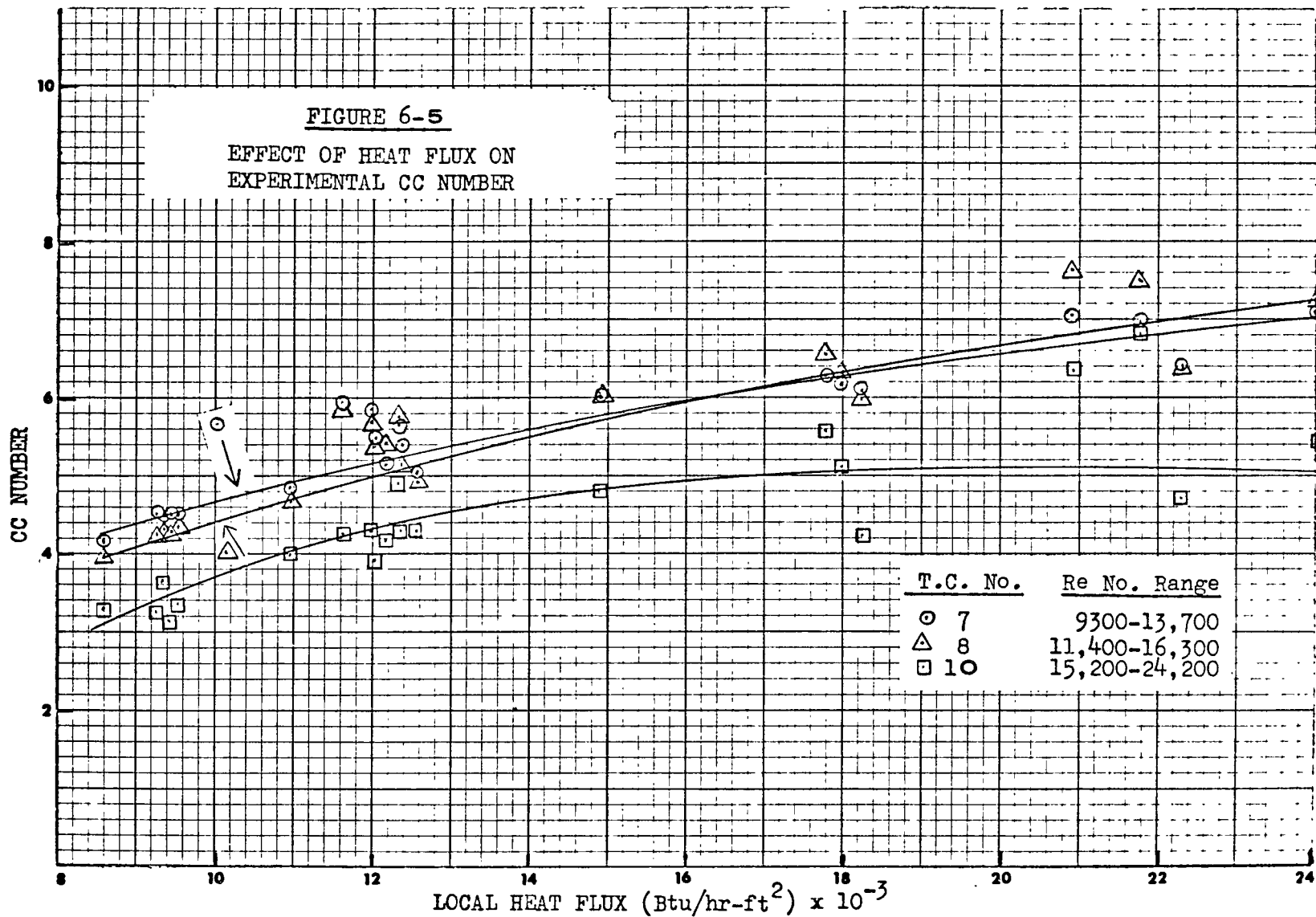
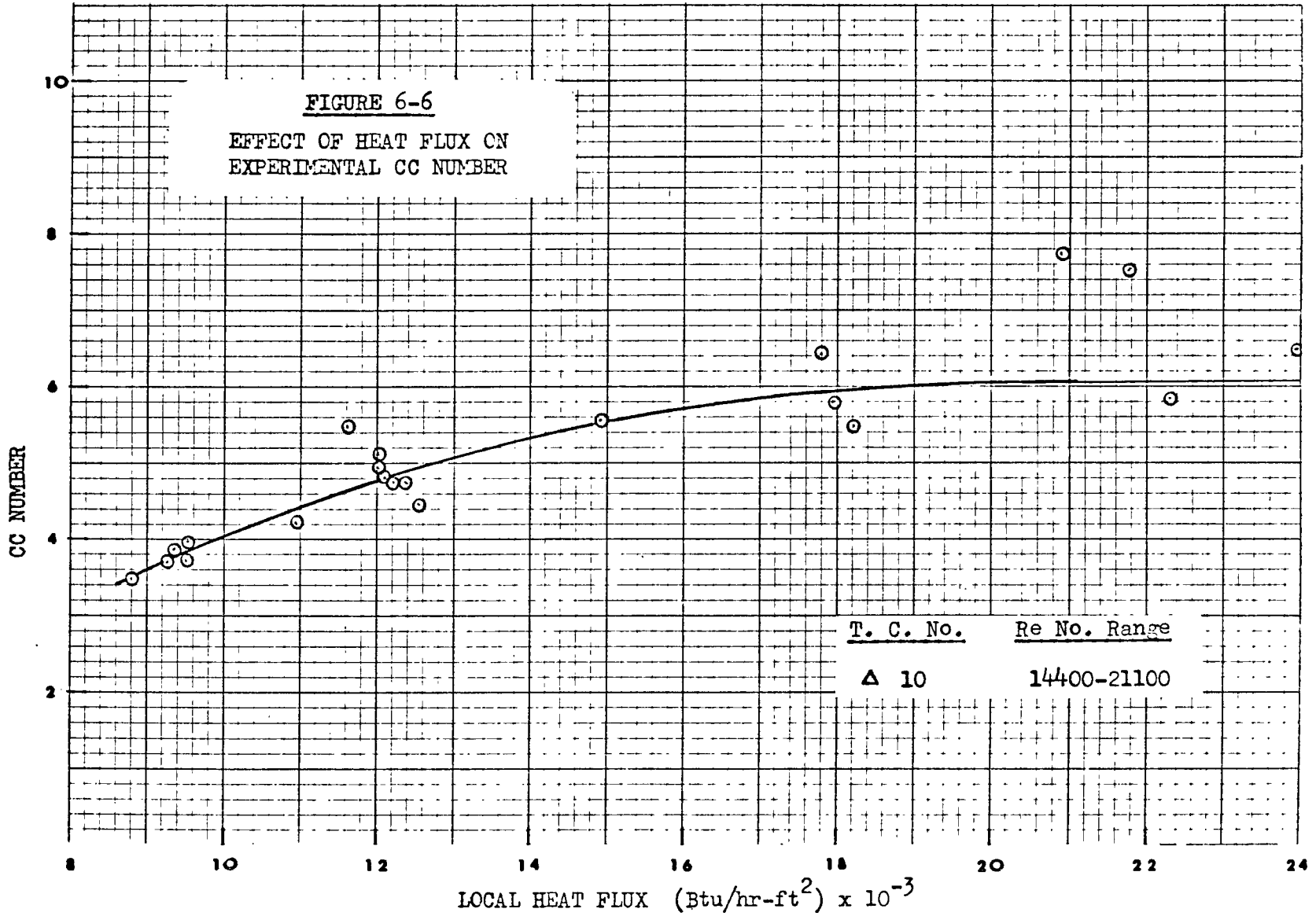


FIGURE 6-5
EFFECT OF HEAT FLUX ON
EXPERIMENTAL CC NUMBER

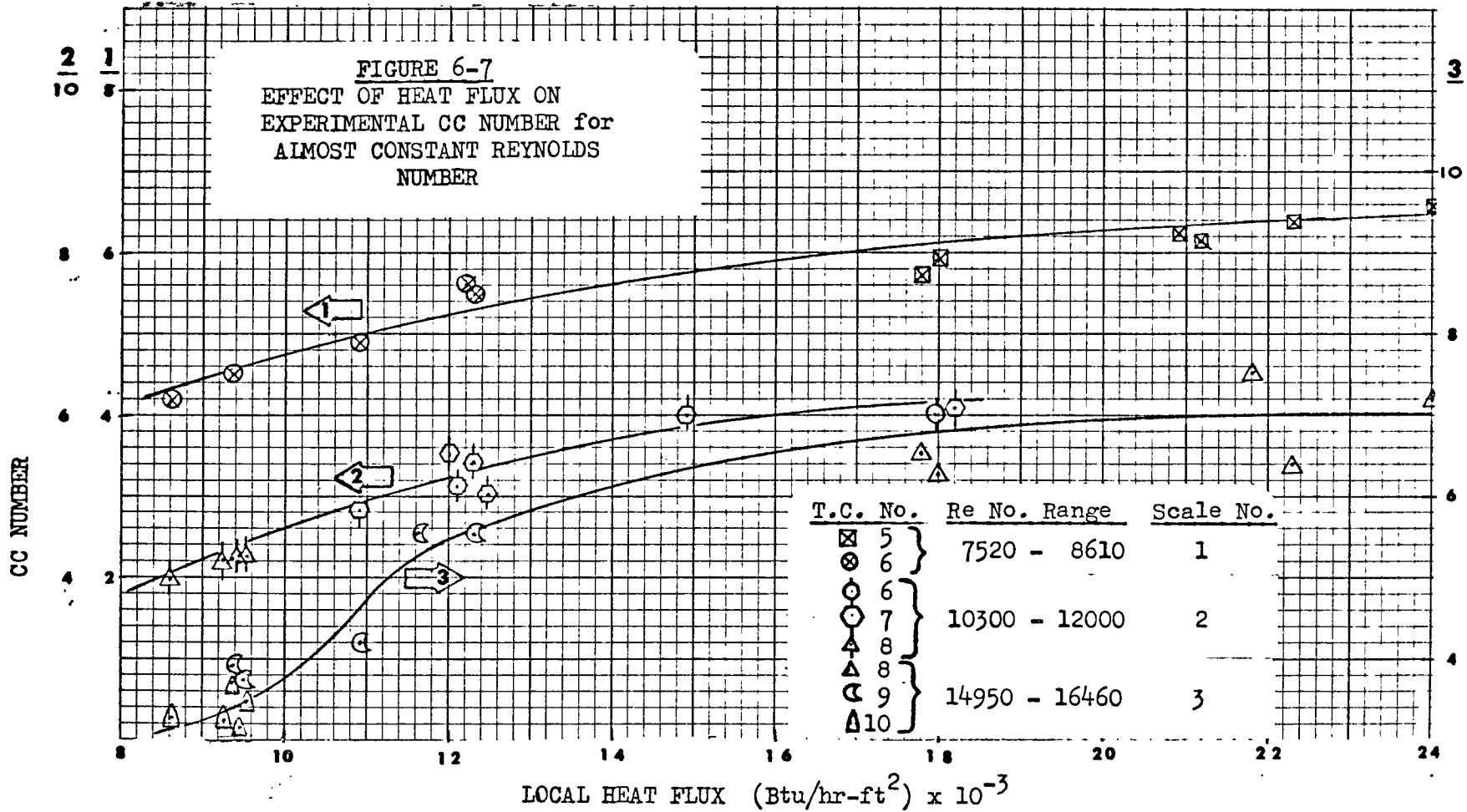




About 90% of the points were considered reliable because they lay within a range of $\pm 10\%$ of the best curves drawn through these data points. The remaining points have been excluded from further consideration in this dissertation, and they have been identified by a \star on Table 6-2.

Another variable that could be controlled externally with the experimental equipment was the temperature of the liquid feed to the boiler. However, even when the feed was subcooled as much as 65 degrees F., the liquid within the boiler reached the saturation temperature while still near the bottom of the boiler because of convection currents induced within the bulk liquid by the interfacial motion. Since only the two bottom thermocouples were ever within the region of subcooled bulk liquid, the extent of subcooling of the feed could not be considered an independent variable for most of the data. For those cases where subcooling did exist, the symbols on Figures 6-3 through 6-6 have been shaded.

Figures 6-3 through 6-6 imply that the experimental CC number increases with increasing heat flux at each thermocouple position. However, these curves do not reflect the effect of the heat flux alone, because the Reynolds number is not constant for all the data points on a single curve. In fact, the Reynolds number increases almost as rapidly as does the heat flux at each thermocouple position. This problem is reduced somewhat in Figure 6-7 where the local Reynolds number rather than the thermocouple position is used as the parameter for the curves of experimental CC number versus the local heat flux. Not many data points are available for these curves since there was not much overlapping of the Reynolds number range from one thermocouple position to the next. The data points that were used reflect a Reynolds number range of about ten per cent for each curve,



which is much smaller than the range for the curves in Figures 6-3 through 6-6. Figure 6-7 indicates that the experimental CC number is definitely a function of the heat flux. This relationship was not anticipated by the quasi-steady theory which is heat flux independent. Thus, the unsteady state theory, which includes the effects of the large waves, must be called upon to account for this trend. This will be discussed further in Section C of this chapter.

The quasi-steady state theory of Chapter III predicted a unique relationship between the CC and Reynolds numbers and ϵ/ν . All of the experimental data points (except those that were discarded as discussed above) are plotted in terms of the CC and Reynolds numbers on Figures 6-8 through 6-11, where each graph represents a narrow range of the heat flux. These Figures also include the theoretical results, shown by the solid curves, with ϵ/ν as a parameter, that were derived from the quasi-steady state theory. The theoretical curves are based on a Prandtl number of 0.7 to simplify the presentation, even though the experimental Prandtl numbers had values between 0.65 and 0.75 as is shown on Table 6-2. The corresponding change in the theoretical CC number is about ± 0.3 units, where the higher CC numbers go with the lower Prandtl numbers. The dashed curves on these Figures indicate the results of the unsteady state theory, and these will be discussed later in the chapter.

The experimental points follow the theoretical curves in general appearance, with the CC number reaching a maxima at a Reynolds number of about 10 to 15 thousand. However, the only data points available for higher Reynolds numbers may be distorted because of end effects and the position

FIGURE 6-8

COMPARISON of THEORETICAL and
EXPERIMENTAL RESULTS

Theoretical curves:

- quasi-steady state theory.
- - - unsteady state theory,
sinusoidal waves, $\eta_0 = .83$

Run
No.
O16
Δ17
□18
O22
D23
X24

CC NUMBER

16
12
8
4
30
100
1000

ϵ/ν

0

$\epsilon/\nu = 0$

$\epsilon/\nu = 5$

$\epsilon/\nu = 30$

10^2

10^3

10^4

REYNOLDS NUMBER

FIGURE 6-9

COMPARISON of THEORETICAL and
EXPERIMENTAL RESULTS

Theoretical curves:

- quasi-steady state theory
- - - unsteady state theory,
sinusoidal waves, $\eta_0 = .83$

Run
No.

- 1
- △ 3
- 5
- 9
- 11
- ▲ 12
- ▲ 13
- X 25

CC NUMBER

16

12

8

4

ϵ/D

0

5

30

100

1000

$\epsilon/D = 0$

$\epsilon/D = 5$

$\epsilon/D = 30$

10^2

10^3

10^4

REYNOLDS NUMBER

FIGURE 6-10

COMPARISON of THEORETICAL and
EXPERIMENTAL RESULTS

Theoretical curves:
 ——— quasi-steady state theory.
 - - - unsteady state theory,
 sinusoidal waves, $\eta_0 = .83$

Run
No.

- 7
- △ 14
- ◊ 19
- 20

CC NUMBER

16

12

8

4

ϵ/d

0

5

30

100

1000

$\epsilon/d = 0$

$\epsilon/d = 5$

$\epsilon/d = 30$

10^2

10^3

10^4

REYNOLDS NUMBER

FIGURE 6-11

COMPARISON of THEORETICAL and
EXPERIMENTAL RESULTS

Theoretical curves:

- quasi-steady state theory.
- - - unsteady state theory,
sinusoidal waves, $\eta_0 = .83$

Run
No.

- 2
- △ 6
- 15
- ◇ 21

CC NUMBER

16

12

8

4

ϵ/ν

0

5

30

100

1000

$\epsilon/\nu = 0$

$\epsilon/\nu = 5$

$\epsilon/\nu = 30$

10^2

10^3

10^4

REYNOLDS NUMBER

of this maxima cannot be definitely established until some high Reynolds number data become available. Of greater significance are the very large values of ϵ'/ν , the interfacial roughness parameter, that are required to provide agreement between the theoretical and experimental results. A very rough and wavy interface is to be expected for vertical film boiling and relatively large values of ϵ'/ν would not be surprising. However, it appears more reasonable to attempt to account for the large amplitude waves according to the unsteady state theory developed in Chapter IV. To this end, the results of the instantaneous surface temperature and heat flux measurements and their implications with respect to interfacial waves will be discussed in the following sections.

The theoretical curves of Figure 6-8 through 6-11 were based on a zero interfacial velocity ($u_i/u_m=0$). The actual value of u_i/u_m was not determined at this point because it can be seen from Figures 3-21 through 3-24b in Chapter III that the theoretical effect of higher interfacial velocities is not large enough to significantly affect the relationship between the data points and the theoretical curves of Figures 6-8 through 6-11. Later in this chapter, after the effects of the large amplitude waves have been investigated and a more realistic value for ϵ'/ν has been estimated, the value of the u_i/u_m ratio will be estimated according to the method of Section F, Chapter III.

TABLE 6-2

 SUMMARY OF EXPERIMENTAL DATA

SYMBOLS AND UNITS ON FOLLOWING PAGES ARE DEFINED AS...

W(LB/HR)..VAPORIZATION RATE BASED ON CONDENSATE MEASUREMENT

Q(BTU/HR)..NET ENERGY TO FLUID, CONVECTION PLUS RADIATION

P(PSIG)..VAPOR SPACE PRESSURE.

TEMP (DEGREE F.)...TSAT, SATURATION...TFD, LIQUID FEED...
 TVAP, EXIT VAPOR...DELTA, TWALL MINUS TSAT.

HCONV AND HRAD(BTU/HR/SQ FT/DEG F)..LOCAL COEFFICIENTS DUE
 TO CONVECTION AND RADIATION

NO...REFERS TO THERMOCOUPLE LOCATION, AS LISTED ON TABLE 5-1

RUN NO. 22 D

P = 16.0 TSAT = 122 TFD = 118 TVAP = 125
 W = 71.4 LB/HR Q/A = 8589 BTU/HR/SQ FT
 HEAT LOSS (BTU/HR)-TOP,BTM,GLAS- 65, 69, 201

LOCAL DATA

NO.	DELTA	HCONV	HRAD	RE NO	CC NO	PR
1	150	55.8	1.4	167	3.16	.74
2	156	53.5	1.4	671	3.31	.74
3	184	45.3	1.5	2532	3.98	.73
4	186	44.8	1.5	3737	4.03	.73
5	196	42.2	1.6	5584	4.31	.73
6	192	43.2	1.5	7510	4.20	.73
7	192	43.2	1.5	9368	4.20	.73
8	183	45.4	1.5	11403	3.97	.73
9	163	51.2	1.4	14387	3.47	.74
10	155	53.9	1.4	15236	3.27	.74

TABLE 6-2 (CONTINUED)

RUN NO. 16 D

P = 15.4 TSAT = 120 TFD = 89 TVAP = 123
 W = 71.6 LB/HR Q/A = 9251 BTU/HR/SQ FT
 HEAT LOSS (BTU/HR)-TOP,BTM,GLAS- 169, 78, 227

LOCAL DATA

NO.	DELT	HCONV	HRAD	RE NO	CC NO	PR
★ 1	144	62.9	1.4	168	2.74	.75
★ 2	151	59.9	1.4	676	2.89	.74
3	196	45.6	1.5	2486	3.93	.73
4	203	44.0	1.6	3643	4.09	.73
5	221	40.2	1.6	5392	4.52	.72
6	218	40.8	1.6	7236	4.45	.72
7	221	40.3	1.6	8992	4.51	.72
8	210	42.5	1.6	10962	4.25	.72
9	188	47.7	1.5	13843	3.73	.73
10	167	53.9	1.4	14937	3.25	.74

RUN NO. 23 C

P = 16.0 TSAT = 122 TFD = 121 TVAP = 128
 W = 78.4 LB/HR Q/A = 9360 BTU/HR/SQ FT
 HEAT LOSS (BTU/HR)-TOP,BTM,GLAS- 71, 88, 233

LOCAL DATA

NO.	DELT	HCONV	HRAD	RE NO	CC NO	PR
1	171	53.1	1.5	177	3.37	.74
2	179	50.7	1.5	711	3.55	.73
3	208	43.4	1.6	2676	4.22	.72
4	211	42.7	1.6	3942	4.30	.72
5	224	40.2	1.7	5876	4.61	.72
6	220	41.0	1.6	7897	4.51	.72
7	220	40.9	1.6	9845	4.53	.72
8	212	42.4	1.6	11957	4.34	.72
9	194	46.8	1.5	15055	3.88	.73
10	185	49.2	1.5	15965	3.67	.73

(SYMBOLS AND UNITS DEFINED ON FIRST PAGE OF TABLE 6-2)

TABLE 6-2 (CONTINUED)

RUN NO. 17-D

P = 15.5 TSAT = 120 TFD = 115 TVAP = 124
 W = 80.2 LB/HR Q/A = 9445 BTU/HR/SQ FT
 HEAT LOSS (BTU/HR)-TOP,BTM,GLAS- 209, 80, 237

LOCAL DATA

NO.	DELT	HCONV	HRAD	RE NO	CC NO	PR
1	174	52.8	1.5	176	3.36	.74
2	181	50.6	1.5	707	3.51	.73
3	213	42.8	1.6	2650	4.24	.72
4	214	42.4	1.6	3913	4.29	.72
5	227	39.9	1.7	5829	4.60	.72
6	231	39.2	1.7	7747	4.68	.72
7	225	40.3	1.7	9752	4.54	.72
8	214	42.5	1.6	11896	4.28	.72
9	190	48.1	1.5	15092	3.72	.73
10	164	56.0	1.4	16438	3.14	.74

RUN NO. 18-C

P = 15.0 TSAT = 119 TFD = 88 TVAP = 122
 W = 74.0 LB/HR Q/A = 9505 BTU/HR/SQ FT
 HEAT LOSS (BTU/HR)-TOP,BTM,GLAS- 207, 75, 235

LOCAL DATA

NO.	DELT	HCONV	HRAD	RE NO	CC NO	PR
★ 1	145	64.2	1.4	173	2.67	.75
★ 2	152	61.3	1.4	694	2.80	.74
3	199	46.3	1.5	2548	3.83	.73
4	207	44.4	1.6	3727	4.02	.73
5	226	40.4	1.6	5504	4.48	.72
6	232	39.3	1.7	7291	4.62	.72
7	227	40.3	1.6	9166	4.49	.72
8	221	41.4	1.6	11091	4.36	.72
9	204	45.0	1.6	13899	3.96	.73
10	178	51.9	1.5	15105	3.38	.74

(SYMBOLS AND UNITS DEFINED ON FIRST PAGE OF TABLE 6-2)

TABLE 6-2 (CONTINUED)

RUN NO. 24 C

P = 16.0 TSAT = 122 TFD = 119 TVAP = 128
 W = 91.5 LB/HR Q/A = 10925 BTU/HR/SQ FT
 HEAT LOSS (BTU/HR)-TOP,BTM,GLAS- 77, 136, 286

LOCAL DATA

NO.	DELT	HCONV	HRAD	RE NO	CC NO	PR
1	207	51.1	1.6	194	3.58	.72
2	220	48.0	1.6	774	3.85	.72
3	250	41.9	1.8	2913	4.49	.71
4	256	40.8	1.8	4272	4.62	.71
5	268	38.9	1.8	6379	4.88	.71
6	268	39.0	1.8	8525	4.88	.71
7	266	39.2	1.8	10663	4.84	.71
8	258	40.5	1.8	12951	4.66	.71
9	237	44.4	1.7	16341	4.21	.72
10	227	46.4	1.7	17347	3.99	.72

RUN NO. 3-B

P = 15.9 TSAT = 122 TFD = 118 TVAP = 136
 W = 100.9 LB/HR Q/A = 11620 BTU/HR/SQ FT
 HEAT LOSS (BTU/HR)-TOP,BTM,GLAS- 456, 94, 361

LOCAL DATA

NO.	DELT	HCONV	HRAD	RE NO	CC NO	PR
1	242	46.3	1.7	196	4.03	.72
2						
3	293	37.7	1.9	2902	5.09	.70
4						
5	316	34.7	2.0	6314	5.60	.70
6						
★ 7	330	33.1	2.1	10317	5.91	.70
★ 8	327	33.4	2.1	12427	5.85	.70
9	313	35.1	2.0	15499	5.54	.70
10	253	44.1	1.8	17707	4.26	.71

(SYMBOLS AND UNITS DEFINED ON FIRST PAGE OF TABLE 6-2)

TABLE 6-2 (CONTINUED)

RUN NO. 11 C

P = 15.2 TSAT = 119 TFD = 121 TVAP = 129
 W = 104.0 LB/HR Q/A = 11977 BTU/HR/SQ FT
 HEAT LOSS (BTU/HR)-TOP,BTM,GLAS- 325, 71, 362

LOCAL DATA

NO.	DELT	HC0NV	HRAD	RE NO	CC NO	PR
1	264	43.5	1.8	198	4.27	.71
2	271	42.4	1.8	797	4.40	.71
3	315	36.0	2.0	2937	5.32	.70
4	312	36.4	2.0	4369	5.25	.70
5	337	33.4	2.1	6400	5.79	.69
6	332	33.9	2.1	8611	5.69	.70
★ 7	340	33.1	2.1	10628	5.85	.69
★ 8	332	33.9	2.1	12891	5.69	.70
9	308	36.8	2.0	16316	5.17	.70
10	266	43.3	1.8	18184	4.29	.71

RUN NO. 5-C

P = 15.0 TSAT = 118 TFD = 124 TVAP = 126
 W = 107.5 LB/HR Q/A = 12015 BTU/HR/SQ FT
 HEAT LOSS (BTU/HR)-TOP,BTM,GLAS- 397, 99, 346

LOCAL DATA

NO.	DELT	HC0NV	HRAD	RE NO	CC NO	PR
1	245	47.3	1.7	207	3.86	.72
2	254	45.6	1.8	828	4.03	.71
3	296	38.7	1.9	3061	4.87	.70
4	295	38.8	1.9	4538	4.85	.70
5	320	35.5	2.0	6646	5.37	.70
6						
7	327	34.7	2.1	10970	5.51	.70
8	321	35.4	2.0	13270	5.40	.70
★ 9	299	38.2	1.9	16754	4.94	.70
10	247	46.9	1.7	18946	3.91	.72

(SYMBOLS AND UNITS DEFINED ON FIRST PAGE OF TABLE 6-2)

TABLE 6-2 (CONTINUED)

RUN NO. 9 B

P = 14.7 TSAT = 118 TFD = 115 TVAP = 124
 W = 104.0 LB/HR Q/A = 12125 BTU/HR/SQ FT
 HEAT LOSS (BTU/HR)-TOP,BTM,GLAS- 242, 148, 356

LOCAL DATA

NO.	DELT	HCONV	HRAD	RE NO	CC NO	PR
1	262	44.6	1.8	199	4.12	.71
2	276	42.1	1.8	791	4.39	.71
3	315	36.5	2.0	2944	5.18	.70
4	316	36.3	2.0	4346	5.22	.70
5	336	34.0	2.1	6425	5.62	.70
6	335	34.1	2.1	8592	5.61	.70
7	312	36.8	2.0	11075	5.13	.70
8	327	35.0	2.1	13014	5.43	.70
9	298	38.8	1.9	16590	4.83	.70
10	266	43.8	1.8	18185	4.20	.71

RUN NO. 13 C

P = 15.8 TSAT = 121 TFD = 91 TVAP = 126
 W = 96.8 LB/HR Q/A = 12258 BTU/HR/SQ FT
 HEAT LOSS (BTU/HR)-TOP,BTM,GLAS- 250, 155, 351

LOCAL DATA

NO.	DELT	HCONV	HRAD	RE NO	CC NO	PR
1	242	49.0	1.7	193	3.81	.72
2	256	46.0	1.8	766	4.08	.71
3	301	38.8	2.0	2834	4.97	.70
4	305	38.2	2.0	4172	5.06	.70
5	324	35.8	2.1	6174	5.46	.70
6	324	35.7	2.1	8240	5.47	.70
7	323	35.8	2.1	10297	5.45	.70
8	316	36.8	2.0	12484	5.29	.70
9	292	40.0	1.9	15778	4.79	.70
10	259	45.5	1.8	17287	4.14	.71

(SYMBOLS AND UNITS DEFINED ON FIRST PAGE OF TABLE 6-2)

TABLE 6-2 (CONTINUED)

RUN NO. 1-D

P = 15.3 TSAT = 120 TFD = 120 TVAP = 140
 W = 102.5 LB/HR Q/A = 12317 BTU/HR/SQ FT
 HEAT LOSS (BTU/HR)-TOP,BTM,GLAS- 229, 95, 368

LOCAL DATA

NO.	DELT	HC0NV	HRAD	RE NO	CC NO	PR
1	244	48.8	1.7	209	3.77	.72
2						
3	295	39.9	1.9	3102	4.76	.70
4						
5	324	36.0	2.1	6688	5.35	.70
6						
7	337	34.4	2.1	10932	5.64	.69
★ 8	342	33.9	2.2	13030	5.74	.69
9	332	35.0	2.1	16157	5.53	.70
★ 10	301	39.0	2.0	17671	4.88	.70

RUN NO. 12 D

P = 15.5 TSAT = 120 TFD = 99 TVAP = 127
 W = 98.4 LB/HR Q/A = 12325 BTU/HR/SQ FT
 HEAT LOSS (BTU/HR)-TOP,BTM,GLAS- 188, 136, 353

LOCAL DATA

NO.	DELT	HC0NV	HRAD	RE NO	CC NO	PR
1	249	47.8	1.7	196	3.89	.71
2	262	45.3	1.8	782	4.13	.71
3	303	38.7	2.0	2904	4.95	.70
4	307	38.2	2.0	4274	5.03	.70
5	326	35.7	2.1	6325	5.43	.70
6	327	35.6	2.1	8440	5.45	.70
7	325	35.8	2.1	10549	5.42	.70
8	318	36.7	2.0	12790	5.26	.70
9	294	40.0	1.9	16172	4.77	.70
10	269	44.0	1.8	17525	4.28	.71

(SYMBOLS AND UNITS DEFINED ON FIRST PAGE OF TABLE 6-2)

TABLE 6-2 (CONTINUED)

RUN NO. 25 D

P = 15.7 TSAT = 121 TFD = 118 TVAP = 127
 W = 105.0 LB/HR Q/A = 12524 BTU/HR/SQ FT
 HEAT LOSS (BTU/HR)-TOP,BTM,GLAS- 83, 166, 336

LOCAL DATA

NO.	DELT	HCONV	HRAD	RE NO	CC NO	PR
1	240	50.5	1.7	212	3.68	.72
2	256	47.2	1.8	840	3.97	.71
3	290	41.3	1.9	3146	4.64	.70
4	297	40.2	2.0	4608	4.78	.70
5	310	38.4	2.0	6872	5.04	.70
6	312	38.1	2.0	9157	5.08	.70
7	311	38.3	2.0	11445	5.05	.70
8	304	39.2	2.0	13861	4.92	.70
★ 9	283	42.3	1.9	17472	4.50	.71
10	272	44.1	1.9	18567	4.29	.71

RUN NO. 19-C

P = 16.5 TSAT = 124 TFD = 119 TVAP = 134
 W = 126.3 LB/HR Q/A = 14846 BTU/HR/SQ FT
 HEAT LOSS (BTU/HR)-TOP,BTM,GLAS- 323, 145, 446

LOCAL DATA

NO.	DELT	HCONV	HRAD	RE NO	CC NO	PR
1	310	45.8	2.0	225	4.30	.70
2	324	43.7	2.1	896	4.54	.70
3	369	38.0	2.3	3314	5.35	.69
4	374	37.3	2.4	4867	5.45	.69
5	395	35.1	2.5	7186	5.85	.68
6	398	34.9	2.5	9564	5.90	.68
7	403	34.3	2.5	11837	6.02	.68
8	404	34.2	2.5	14186	6.03	.68
9	382	36.4	2.4	17875	5.61	.69
10	338	41.8	2.2	19911	4.78	.69

(SYMBOLS AND UNITS DEFINED ON FIRST PAGE OF TABLE 6-2)

TABLE 6-2 (CONTINUED)

RUN NO. 7-B

P = 15.3 TSAT = 120 TFD = 120 TVAP = 135
 W = 151.3 LB/HR Q/A = 17765 BTU/HR/SQ FT
 HEAT LOSS (BTU/HR)-TOP,BTM,GLAS- 332, 241, 534

LOCAL DATA

NO.	DELT	HCØNV	HRAD	RE NO	CC NO	PR
1	349	48.7	2.2	258	4.01	.69
2	373	45.3	2.3	1014	4.37	.69
3	422	39.6	2.6	3732	5.11	.68
4	435	38.2	2.6	5428	5.32	.68
5	459	35.9	2.8	7979	5.73	.68
6						
7	491	33.2	3.0	12740	6.29	.67
8	507	32.0	3.1	14980	6.56	.67
9	501	32.4	3.0	18453	6.45	.67
10	451	36.6	2.7	20615	5.59	.68

RUN NO. 20-B

P = 16.0 TSAT = 122 TFD = 117 TVAP = 134
 W = 150.3 LB/HR Q/A = 17925 BTU/HR/SQ FT
 HEAT LOSS (BTU/HR)-TOP,BTM,GLAS- 305, 194, 535

LOCAL DATA

NO.	DELT	HCØNV	HRAD	RE NO	CC NO	PR
1	368	46.4	2.3	250	4.32	.69
2	388	43.8	2.4	989	4.62	.68
3	437	38.3	2.7	3640	5.40	.68
4	444	37.7	2.7	5340	5.51	.68
5	469	35.4	2.9	7851	5.93	.67
6	475	34.9	2.9	10406	6.03	.67
7	484	34.1	2.9	12823	6.20	.67
8	490	33.6	3.0	15276	6.29	.67
9	463	35.9	2.8	19347	5.83	.67
10	418	40.3	2.6	21488	5.09	.68

(SYMBOLS AND UNITS DEFINED ON FIRST PAGE OF TABLE 6-2)

TABLE 6-2 (CONTINUED)

RUN NO. 14 D

P = 15.7 TSAT = 121 TFD = 52 TVAP = 130
 W = 127.6 LB/HR Q/A = 18187 BTU/HR/SQ FT
 HEAT LOSS (BTU/HR)-TOP,BTM,GLAS- 459, 202, 540

LOCAL DATA

NO.	DELT	HCONV	HRAD	RE NO	CC NO	PR
1	343	50.9	2.2	228	3.87	.69
2	363	47.8	2.3	901	4.16	.69
3	440	38.7	2.7	3223	5.33	.68
4						
5	481	34.9	2.9	6891	6.02	.67
6	492	33.9	3.0	9083	6.21	.67
7	486	34.5	2.9	11427	6.09	.67
8	480	35.0	2.9	13801	6.00	.67
9	447	37.9	2.7	17560	5.45	.68
★10	382	45.3	2.4	19933	4.43	.69

RUN NO. 2-B

P = 15.0 TSAT = 119 TFD = 114 TVAP = 146
 W = 170.6 LB/HR Q/A = 20903 BTU/HR/SQ FT
 HEAT LOSS (BTU/HR)-TOP,BTM,GLAS- 531, 158, 662

LOCAL DATA

NO.	DELT	HCONV	HRAD	RE NO	CC NO	PR
1	417	47.6	2.5	273	4.21	.68
2						
3	505	38.3	3.0	3886	5.43	.67
4						
5	556	34.2	3.4	8191	6.21	.66
6						
7	607	30.7	3.7	12798	7.06	.66
★8	642	28.6	4.0	14730	7.66	.66
★9	647	28.3	4.0	17894	7.76	.66
★10	564	33.6	3.4	20716	6.34	.66

(SYMBOLS AND UNITS DEFINED ON FIRST PAGE OF TABLE 6-2)

TABLE 6-2 (CONTINUED)

RUN NO. 6-B

P = 15.3 TSAT = 120 TFD = 119 TVAP = 143
 W = 178.4 LB/HR Q/A = 21756 BTU/HR/SQ FT
 HEAT LOSS (BTU/HR)-TOP,BTM,GLAS- 276, 229, 672

LOCAL DATA

NO.	DELT	HCONV	HRAD	RE NO	CC NO	PR
1	431	47.9	2.6	281	4.24	.68
2	455	45.0	2.8	1106	4.56	.68
3	519	38.8	3.1	4002	5.45	.67
4	526	38.2	3.2	5876	5.54	.67
5	566	35.0	3.4	8477	6.15	.66
6						
7	618	31.4	3.8	13245	6.97	.66
8	649	29.5	4.0	15294	7.51	.66
★ 9	651	29.4	4.1	18647	7.55	.66
★ 10	609	32.0	3.7	20532	6.83	.66

RUN NO. 15-C

P = 15.3 TSAT = 120 TFD = 58 TVAP = 131
 W = 158.5 LB/HR Q/A = 22292 BTU/HR/SQ FT
 HEAT LOSS (BTU/HR)-TOP,BTM,GLAS- 532, 256, 661

LOCAL DATA

NO.	DELT	HCONV	HRAD	RE NO	CC NO	PR
1	444	47.5	2.7	249	4.30	.68
2	472	44.4	2.8	979	4.66	.67
3	554	36.9	3.4	3493	5.80	.66
4						
5	590	34.1	3.6	7527	6.35	.66
6						
7	595	33.8	3.6	12474	6.43	.66
8	593	34.0	3.6	15012	6.39	.66
9	556	36.7	3.4	19166	5.82	.66
★ 10	474	44.2	2.9	22106	4.69	.67

(SYMBOLS AND UNITS DEFINED ON FIRST PAGE OF TABLE 6-2)

TABLE 6-2 (CONTINUED)

RUN NO. 21-A

P = 15.6 TSAT = 121 TFD = 119 TVAP = 126
 W = 206.7 LB/HR Q/A = -24007-BTU/HR/SQ FT
 HEAT LOSS (BTU/HR)-TOP,BTM,GLAS- 466, 183, 745

LOCAL DATA

NO.	DELT	HCO NV	HRAD	RE NO	CC NO	PR
1	509	44.1	3.1	279	4.80	.67
2						
3	601	36.2	3.7	3971	6.04	.66
4						
5	639	33.6	4.0	8528	6.60	.66
6						
7	669	31.7	4.2	13693	7.09	.66
8	677	31.2	4.3	16275	7.22	.65
9	629	34.3	3.9	21091	6.46	.66
10	557	39.7	3.4	24139	5.43	.66

B. INSTANTANEOUS LOCAL MEASUREMENTS

The instantaneous fluctuations of the temperature at the heater surface were recorded on a multi-channel tape recorder as discussed in Section D, Chapter V. The signal on tape then provides the input to the heat meter circuit, and the heat meter output represents the instantaneous surface heat flux. The temperature and heat flux signals for each run were recorded simultaneously on a dual channel Sanborn strip chart recorder. Typical records from these runs are shown on Figures 6-12a through 6-12z at the end of this section. In each case, the upper record represents temperature fluctuations while the lower is for the heat flux. The time scale is on the abscissa where one division represents 2.5 milli-seconds. The amplification factor was not the same in all cases, so the actual temperature and heat flux scales are indicated on each chart. Mechanical linkages within the strip chart recorder limited accurate reproduction of the signal to those components with frequencies well below 100 cps.

The zero position on the temperature records does not represent the time average surface temperature, but only reflects the extent to which the DC component of the signal was removed by the bucking circuit of Figure 5-15. The time average temperature was measured with a precision potentiometer, as has been mentioned, and the temperature traces are used to show the peak-to-peak magnitude of the temperature fluctuations. The zero position on the heat flux record, on the other hand, represents the time average heat flux. Excursions from this line indicate actual positive and negative changes in the heat flux from time average values. In

reality, there is a small DC voltage included in the heat flux records that corresponds to the DC component remaining in the thermocouple signal. However, this DC voltage has been reduced many times by the factor:

$$\frac{r_1}{\sum_i r_i}$$

where r represents the resistors within the heat meter shown in Figure 5-16. This factor is of the order of 0.001, so the DC component in the heat flux signal can be ignored.

The recordings for the No. 1 surface thermocouple during the low heat flux runs (runs 22 through 25) are shown in Figures 6-12a through 6-12d. These curves are unusual in that the fluctuations are relatively large and in the form of sharp peaks. This behavior has been attributed to momentary liquid-solid contact and consequent quenching of the heater surface. The nature of this contact is discussed in detail in Section E of this chapter.

The fluctuations in surface temperature and heat flux are smaller and different in character for the other two thermocouple positions farther up the heater wall and also for the No.1 surface thermocouple position for the higher heat flux runs. In general, it can be seen that an increase in heat flux (downward movement on the lower record) is soon followed by a decrease in temperature (upward movement on the upper record). A typical lead time is 0.005 seconds. Since the heat flux changes are expected to lead the temperature changes by an eighth of a cycle according to equation 5-8, the 0.005 second lead time would correspond to a frequency

of 25 cps. This is within the range of "preferred frequencies" as will be shown in the next section.

Besides providing an indication of the general nature of the fluctuations, Figures 6-12a through 6-12z also allow a measure of their peak values. Voltage changes measured on the upper curves of Figure 6-12 were multiplied by the thermocouple constant to give the corresponding temperature changes, according to equation 5-11:

$$\Delta T = a_1 \Delta v$$

The voltage to heat flux conversion was accomplished according to equation 5-13:

$$q = \frac{a_1 k_{Ni}}{\sqrt{\frac{1}{2} \alpha_{Ni} r_1 C_1}} \cdot \Delta v$$

where Δv is measured on the lower curves of Figure 6-12 and k_{Ni} , α_{Ni} , and a_1 are evaluated at the time average surface temperature. These results are presented in Table 6-3 where the size of the largest fluctuations in surface heat flux and temperature are recorded. (Average values are presented in the next section.) In the case of the heat flux measurements, the table includes both the positive-going and negative-going peaks, measured with respect to the time average heat flux. The temperature fluctuations, however, are peak-to-peak values.

Table 6-3 indicates that the maximum positive-going heat flux pulses always exceed the time average heat flux in magnitude except for those

TABLE 6 - 3

Peak Instantaneous Values of Fluctuating Components
of Surface Heat Flux and Temperature

Sur. TC ¹	Run No.	$\bar{q} \times 10^{-3}$ (Btu/hr-ft ²)	$q' \times 10^{-3}$ (Btu/hr-ft ²)		T' (°F) Max. peak-to- peak values
			Maximum Plus	Peaks Minus	
1	12 ²	12.4	7.8	5.6	.52
	14 ²	18.2	13.9	8.1	.69
	15	22.3	16.	11.7	.68
	22	8.6	320.	8.7	15.4
	23	9.4	180.	140.	7.9
	24	10.9	76.	44.	6.9
	25	12.5	62.	24.	3.1
	19	14.9	33.	6.9	1.7
	20	18.0	37.	8.4	1.5
	2	22	8.6	33.	11.9
23		9.4	19.8	6.6	2.7
17		9.5	24.	6.6	1.2
24		10.9	17.6	5.4	1.2
12		12.4	30.	6.8	1.8
25		12.5	29.	6.8	1.3
19		14.9	27.	8.4	1.8
20		18.0	43.	8.5	1.4
3		22	8.6	29.	6.6
	23	9.4	21.	4.0	1.2
	17	9.5	18.6	5.3	1.0
	24	10.9	22.	6.8	1.2
	12	12.4	20.	6.8	1.2
	25	12.5	33.	8.3	1.4
	19	14.9	25.	11.2	1.2
	20	18.0	24.	12.8	2.0
	14	18.2	48.	14.3	2.0

¹ See Table 5-1 for location of surface thermocouples

² Bulk liquid opposite No. 1 surface thermocouple was subcooled

cases where the bulk liquid was subcooled. The maximum and minimum instantaneous values of heat flux are obtained by adding or subtracting the peak values of the fluctuations (q') to the time average heat flux. This is shown later by equations 6-15 and 6-16. Applying these equations to Table 6-3, it can be seen that for surface thermocouples 2 and 3, the instantaneous heat flux reaches peak values that are two to five times greater than the average value. The minimum instantaneous heat flux, on the other hand, ranges from 20 to 40 per cent of the average value except for run 22 at the No. 2 surface thermocouple which appears to be anomalous.

At surface thermocouple No. 1, several unusual characteristics are noted. For runs 12, 14 and 15 with subcooled bulk liquid, the heat flux peaks are much smaller. Apparently the subcooled liquid was able to significantly inhibit wave action. During runs 19 and 20 with saturated bulk liquid and a large time average heat flux, the fluctuations are of the same order of magnitude as at the other two surface thermocouples. However, during runs 22 through 25 with saturated bulk liquid and relatively low average heat flux values, very large fluctuations were experienced. Peak heat flux values were as much as 40 times greater than the average while the negative going pulses were 10 to 15 times the mean. The implication of these large negative peaks in heat flux is that energy momentarily flows from the fluid to the heater wall, even though the wall always remains considerably hotter than the average vapor temperature. This may be explained by recognizing that the vapor near the wall remains at the wall temperature. Thus, although a local cooling of the wall surface will result in a cooling of the adjacent vapor, this vapor will soon be replaced by warmer vapor

rising from below where it had been in contact with a warmer portion of the wall. If the local cooling had been great enough, then heat will be momentarily transferred from the newly arrived vapor to the cool spot on the wall.

Temperature fluctuations at the heater surface are also noted on Table 6-3. The maximum values are typically one to three degrees F. Higher values of up to 15 degrees F. for some runs are associated with liquid-solid contact. It should be mentioned again that these temperature fluctuations are strongly influenced by the nature of the heater surface and in themselves are not necessarily characteristic of the film boiling mechanism. It follows from equations 5-6 and 5-8 that the physical properties of the heater wall largely determine the size of the temperature fluctuations that result from a change in surface heat flux. Thus, the heat flux rather than the temperature is the subject of primary concern. Nevertheless, it was pointed out in Chapter IV that there will be some coupling between the surface heat flux and the heating system. This coupling effect could be significant for a system with unusual properties, such as a non-metallic heater wall with a very low thermal conductivity. Further experimental measurements of this point would be of great value.

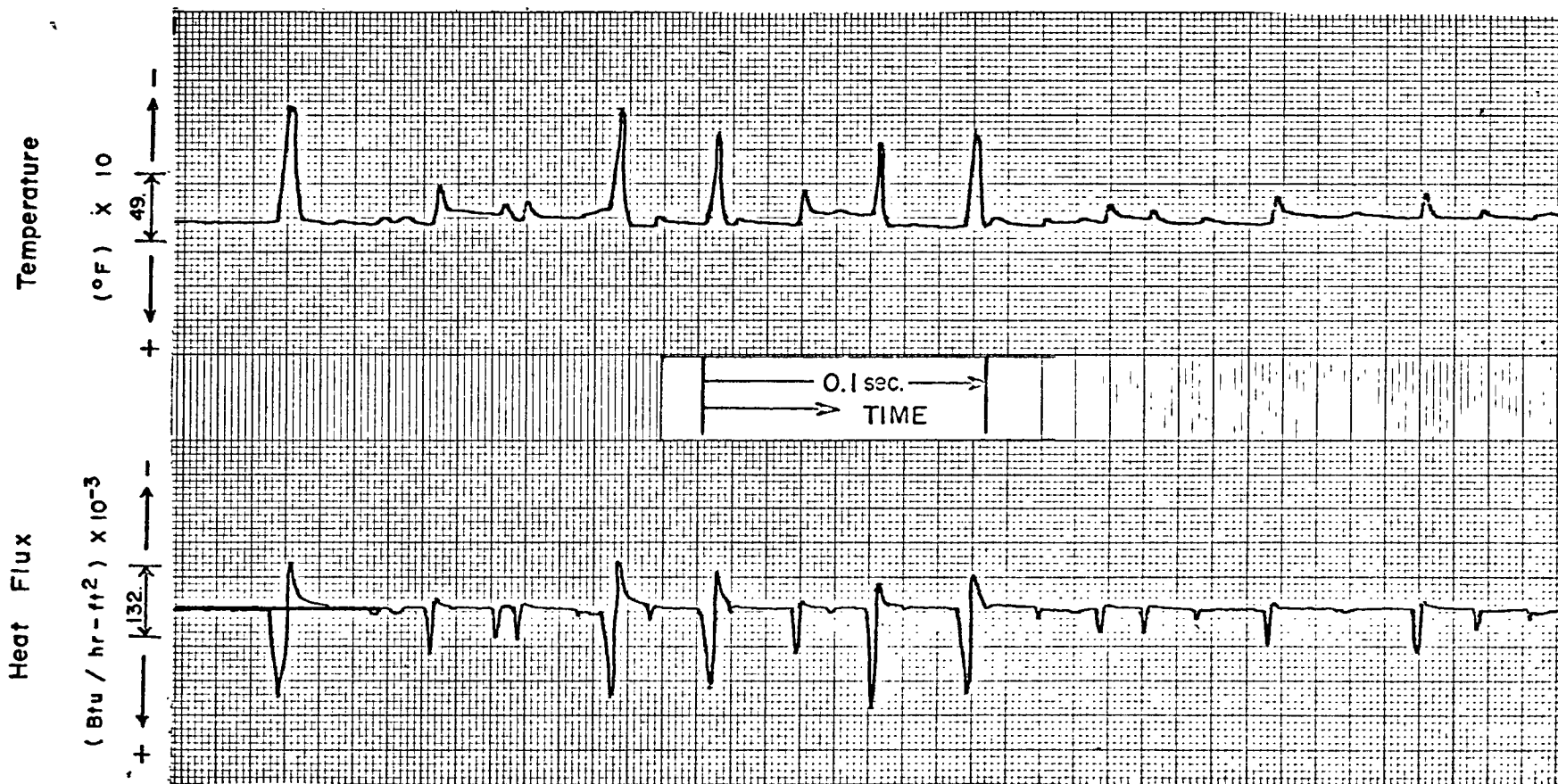
In summary, it may be stated that large fluctuations in surface heat flux were measured and are indicative of violent wave action at the vapor-liquid interface. The implications of these waves in terms of the unsteady state theory will be discussed in Section D. The measured peak heat flux values will be compared to theoretical peak values at that point. In Section F, a qualitative measure of the relationship between the interfacial activity and the surface temperature will be presented.

FIGURE 6-12 a
Instantaneous Surface Temperature
and Heat Flux Records



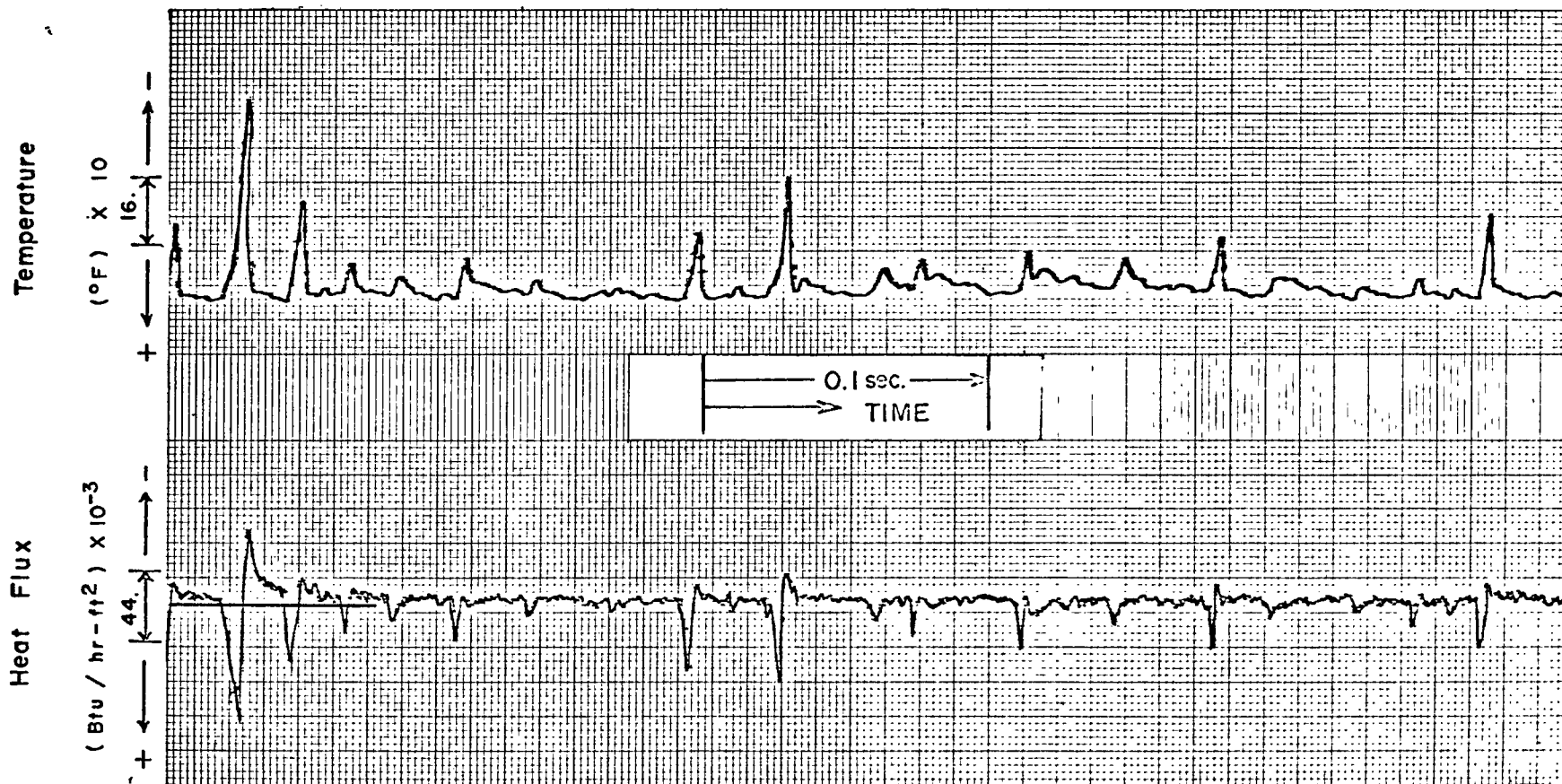
Run No. 22
Surface Thermocouple No. 1
(Liquid - Solid Contact)
 $\bar{q} = 8.6 \times 10^3 \text{ Btu/hr-ft}^2$

FIGURE 6-12 b
Instantaneous Surface Temperature
and Heat Flux Records



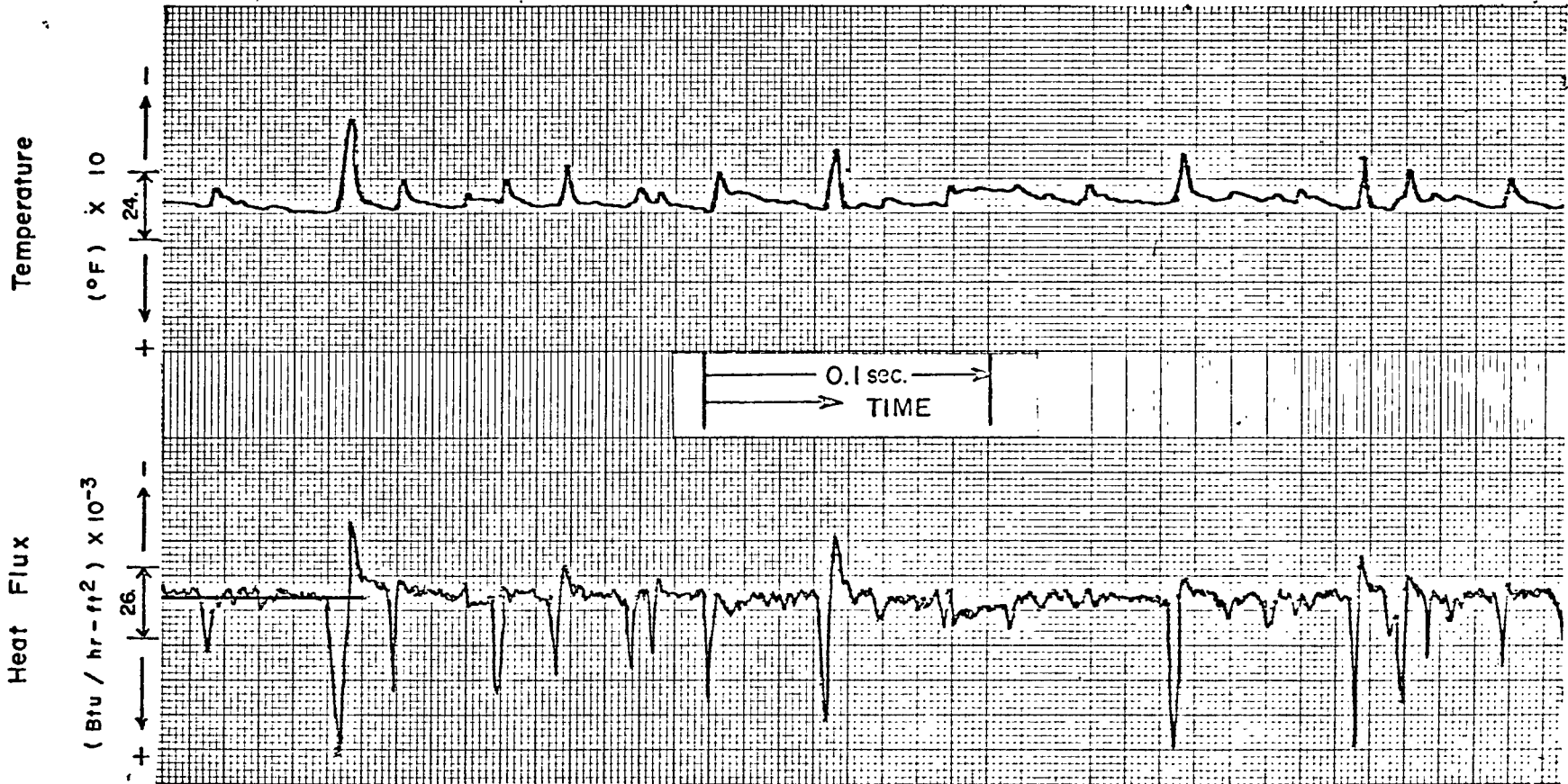
Run No. 23
Surface Thermocouple No. 1
(Liquid-Solid Contact)
 $\bar{q} = 9.4 \times 10^3 \text{ Btu/hr-ft}^2$

FIGURE 6-12 c
Instantaneous Surface Temperature
and Heat Flux Records



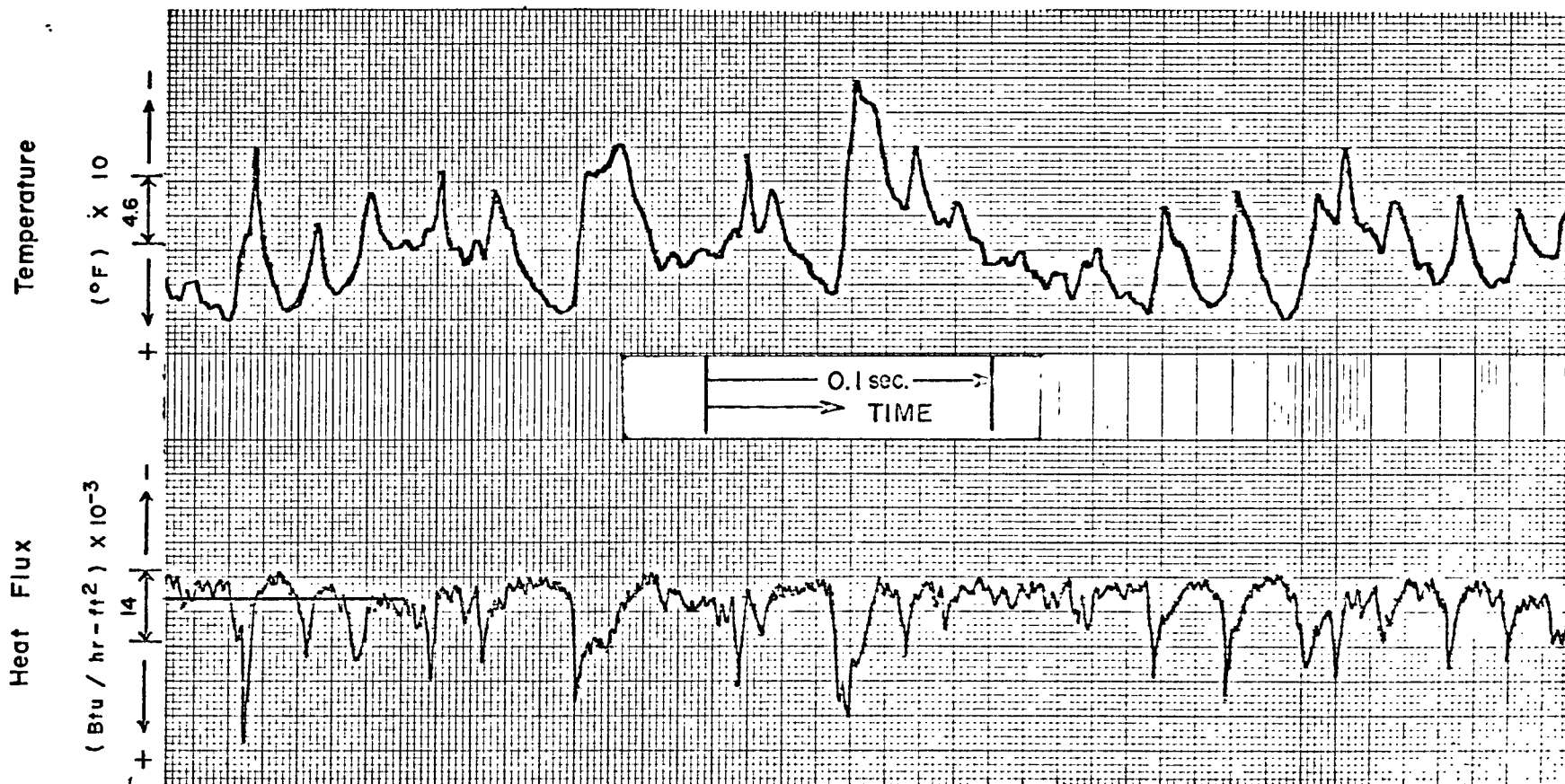
Run No. 24
Surface Thermocouple No. 1
(Liquid - Solid Contact)
 $\bar{q} = 10.9 \times 10^3 \text{ Btu/hr-ft}^2$

FIGURE 6-12 d
Instantaneous Surface Temperature
and Heat Flux Records



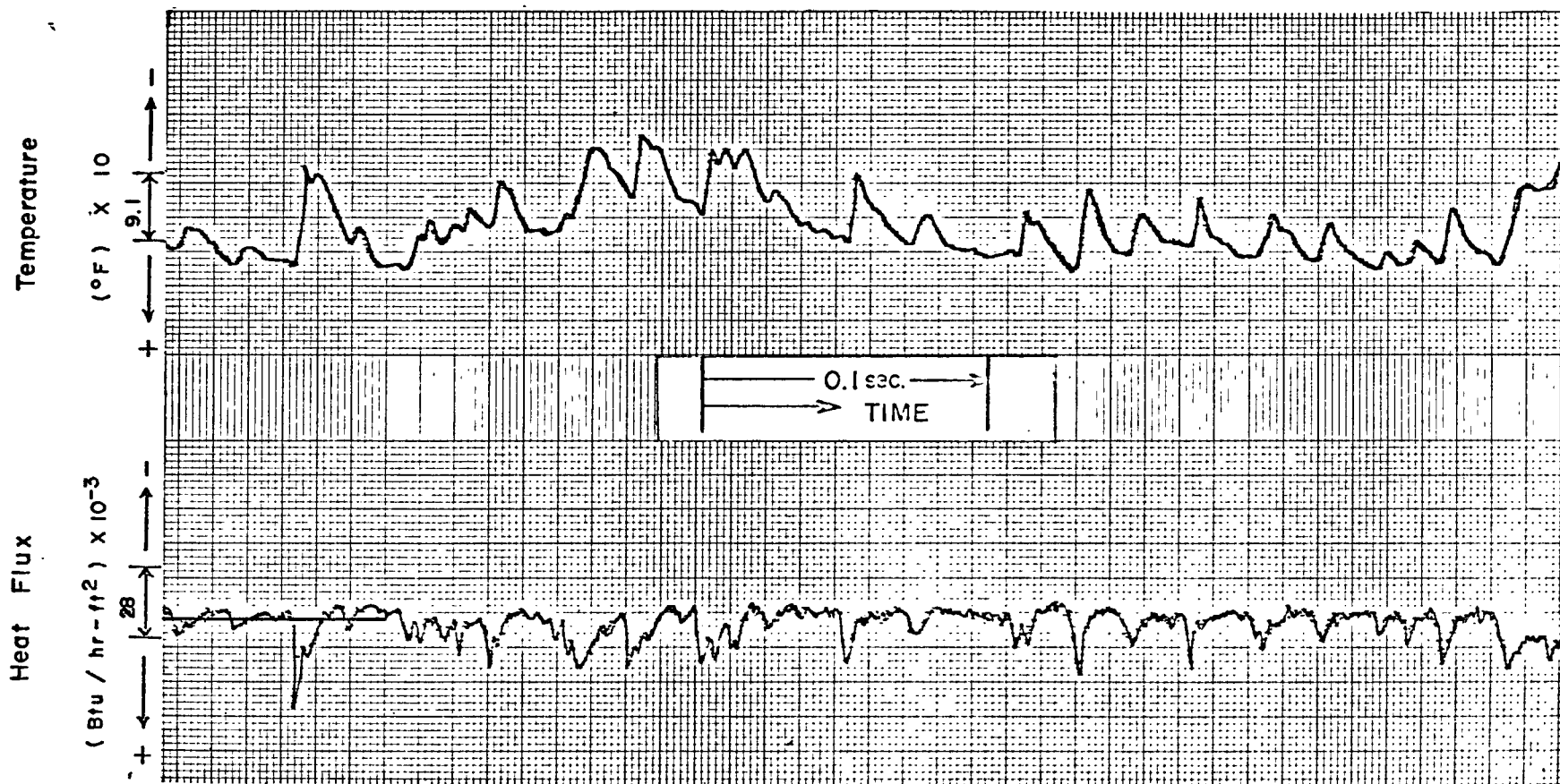
Run No. 25
Surface Thermocouple No. 1
(Liquid-Solid Contact)
 $\bar{q} = 12.5 \times 10^3 \text{ Btu/hr-ft}^2$

FIGURE 6-12 e
Instantaneous Surface Temperature
and Heat Flux Records



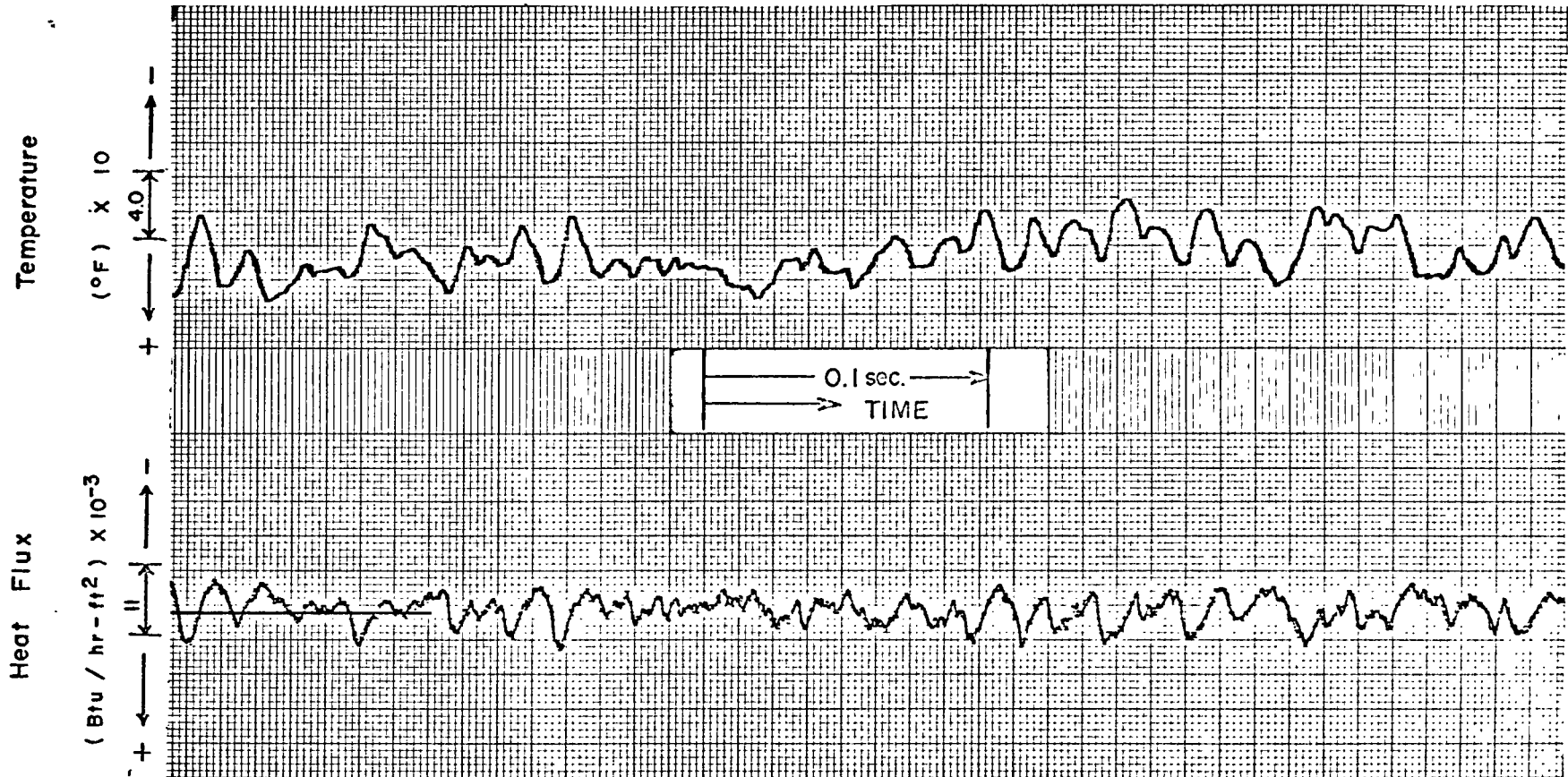
Run No. 19
Surface Thermocouple No. 1
 $\bar{q} = 14.9 \times 10^3 \text{ Btu/hr-ft}^2$

FIGURE 6-12 f
Instantaneous Surface Temperature
and Heat Flux Records



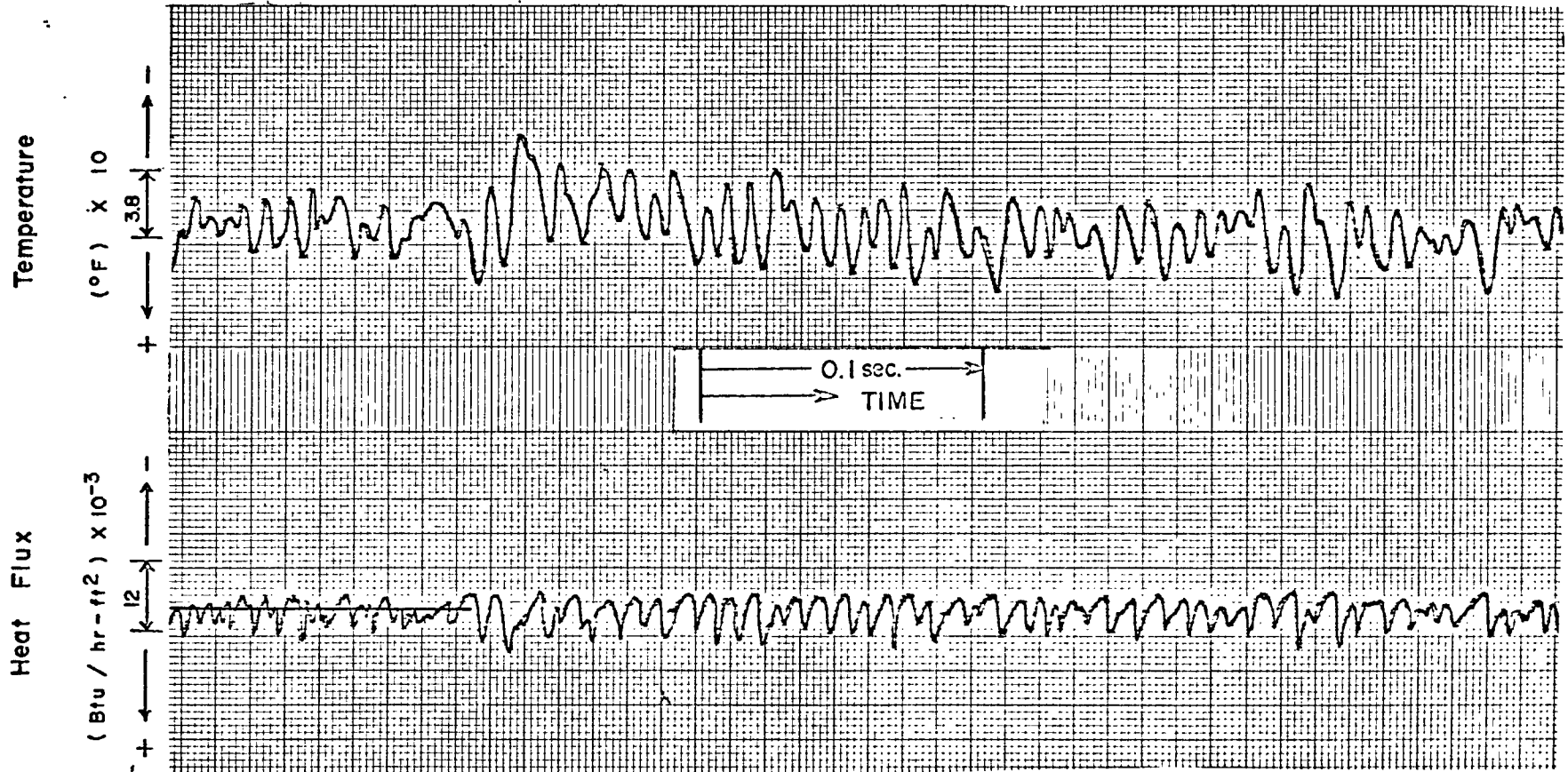
Run No. 20
Surface Thermocouple No. 1
 $\bar{q} = 18.0 \times 10^3 \text{ Btu/hr-ft}^2$

FIGURE 6-12 g
Instantaneous Surface Temperature
and Heat Flux Records



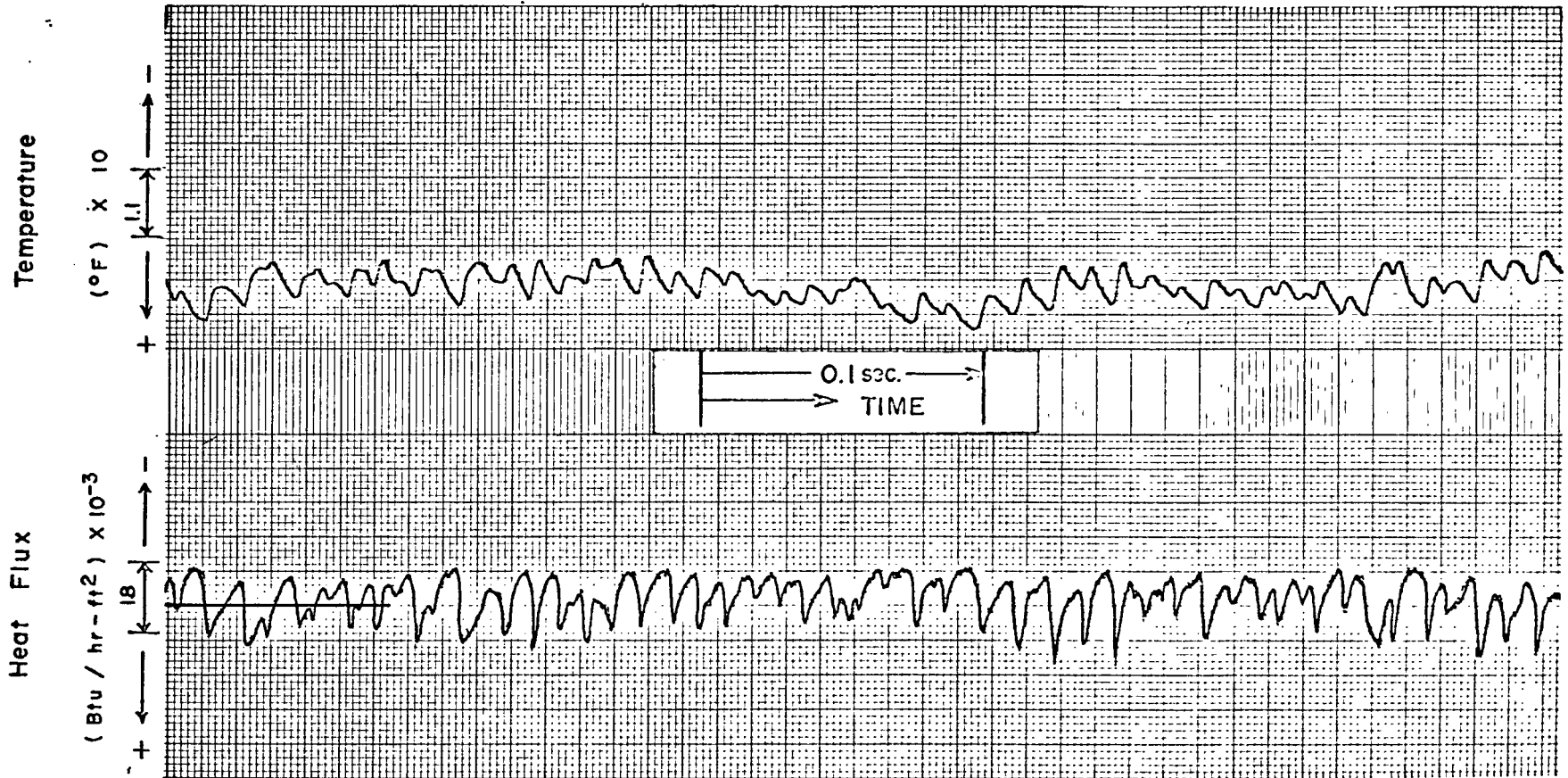
Run No. 12
Surface Thermocouple No. 1
 $\bar{q} = 12.4 \times 10^3 \text{ Btu/hr-ft}^2$

FIGURE 6-12 h
Instantaneous Surface Temperature
and Heat Flux Records



Run No. 14
Surface Thermocouple No. 1
 $\bar{q} = 18.2 \times 10^3 \text{ Btu/hr} - \text{ft}^2$

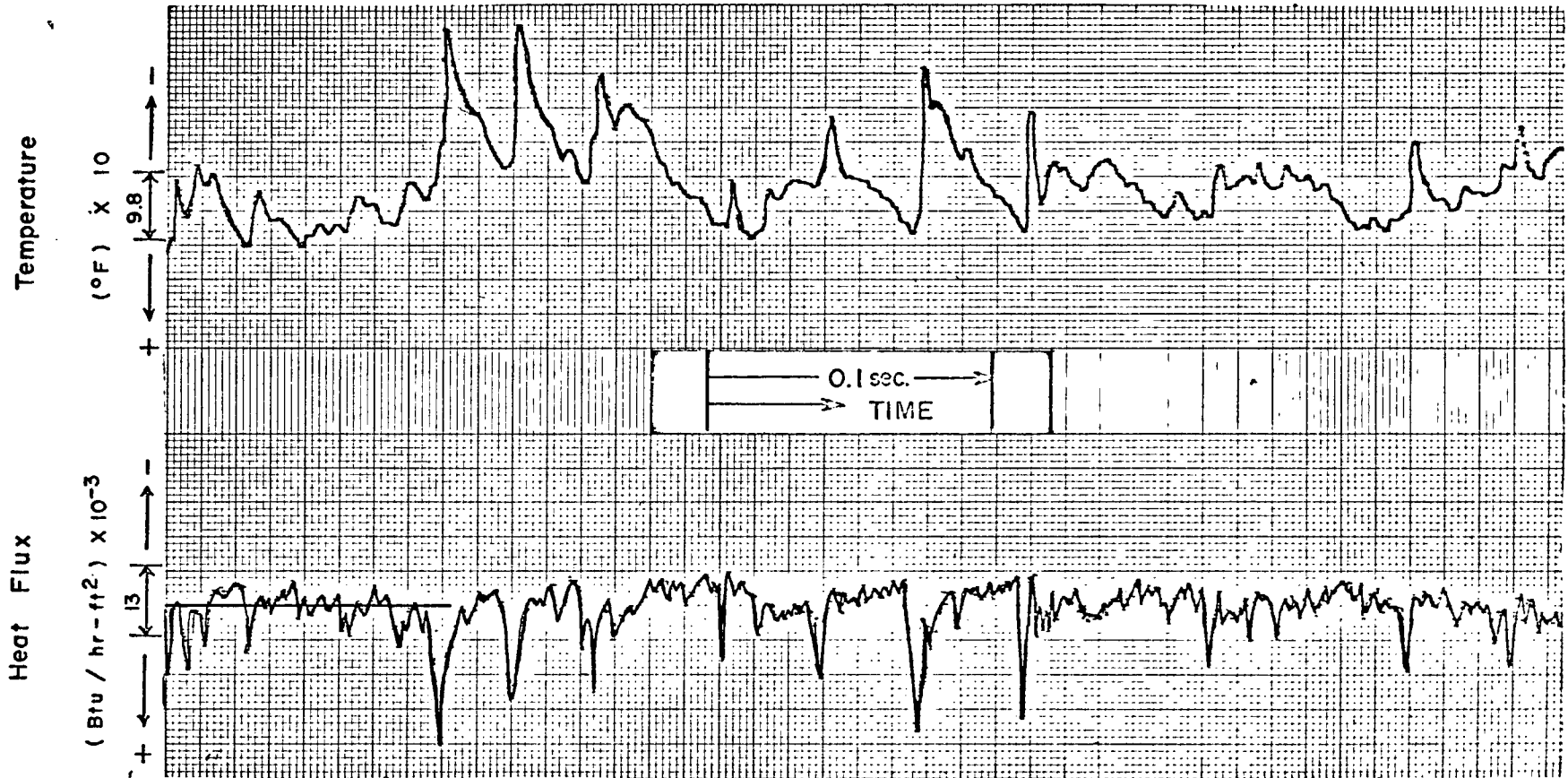
FIGURE 6-12 i
Instantaneous Surface Temperature
and Heat Flux Records



Run No. 15
Surface Thermocouple No. 1
 $\bar{q} = 22.3 \times 10^3 \text{ Btu/hr-ft}^2$

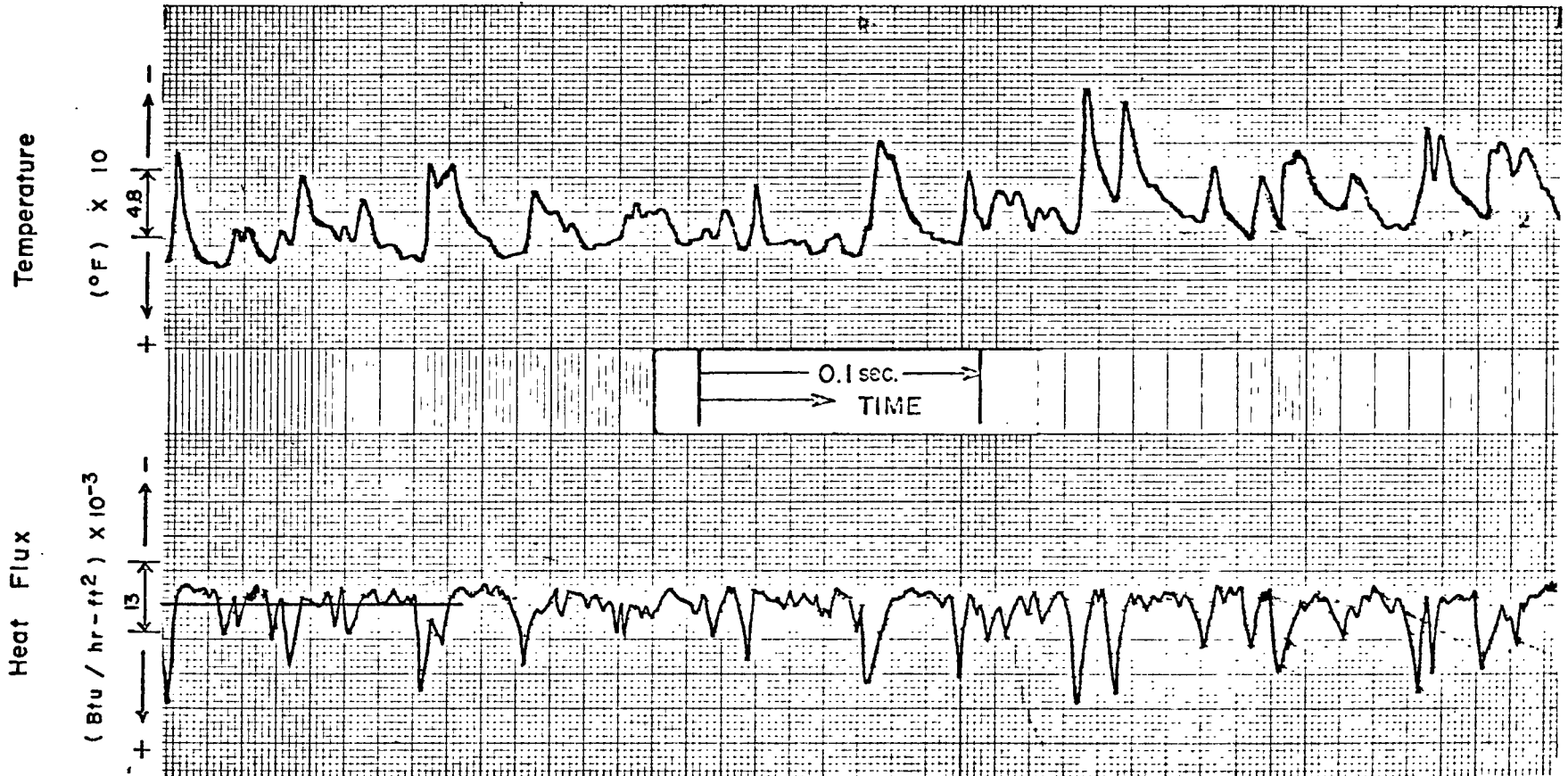
FIGURE 6-12 j

Instantaneous Surface Temperature
and Heat Flux Records



Run No. 22
Surface Thermocouple No. 2
 $\bar{q} = 8.6 \times 10^3 \text{ Btu/hr-ft}^2$

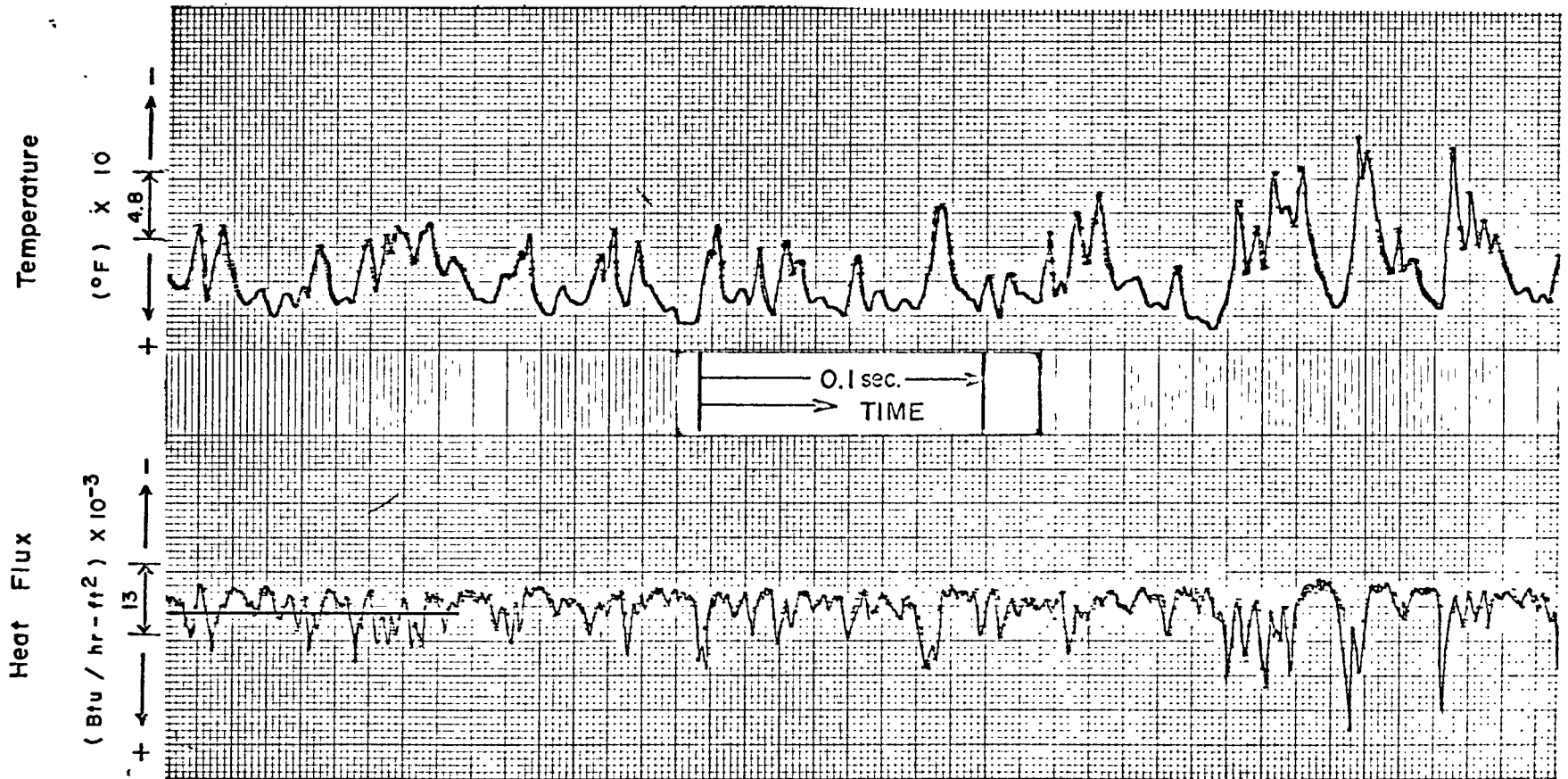
FIGURE 6-12 k
Instantaneous Surface Temperature
and Heat Flux Records



Run No. 23
Surface Thermocouple No. 2
 $\bar{q} = 9.4 \times 10^3 \text{ Btu/hr-ft}^2$

FIGURE 6-12 I

Instantaneous Surface Temperature
and Heat Flux Records

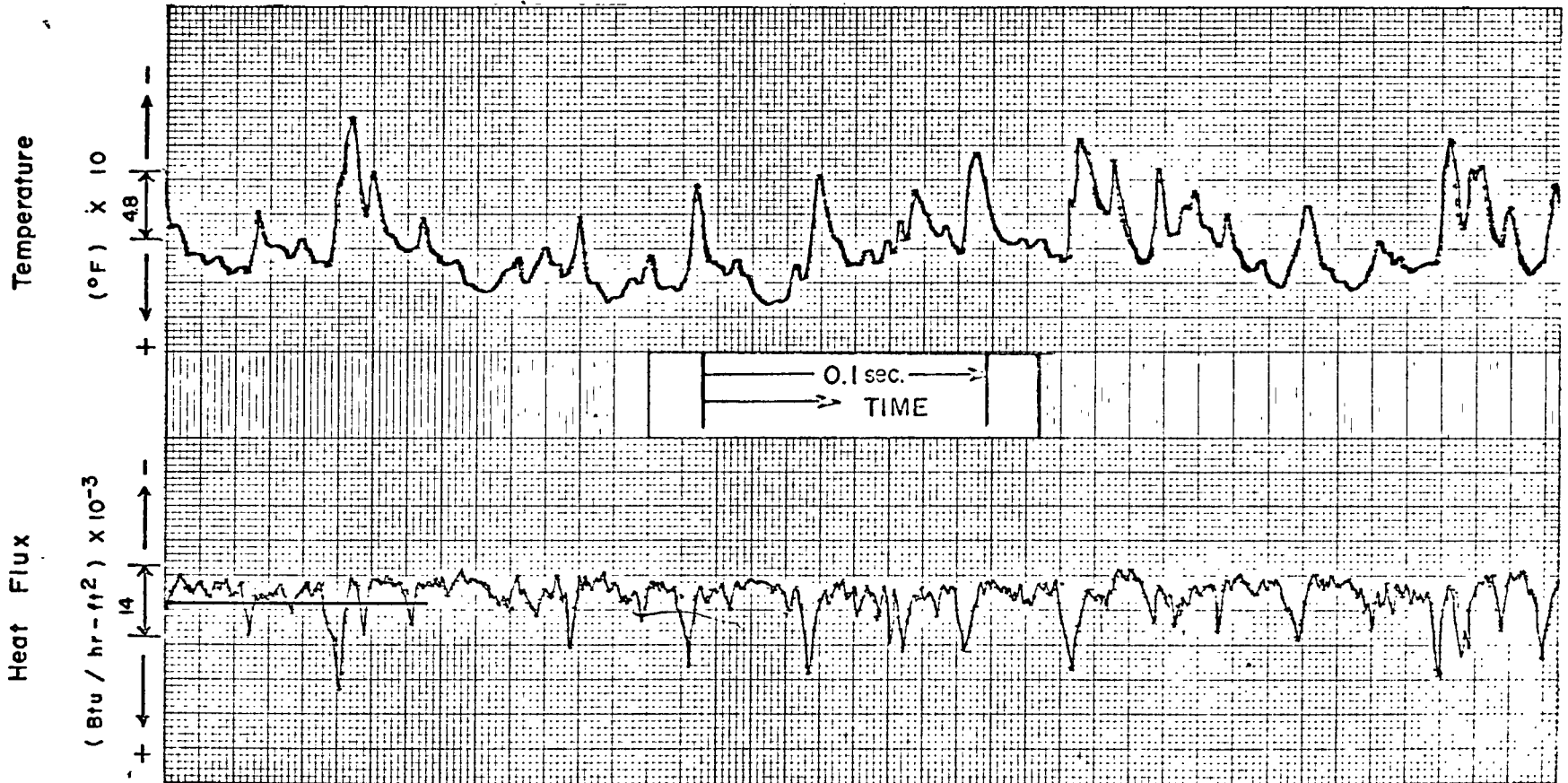


Run No. 17

Surface Thermocouple No. 2

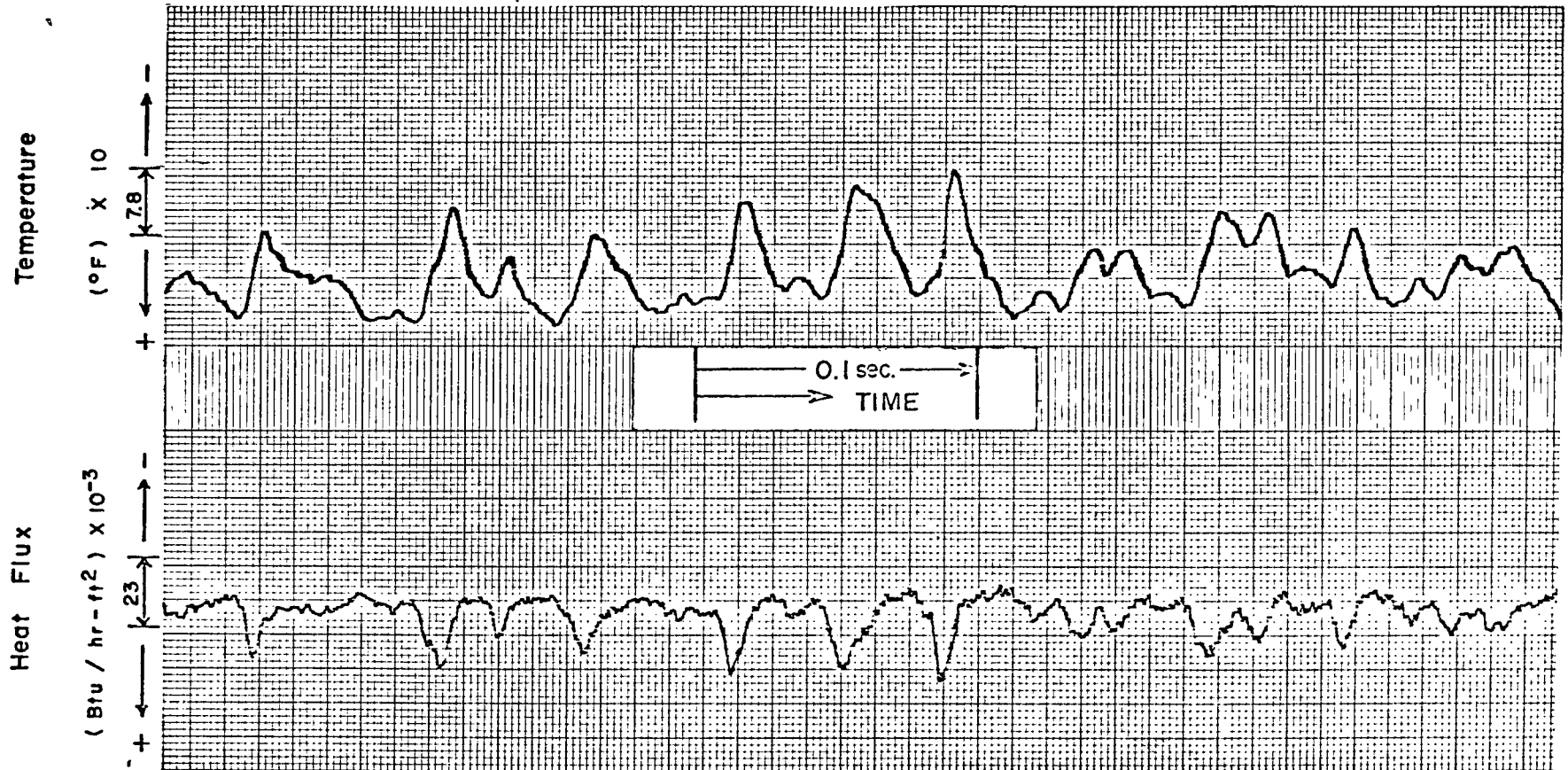
$\bar{q} = 9.5 \times 10^3$ Btu/hr-ft²

FIGURE 6-12 m
Instantaneous Surface Temperature
and Heat Flux Records



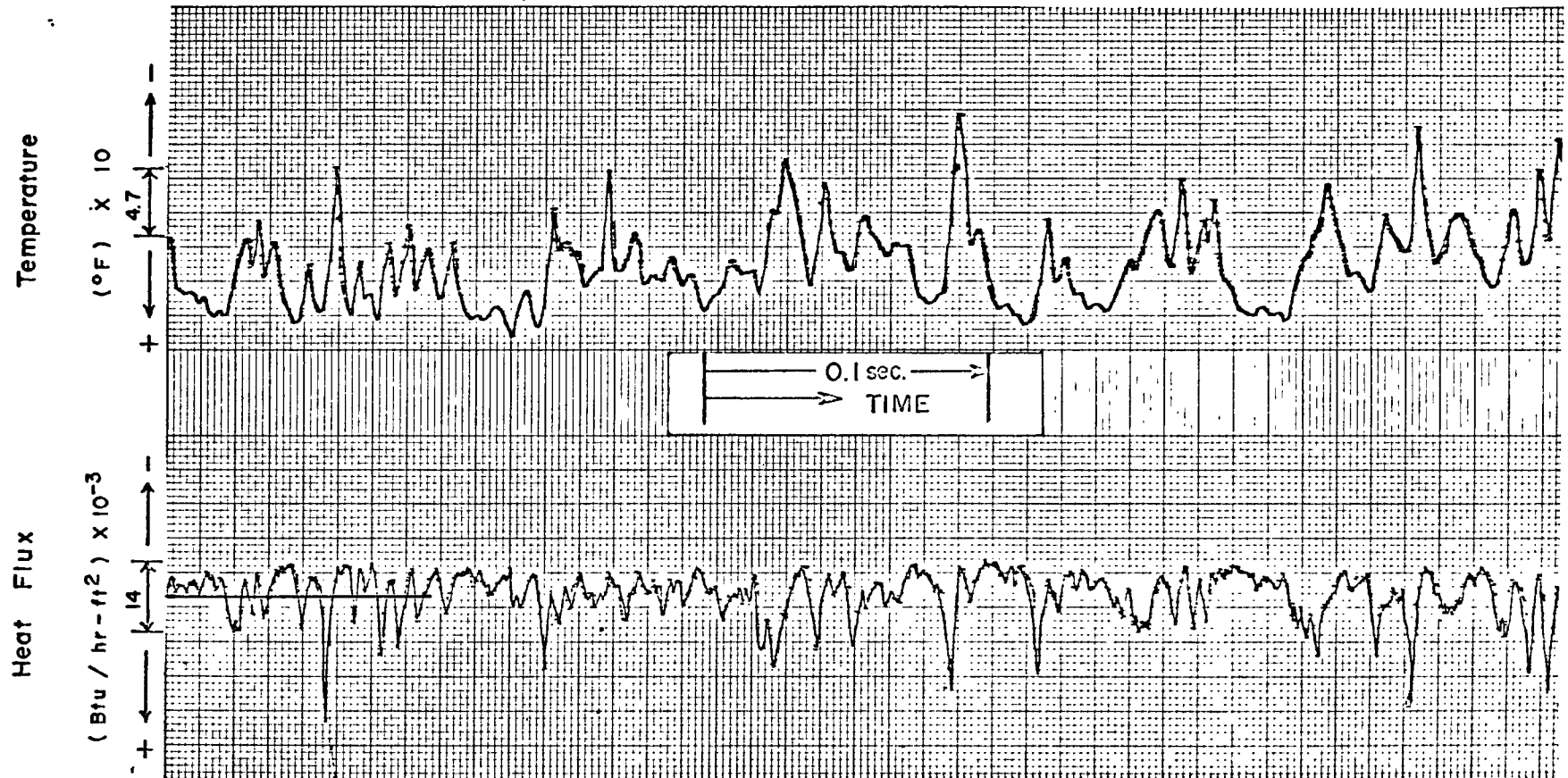
Run No. 24
Surface Thermocouple No. 2
 $\bar{q} = 10.9 \times 10^3 \text{ Btu/hr-ft}^2$

FIGURE 6-12 n
Instantaneous Surface Temperature
and Heat Flux Records



Run No. 12
Surface Thermocouple No. 2
 $\bar{q} = 12.4 \times 10^3 \text{ Btu/hr-ft}^2$

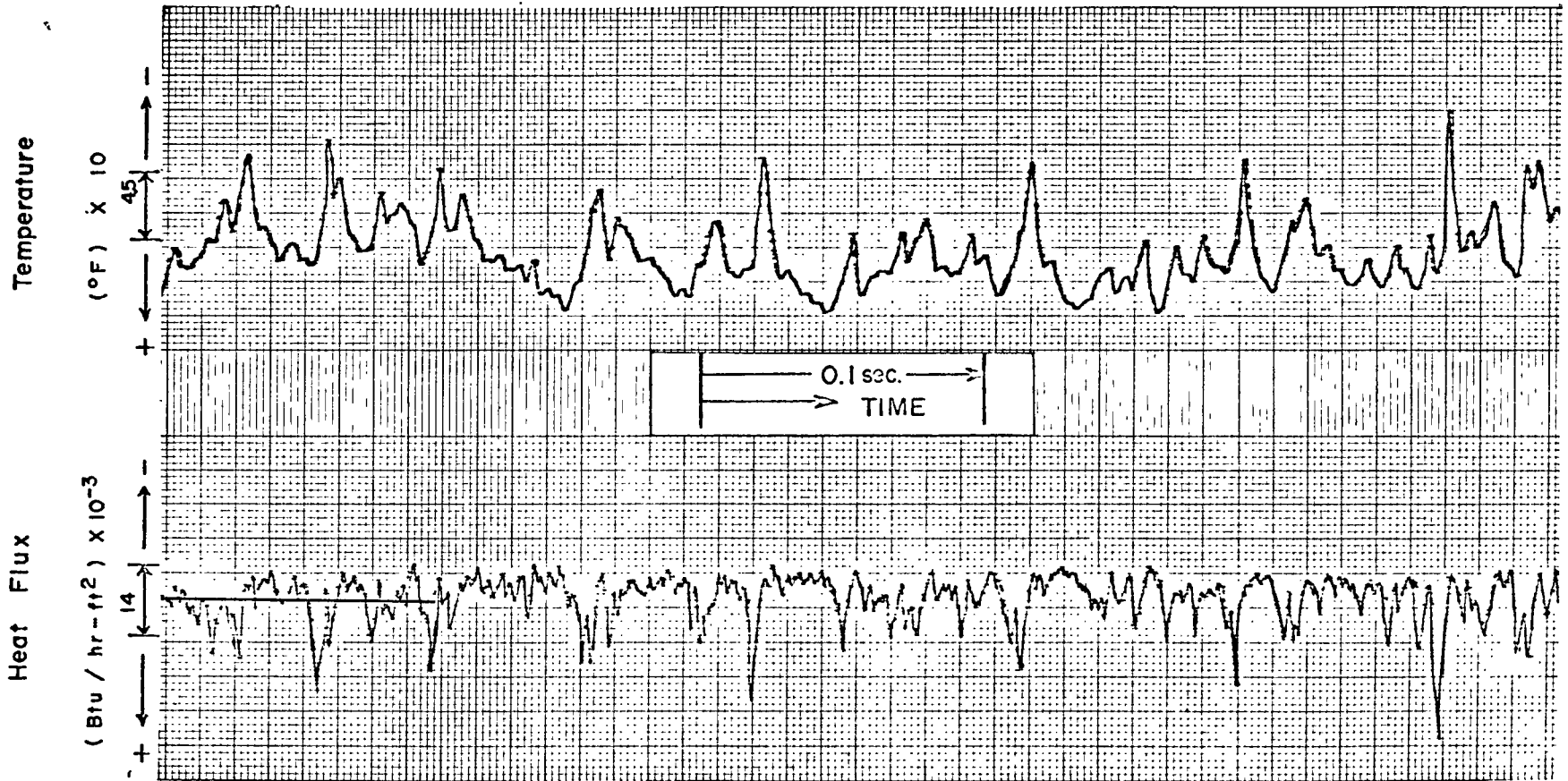
FIGURE 6-12 o
Instantaneous Surface Temperature
and Heat Flux Records



Run No. 25
Surface Thermocouple No. 2
 $\bar{q} = 12.5 \times 10^3 \text{ Btu/hr-ft}^2$

FIGURE 6-12 p

Instantaneous Surface Temperature
and Heat Flux Records

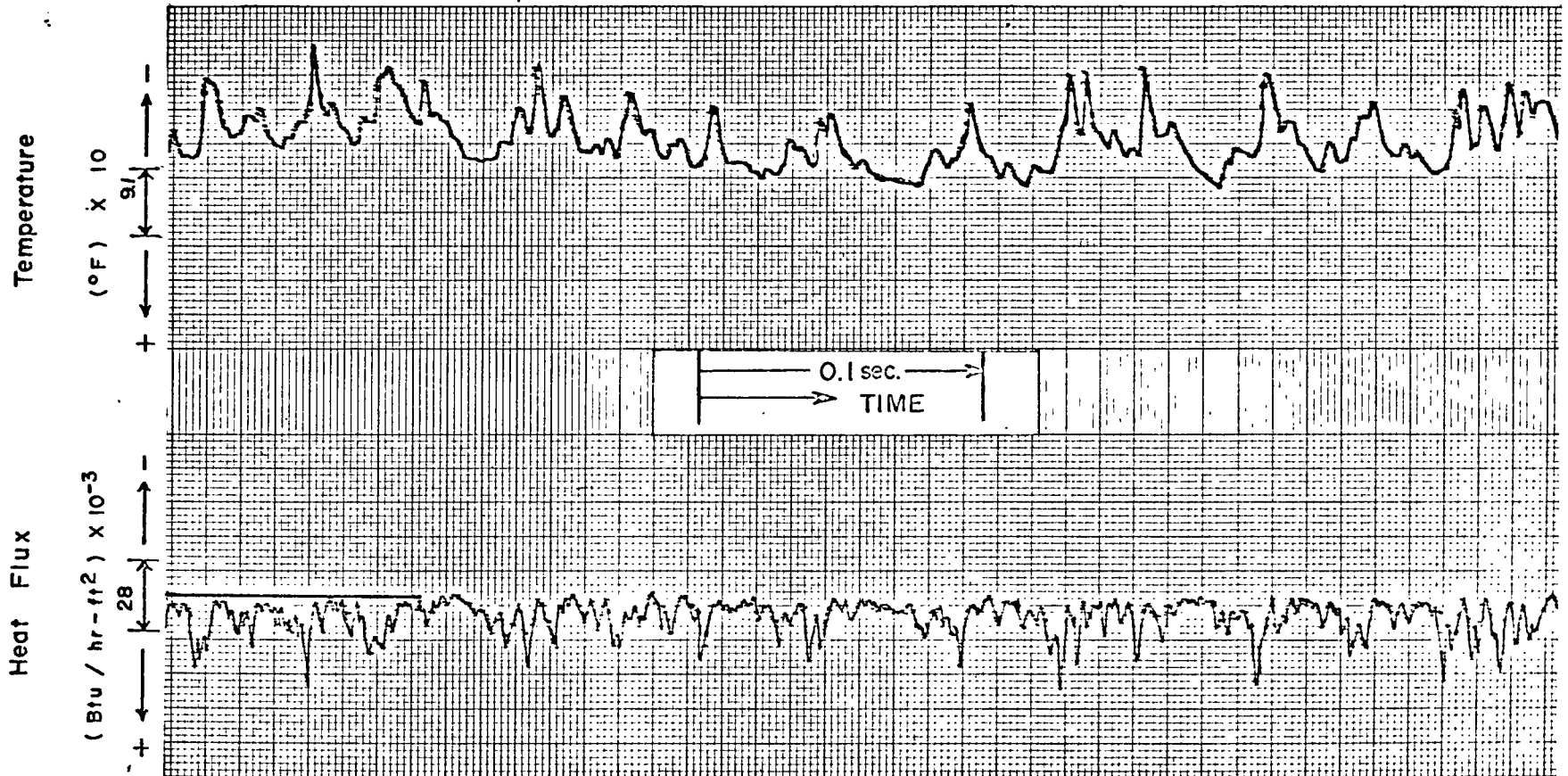


Run No. 19

Surface Thermocouple No. 2

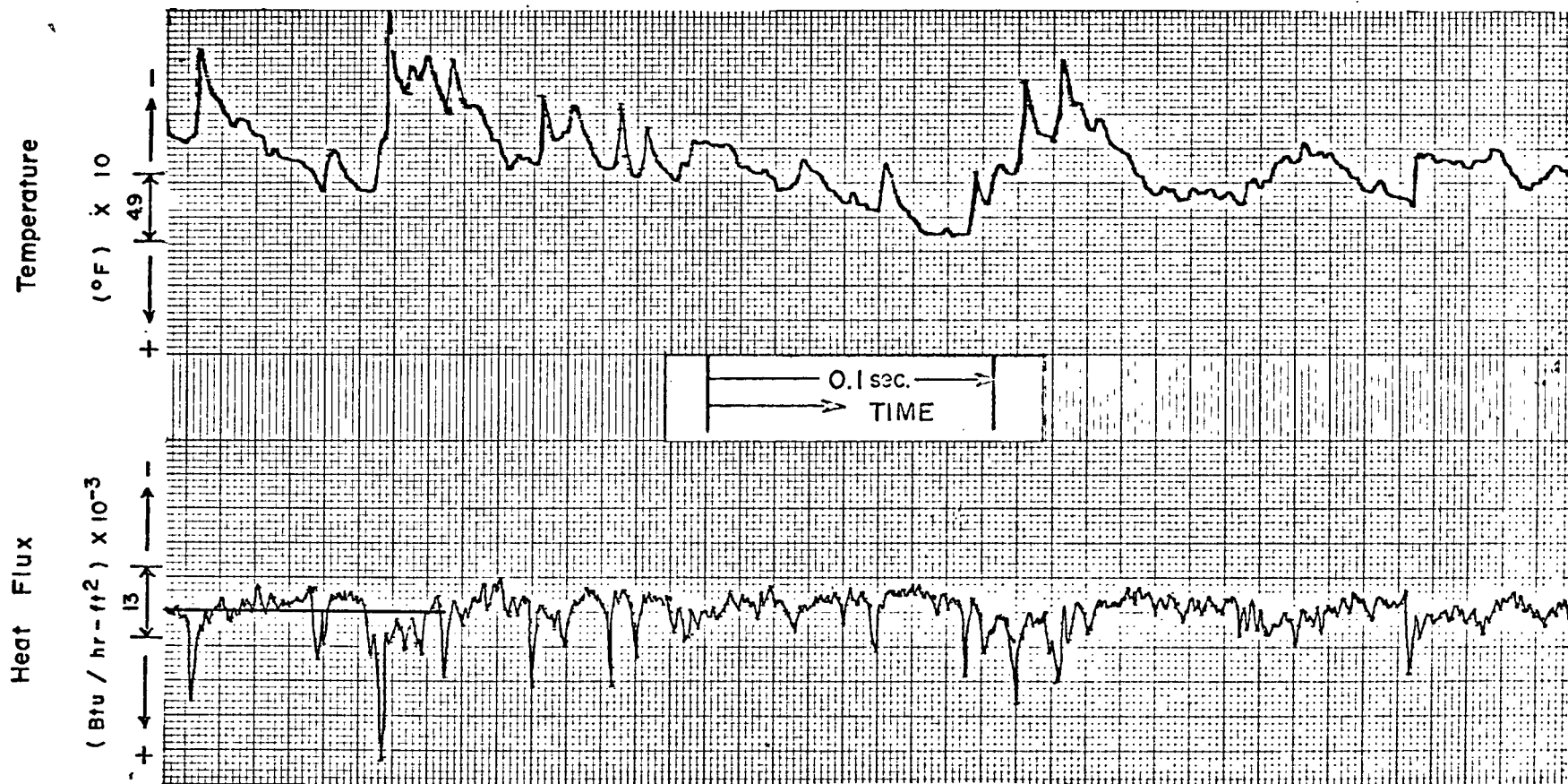
$$\bar{q} = 14.9 \times 10^3 \text{ Btu/hr-ft}^2$$

FIGURE 6-12 q
Instantaneous Surface Temperature
and Heat Flux Records



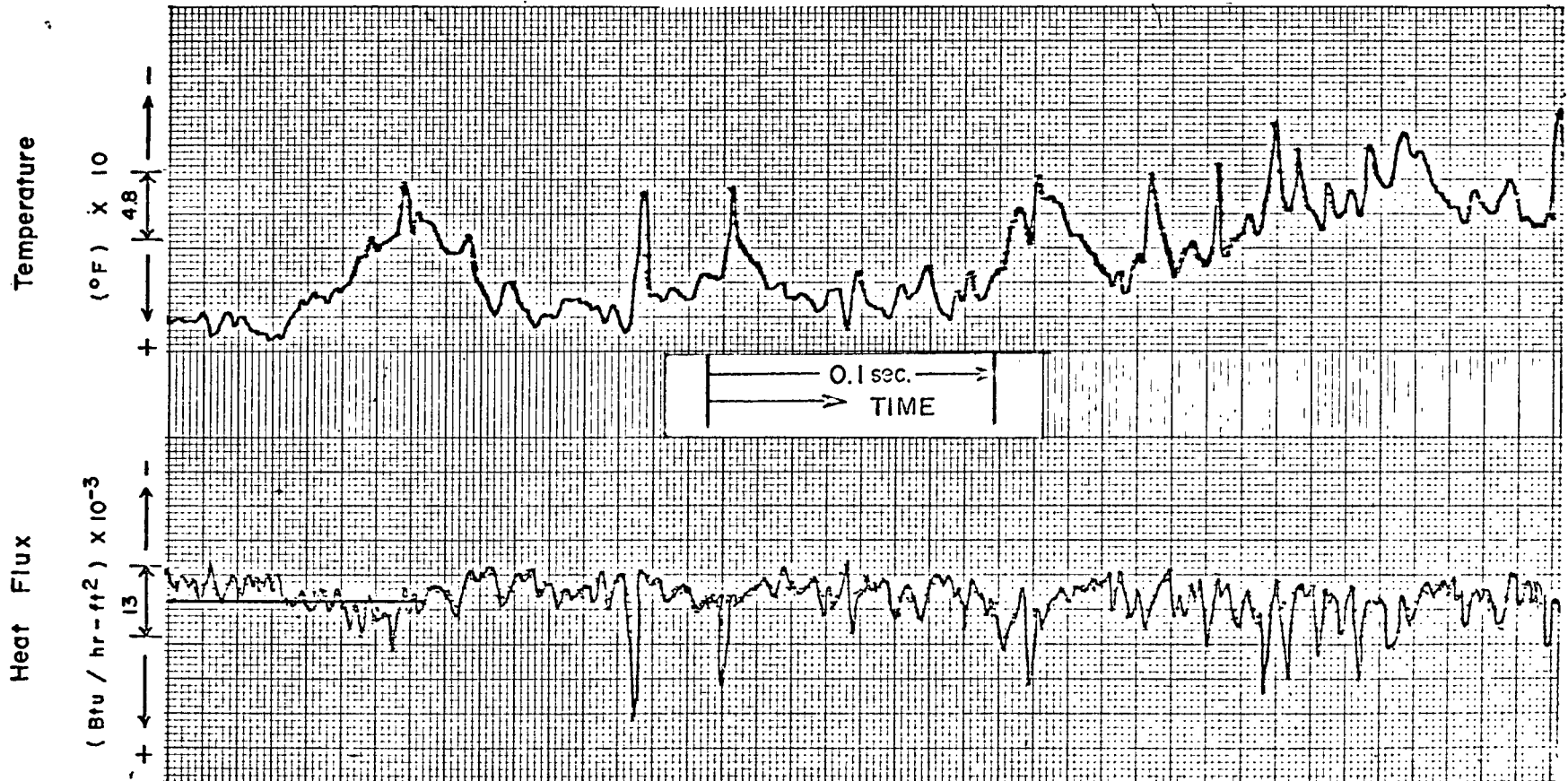
Run No. 20
Surface Thermocouple No. 2
 $\bar{q} = 18.0 \times 10^3 \text{ Btu/hr-ft}^2$

FIGURE 6-12 r
Instantaneous Surface Temperature
and Heat Flux Records



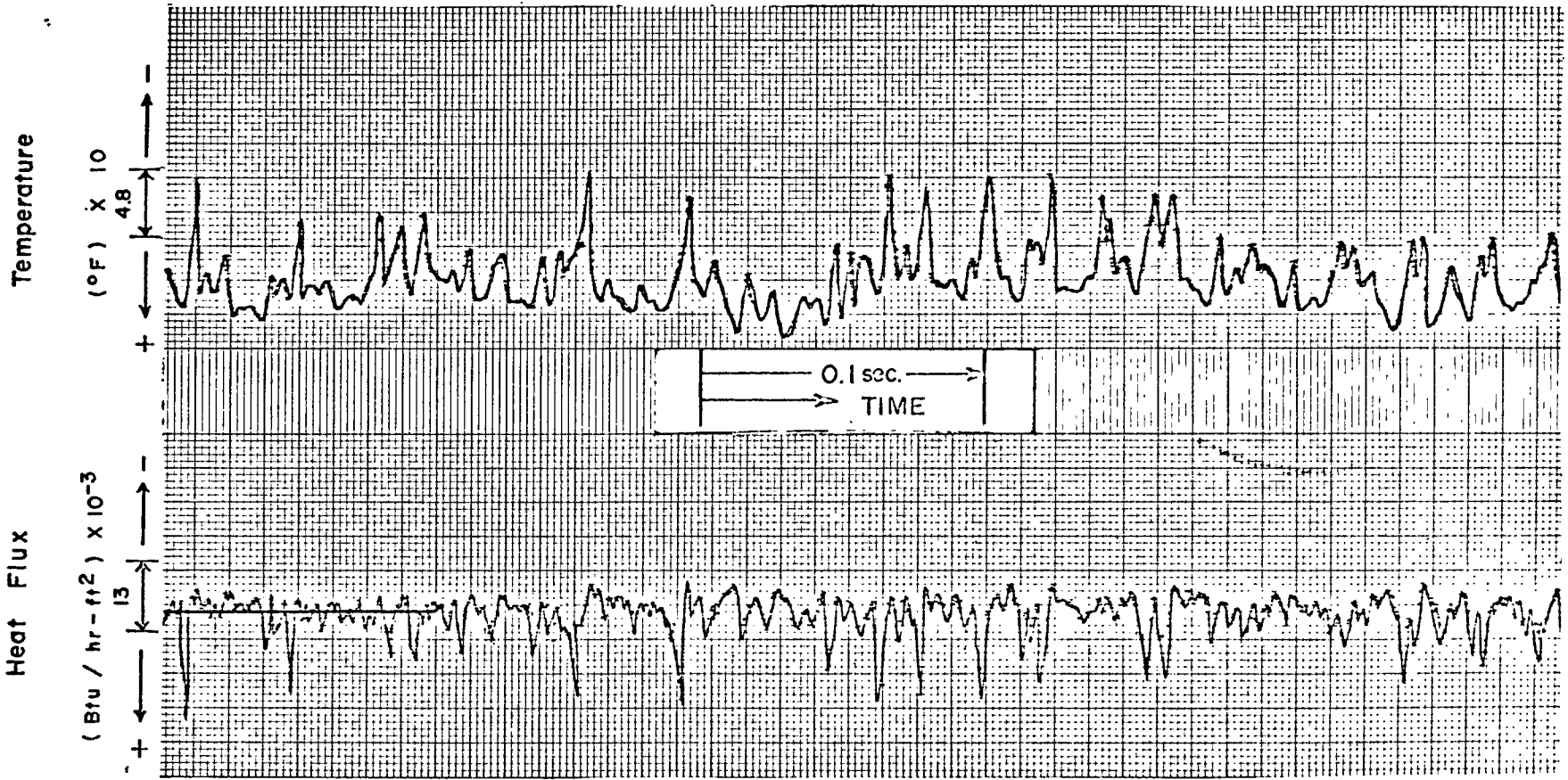
Run No. 22
Surface Thermocouple No. 3
 $\bar{q} = 8.6 \times 10^3 \text{ Btu/hr-ft}^2$

FIGURE 6-12 s
Instantaneous Surface Temperature
and Heat Flux Records



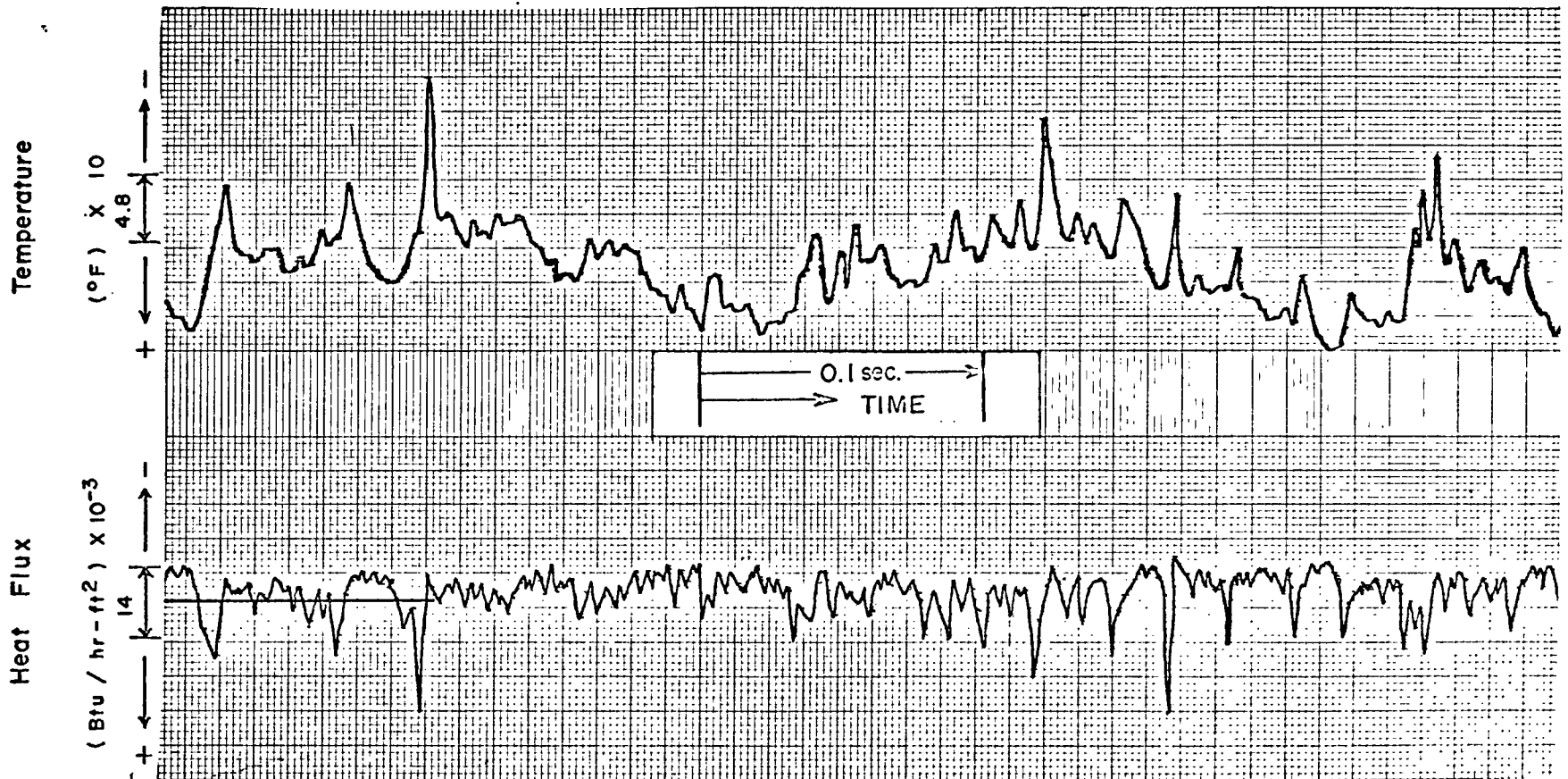
Run No. 23
Surface Thermocouple No. 3
 $\bar{q} = 9.4 \times 10^3 \text{ Btu/hr-ft}^2$

FIGURE 6-12 †
Instantaneous Surface Temperature
and Heat Flux Records



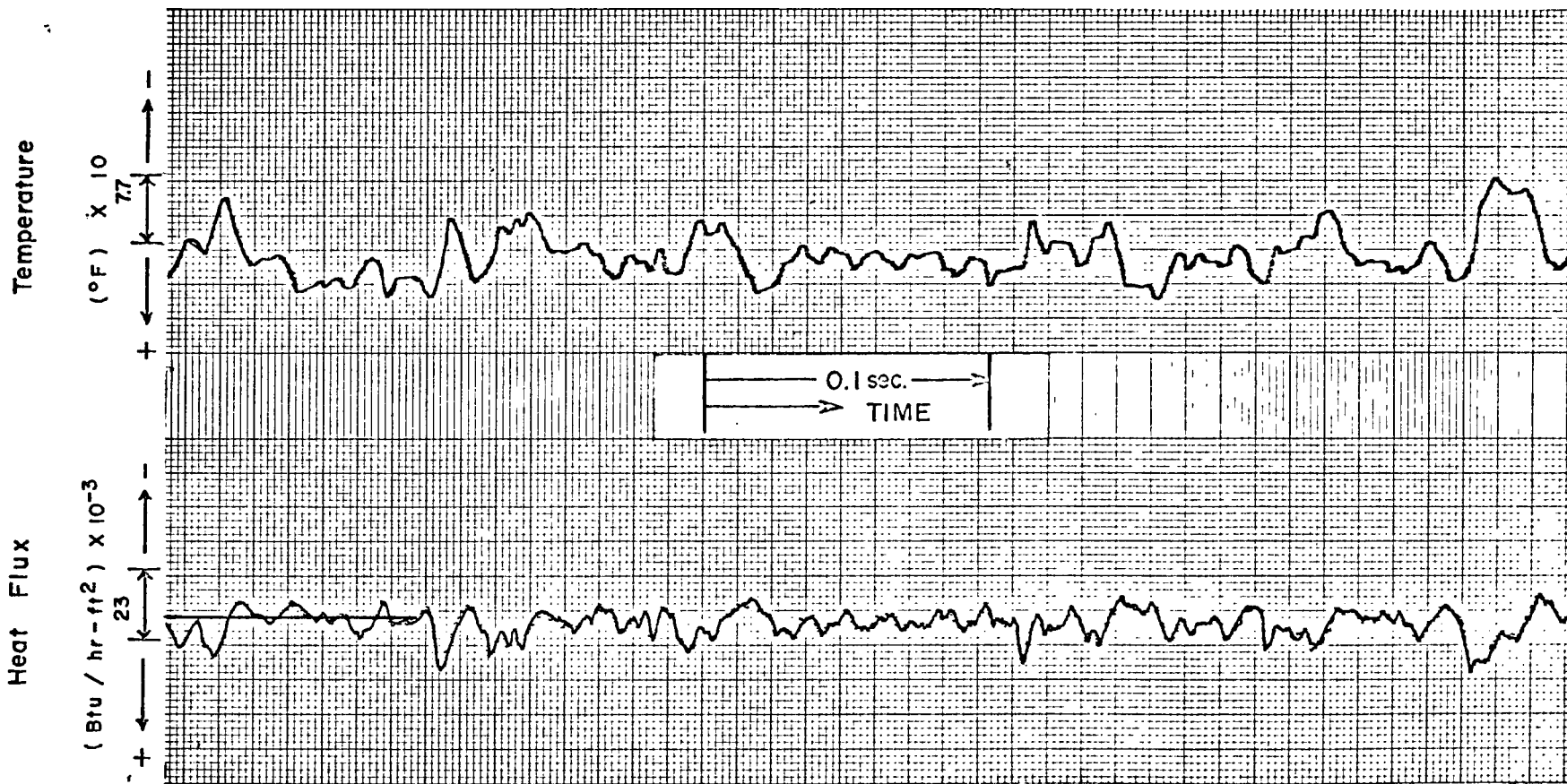
Run No. 17
Surface Thermocouple No. 3
 $\bar{q} = 9.5 \times 10^3 \text{ Btu/hr-ft}^2$

FIGURE 6-12 u
Instantaneous Surface Temperature
and Heat Flux Records



Run No. 24
Surface Thermocouple No. 3
 $\bar{q} = 10.9 \times 10^3 \text{ Btu/hr-ft}^2$

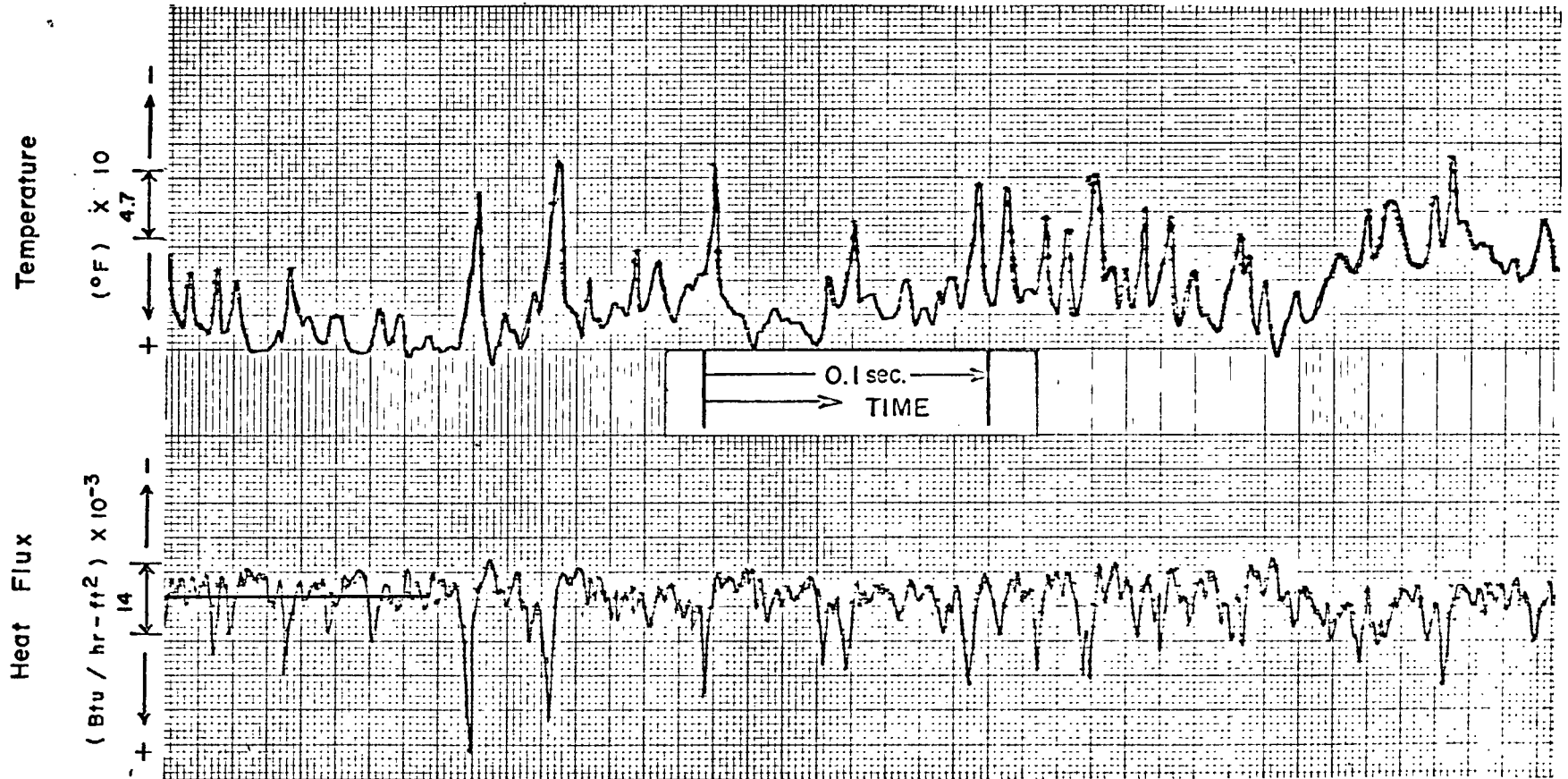
FIGURE 6-12 v
Instantaneous Surface Temperature
and Heat Flux Records



Run No. 12
Surface Thermocouple No. 3
 $\bar{q} = 12.4 \times 10^3 \text{ Btu/hr-ft}^2$

FIGURE 6-12 w

Instantaneous Surface Temperature
and Heat Flux Records



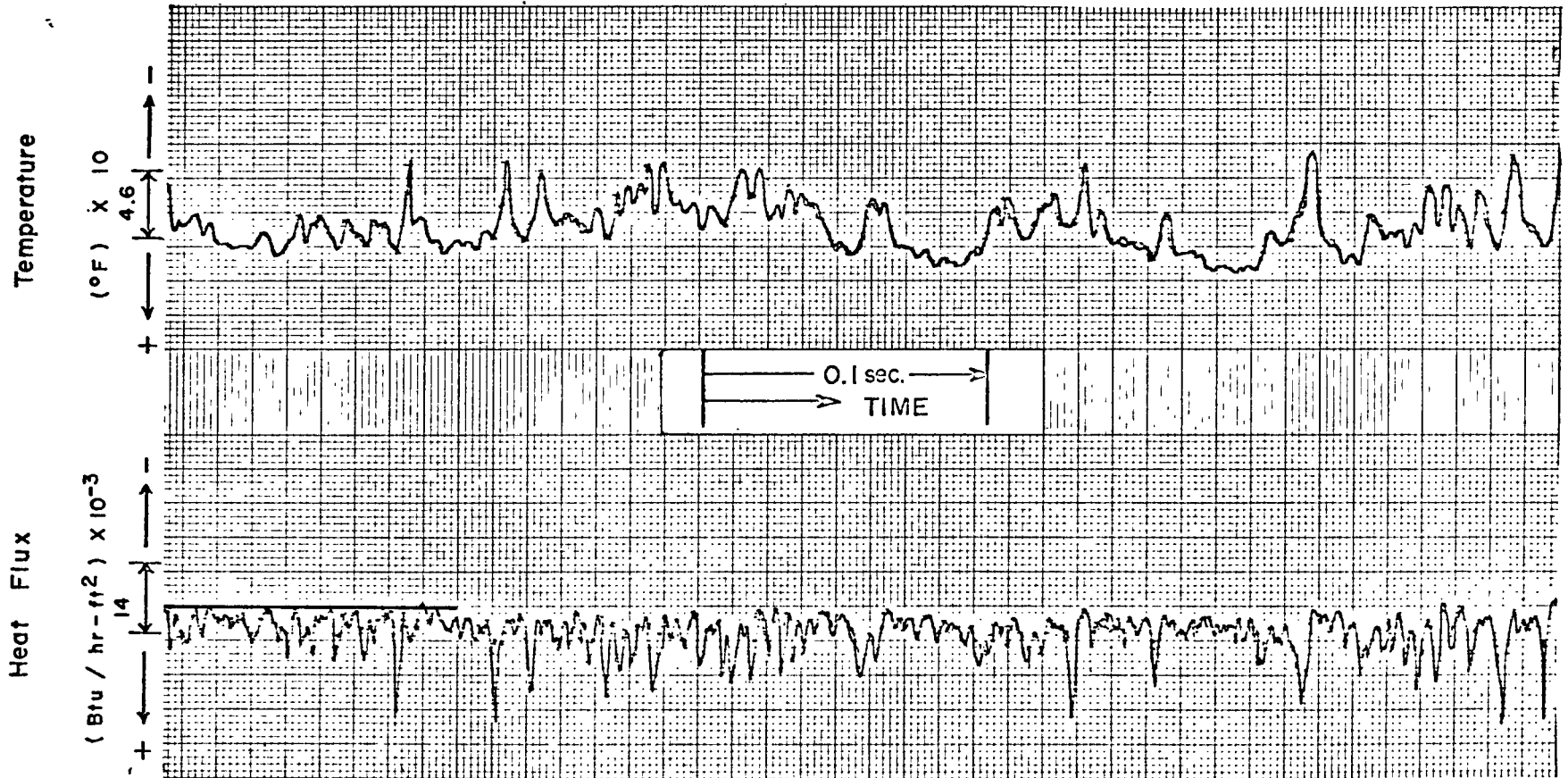
Run No. 25

Surface Thermocouple No. 3

$$\bar{q} = 12.5 \times 10^3 \text{ Btu/hr-ft}^2$$

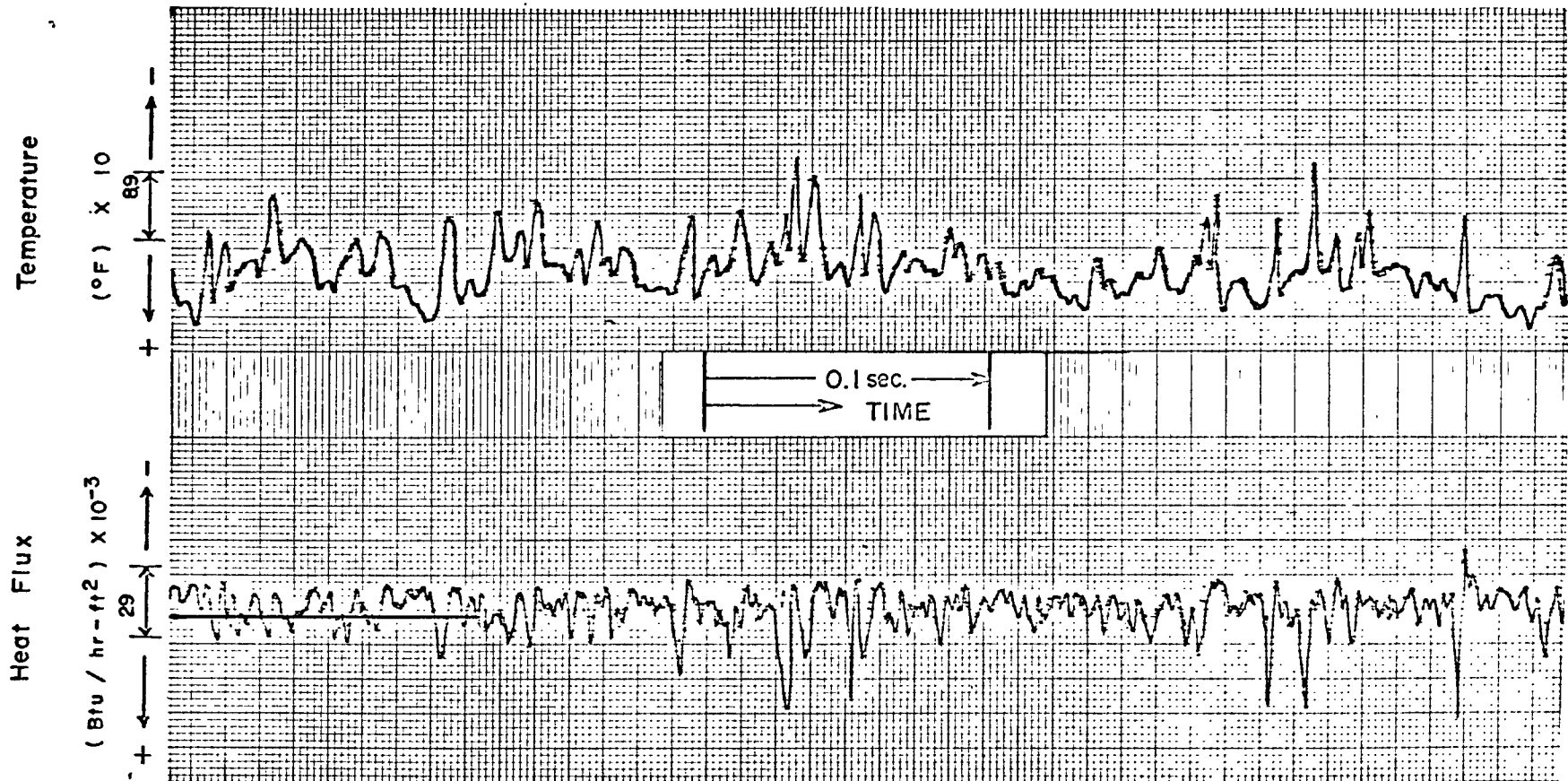
FIGURE 6-12 x

Instantaneous Surface Temperature
and Heat Flux Records



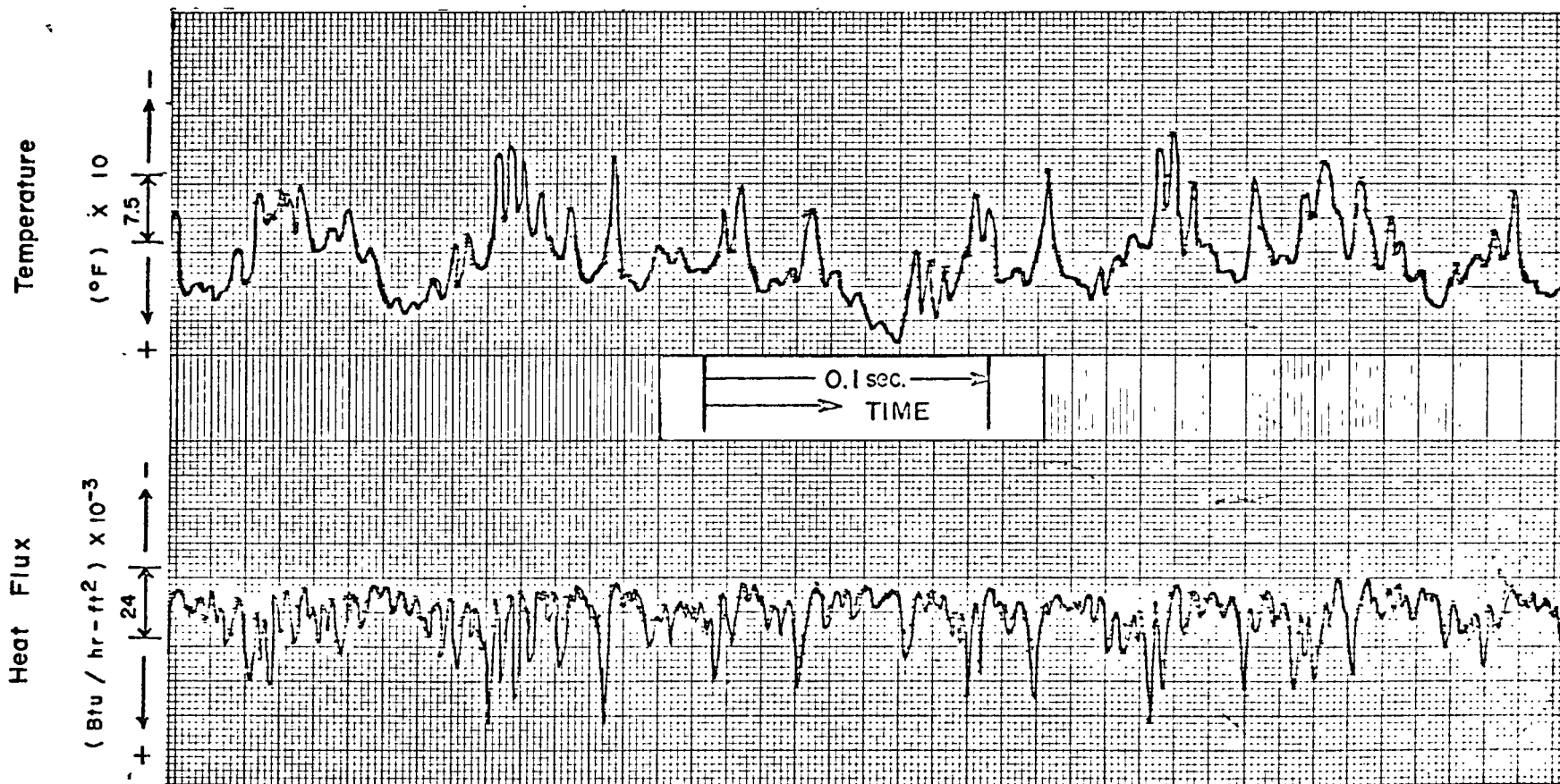
Run No. 19
Surface Thermocouple No. 3
 $\bar{q} = 14.9 \times 10^3 \text{ Btu/hr-ft}^2$

FIGURE 6-12 y
Instantaneous Surface Temperature
and Heat Flux Records



Run No. 20
Surface Thermocouple No. 3
 $\bar{q} = 18.0 \times 10^3 \text{ Btu/hr-ft}^2$

FIGURE 6-12 z
Instantaneous Surface Temperature
and Heat Flux Records



Run No. 14
Surface Thermocouple No. 3
 $\bar{q} = 18.2 \times 10^3 \text{ Btu/hr-ft}^2$

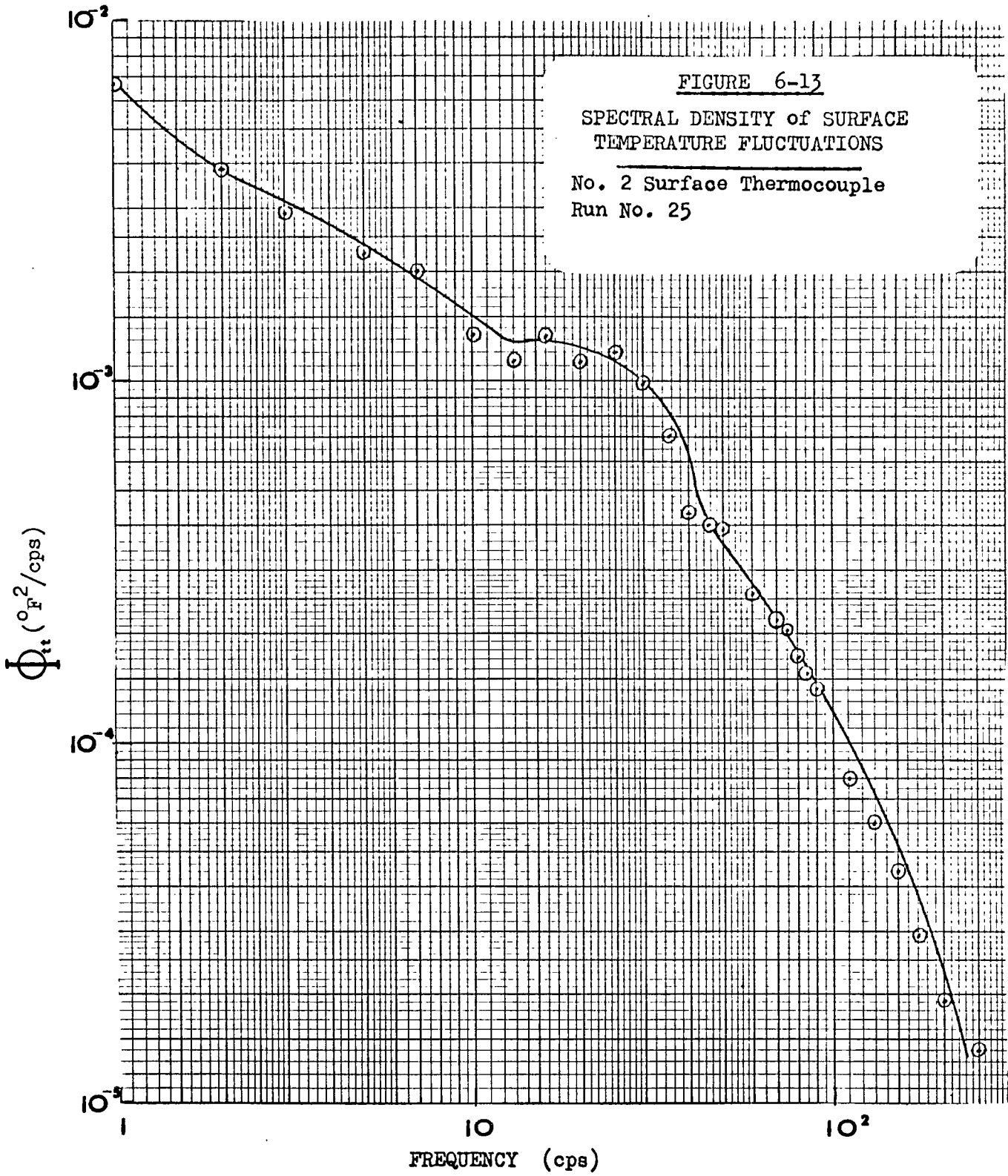
C. SPECTRAL DENSITIES AND AVERAGE VALUES OF THE FLUCTUATIONS

The records of instantaneous heat flux that were presented in the last section are very valuable for providing qualitative insights into the mechanisms of film boiling. However, it is difficult to characterize the heat transfer situation with such records because of the random nature of the fluctuations. Therefore, more detailed statistical information was obtained by analyzing the tape recordings of the instantaneous surface temperature on the Weston-Boonshaft and Fuchs Waveform Analyzer. The results of these analyses will be presented in this section.

The spectral density of the surface temperature fluctuations were typically as shown in Figure 6-13, which emphasizes the random nature of these fluctuations. Of more immediate interest is the cross-spectral density of the signals from two surface thermocouples. If the cross-spectral density has values other than zero, this would be an indication that disturbances are propagated from one measuring station to the next. It would also provide a means of calculating the propagation velocity, c :

$$c = \frac{2\pi fL}{\theta}$$

where f is the frequency of the fluctuation, L is the distance between measuring stations and θ is the measured phase angle in radians between the two signals. Telles (T-2) used this technique to measure the propagation velocity of waves on the surface of a falling liquid film. In this film boiling study, however, there was no indication of cross-correlation



between any pair of signals from the three surface thermocouples. It is concluded, therefore, that the interfacial disturbances are not propagated over distances as large as the surface thermocouple spacing, the minimum of which was five inches.

The explanation for this unexpected result is probably connected with the boundary-layer type development of the vapor film. A portion of the liquid making up the waves at one location is vaporized before the next location, and the basic identity of the wave may be destroyed. Also, the Reynolds number changes significantly from one thermocouple position to another. It is probable that the "preferred" wave frequency is a function of the Reynolds number. If this were the case, the frequency of the waves would be undergoing continual distortion as they propagated in the vertical direction, and the propagation velocity would then not be detectable with the method used.

The spectral density of the fluctuations in the surface heat flux was also determined for each run. In some instances, the spectral densities of the surface temperature and heat flux were measured simultaneously. To accomplish this, the thermocouple signal was directed both to the heat meter and to one channel of the wave form analyzer, while the heat meter output signal went to the other channel of the analyzer. As expected from equation 5-8, the heat flux signal led the temperature signal by a measured 45 (± 5) angular degrees for all frequencies. Also, the measured amplitude spectrum of the heat flux signal agreed within $\pm 10\%$ of the value that would be calculated from the amplitude spectrum of the temperature signal, according to the transfer function implied by equation D-41:

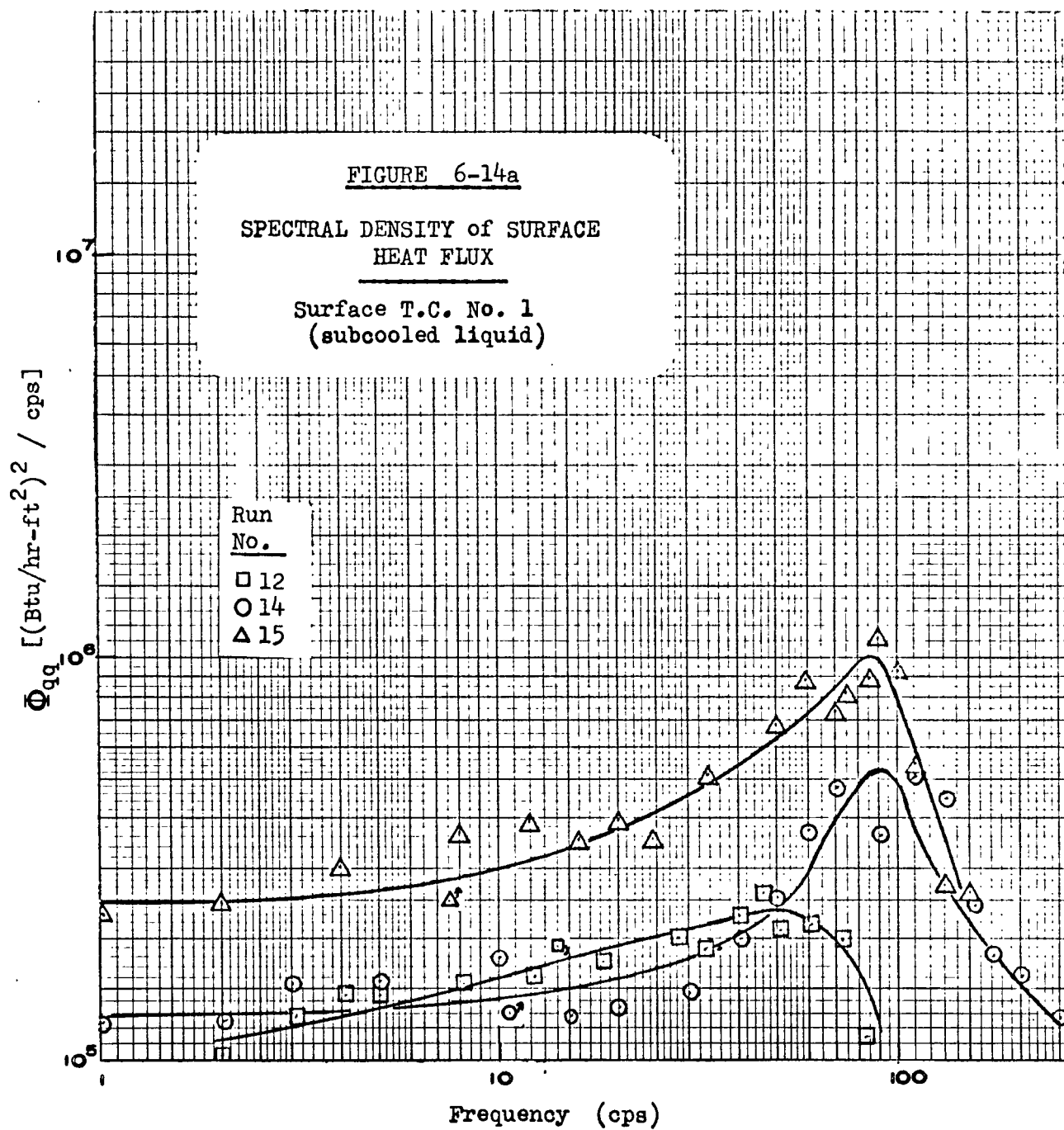
$$\Phi_{qq} = \Phi_{tt} \cdot \left(\frac{1}{2} W R_1 C_1 \right)$$

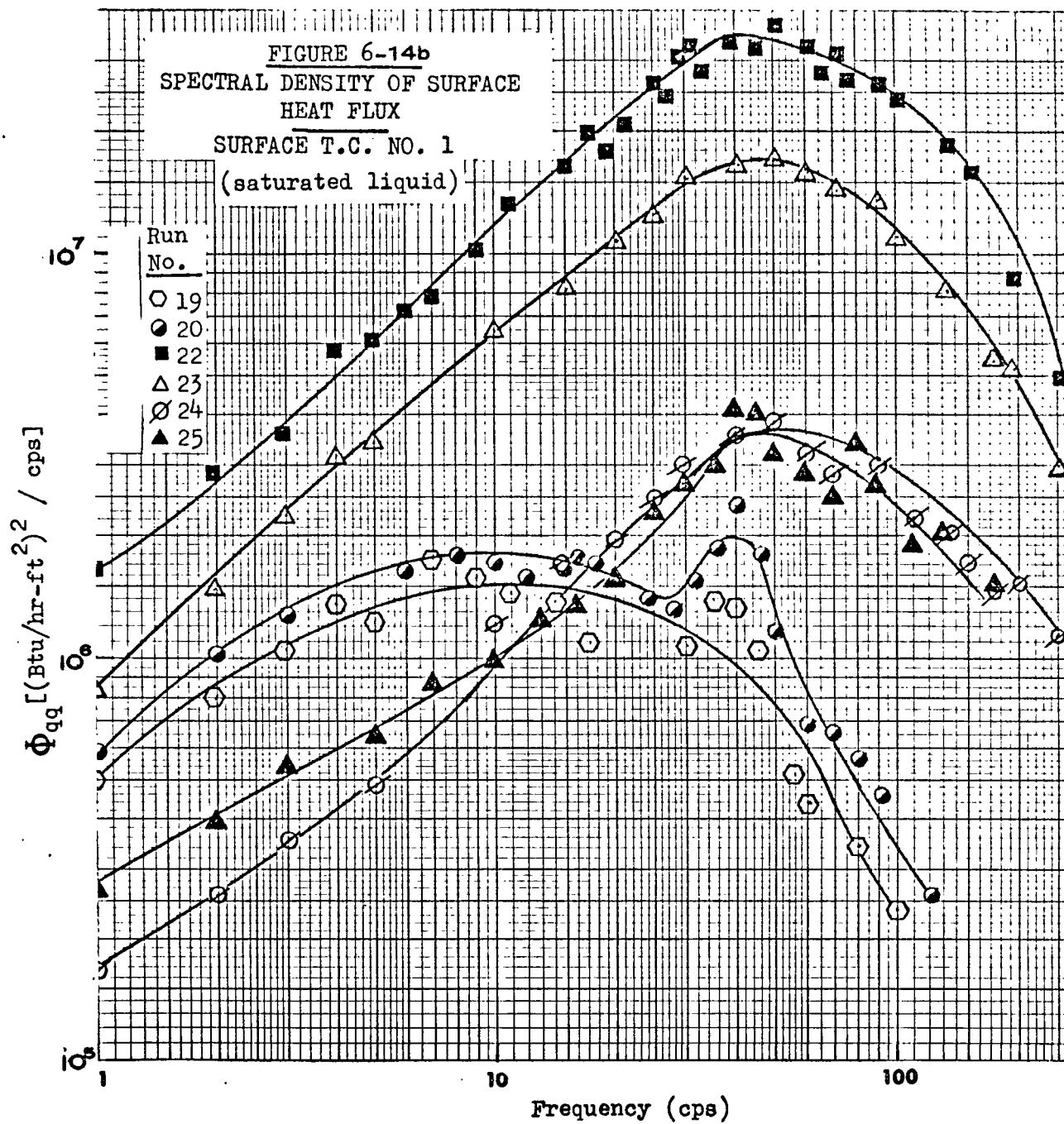
6-5

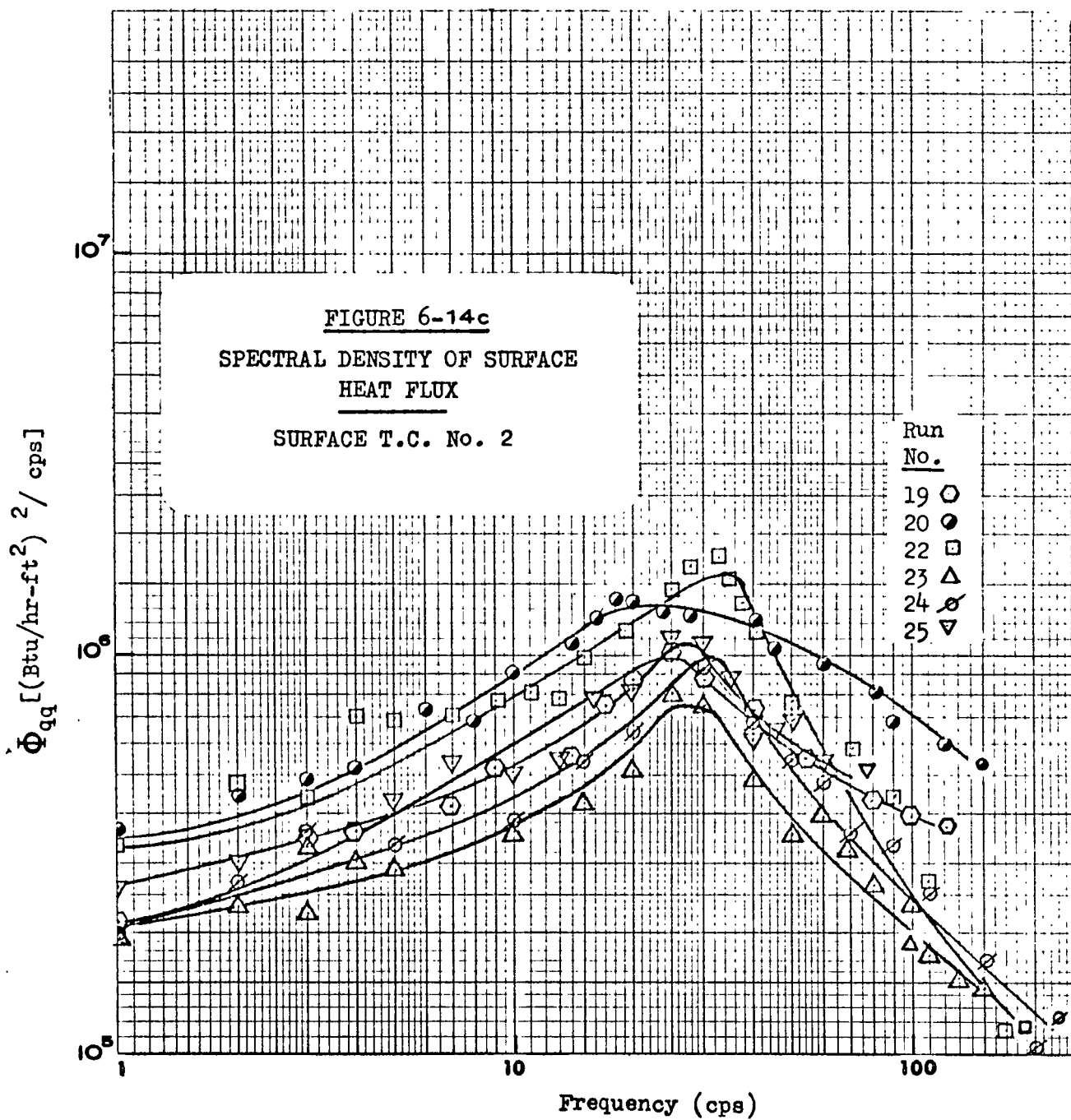
Upon verifying that this theoretical relationship existed experimentally, the spectral density of the heat flux signal for all the remaining runs was calculated from the measured spectral density of the temperature fluctuations. These results are presented in Figures 6-14a through 6-14d. The experimental conditions for these runs are summarized in Table 6-4. It can be seen that there is no overlapping of the Reynolds number values from one thermocouple position to the next.

A general characteristic of these curves is that disturbances exist over a broad frequency range between roughly 10 and 100 cps. The effect of subcooling is shown by the curves for No. 1 surface thermocouple for runs 12, 14 and 15 in Figure 6-14a. The intensity of the spectra is less than for the other runs at about the same Reynolds numbers, and the peak frequency appears to be generally higher as though subcooling caused a general suppressing of the waves but suppressed the low frequency waves to a greater extent. The peak values are concentrated between 60 and 110 cps for runs 14 and 15 and between 20 and 60 cps for run 12. For these subcooled situations, the intensity of the disturbances increases with heat flux. This same trend was shown for these runs by the peak values of the instantaneous signal which were summarized in Table 6-3.

The bulk liquid was saturated at the No. 1 surface thermocouple for all the other runs. The spectra for these are shown in Figure 6-14b. For runs 22 through 25 during which liquid occasionally touched the wall,







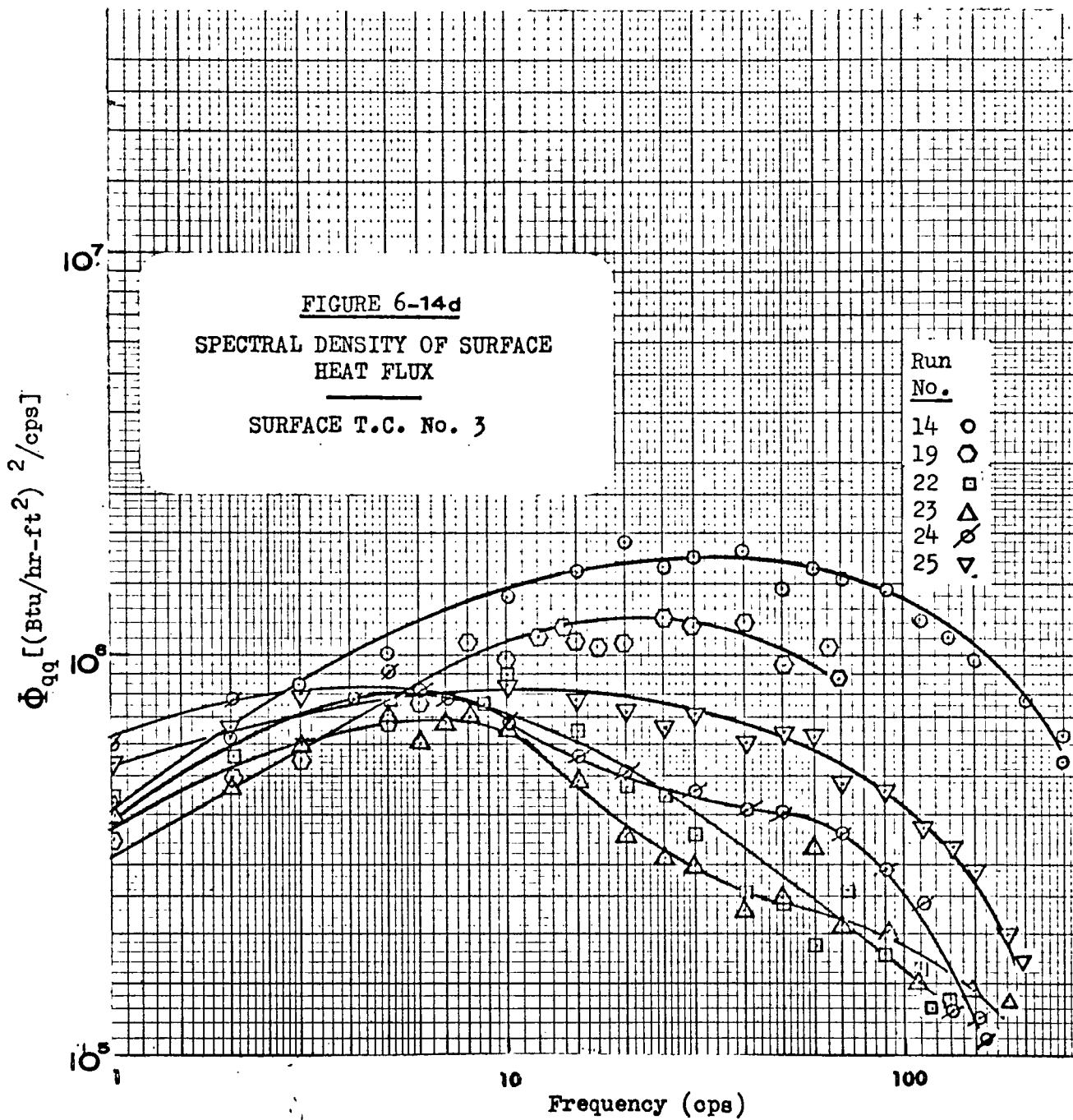


TABLE 6 - 4

RMS Average of the Fluctuating Component of the
Surface Heat Flux

Sur. T.C.	Run No.	Re No.	$\bar{q} \times 10^{-3}$ (Btu/hr-ft ²)	$q'(\text{RMS}) \times 10^{-3}$ (Btu/hr-ft ²)	ΔT (°F)
1	13*	770	12.3	4.9	256
	12*	780	12.4	5.0	262
	14*	900	18.2	8.8	363
	15*	980	22.3	11.4	472
	22	670	8.6	65.0	156
	23	710	9.4	46.9	179
	24	780	10.9	23.7	220
	25	840	12.5	24.2	256
	19	900	14.9	11.9	324
	20	990	18.0	14.1	388
2	22	3740	8.6	10.9	186
	23	3950	9.4	8.3	211
	17	3920	9.5	8.6	214
	24	4280	10.9	9.6	256
	13	4180	12.3	11.4	305
	12	4280	12.4	11.4	307
	25	4620	12.5	10.6	297
	19	880	14.9	10.9	374
	20	5350	18.0	15.2	444
	3	22	7520	8.6	7.5
23		7910	9.4	7.6	220
17		7760	9.5	8.6	231
24		8540	10.9	9.2	268
13		8260	12.3	8.2	324
12		8460	12.4	8.6	327
25		9170	12.5	10.7	312
19		9590	14.9	17.2	398
20		10400	18.0	18.2	475
14		9110	18.2	18.7	492

* Bulk liquid opposite No. 1 surface thermocouple was subcooled.

the magnitudes of the spectral densities were relatively high and decreased with increasing heat flux. This trend is opposite to the trend at the other thermocouple positions, and follows from the reduced heat flow during a period of liquid-solid contact as the average heat flux increases. This is discussed further in Section E of this chapter. Peak values in the spectra for these runs were found in the range of 40 to 60 cps. Runs 19 and 20, which had a higher time average heat flux and no liquid-solid contact, have spectral density curves that are more similar to the curves for the upper thermocouple positions.

The spectra of the signals from No. 2 surface thermocouple are shown in Figure 6-14c. Saturated bulk liquid prevailed in each case. These spectra are generally more uniform from run to run than the spectra for the lower thermocouple position, and their magnitude generally increases with increasing heat flux. Peak values are reached between 15 and 35 cps. The fluctuations in heat flux at the No. 3 surface thermocouple exhibit a somewhat different behavior as shown in Figure 6-14d. These curves are much flatter than the others and do not possess well defined peaks. The range of maximum values is from about 5 to 70 cps. An increasing heat flux generally meant an increasing spectral intensity. Hsu and Westwater (H-6) measured the frequency of the interfacial oscillations in film boiling from high-speed motion pictures taken of nitrogen, argon and methanol. They reported frequencies in the range of 20 to 60 cps. These values correspond reasonably well to the dominant frequencies indicated here by the spectral density curves.

The mean square average, Ψ_{qq} , of the fluctuating heat flux signal

was also determined. This quantity is the integral of the spectral density function with respect to frequency:

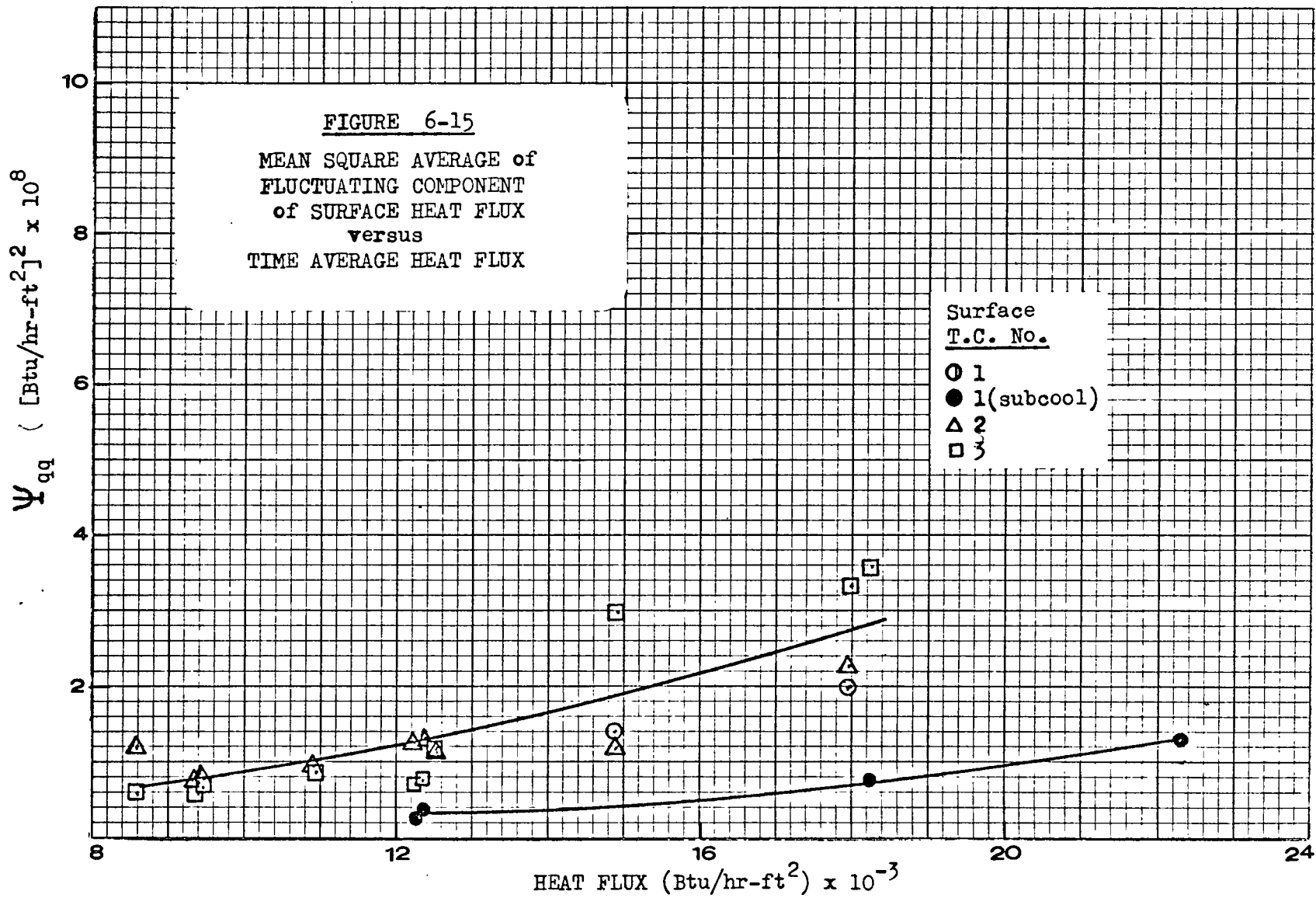
$$\Psi_{qq} = \int_0^{\infty} \Phi_{qq}(f) df$$

The integration was performed by the wave form analyzer over a frequency range of essentially 0.01 to 200 cps. These limits include all but a negligible fraction of the signal.

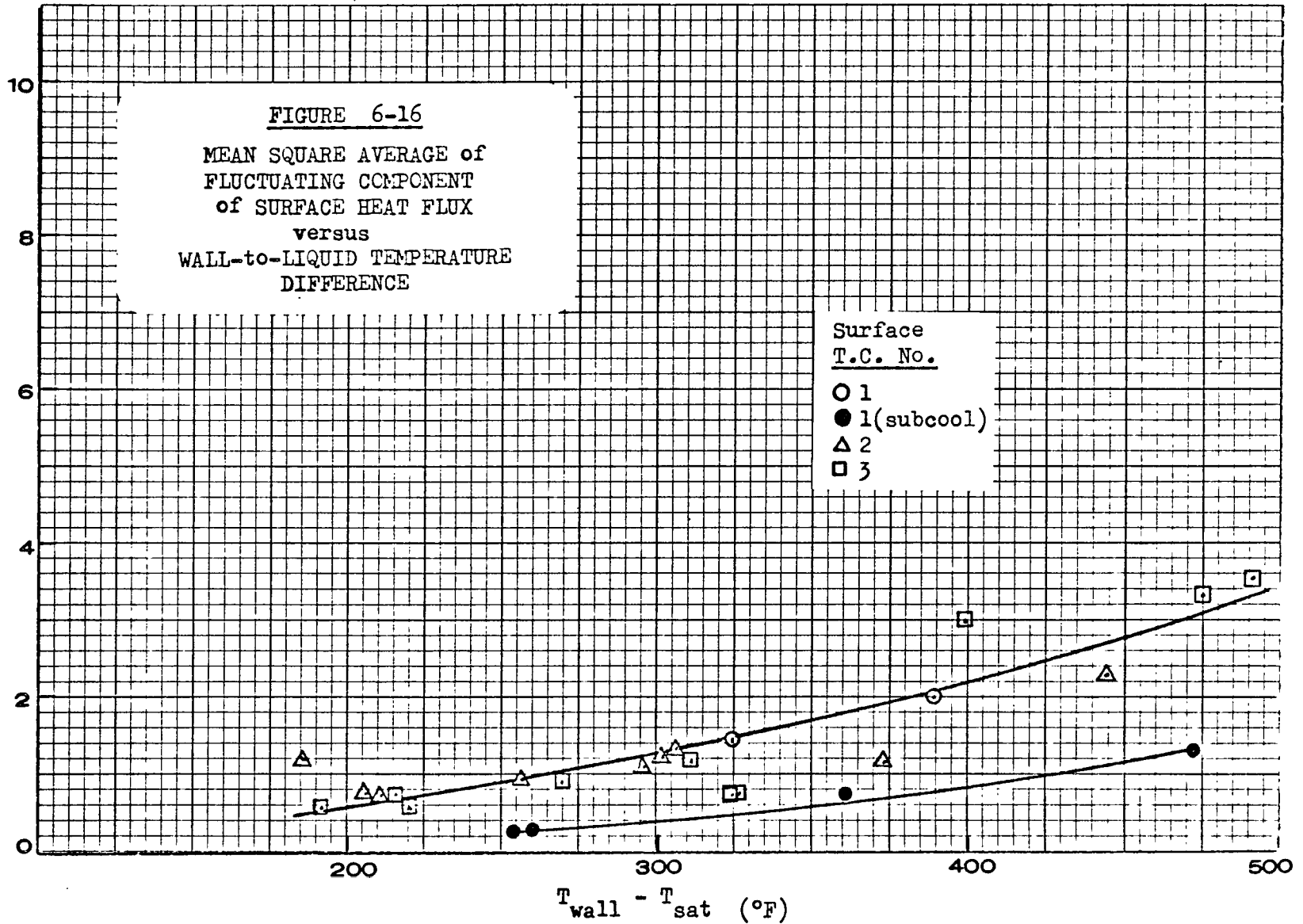
The root mean square averages ($\sqrt{\Psi_{qq}}$) are included in Table 6-4. In addition, Ψ_{qq} is plotted on Figures 6-15 to 6-17 as a function of the time average heat flux, the local wall to liquid temperature difference, and the local vapor film Reynolds number, respectively. The thermocouple position corresponding to each data point is indicated on the graphs and those points for which the subcooling effect was significant are shaded.

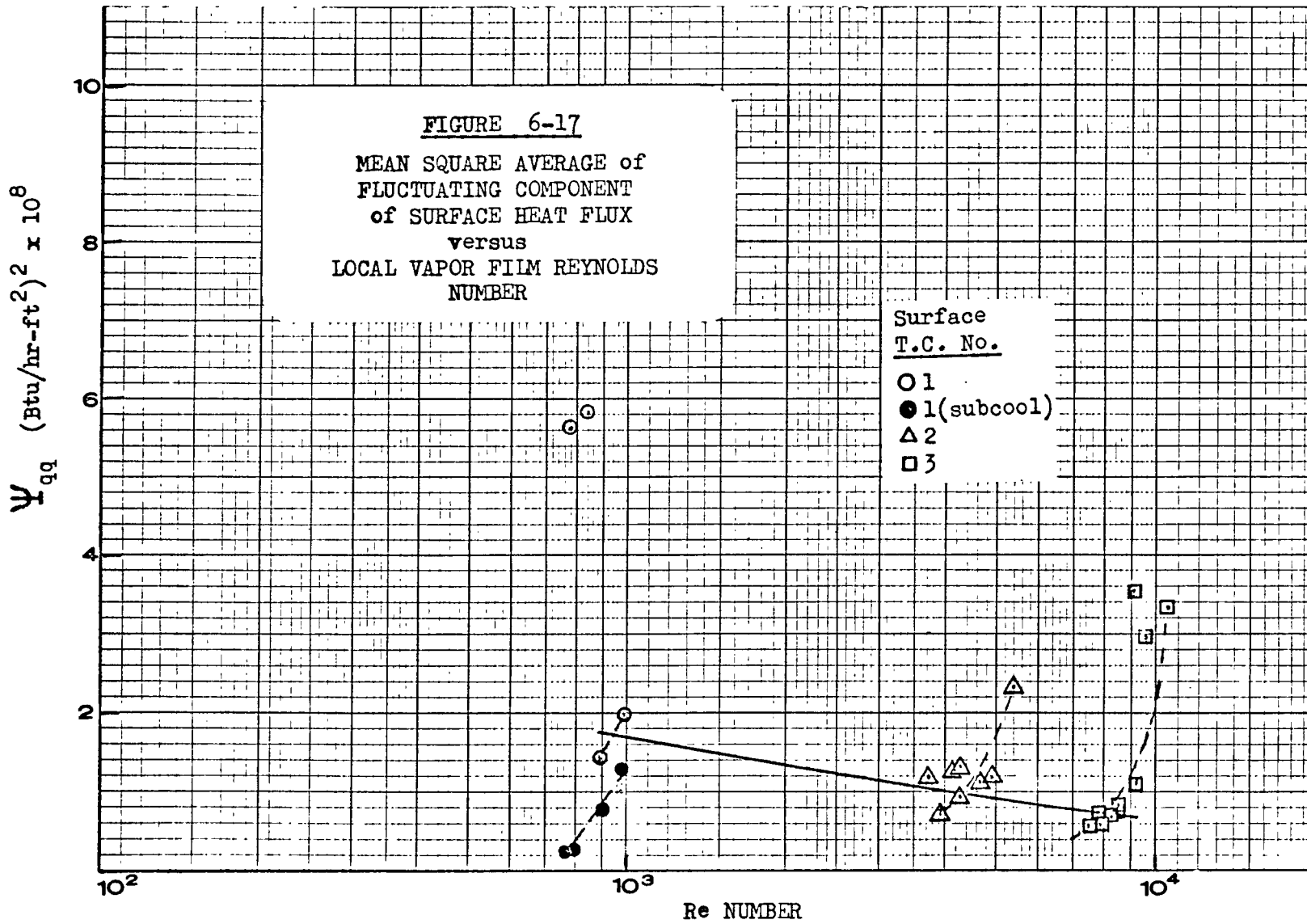
Figures 6-15 and 6-16 indicate that the average intensities of the heat flux fluctuations can be fairly well correlated by either the time average heat flux or the temperature difference. The four subcooled points lie on a curve of their own, while those points which include liquid-solid contact appear unrelated to the others. With a few exceptions, the other points appear to be reasonably close to a single curve.

Figure 6-17 indicates that Ψ_{qq} generally decreases as the Reynolds number is greatly increased from one thermocouple position to the next. Within the narrow range of Reynolds numbers at a single position, however, the effect of heat flux on Ψ_{qq} is clearly shown by the spread of the



Ψ_{qq} (Btu/hr-ft²)² x 10⁸





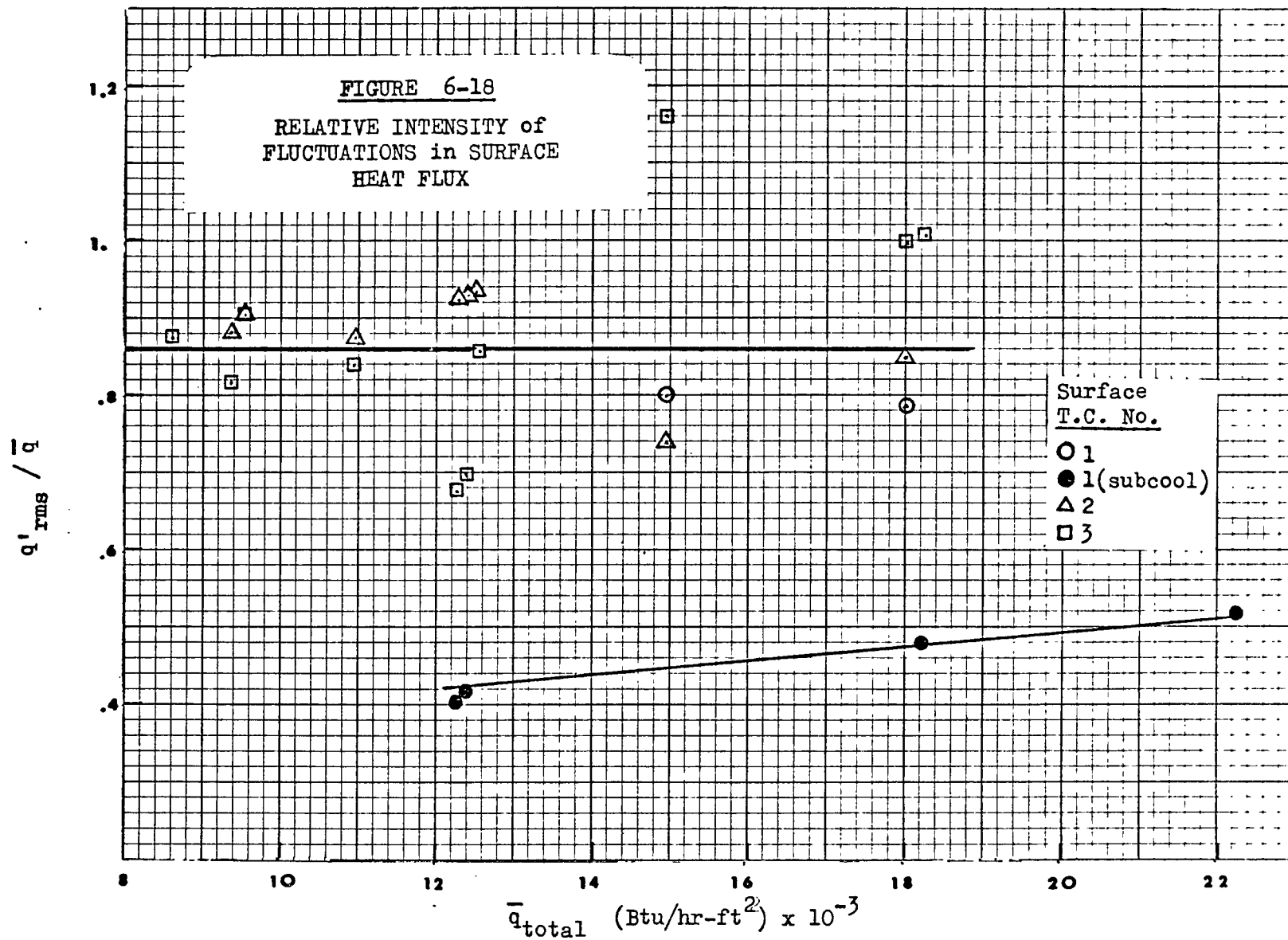
points and is indicated by the dashed curves. The four data points for subcooled liquid at the No. 1 surface thermocouple position show the effect of heat flux, but there are not enough subcooled data to show the long range Reynolds number effect.

The decreasing intensity of the fluctuating heat flux for higher Reynolds numbers was as anticipated. It appears reasonable that the larger shear stresses that correspond to higher Reynolds numbers would tend to smooth out the interface and thereby reduce the fluctuations in heat flux. The increase in Ψ_{qs} with increasing time average heat flux implies larger interfacial waves at these conditions. This result was not expected. It was felt that the hot surface that occurs with large values of the heat flux would be a large reservoir of energy. Thus, it should be able to release large amounts of energy rapidly and repel the approaching interface relatively easily. This apparently was not the case. Some additional insight is provided by Figure 6-18 where the ratio of the intensity of the fluctuations to the time average heat flux is presented as a function of the average heat flux. Regression analysis showed that the best curve through these points was an almost horizontal straight line with a value of about 0.86. The standard deviation of the points from this line was only 8%, and all but six points fell within $\pm 15\%$ of the line.

D. WAVE SHAPE AND AMPLITUDE

1. A Sinusoidal Interface

The intensity of the fluctuations in surface heat flux that were reported in the previous section will now be used to calculate



the nature of the interfacial oscillations according to the discussion of Section D, Chapter IV. This requires that the wave shape be postulated, and two possible wave shapes will be pursued here. In the first instance, it will be assumed that the waves are sinusoidal and given by the following equation:

$$\eta = \mathcal{N}_0 \sin(\omega t - kx)$$

where η , defined by equation 4-32, represents the deviation of the interface from its time average position, and \mathcal{N}_0 is the ratio of the wave amplitude to p_s , the quasi-steady state film thickness. From equations 4-47 and 4-50:

$$\mathcal{N}_0 = \sqrt{\frac{1}{\left[1 + \left(\frac{H_{rms}}{\bar{h}}\right)^2\right]^2}} \quad 6-6$$

Also, from equations 4-35 and 6-6:

$$\frac{\bar{h}}{h_s} = 1 + \left(\frac{H_{rms}}{\bar{h}}\right)^2 \quad 6-7$$

The value of \bar{h} is the experimentally measured time-average convective heat transfer coefficient which is listed as HCONV in Table 6-2. H_{rms} is calculated from the equation:

$$H_{rms} = \frac{\sqrt{\Psi_{99}}}{\Delta T}$$

where $\sqrt{\Psi_{99}}$ is the experimentally measured rms value of the fluctuations listed in Table 6-4 and ΔT is the time-average surface to fluid temperature difference listed in the same Table.

Values of n_o and $\frac{\bar{h}}{h_s}$ calculated by equations 6-6 and 6-7 are given in Table 6-5. These results are presented graphically in Figure 6-19. Except for the runs with subcooled liquid or with liquid-solid contact, n_o and $\frac{\bar{h}}{h_s}$ were essentially constant with values of 0.83 and 1.6, respectively. It is interesting to note that n_o is about one for those runs with liquid-solid contact. For the subcooled runs, n_o and $\frac{\bar{h}}{h_s}$ both increase with heat flux, with n_o being in the range of 0.5 to 0.7. In general, the values of n_o may be too large to be consistent with the assumptions given in Chapter IV when the unsteady state theory was being rationalized. With this limitation in mind, the results will be carried forward to provide an approximate indication of the quantitative wave effects.

The effect of a sinusoidal interface on the CC number will be calculated next. The experimental CC numbers in Figures 6-8 to 6-11 are time average values based on \bar{h} and will be designated by \overline{CC} from this point. On the other hand, the theoretical curves in these same figures represent the CC numbers that are predicted by the quasi-steady state theory based on h_s . They will be called CC_s in this discussion. A general theoretical approach would include n_o as a parameter so that \overline{CC} could be calcu-

TABLE 6 - 5

Relative Wave Amplitude and Heat Transfer Coefficient Correction Factor
for Sinusoidal Waves

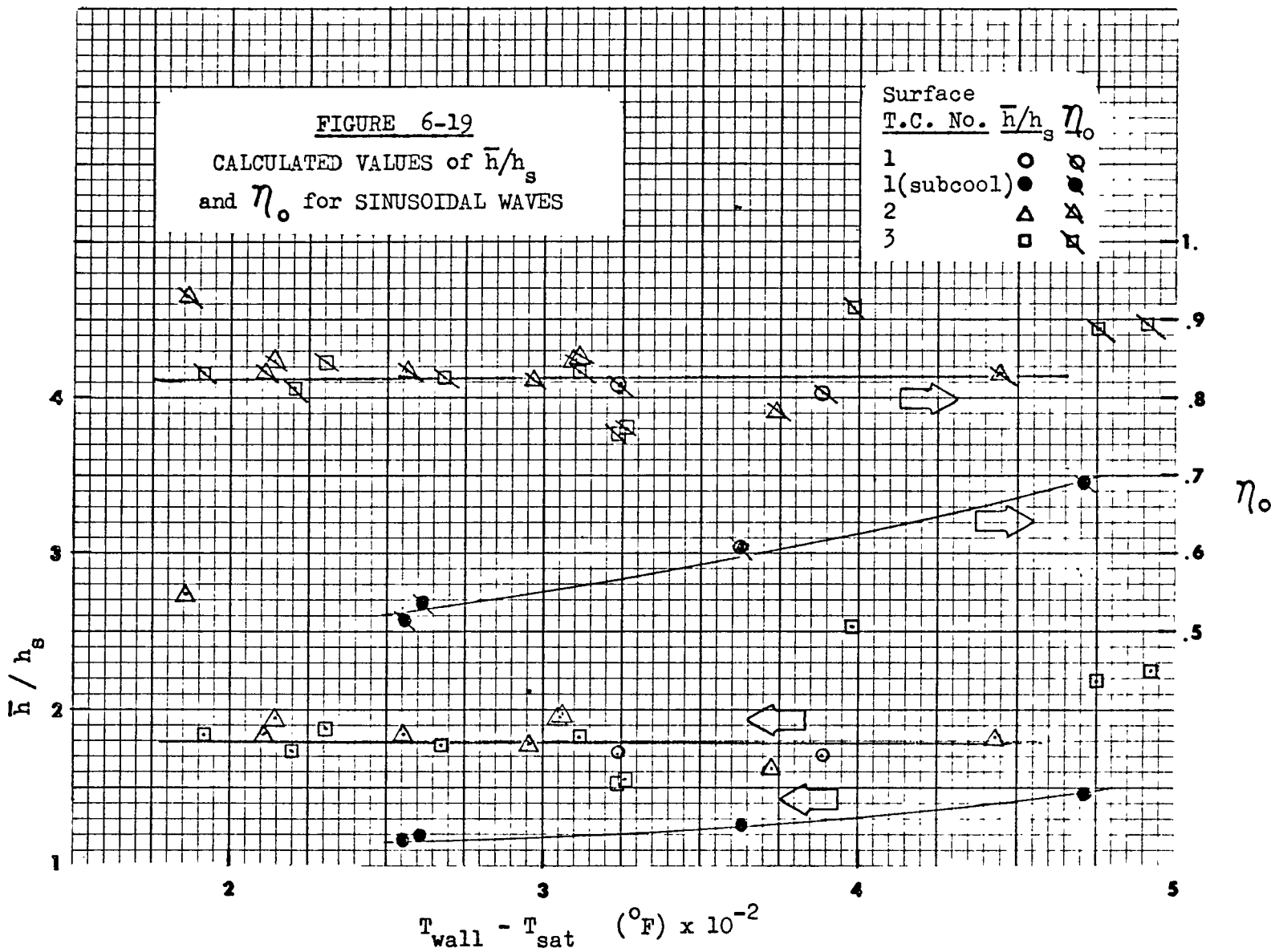
Surface T.C.No.	Run No.	(\bar{q}/A) (Btu/hr-ft ²)	Re	$\frac{\bar{h}}{h_s}$	N_o	\bar{CC}	CC_s
1	13 ¹	12280	770	1.17	.51	4.08	4.77
	12 ¹	12350	780	1.18	.53	4.13	4.87
	14 ¹	18200	900	1.26	.60	4.15	5.21
	15 ¹	22300	980	1.39	.69	4.66	6.48
	22 ²	8600	670	61.0	.99	3.30	203.
	23 ²	9370	710	27.0	.99	3.55	98.
	24 ²	10900	780	6.0	.98	3.84	23.
	25 ²	12500	840	4.9	.98	3.97	20.
	19	14900	900	1.70	.82	4.53	7.73
	20	18000	990	1.68	.80	4.61	7.77
2	22	8600	3740	2.72	.93	4.02	10.9
	23	9370	3950	1.83	.84	4.30	7.86
	17	9460	3920	1.90	.85	4.28	8.11
	24	10900	4280	1.84	.84	4.62	8.50
	13	12280	4180	1.94	.86	5.05	9.83
	12	12350	4280	1.95	.86	5.02	9.76
	25	12500	4620	1.79	.82	4.77	8.50
	19	14900	4880	1.61	.78	5.44	8.74
	20	18000	5350	1.82	.83	5.50	10.0
	3	22	8600	7520	1.82	.83	4.19
23		9370	7910	1.72	.81	4.51	7.78
17		9460	7760	1.89	.84	4.68	8.85
24		10900	8540	1.78	.82	4.87	8.50
13		12280	8260	1.51	.74	5.46	8.24
12		12350	8460	1.54	.76	5.44	8.35
25		12500	9170	1.81	.83	5.07	9.20
19		14900	9590	2.52	.92	5.89	14.8
20		18000	10430	2.19	.89	6.02	13.2
14		18200	9110	2.25	.90	6.20	14.0

¹ Runs affected by subcooled liquid

² Runs with liquid-solid contact

FIGURE 6-19
 CALCULATED VALUES of \bar{h}/h_s
 and η_o for SINUSOIDAL WAVES

Surface T.C. No.	\bar{h}/h_s	η_o
1	○	○
1(subcool)	●	●
2	△	△
3	□	□



lated from the theoretical value of CC_s . However, since the wave shape and the roughness parameter are not known, an alternate approach will be more convenient here. The experimental value of \overline{CC} will be converted to the value of CC_s that would have been predicted for the same Reynolds number had there been no waves. The conversion factor follows from the definitions:

$$CC_s = \frac{k}{h_s} \left[\frac{g\rho(\eta_{sp} - \rho)}{\mu^2} \right]^{1/3} = \overline{CC} \left(\frac{\bar{h}}{h_s} \right) \quad 6-8$$

These results are also included in Table 6-5.

The results of this analysis are presented in Figure 6-20 where CC numbers from the three surface thermocouples are plotted, together with the theoretical curves from the quasi-steady state theory. The values of \overline{CC} (which were calculated directly from experimental data without consideration of the effects of the large waves) are indicated by the open symbols. As was discussed in Section A of this chapter, the values of ϵ/ν that would be required to reconcile these \overline{CC} numbers with the steady state theory are too high to be reasonable. The values of CC_s which were calculated from the data using a model of sinusoidal waves are indicated by the symbols containing a diagonal line. These compare very favorably with the steady state theory, and most of the CC_s points can be correlated by the relatively small ϵ/ν values of zero to five. The irregular closed curves on Figure 6-20 indicate the range of data taken by Dougall and Rohsenow (D-5). Their data will be discussed in more detail in Section H, but it was included here because their process was probably relatively free of large amplitude waves. It can be seen that

FIGURE 6-20

CC NUMBER vs. RE NUMBER

(○, Δ, □): experimental points from surface thermocouples.
(◐, ◑, ◒): corrected values based on sinusoidal waves.
shaded areas: data range of (D-5)

Surface
T.C. No.

- 1
- 1(subcool)
- △ 2
- 3

CC NUMBER

16

12

8

4

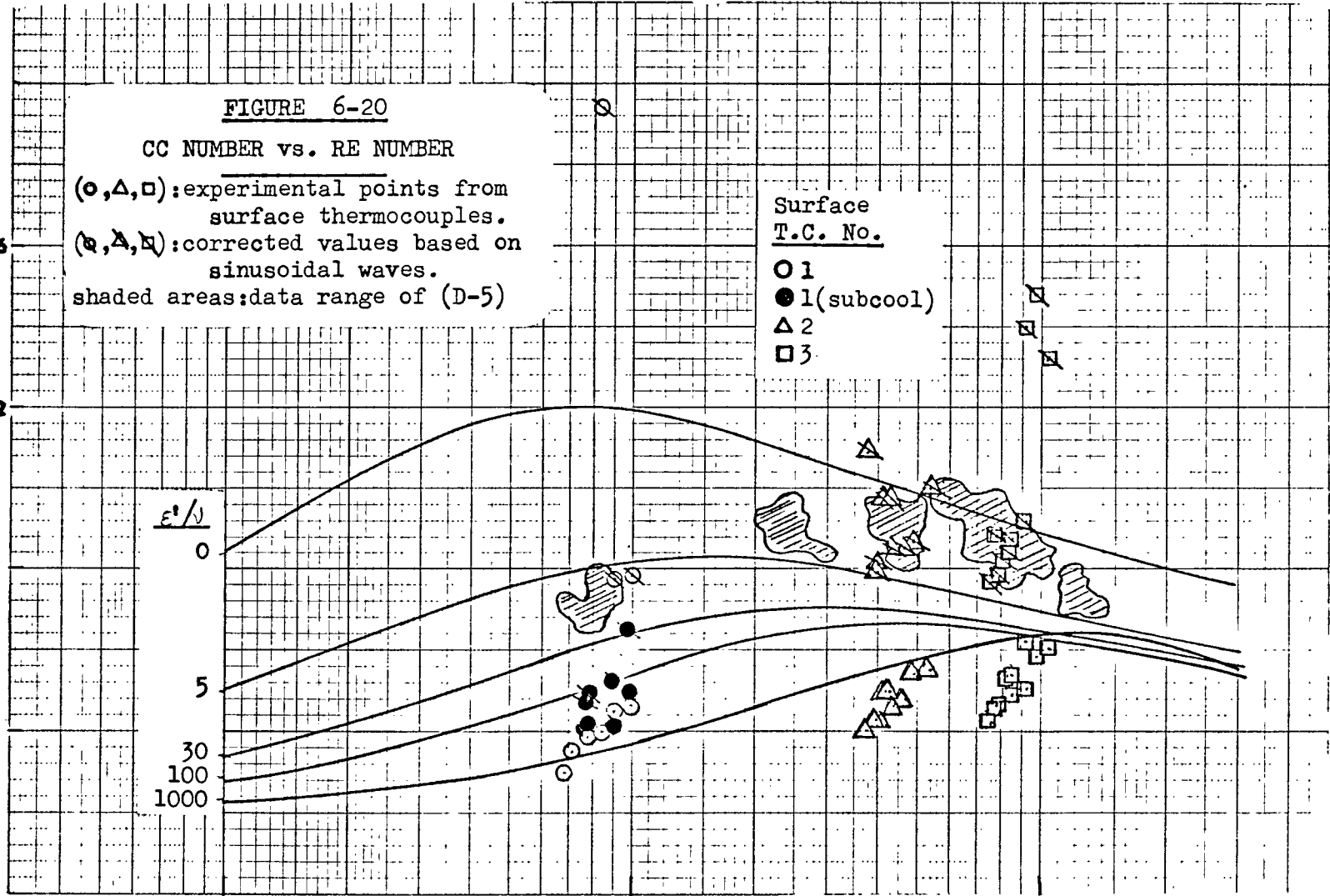
ϵ' / λ
0
5
30
100
1000

10^2

10^3

10^4

RE NUMBER



the CC_s values, which do not reflect the effects of the large waves, compare well with the data of Dougall and Rohsenow. These results strongly support the premise of this dissertation that two mechanisms determine the heat transfer coefficient. The normal turbulent transport of energy through the vapor film is increased because of the oscillations within the film that result from interfacial motion.

Three groups of corrected data points appear unusual in Figure 6-20 and Table 6-5. The CC_s values are very large for those runs where liquid touched the wall. This condition is outside the realm of a stable film boiling theory, however, and other methods are required to correlate these data points. The four points that fall above the curve for zero ϵ/ν possessed very large values of $\sqrt{\Psi_{qs}/q}$. It may be that the sinusoidal interface is not a good assumption for these circumstances and another assumption will be explored later. Finally, the four points representing subcooled liquid at No. 1 surface thermocouple also appear out of line. In Figures 6-8 through 6-11, their \overline{CC} values were consistent with other data points at the same Reynolds numbers, even though the interfacial activity was relatively small for these subcooled runs. In Figure 6-20, however, the CC_s values for these points are much less than others at similar Reynolds numbers. This behavior is unexpected since the theory implies that the CC_s value is hydrodynamically determined by only the Reynolds number, and that the effect of a subcooled liquid can only enter through the interfacial waves. Thus, when the waves are small, the \overline{CC} value should be relatively large. The explanation may be that the Reynolds number is greatly overstated for these points. In calculating the Reynolds number for the subcooled runs, it had been assumed that the energy

required to heat the liquid to the saturation temperature was uniformly removed from the heater over its entire two-foot long surface. If, in fact, a large proportion of this energy came from the lower part of the heater surface, the actual mass of vapor generated in this region would be less than was calculated. Therefore, the actual Reynolds numbers would be smaller than the calculated values for the lower thermocouple position. This was probably the case since the bulk liquid always reached the saturation temperature within 3 inches of the bottom of the heater (12% of the surface area), while the sensible heating of the liquid required about 7% of the total energy transferred. (This uncertainty, however, would have a negligible effect for the thermocouple positions farther up the heater wall.) While it is not possible to resolve this question quantitatively, it should be realized that the Reynolds numbers for the four subcooled runs may well be less than a hundred (instead of 600 to 1,000), in which case the CC_s numbers would fall within a range of zero to five for the roughness parameter.

It is clear from the traces of the instantaneous surface temperature and heat flux in Figures 6-12a to 6-12z that the interfacial disturbances are neither regular nor sinusoidal. However, it will be informative to compare the measured peak heat flux values with the peak values that would be expected with sinusoidal waves having amplitudes as calculated in this section. The theoretical instantaneous heat transfer coefficient is given by equation 4-30:

$$\frac{h}{h_s} = \frac{p_s}{\bar{p}}$$

The amplitude of the sinusoidal wave is $\mathcal{N}_0 p_s$, according to the definition of \mathcal{N}_0 . The minimum and maximum distances of the interface from the heated surface would then be:

$$p_{min} = p_s - \mathcal{N}_0 p_s \quad 6-9$$

$$p_{max} = p_s + \mathcal{N}_0 p_s \quad 6-10$$

The corresponding extreme values of h consistent with this wave shape are:

$$\frac{h_{max}}{h} = \frac{h_s}{h} \cdot \frac{p_s}{p_{min}} = \frac{h_s}{h} \cdot (1 - \mathcal{N}_0)^{-1} \quad 6-11$$

$$\frac{h_{min}}{h} = \frac{h_s}{h} \cdot \frac{p_s}{p_{max}} = \frac{h_s}{h} \cdot (1 + \mathcal{N}_0)^{-1} \quad 6-12$$

The instantaneous heat flux, q , is essentially proportional to the heat transfer coefficient since the changes in surface temperature are small.

Therefore:

$$\frac{q_{max}}{q} = \frac{h_{max}}{h} \quad 6-13$$

$$\frac{q_{min}}{q} = \frac{h_{min}}{h} \quad 6-14$$

The minimum and maximum values of the instantaneous heat flux can be written as:

$$q_{max} = \bar{q} + q'_{(+)\max} \quad 6-15$$

$$q_{min} = \bar{q} - q'_{(-)\max} \quad 6-16$$

where the prime superscripts indicate the fluctuating components and the (+) and (-) subscripts indicate positive and negative going fluctuations, respectively. Thus, the theoretical relative peak values of heat flux are given by:

$$\frac{q'_{(+)\max}}{\bar{q}} = \frac{h_s}{h} \cdot (1 - \mathcal{N}_0)^{-1} - 1 \quad 6-17$$

$$\frac{q'_{(-)\max}}{\bar{q}} = 1 - \frac{h_s}{h} \cdot (1 + \mathcal{N}_0)^{-1} \quad 6-18$$

Calculated values of \mathcal{N}_0 and $\frac{\bar{h}}{h_s}$ and measured values of \bar{q} from Table 6-5 were used to predict $q'_{(+)\max}$ and $q'_{(-)\max}$ by the above equations. In Table 6-6, these predicted peak values are compared to the measured peak values of q' that were reported in Table 6-3. Neglecting the four points so indicated on the table, the measured positive peak values of q' agree with the predicted values within the limits of +49% and -57%, with a mean deviation of -10% and a standard deviation of 5%. The corresponding limits for the negative q' peaks are +56%

TABLE 6-6

Ratio of Predicted ¹ Peak Values in Instantaneous
Heat Flux for Sinusoidal Waves to Measured Peak Values

Surface Thermo- couple No.	Run No.	(Measured) / (Predicted) Values / Values	
		Positive Peaks	Negative Peaks
1	12 ²	.81	1.18
	14 ²	.76	.89
	15 ²	.54	.90
	22 ³	.23	10.2
	23 ³	.45	15.2
	24 ³	.84	4.35
	25 ³	.57	2.18
	19	1.05	.68
	20	1.01	.70
	2	22	.93
23		.90	1.01
17		1.01	1.56
24		.69	.71
12		.94	.77
25		1.04	.79
19		.95	.87
20		1.04	.68
3	22	1.49	1.10
	23	1.10	.63
	17	.81	.79
	24	.89	.90
	12	1.00	.92
	25	1.16	.94
	19	.46	1.04
	20	.43	.93
14	.81	1.03	

¹ Based on measured values of \bar{h} and H_{rms}

² Runs affected by subcooled liquid.

³ Data points that appear out of line because of liquid-solid contact.

and -37%, with a mean deviation of -6% and a standard deviation of 27%.

On the basis of these results, some tentative conclusions may be presented. A simple sinusoidal model of the interface leads to predicted peak values of the instantaneous heat flux that are reasonably close to measured values. The relative wave amplitude, η_0 , is very close to 0.8 over a wide range of heat flux values and Reynolds numbers. Using this value of η_0 and ϵ/ν values between zero and five leads to theoretical CC numbers that closely match experimental data for many of the test runs.

2. A Square-Pulse Type Interfacial Wave

The calculations of the last section will be repeated with the assumption that a pulse type wave as depicted in Figure 4-2, with the pulse having a constant amplitude, describes the interfacial behavior. It will be recalled from Section D of Chapter IV that experimental measurements of \bar{h} , H_{rms} and λ_b allows the calculation of $\frac{\bar{h}}{h_s}$, $\frac{\rho_p}{\rho_s}$ and $\frac{\rho_b}{\rho_s}$ for this case. The values of \bar{h} and H_{rms} that apply here are the same as those that were used to calculate η_0 and $\frac{\bar{h}}{h_s}$ for a sinusoidal interface. An experimental indication of the value of λ_b was found with the film thickness probe as described later in this Chapter. Based on limited measurements, λ_b was estimated to be 0.3.

Simultaneous solution of equations 4-42, 4-43, 4-50 and 4-51 leads to:

$$\frac{\rho_p}{\rho_s} = \frac{1}{1 - \lambda_b(1 - \beta)}$$

$$\frac{p_b}{p_s} = \beta \cdot \frac{p_p}{p_s} \quad 6-20$$

$$\frac{\bar{h}}{h_s} = \frac{1 - \lambda_b + \frac{\lambda_b}{\beta}}{\left(\frac{p_b}{p_s}\right)} \quad 6-21$$

where:

$$\beta = \frac{\lambda_b - \frac{\mathcal{H}}{1 + \mathcal{H}^2} \sqrt{\frac{\lambda_b}{1 - \lambda_b}}}{\lambda_b - \frac{\mathcal{H}^2}{(1 + \mathcal{H}^2)}} \quad 6-22$$

$$\mathcal{H} = \frac{H_{rms}}{\bar{h}} \quad 6-23$$

The results of the calculations are presented in Table 6-7. The ratio of $\frac{\bar{h}}{h_s}$ here represents the increase in the quasi-steady state heat transfer coefficient to be expected with square-pulse type interfacial waves. Multiplying the experimental \overline{CC} numbers by this ratio gives the corresponding values of CC_s , which are also included in Table 6-7.

These CC_s values are seen to be very nearly the same as the values for the sinusoidal waves which are plotted in Figure 6-20. Both sets of CC_s numbers have not been plotted there since many of the points would fall very close together and obscure the results. In order to bring the CC_s values for runs 14, 16 and 20 at No. 3 surface thermocouple below the values corresponding to $\epsilon/\nu = 0$, λ_b would have to be about 0.1 for these runs. This would indicate a wave pattern that was usually far

TABLE 6-7

Relative Wave Amplitudes and Heat Transfer Coefficients
for Square - Pulse Type Waves ¹

Surface T.C. No.	Run No. ²	$\frac{p_p}{p_s}$	$\frac{p_h}{p_s}$	$\frac{\bar{h}}{\bar{h}_s}$	\overline{CC}	\overline{CC}_s
1	13 ³	1.20	.539	1.14	4.08	4.66
	12 ³	1.21	.519	1.16	4.13	4.78
	14 ³	1.23	.465	1.22	4.15	5.04
	15 ³	1.22	.486	1.19	4.66	5.55
	19	1.32	.261	1.68	4.53	7.62
	20	1.31	.265	1.66	4.61	7.67
2	22	1.40	.066	5.02	4.02	20.1
	23	1.33	.225	1.86	4.30	7.80
	17	1.34	.208	1.96	4.28	8.39
	24	1.33	.223	1.87	4.62	8.64
	13	1.34	.197	2.05	5.05	10.3
	12	1.34	.196	2.05	5.02	10.3
	25	1.33	.236	1.80	4.77	8.57
	19	1.30	.292	1.57	5.44	8.52
	20	1.33	.228	1.84	5.50	10.1
3	22	1.33	.227	1.85	4.19	7.75
	23	1.32	.255	1.71	4.51	7.70
	24	1.33	.239	1.78	4.87	8.69
	13	1.29	.329	1.46	5.46	7.95
	12	1.29	.317	1.49	5.44	8.10
	25	1.33	.230	1.83	5.07	9.29
	19	1.39	.093	3.72	5.89	21.9
	20	1.37	.146	2.57	6.02	15.5
	14	1.37	.136	2.72	6.20	16.9
	17	1.34	.210	1.95	4.68	9.12

¹ See Figure 4-2. $\lambda_b = 0.3$

² See Table 6-4 for values of (\bar{q}/A) and Re.

³ Runs affected by subcooled bulk liquid.

removed from the wall with an occasional tongue of liquid approaching the wall. At the other extreme, λ_b would have to be about 0.75 for the subcooled runs (Runs 12 through 15 at No. 1 surface thermocouple) for the CC_s values to be in the ϵ/ν range of 0 to 5. This wave pattern would have liquid usually near the wall with occasional bursts of vapor penetrating deeper into the liquid. These conclusions seem intuitively acceptable and more satisfactory than the less flexible conclusions that can be derived from the concept of a sinusoidal interface.

3. Application of the Large-Wave Corrections

The assumption of sinusoidal interfacial waves led to theoretical results that matched the results from apparently non-wavy boiling tests, as was indicated by Figure 6-20. In an attempt to generalize this preliminary conclusion, all the data taken in this work were compared to theoretical curves that were developed for a sinusoidal interface. For this purpose, the relative wave amplitude, η_o , was taken to be 0.83 from Figure 6-19. Then the theoretical CC_s curves were converted to theoretical \overline{CC} curves according to the following relationship, which was derived from equations 6-6, 6-7 and 6-8:

$$\overline{CC} = (1 - \eta_o^2)^{\frac{1}{2}} \cdot CC_s = 0.56 C_s$$

This conversion was applied to the CC_s curves derived for ϵ/ν values of 0, 5 and 30, and the resultant theoretical \overline{CC} curves are shown as dashed lines on Figures 6-8 to 6-11. This procedure provides a reasonable

correlation of the low heat flux data shown on Figures 6-8 and 6-9, and of the high heat flux, low Reynolds number data on Figures 6-10 and 6-11. However, the high Reynolds number runs at high heat flux were overcorrected by these calculations, as is evident in Figures 6-10 and 6-11. This is consistent with the results shown on Figure 6-20. The correction for large waves based on a sinusoidal interface resulted in CC_s values beyond the theoretical limits ($\epsilon/\nu = 0$) for the high heat flux runs at No. 3 surface thermocouple. Thus, it appears that a different technique is required for these conditions. The pulse type wave seems most promising as a means of accounting for the effects of interfacial action. To firmly establish this conclusion, experimental measurements would have to show that λ_b is a function of the Reynolds number and the heat flux. The range of the λ_b values would have to be from about 0.1 to 0.75, as was discussed in the last section.

E. LIQUID-SOLID CONTACT

1. Experimental Evidence

There are strong indications that the liquid interface contacted the heater wall in the vicinity of No. 1 surface thermocouple during the low heat flux runs (22 through 25). This conclusion was based on the sudden large decreases in surface temperatures that are shown on the strip chart records of Figures 6-12a through 6-12d. As shown on Table 6-3, peak temperature changes for these four runs ranged from 3.1 to 15.4 degrees F. while the maximum range for the other runs was a 2.7 degrees F. peak-to-peak change. In addition, the shape of the peaks for the four runs in question imply that a drastic change of conditions had

occurred, while the other records seem to be consistent with more regular, although random, oscillations. The maximum instantaneous heat flux for these four runs varied from 62,000 to 320,000 Btu/hour-ft², which is in the range to be expected for transition or nucleate boiling.

In order to more conclusively prove that liquid-solid contact had occurred, an estimate was made of the expected wall temperature change following such contact. This was accomplished by solving the one-dimensional heat conduction equation for the nickel wall:

$$\frac{d^2 T}{dx^2} = \frac{1}{\alpha} \frac{dT}{dt}$$

The initial and boundary conditions for this situation are:

$$t < 0 : T = T_w$$

$$t \geq 0 : x = 0, q = -k_{Ni} \frac{dT}{dx} = h_c (T - T_s) \quad 6-24$$

$$x \rightarrow \infty, T \rightarrow T_w$$

where h_c is the wall to liquid heat transfer coefficient after contact occurs and T_w and T_s are the wall liquid temperatures, respectively.

The solution to this equation given by Carslaw (C-2) reduces to:

$$\Delta T = (T_w - T_s) \left[1 - e^{z^2} \cdot \operatorname{erfc}(z) \right] \quad 6-25$$

where ΔT is the change in the surface temperature and:

$$Z = \frac{h_c}{k_{Ni}} \sqrt{\alpha_{Ni} t} \quad 6-26$$

$$\text{erfc}(Z) = 1 - \frac{2}{\sqrt{\pi}} \int_Z^{\infty} e^{-\tau^2} d\tau \quad 6-27$$

For values of Z less than 0.2, equation 6-25 can be approximated within 5% by:

$$\Delta T = Z \cdot (T_w - T_s) \quad 6-28$$

Equation 6-28 can now be used to estimate the extent of cooling to be expected at the surface of the heater after liquid contacts it. The value of "t" for equation 6-26 is estimated from Figures 6-12a through 6-12d to be about 0.005 to 0.01 seconds. The value of h cannot be specified with certainty but it should be of the order of the heat transfer coefficient at the critical heat flux (point A in Figure 1-1). Rankin's data (R-1) with Freon-113 show that h may be as high as 1800 Btu/hour-ft²-°F at the critical point. With this value of h and a contact time of 0.005 seconds, $z=0.046$. Then, for $(T_w - T_s) = 200^\circ\text{F}$, $\Delta T = 9.2^\circ\text{F}$. This is of the order of the peak temperature changes as reported in Table 6-4 and it is concluded that liquid-solid contact did occur.

To reverse the above procedures, the heat transfer coefficients that would be required to produce the measured peak temperature changes

were calculated from equation 6-28 for Runs 22 through 25 for No. 1 surface thermocouple. These calculations were made for the maximum peak temperature changes for contact times of both 0.005 and 0.01 seconds. The range of the h values required to satisfy these conditions are reported for each run in the table below:

<u>Run No.</u>	<u>$(T_w - T_s)$ ($^{\circ}\text{F}$)</u>	<u>Range of Required h Values ($\text{Btu/hr-}^{\circ}\text{F-ft}^2$)</u>	<u>Corresponding Peak Heat Flux Values (Btu/hr-ft^2)</u>
22	156	1470 to 3840	230000 to 600000
23	179	1020 to 1720	183000 to 308000
24	220	514 to 1220	103000 to 268000
25	256	172 to 242	44000 to 62000

Except for the peak value for Run 22, these are in the range of time- and space-average heat transfer coefficients reported in the literature for nucleate and transition boiling. The decrease in the required heat transfer coefficients with increasing values of $(T_w - T_s)$ indicates that the transition regime (the region between points A and B in Figure 1-1) is dominant during the brief contact period. The very large instantaneous heat flux values shown in the above table are in line with measurements of Moore and Mesler (M-4). Using a surface thermocouple, they found the instantaneous heat flux to average over a million Btu/hr-ft^2 over a time interval of about one milli-second during the nucleation of a bubble in nucleate boiling.

2. Theory of Hamill and Bankoff

A theoretical study of Hamill and Bankoff (H-1) appears to be consistent with these results. They considered the case of a saturated liquid that is suddenly brought into contact with a much hotter solid.

Upon assuming that film boiling begins immediately and uniformly over the entire solid surface, they calculated the rate of growth of the vapor film thickness. Other idealizations were imposed, such as the assumptions that radiant heat transfer was negligible, the vapor behaved as a perfect gas and the interface was smooth. Upon applying their theoretical solution to the conditions at which liquid-solid contact occurred in the present experimental work, the following results were attained. The vapor film thickness to be expected for the range of experimental wall temperatures encountered would be 4.1 to 5.3 mils after 0.005 seconds and 5.8 to 7.5 mils after 0.01 seconds. The heat flux averaged over these time intervals would be in the range of 87,000 to 160,000 Btu/hour-ft².

These theoretical results lead to a qualitative model that is consistent with the experimental measurements. Following liquid-solid contact, the vapor film soon reaches the thicknesses calculated above and vapor in the film below the point of contact is then able to sweep up past the projecting wave. The liquid interface is then driven from the wall, the local heat transfer coefficient decreases to normal values for film boiling, and the wall surface temperature increases again. This is consistent with the strip chart records of the temperature history. The heat flux values calculated by the theory of Hamill and Bankoff are average results over the short time interval of contact. It is expected that instantaneous theoretical values would be somewhat higher. In any case, they are of the same order as the heat flux ranges listed in the previous table.

3. Theory of Bankoff and Mehra

The theoretical work of Bankoff and Mehra (B-1) with respect to the transition boiling regime is also of interest within the context of the present discussion. They postulated that almost all the heat transfer for transition boiling occurs during periods of momentary liquid-solid contact. It was necessary to their work to determine the frequency of contacts as well as the time duration of each contact and the surface area covered during this time. Of particular interest here, however, is their proposed heat transfer mechanism during the contact period. They assumed that energy was transferred by one-dimensional conduction from the surface and into the fluid. If this were the case, the temperature at the point of contact, T_c , would be the same for both phases and constant with time. According to Carslaw and Jaeger (C-3), this value would be:

$$T_c = T_w - (T_w - T_s) \cdot \left[1 + \frac{k_w}{k_L} \sqrt{\frac{\alpha_L}{\alpha_w}} \right]^{-1} \quad 6-29$$

The subscripts L and w refer to liquid and wall physical properties, respectively. Surface temperature changes, from T_w to T_c , were calculated with this equation for conditions corresponding to those in the experimental work done here. These results are listed below together with the measured peak changes in surface temperature.

<u>Run No.</u>	$(T_w - T_s)$ expt.	Calc.	$(T_w - T_c)$ °F
	(°F)		Expt.
22	156	3.6	15.9
23	179	4.1	7.9
24	220	5.1	6.9
25	256	5.9	3.1

Thus, for the experimental conditions in question, this theory leads to the wrong trend for the surface temperature changes as a function of $(T_w - T_s)$. It appears that the assumption of pure conduction as the only mechanism of heat transfer does not apply to the data taken here. Rather, a large convective or boiling heat transfer coefficient must be postulated to account for the large temperature peaks that were measured. The experimental heat transfer coefficient decreases for higher values of the temperature difference and the surface temperature change decreases accordingly. When the mechanism is pure conduction, the opposite trend occurs. The Bankoff-Mehra theory may be more consistent with experimental results when transition boiling is the normal mode rather than film boiling. The time average surface temperature would be considerably cooler in that case and the convective heat transfer process might be less significant. No other data appear to be available for checking this point.

4. Other Considerations

The local effects of liquid-solid contact have been discussed from the experimental and theoretical viewpoints. Less certain are the conditions under which liquid-solid contact will occur. The conclusion drawn from this work is that such contact occurs only at low Reynolds numbers when either the heat flux or the wall-to-liquid temperature

difference is small. Which of the latter two parameters is controlling in this respect is not clear from the limited data taken here. However, Stock (S-9) and others have presented evidence of liquid-solid contact during transition boiling where the heat flux may be very large but the temperature difference is relatively small. This implies that the temperature difference is the most important variable of the two. In either case, it will be recalled from the discussion of Chapter IV, Section F, that the term "small" as used here is relative, and that the absolute values of Re , ΔT , and \bar{q} at which liquid-solid contact occurs are strongly dependent on the nature of the heating surface and the heat source.

The effect of local liquid-solid contact on the rest of the system should also be explored. It appears probable that some of the vapor formed during the contact will move into the bulk liquid as bubbles instead of remaining in the vapor film. If this were the case, the film Reynolds number would be less than the calculated value at positions farther along the heater surface. However, visual observations indicated that vapor removal from the film was not excessive during these runs. The fact that the graphs of CC versus Reynolds number for these runs were not out of line, as shown in Figures 6-8 to 6-11, is considered as further evidence that this was not an important factor.

F. MEASUREMENTS OF INTERFACIAL CHARACTERISTICS

The nature of the interfacial structure was investigated by means of the probe described in Section G, Chapter V. There were two primary goals of these studies. The first intention was to show the relationship

between interfacial motion and the instantaneous surface heat flux. In addition, measurements of the mean vapor film thickness were desired. The probe tip was located at a specified distance from the wall at the same vertical elevation as one of the surface thermocouples. Then the signals from the probe and the surface thermocouple were recorded simultaneously on tape. The probe signal was also recorded directly on the strip chart recorder. This procedure was repeated with the probe at several different distances from the wall.

To determine the relationship between the two signals, their spectral densities and cross-spectral density were determined on the wave form analyzer. The typical curves shown on Figures 6-21a and 6-21b are for probe positions of 20 and 70 mils away from the wall at the location of the No. 3 surface thermocouple. The ordinate on the spectral density curves is expressed in terms of arbitrary voltage units, and the graph shows only the relative nature of the curves. Figure 6-21c shows that the signal from the probe leads the signal from the thermocouple by a variable phase angle that becomes quite small at the higher frequencies. For these higher frequencies, the reliability of the phase angle measurements on the wave form analyzer becomes very low because the cross-power density is quite small in this region. The existence of the cross-spectral density function indicates that a relationship exists between the two signals. Thus, it can be concluded that the surface temperature fluctuations and the hydrodynamic activity relatively far from the wall have a common physical source.

Typical strip chart records of the signal from the film thickness

FIGURE 6-21a

SPECTRAL and CROSS-SPECTRAL
DENSITIES of SIGNALS from
PRESSURE PROBE and No. 3
SURFACE THERMOCOUPLE

Pressure probe 20 mils from wall.

Φ_{ij} (volts²/cps) $\times 10^{-1}$

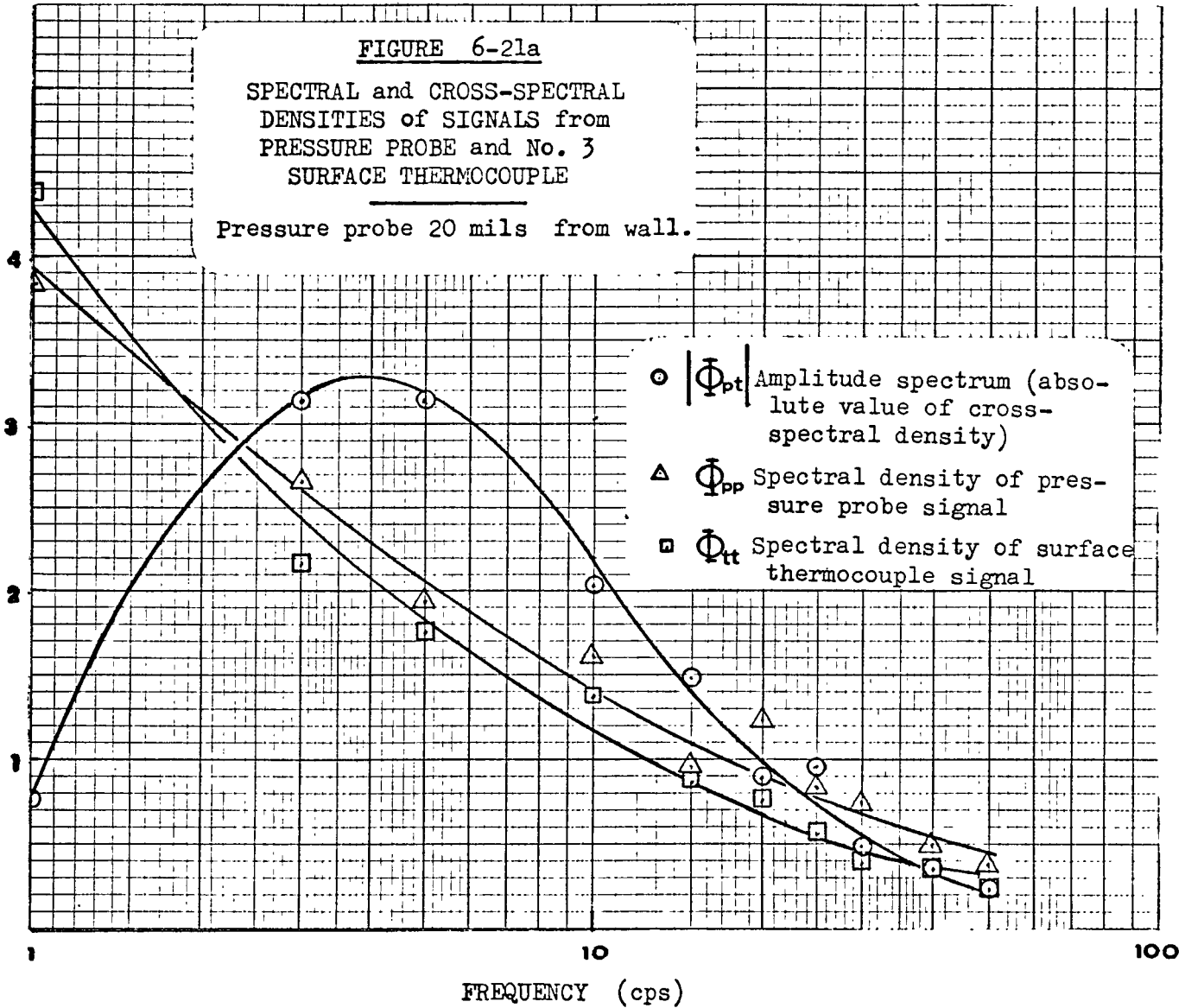


FIGURE 6-21b

SPECTRAL and CROSS-SPECTRAL
DENSITIES of SIGNALS from
PRESSURE PROBE and No. 3
SURFACE THERMOCOUPLE

Pressure probe 70 mils from wall.

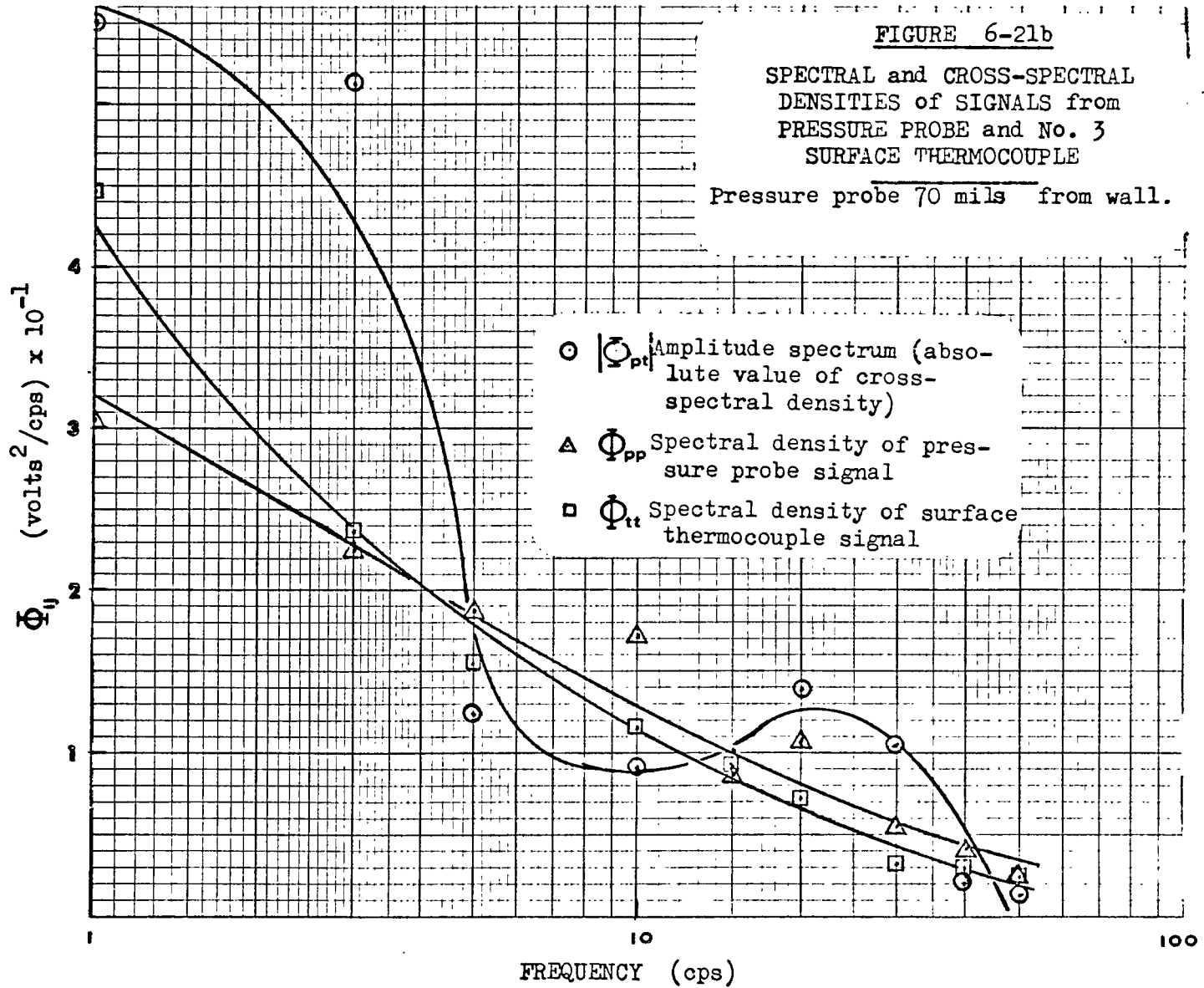
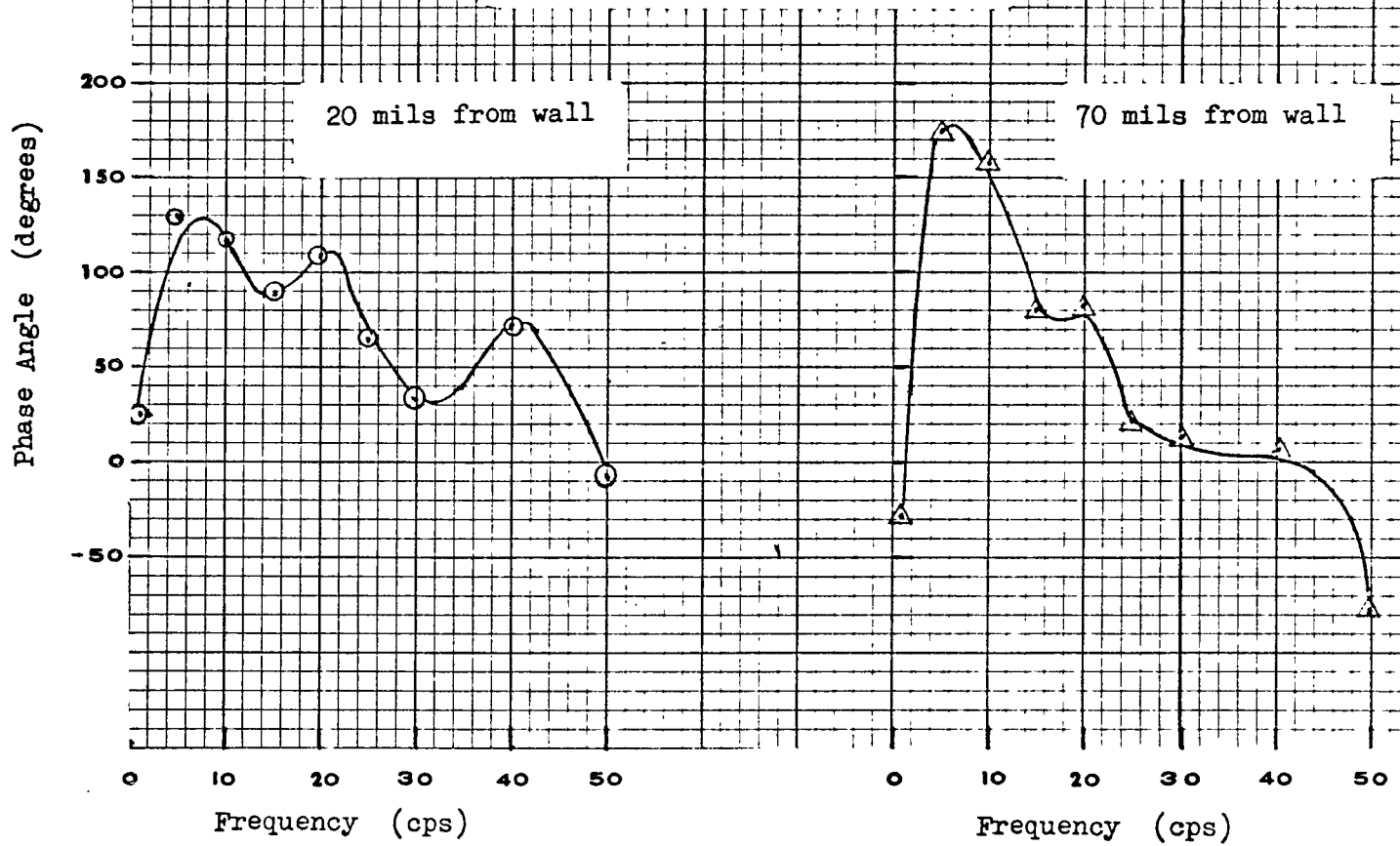


FIGURE 6-21c

PHASE ANGLE BETWEEN SIGNALS
from PRESSURE PROBE and
No. 3 SURFACE THERMOCOUPLE

(Positive angle indicates probe
signal leads)



probe are shown on Figure 6-22. These records were essentially the same for probe positions ranging from 5 to 200 mils from the wall. From a relatively smooth base line indicating a fairly constant pressure, occasional large fluctuations occur indicating an increasing pressure. The pressure peaks were as great as 0.12 psi with 0.08 psi being a more typical value. The nature of the signal was the same for the three test positions of the orifice in the probe tip. In the first position with the orifice facing down, the velocity head of the upwards moving liquid or vapor would be measured in addition to the static pressure. With the orifice facing up, the total pressure would again be measured but the contribution of the velocity head would be attenuated because of frictional pressure loss and perhaps because of boundary layer separation. With the orifice facing downwards but 30 degrees from the vertical, however, no component of the velocity head would be expected according to the hydrodynamic equations for fluid flow past a cylinder. In the latter orientation, only the static pressure should affect the probe.

However, the pressure signal from the probe appeared to be independent of the orifice orientation. It was therefore concluded that static pressure changes are much greater than pressure changes due to a changing velocity head. The increasing static pressure apparently arises as the liquid interface approaches the wall. The heat transfer coefficient, and therefore the rate of vapor generation, increases greatly as this occurs. This new vapor accumulates locally since the normal upwards flow within the vapor film cannot remove it fast enough. Thus, the local pressure begins to increase rapidly and finally pushes the liquid interface back,

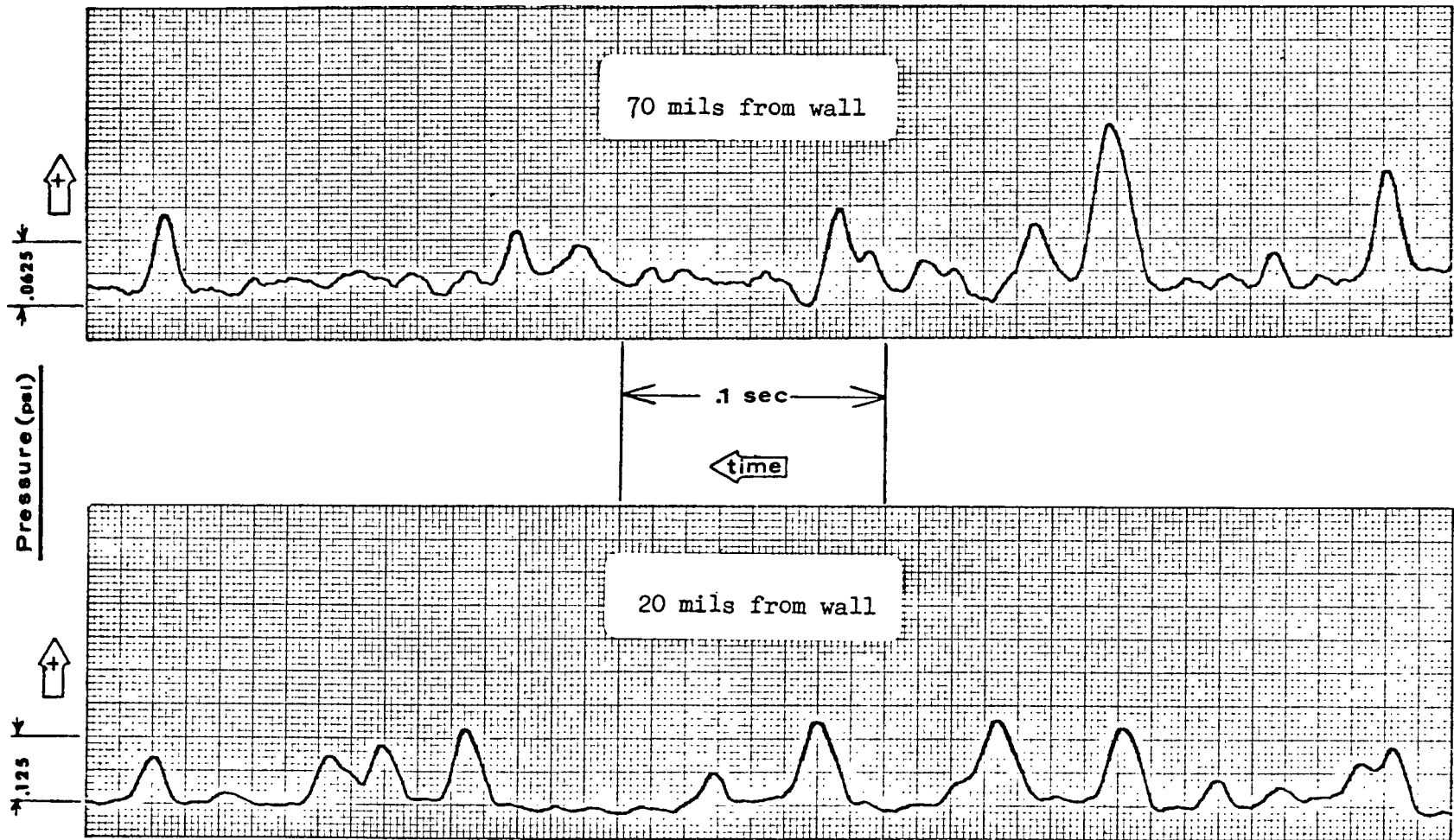


FIGURE 6-22
TYPICAL SIGNALS from
PRESSURE PROBE

probably explosively as evidenced by the motion pictures of Westwater (W-2) for horizontal transition boiling. The pressure then quickly returns to its normal value, because of the increased volume available to contain the vapor and also because of the reduced vapor generation rate as the film thickness increases.

This conception can be discussed with respect to Figure 4-2 if the pulse type wave shown there is considered to be a time record at a given position. As the portion of the wave indicated by λ_1 , passes a point on the wall, the local pressure begins to increase. Finally, the pressure is great enough to overcome the inertia of the liquid and the interface is pushed back to its position in the region shown as λ_2 . From an examination of strip charts such as those of Figure 6-22, it was estimated that the high pressure region exists about 30% of the time. Thus, λ_b is about 0.3, which is the value that was used in the calculations of Section D-2 of this chapter. These records were taken during a run with a heat flux of about 14,000 Btu/hr-ft².

Since the static pressure changes were much greater than pressure fluctuations due to velocity head changes, this probe could not detect the difference between the vapor and liquid phases as had been intended. Therefore, the vapor film thickness could not be determined.

G. THEORETICAL TIME AVERAGE CHARACTERISTICS OF THE VAPOR FILM

It will be of interest to examine the actual dimensions, velocities, and shear stresses that are predicted by the quasi-steady state theory for the vapor film. These calculations were made for ϵ/ν values of 0, 5, 10 and 30 which are in the range required to correlate the data of

this work after the corrections for large amplitude waves were made. These same values of ϵ/ν were consistent with the data of Dougall and Rohsenow (D-5) which will be presented later. The calculations of the desired quantities follow from the relationships given in Chapter III. The film thickness was given by:

$$\rho = A + B$$

6-30

From equations 3-22 or 3-26 and 3-30, it can be shown that:

$$A = A^{* \frac{2}{3}} \cdot \left[\frac{\mu^2}{g\rho(\eta_f \rho_L - \rho)} \right]^{1/3}$$

6-31

$$B = B^{* \frac{2}{3}} \cdot \left[\frac{\mu^2}{g\rho(\eta_f \rho_L - \rho)} \right]^{1/3}$$

6-32

From these same equations, it follows that:

$$\tau_w = A^{* \frac{2}{3}} \cdot \left\{ \frac{[\mu g(\eta_f \rho_L - \rho)]^2}{\rho} \right\}^{1/3}$$

6-33

$$\tau_i = B^{* \frac{2}{3}} \cdot \left\{ \frac{[\mu g(\eta_f \rho_L - \rho)]^2}{\rho} \right\}^{1/3}$$

6-34

Then, from equations 3-39, 6-31 and 6-32:

$$\bar{u} = \frac{Re}{A^{+2/3} + B^{+2/3}} \cdot \frac{1}{2} \left[\frac{g\mu(\eta_f \rho_L - \rho)}{\rho^2} \right]^{1/3} \quad 6-35$$

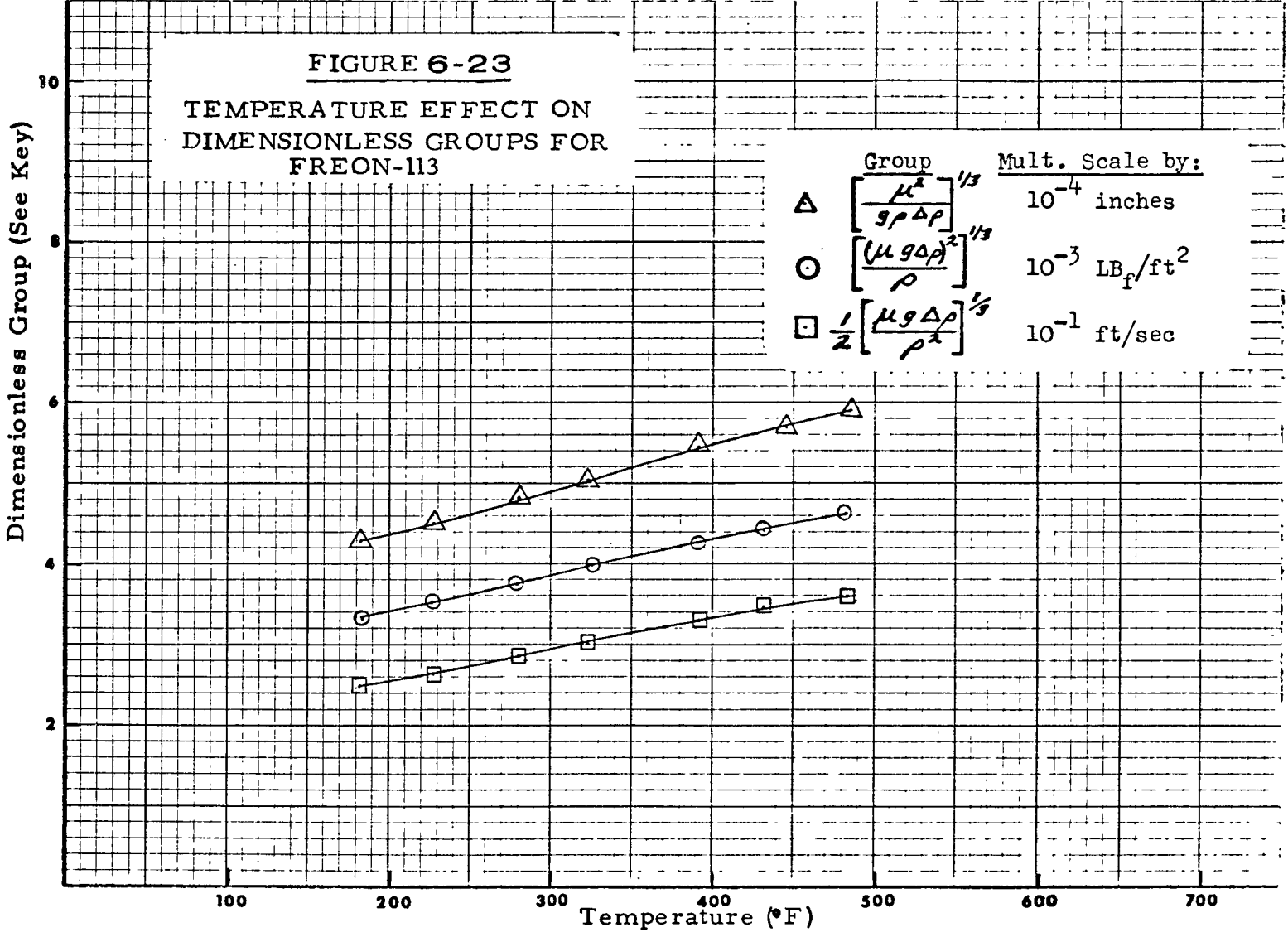
Finally, from equation 6-33 and the definition of u^+ :

$$u_m = u_m^+ \cdot A^{+1/3} \cdot \left[\frac{\mu g (\eta_f \rho_L - \rho)}{\rho^2} \right]^{1/3} \quad 6-36$$

$$u_i = \frac{u_i}{u_m} \cdot u_m \quad 6-37$$

The dimensionless groups in equations 6-31, 6-33 and 6-35 are functions of the physical properties for the case of natural convection film boiling where $\eta_f=1$. These groups were evaluated for Freon - 113 and are presented as functions of the wall surface temperature in Figure 6-23. In order to calculate actual values of the shear stresses, film thickness, and vapor velocity for a given experimental Reynolds number, the values of A^+ , B^+ , u_m^+ and u_i/u_m must first be determined as functions of Re and \mathcal{E}/ν . This can be done by using the results of the quasi-steady state theory. The calculations will first be made with the assumptions that u_i/u_m is either zero or 0.5. Then, the actual value of u_i/u_m will be estimated by the methods of Section F in Chapter III.

First, A^+ is found from Figure 3-19 if u_i/u_m is zero, or from Figure 3-20 if u_i/u_m is 0.5. (Other values of u_i/u_m would have led to similar graphs.) Then, u_m^+ is found on Figure 3-7 from the curve for



$\epsilon/\delta = 0$. Equation 3-66 is now used to determine B^+ :

$$B^+ = A^+ \cdot \left[\frac{u_m^+ (1 - u_i/u_m)}{v_{mb}^+} \right]^3 \quad 6-38$$

A^+ , u_m^+ , and u_i/u_m are known, but v_{mb}^+ is a function of B^+ as given on Figure 3-7, where the correct ϵ/δ curve must be used. Therefore, solution of the above equation for B^+ must be accomplished by a trial and error procedure. If u_i/u_m is zero, a simpler approach may be taken. Re_a can be found from Figure 3-8 from the curve for $\epsilon/\delta = 0$, using the value of A^+ that had been found on Figure 3-19. Then, from equation 3-67:

$$Re_b = 2 Re - Re_a$$

Finally, B^+ is determined from Figure 3-8 as a function of Re_b and ϵ/δ .

The results of these calculations are presented in Tables 6-8 and 6-9. As seen in Table 6-8, increasing ϵ/δ for a given Reynolds number tends to increase the film thickness and the boundary shear stresses while reducing the average velocity. The B-side gets proportionately larger. Increasing the Reynolds number, however, tends to increase all three of these quantities. The larger value of u_i/u_m given on Table 6-9 results in an increase in the average velocity but a decrease in the film thickness and the boundary shear stresses.

The actual value of u_i/u_m that applies to a given situation is such that the interfacial shear stress calculated from the vapor film equations given in this section is equal to the interfacial shear stress consistent with the boundary layer development in the liquid, as calculated by equation 3-78 in Chapter III. Consider as an example the entry in Table 6-9

TABLE 6 - 8

Properties of the Vapor Film for Freon - 113

<u>Conditions</u>		$u_i/u_m=0, \quad T_{\text{sat}} = 120^{\circ}\text{F}, \quad T_{\text{wall}} = 570^{\circ}\text{F}$									
ϵ/D	Re	A ⁺	B ⁺	u _m ⁺	(mils)			(LB _F /ft ²)		(ft/sec)	
					A	B	p	T _w	T _i	\bar{u}	u _M
0	700	24.9	24.9	9.5	4.3	4.3	8.6	3.5	3.5	12.7	17.1
	2500	58.8	58.8	13.1	7.8	7.8	15.6	6.1	6.1	25.8	31.5
	5000	99.5	99.5	14.9	11.1	11.1	22.2	8.8	8.8	36.2	42.9
	10000	173.	173.	16.5	16.1	16.1	32.2	12.7	12.7	50.0	57.5
	20000	308.	308.	18.0	23.8	23.8	47.6	18.7	18.7	67.7	75.7
5	700	16.9	75.3	7.4	3.3	9.3	12.6	2.7	7.3	8.9	11.8
	2500	37.3	172.	11.3	5.7	16.1	21.8	4.5	12.7	18.4	23.6
	5000	62.9	276.	13.3	8.1	22.1	30.2	6.4	17.3	26.7	33.2
	10000	111.	454.	15.2	12.0	30.7	42.7	9.4	24.2	37.8	45.5
	20000	202.	759.	17.0	17.9	43.9	61.8	14.5	34.4	52.1	62.5
10	700	14.8	104.	6.7	3.1	11.5	14.6	2.4	9.0	7.7	10.2
	2500	32.2	231.	10.7	5.2	19.6	24.8	4.1	15.4	16.2	21.4
	5000	54.1	364.	12.8	7.4	26.6	34.0	5.8	20.9	23.7	30.2
	10000	96.1	587.	14.7	10.8	36.7	47.5	8.5	28.8	33.9	42.1
	20000	176.	962.	16.5	16.3	50.1	66.4	12.8	39.4	48.5	58.1
30	700	12.0	175.	5.7	2.7	16.2	18.9	2.1	12.8	6.0	8.1
	2500	25.2	370.	9.6	4.4	26.9	31.3	3.5	21.1	12.9	17.5
	5000	41.8	566.	11.7	6.2	35.6	41.8	4.9	28.0	19.2	25.1
	10000	74.2	882.	13.9	9.1	47.7	56.8	7.1	37.5	28.2	36.4
	20000	138.	1400.	15.8	13.9	64.5	78.4	11.0	50.6	41.1	50.8

TABLE 6 - 9

Properties of the Vapor Film for Freon - 113

Conditions $u_i/u_m=0.5$, $T_{sat} = 120^{\circ}\text{F}$, $T_{wall} = 570^{\circ}\text{F}$

ϵ/ν	Re	A ⁺	B ⁺	u _M ⁺	(mils)			(LB F/ft ²)		(ft/sec)		
					A	B	p	τ_w	τ_i	\bar{u}	u _M	u _i
0	700	27.5	13.4	10.0	4.7	2.9	7.6	3.7	2.5	14.8	18.8	9.4
	2500	71.9	21.5	13.8	8.9	4.0	12.9	7.0	3.1	31.3	35.6	17.8
	5000	127.	38.8	15.6	13.1	5.9	19.0	10.2	4.8	42.6	48.9	24.4
	10000	228.	62.3	17.2	19.3	8.1	27.4	15.2	6.4	59.9	65.6	32.8
	20000	415.	105.	19.0	28.8	11.5	40.3	22.7	9.0	80.0	87.7	43.8
5	700	19.5	42.8	8.4	3.7	6.3	10.0	2.9	4.9	11.2	14.0	7.0
	2500	48.2	87.7	12.4	6.8	10.2	17.0	5.4	8.0	23.6	28.1	14.0
	5000	85.9	134.	14.3	7.4	13.5	20.9	7.9	10.6	34.2	39.4	19.7
	10000	158.	209.	16.2	14.6	18.1	32.7	11.5	14.3	49.3	55.1	27.6
	20000	296.	333.	17.9	23.0	24.9	47.9	18.1	19.6	67.3	74.5	37.2
10	700	16.9	60.5	7.4	3.4	7.9	11.3	2.7	6.2	10.4	11.8	5.9
	2500	41.0	124.	11.6	6.1	12.8	18.9	4.8	10.1	21.2	25.0	12.5
	5000	73.3	187.	13.8	9.0	16.8	25.8	7.1	13.3	31.1	36.1	18.0
	10000	137.	287.	15.7	13.7	22.5	36.2	10.8	17.7	44.6	50.5	25.2
	20000	259.	449.	17.5	20.9	30.4	51.3	16.5	24.9	62.8	69.5	34.8
30	700	13.3	106.	6.2	2.9	11.6	14.5	2.3	9.1	7.8	9.2	4.6
	2500	30.7	212.	10.6	5.0	18.3	23.3	3.9	14.4	17.3	20.6	10.3
	5000	54.5	313.	12.8	7.4	23.5	30.9	5.8	18.5	26.1	30.3	15.2
	10000	103.	469.	14.9	11.3	31.2	42.5	8.9	24.6	37.7	43.5	21.8
	20000	202.	715.	17.0	17.8	41.3	59.1	14.0	32.5	54.5	62.3	31.2

for $\epsilon/\nu = 10$ and $Re = 10000$. In this case, if $u_i/u_m = 0.5$, then

$$\tau_i = 0.18 \text{ LB}_F/\text{ft}^2 \quad \text{and } u_i = 25 \text{ feet per second.}$$

According to equation 3-78, however, an interfacial shear stress of 0.28 is required to produce an interfacial velocity of 25 feet per second if α is one foot. (As seen in Table 6-2, Reynolds numbers of 10000 occurred at a distance of about one foot from the bottom edge of the heater wall.) Since the shear stresses calculated by the two methods are not the same (0.18 versus 0.28), the calculations will have to be repeated with a new assumed value of u_i/u_m .

Lowering the u_i/u_m ratio will result in a smaller calculated interfacial velocity. This will then lead, as desired, to a higher interfacial shear stress as calculated from the vapor film equations, and to a lower interfacial shear stress as calculated by the boundary layer equation, 3-78.

Repeated trials lead to 0.43 for the u_i/u_m ratio, 19 feet per second for u_i , and $0.19 \text{ LB}_F/\text{ft}^2$ for τ_i . These values then apply when a Reynolds number of 10000 is attained at a distance of one foot from the leading edge of the heater if the value of ϵ/ν is 10. The data of Dougall and Rohsenow (D-5) were also taken during the film boiling of Freon - 113. Several calculations made for their test conditions led to u_i/u_m ratios that were usually a little less than 0.5.

As has been previously stated, there is not yet a method for predicting a priori the correct value of ϵ/ν . To provide some insight into this situation, the method suggested in Section C-2, Chapter III, will be followed to provide a theoretical estimate of the relationship between ϵ/ν and the size of the interfacial ripples (as opposed to the large amplitude waves). To accomplish this, equation 3-13 has been solved for the amplitude of the interfacial ripples that would

correspond to each set of ϵ/ν and τ_i values that are given on Tables 6-8 and 6-9. These results are shown in Table 6-10. For these calculations, the proportionality constant, k_1 , was assumed to be one. The corresponding amplitudes range from 0.3 to 4.0 mils. No experimental evidence of the actual ripple size in film boiling is available for comparison to these calculated values. Kapitsa (K-1), however, has measured the ripple size on the surface of a thin falling film of water. In those experiments, there was no interfacial shear stress and the liquid film Reynolds number was very low, so that large amplitude waves had not yet formed. The measured amplitudes ranged from 0.7 to 3.5 mils.

Of more direct bearing to the physical situation being considered here are the data of Lilleleht (L-6). He made measurements of co-current, stratified air-water flow in horizontal rectangular channels. The mean water film thickness was about 0.1 to 0.2 inches, while the channel width available for air flow ranged from about 0.4 to 0.6 inches. The flow conditions were such that the vapor-liquid interface was rough with a three-dimensional pebbled appearance. Thus, the gas flowed between one smooth and one rough boundary. As expected, the measured velocity profile was not symmetrical. This experimental velocity profile could be closely duplicated by theoretical calculations based on the quasi-steady state theory if an ϵ/ν value of about 1.0 was used. The ripple wave amplitudes consistent with this value of ϵ/ν were then calculated from equation 3-13, with the proportionality constant set equal to one and using the interfacial shear stress values measured by Lilleleht. These calculations indicated that the wave amplitude should range from 1.6 to

TABLE 6 - 10

Predicted Amplitudes of Interfacial Ripples for Specified Values
of ϵ/ν for Freon - 113

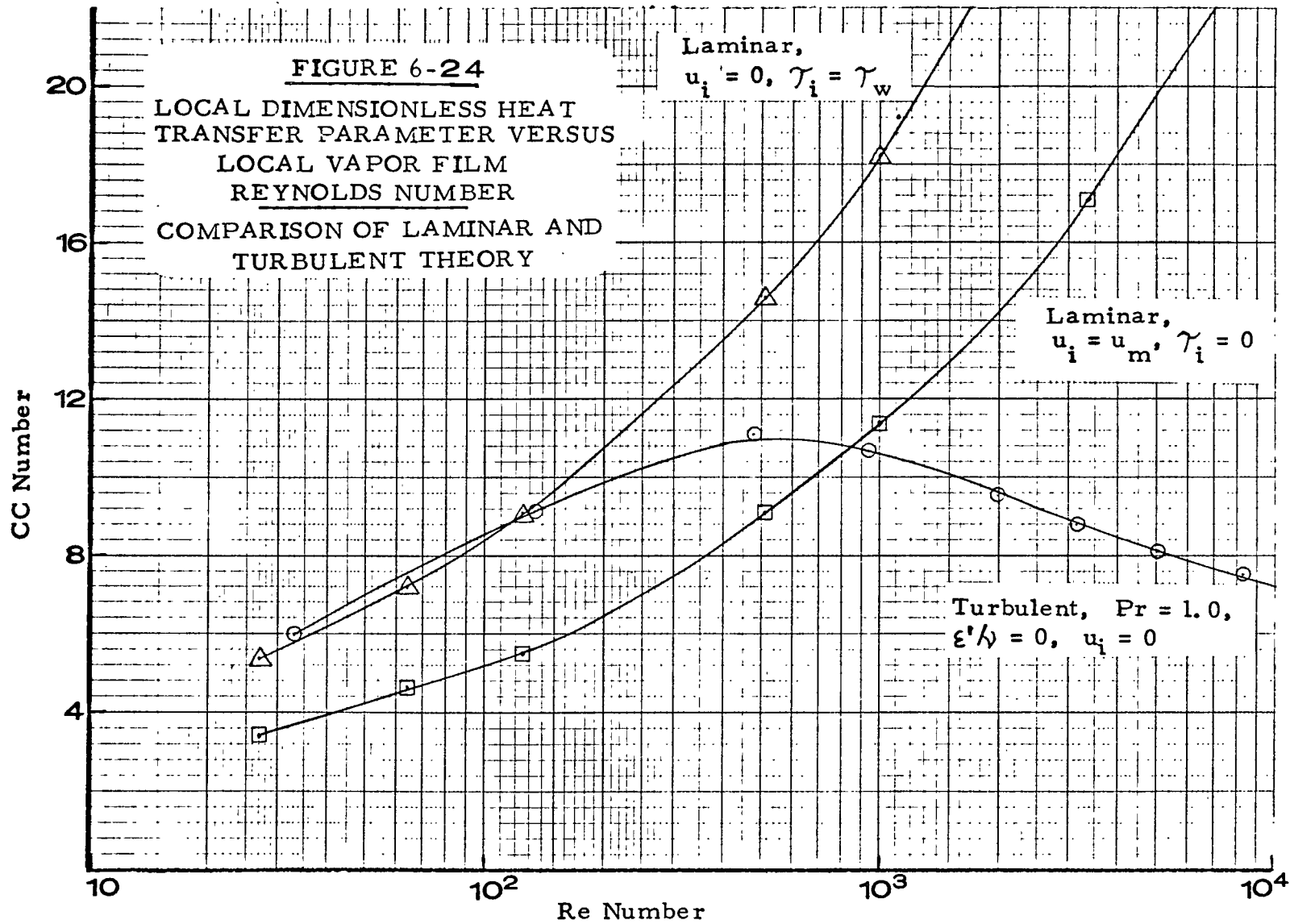
ϵ/ν	Re	$u_i/u_m = 0$		$u_i/u_m = .5$	
		p(mils)	l'(mils)	p(mils)	l'(mils)
0	700	8.6	0	7.6	0
	2500	15.6	0	12.9	0
	5000	22.2	0	19.0	0
	10000	32.2	0	27.4	0
	20000	47.6	0	40.3	0
5	700	12.6	.72	10.0	.88
	2500	21.8	.55	17.0	.69
	5000	30.2	.47	20.9	.60
	10000	42.7	.40	32.7	.51
	20000	61.8	.33	47.9	.42
10	700	14.6	1.24	11.3	1.44
	2500	24.8	.95	18.9	1.17
	5000	34.0	.82	25.8	1.02
	10000	47.5	.70	36.2	.88
	20000	66.4	.60	51.3	.75
30	700	18.9	3.31	14.5	3.92
	2500	31.3	2.58	23.3	3.11
	5000	41.8	2.24	30.9	2.74
	10000	56.8	1.93	42.5	2.38
	20000	78.4	1.67	59.1	2.07

4.6 mils for the various test runs that were reported. Actual amplitudes ranging from 9 to 20 mils were reported by Lilleleht and Hanratty (L-7) for these same runs. If the proportionality constant in equation 3-13 were 0.2 instead of unity, predicted amplitudes of 8 to 23 mils would be within the range of the data.

These results are in close enough agreement to encourage further work in the area. However, even if the value of ϵ/ν can be closely tied to the wave amplitude and interfacial shear stress, there still remains the imposing task of predicting wave amplitudes from a knowledge of the hydrodynamic conditions in the liquid and gas phases.

H. EVALUATION OF OTHER WORK FROM THE LITERATURE

In this section, some of the film boiling research that has been previously reported in the literature will be compared to the results of this work. The theoretical curves for laminar film boiling, which are equivalent to the theory of Bromley (B-8), are shown in Figure 6-24 with a typical curve from this work for the turbulent case. The two laminar curves are for the extreme situations of zero interfacial velocity and zero interfacial shear stress. This Figure indicates that the laminar theory predicts much smaller heat transfer coefficients (larger CC numbers) than does the turbulent theory for Reynolds numbers above 1000. In view of the data on Figure 6-8 and elsewhere, it can be concluded that the laminar theory is not applicable except for very low Reynolds numbers. In the rest of this Section, other turbulent studies will be discussed.



1. The Data and Theory of Dougall and Rohsenow (D-5)

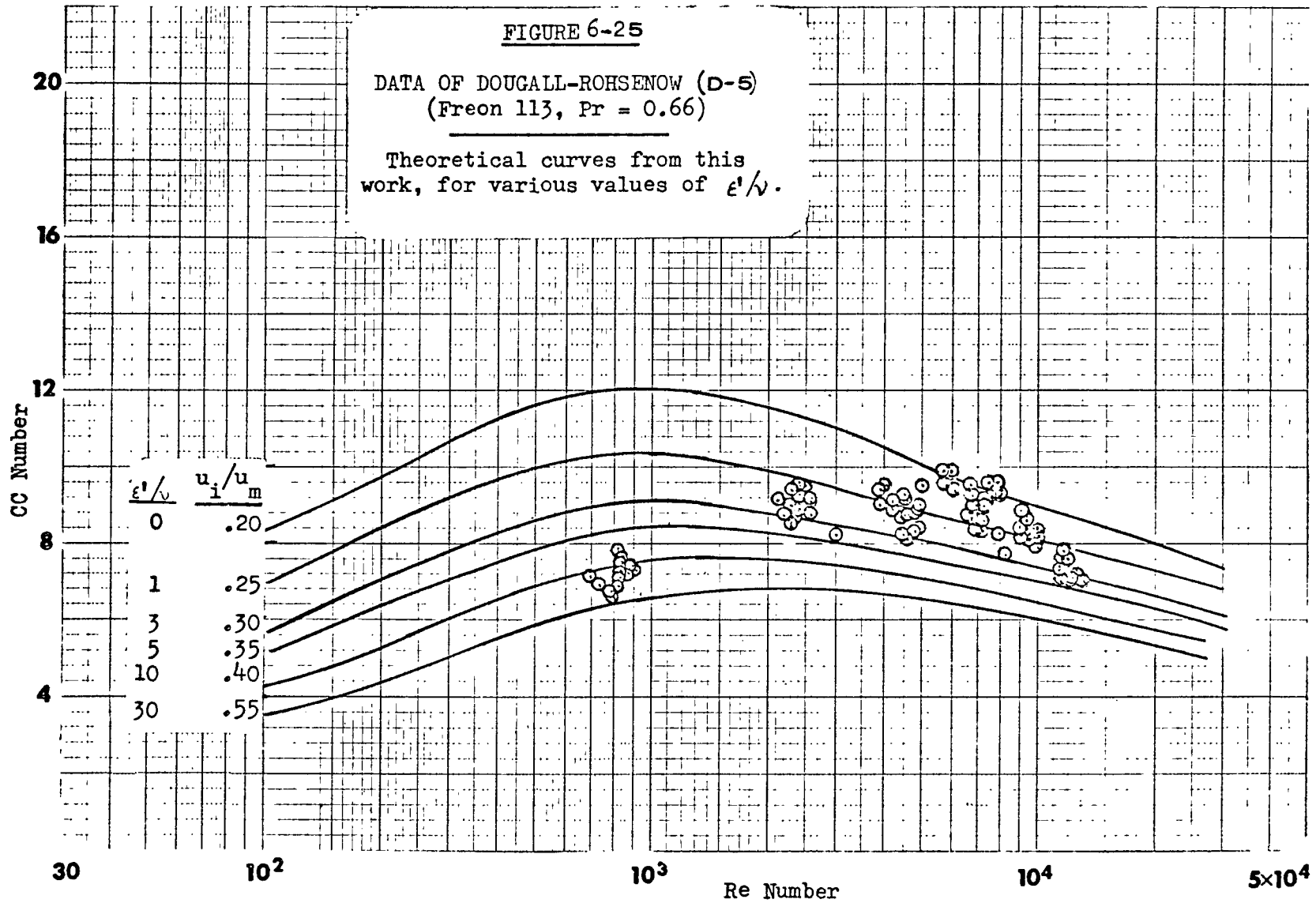
This data was taken with Freon - 113 boiling on the inside of a vertical, electrically heated tube 15 inches long by 0.408 inches in diameter. The liquid flowed upwards by forced convection at average inlet velocities of 1.4 to 2.5 feet per second. Subcooling of the feed ranged from 17 to 32 degrees F. Total vaporization rates within the heater ranged from 2.7 to 4.8 per cent by weight of the feed, based on the assumption that no sensible heating of the unvaporized bulk liquid occurred. Local wall temperatures were measured at six positions up the tube. The CC and Reynolds numbers were calculated for each position in much the same manner as was described in Section A of this chapter.

The CC numbers for each position were plotted as functions of the heat flux to help determine the internal consistency of this data. On this basis, 22 of their 132 data points were discarded because they were 10% or more removed from a smooth curve through the data. The remaining points are plotted in Figure 6-25. It was assumed that no energy was transferred to unvaporized liquid, and that the temperature of the bulk liquid leaving the boiler was the same as that of the liquid entering. The calculated Reynolds numbers will be high to the extent that this assumption is in error. However, as discussed in Chapter II, the data showed no trend that depended on the amount of subcooling and the assumption made is believed to be reasonably accurate. The theoretical curves corresponding to the quasi-steady state theory are also included in Figure 6-25. The u_i/u_m values shown on this graph were calculated accord-

FIGURE 6-25

DATA OF DOUGALL-ROHSENOW (D-5)
(Freon 113, Pr = 0.66)

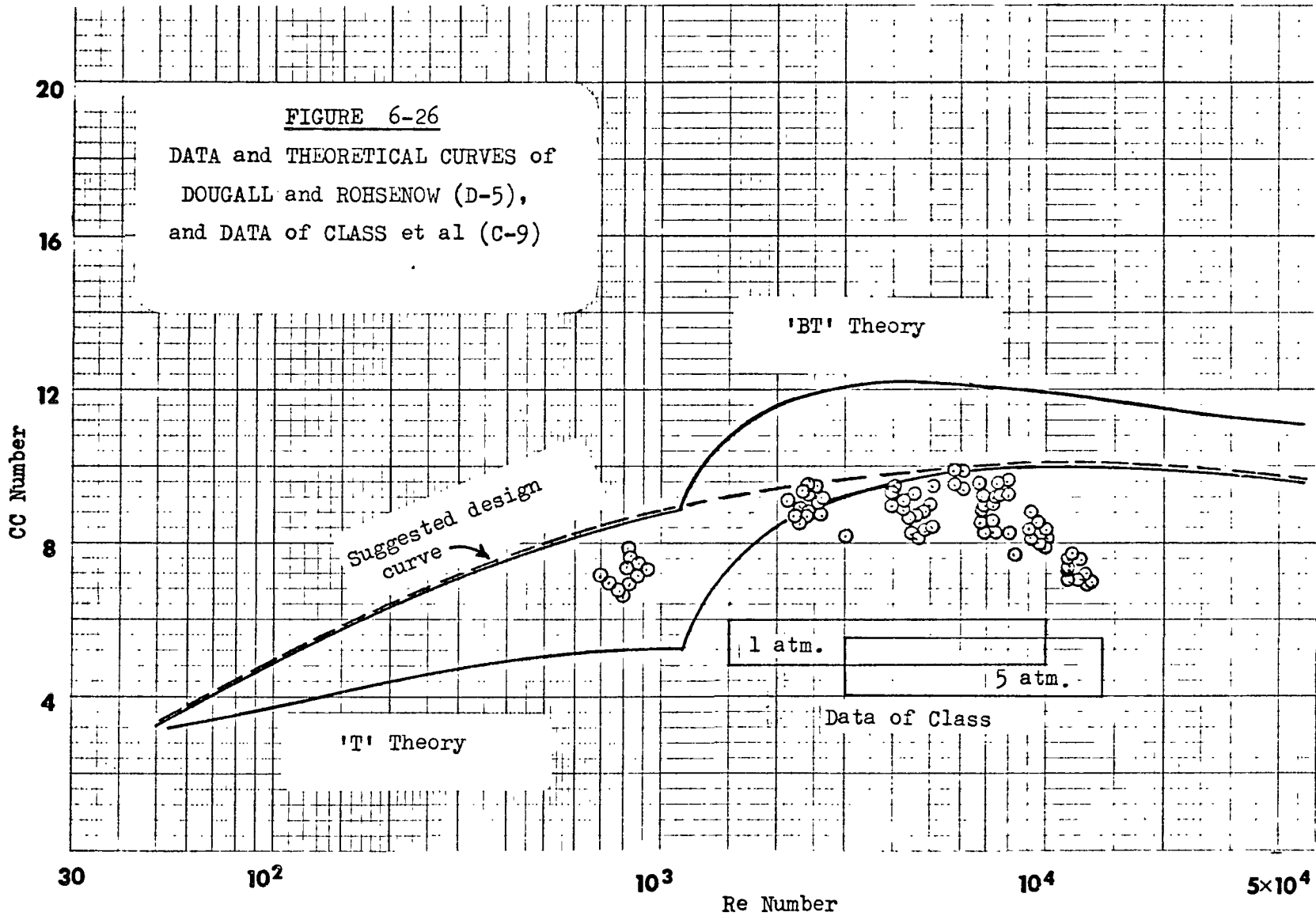
Theoretical curves from this
work, for various values of ϵ'/ν .



ing to the theory that was presented in Chapter III, Section F.

The spread of these data points was indicated by closed curves on Figure 6-20 to compare the data of Dougall and Rohsenow to that of this work. It is interesting to note that these two data sets generally coincide, even though the data from this work had been corrected for the effect of large waves while their data set had not. The implication, then, is that "large" amplitude waves were not present during the test runs of Dougall and Rohsenow. This conclusion was anticipated because the subcooled bulk liquid in their boiler would be expected to suppress wave motion. When vapor starts to push the interface back into the bulk liquid, the liquid thermal boundary layer would be penetrated and the vapor would come into contact with subcooled liquid. Vapor condensation would begin and the wave growth would thus be inhibited. According to this mechanism, the higher frequency waves would not be damped as much as those of lower frequency because of their more rapid rate of penetration into the liquid. This effect is manifested in the spectral density curves of Figure 6-14a for the subcooled runs of the present work.

The theoretical developments of Dougall and Rohsenow are presented with their data in Figure 6-26. The two curves labeled "BT" and "T" correspond to different assumptions with respect to the interfacial resistance to turbulent energy transport, while the dashed line represents their suggested design curve. They originally correlated their data in terms of a modified Nusselt number as a function of the Reynolds and Prandtl numbers. Their Nusselt number was defined as $\frac{hD}{k}$, where D is the diameter of the surface at which film boiling occurs. Their



theory was re-derived in terms of the CC number in order to make a direct comparison to the theory of this work. The details of this re-derivation are presented in Appendix E.

Figure 6-26 indicates that the theory of Dougall and Rohsenow generally predicts heat transfer coefficients that are somewhat lower than their data. In addition, the trend of their theory diverges from their data trend at higher Reynolds numbers. They accounted for this divergence by assuming that film boiling became unstable and a dispersed two-phase flow regime developed at this point, but they had no quantitative evidence that this had occurred. It was shown by the data of this work that film boiling remains stable at these high Reynolds numbers in a natural convection boiler, and that the experimental CC number does begin to decrease. Thus, the Dougall-Rohsenow theory appears inadequate for stable film boiling at high Reynolds numbers. In addition, it cannot account for the effects of large amplitude waves.

2. Data of Class et al

Class et al (C-9) measured local heat transfer coefficients during the natural convection film boiling of saturated hydrogen on a vertical flat strip. As was discussed in Chapter II, there is some doubt as to whether stable film boiling existed during these tests. With this limitation in mind, the data will be presented here for a qualitative comparison to the quasi-steady state theory.

The raw data were reduced to CC and Reynolds numbers in the same manner as described in Section A of this chapter. Physical properties

were taken from the reports of Johnson (J-2) and Roder and Goodwin (R-2). The two top and bottom thermocouple positions were not considered because of reported end effects. The remaining 84 data points fall within the narrow ranges shown by the two rectangles on Figure 6-26. The upper rectangle refers to data taken at essentially one atmosphere and the lower rectangle is for data at about 5 atmospheres.

The plotted data points fall within the range of data taken with Freon - 113 in this work. Vigorous interfacial wave action probably occurred during the hydrogen boiling tests as had been the case with Freon-113, since both tests were made with saturated liquid. If this were so, presumably the same large amplitude wave correction could be applied to the hydrogen data. Indeed, Class et al had measured temperature fluctuations of up to 4 degrees F., even though their thermocouples were installed behind an 0.005 inch thick layer of Mylar insulation which, in turn, was bonded to the back of the 0.005 inch thick heater strip. This indicates that fairly violent surface temperature fluctuations had occurred. However, it is not known whether these fluctuations were due to normal wave action to which the large amplitude wave correction would apply, or whether they resulted from liquid contact at the long vertical edge of the heater in the manner of the waves reported by Morgan (M-6). Thus, the data of Class et al can only be said to be qualitatively in line with the data taken in this work.

3. The Theory of Hsu

The model used by Hsu (H-5) to represent vertical turbulent film boiling is shown in Figure 6-27. The vapor film is developing as

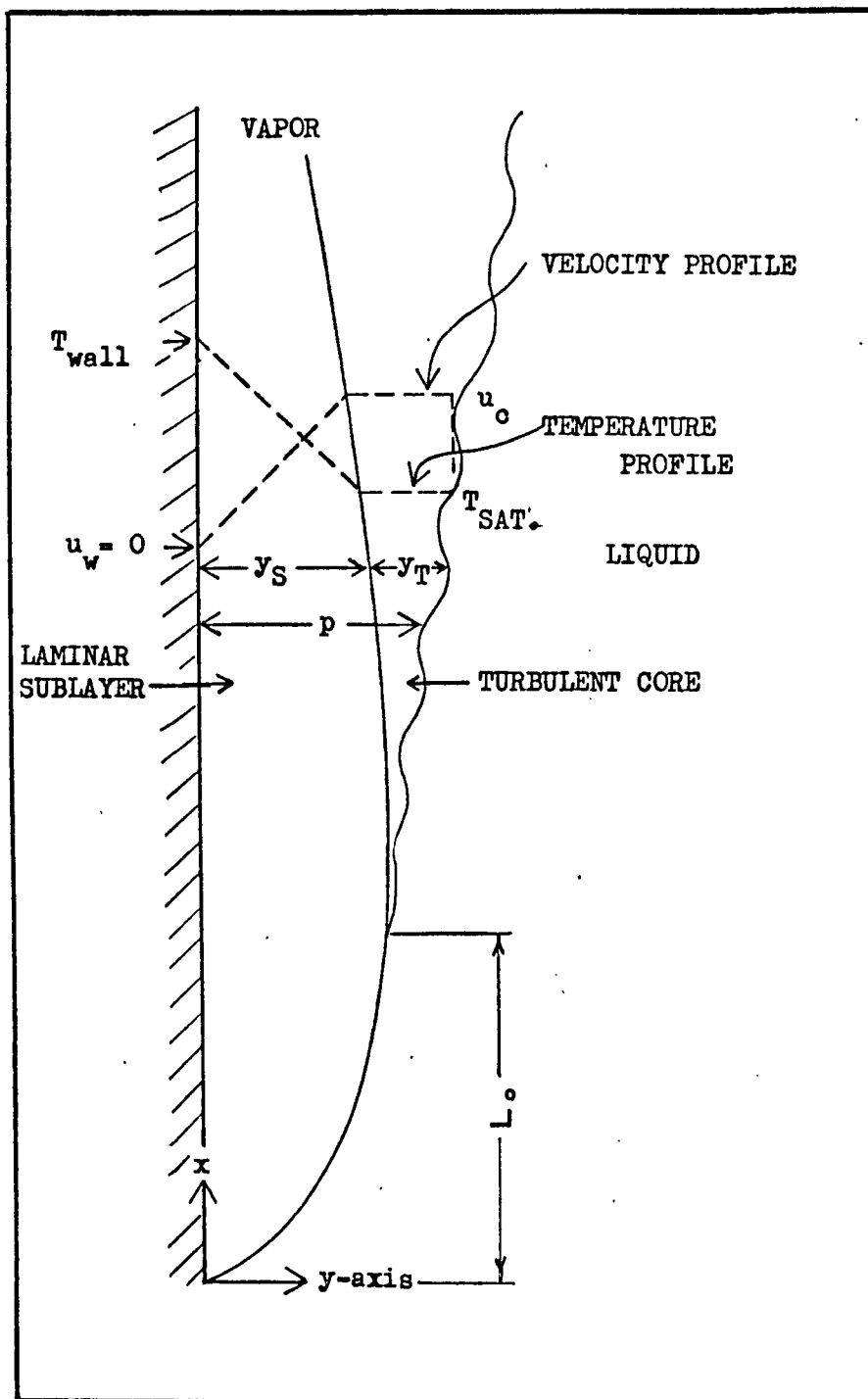


FIGURE 6-27

HSU'S MODEL OF FILM BOILING

a boundary layer in the x-direction. Laminar flow exists over the distance L_0 , and thereafter the flow consists of a laminar sublayer of thickness y_s near the wall and a turbulent core adjacent to the liquid. The transition Reynolds number (Re_t) was assumed to be 100. Velocity and temperature profiles were assumed to be linear in the laminar sublayer and constant in the turbulent core. However, the vapor velocity was assumed to fall very rapidly near the interface to a value near the average liquid velocity. The interfacial shear stress was then calculated from an empirical friction factor (f_i) correlation based on the velocity in the turbulent core, u_c :

$$\tau_i = \frac{1}{2} \rho_s u_c^2 f_i \quad 6-39$$

where ρ_s is the density of saturated vapor. Hsu included the effects of momentum changes within the vapor film in his theory by considering the change in u_c with respect to x . He was able to attain an analytical solution of his equations for the case of film boiling with a constant wall temperature. His results were presented in the form of local and space average heat transfer coefficients as a function of x .

In this work, an attempt was made to present Hsu's theory in the form of the local CC and Reynolds numbers to allow comparisons to be made between his and other theories. The resulting equations could not be solved, however, so the solutions for two special cases were developed instead. The details of these derivations are included in Appendix E. It is believed that these special solutions closely approximate the

results of Hsu's theory. His theory was first applied to the case of a constant wall-to-liquid temperature difference and the resultant theoretical curves are shown on Figure 6-28 as Case 1. The data of Dougall and Rohsenow (D-5) and the data of this work are also included in the Figure. These data were taken with constant heat flux boilers and will not be strictly applicable to the constant temperature theory. This factor is expected to be only of minor importance, however, because the wall temperatures were fairly constant over much of the heater surface during both of these experimental tests. Moreover, the predicted heat transfer coefficients by Hsu's theory, as presented in reference (H-5), were almost constant as ΔT changed, so his theory suggests that constant heat flux and constant temperature boilers will be similar.

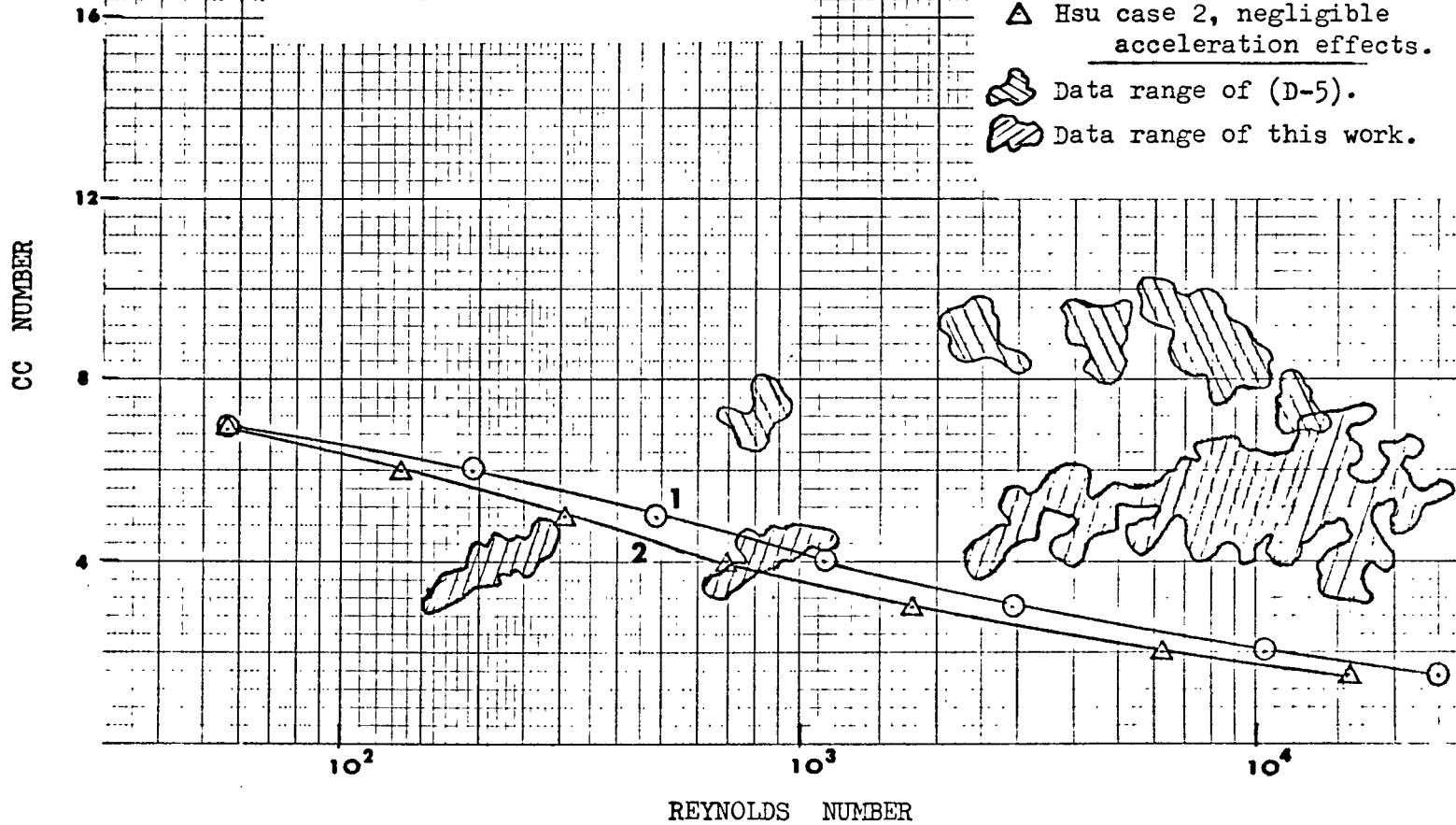
The second special case of Hsu's theory to be presented here did not include the acceleration terms. An analytical solution was then attainable and these results are presented in Figure 6-28 as Case 2. Some groupings of physical properties remain in the final solution for both special cases. Therefore, the theoretical curves include the saturation temperature and the average vapor temperature as parameters. The curves of Figure 6-28 were based on the physical properties of Freon-113 boiling at one atmosphere pressure with a temperature difference of 400 degrees F. These conditions approximate the data reported, but the position of the curves changes very little when much different temperatures are used.

It can be seen from Figure 6-28 that Hsu's theory predicts CC numbers that are much lower (heat transfer coefficients that are much

FIGURE 6-28

THEORY of HSU (H-5)
Applied to Freon-113 boiling at
1 atm. pressure and 400° F. ΔT

- Hsu case 1, constant ΔT .
- △ Hsu case 2, negligible acceleration effects.
- ▨ Data range of (D-5).
- ▨ Data range of this work.



higher) than the experimental data except at low Reynolds numbers. In addition, the trend of the CC numbers predicted by the theory is not the same as the experimental trend. These conclusions apply to both special cases. The divergence between the data and the theory is apparently the result of understating the resistance to turbulent momentum and energy transport within the vapor film. A significant fraction of this resistance is included in the turbulent core, but this region was not considered by Hsu.

CHAPTER VIICONCLUSIONS AND RECOMMENDATIONS

It has been shown that the vertical film boiling process is controlled by both the velocity distribution within the vapor and liquid phases and the oscillations of the vapor-liquid interface. This complex process can be approximated by a two step analysis. First, the quasi-steady state condition is analyzed at one instant in time and the heat transfer rate is predicted according to the velocity and temperature profiles that exist at that instant. Then the unsteady state condition, which is characterized by a variable location of the interface due to wave motion, is analyzed and the heat transfer rate at each instant is determined from the results of the quasi-steady state analysis. For the quasi-steady state condition, a full theory has been developed which includes the interfacial velocity and roughness, but the roughness effects are developed through a parameter that is not yet fully defined. A partial theory has been developed for the effects of the interfacial oscillations, and measurements of the wall heat flux variations indicate a remarkable constancy of the wave parameter, η_0 , over a fairly wide range of conditions. This theoretical analysis has provided a framework within which some apparently divergent data sets can be contained, including the data of Dougall and Rohsenow which involved relatively little wave action and the data from this study for which wave action was large.

The experimental studies have touched upon several important aspects

of the mechanisms of film boiling, and some previously unreported observations were made. It was noticed that the direction of heat transfer is momentarily reversed under some conditions with energy flowing from the vapor to the heater surface. Also, large pressure pulses were observed within the fluid near the heater wall. These phenomena are the results of large interfacial waves. In addition, it was affirmed that the waves can be large enough to cause occasional liquid-solid contact without destroying the film boiling regime. On the other hand, the interfacial wave action was reduced in the presence of subcooled bulk liquid and the dominant frequencies of the waves were then shifted to higher values.

Because film boiling is such a complex physical process, many questions regarding its controlling mechanisms are not yet fully answered. The need for additional experimental and theoretical studies has been demonstrated. Local heat transfer rates at high Reynolds numbers should be measured to clearly define the data trend in this region. The stability characteristics of forced convection film boiling in a conduit should be investigated to determine the conditions at which a two-phase flow regime becomes the stable mode. Studies of the interaction between the transport phenomena within the fluid and the nature of the heating surface are required to provide criteria for predicting the occurrence of liquid-solid contact. Finally, theoretical and experimental guidance is needed for predicting the effects of interfacial activity on the transport processes. In particular, a generalized method for estimating the value of the interfacial roughness parameter (ϵ'/ν) is required, as are more detailed measurements of the shape and size of the interfacial waves.

APPENDIX A

FORCED CONVECTION FILM BOILING IN A VERTICAL CONDUIT
WITH
LAMINAR FLOW OF BOTH PHASES

Symmetrical flow between parallel plates will be considered with film boiling occurring at the same rate on each plate. The geometry is illustrated in Figure A-1. For simplicity, the flow is assumed to be fully developed and the interfaces to be smooth. The pressure gradient is such as to cause a liquid mass flow rate of W_L and a gas flow rate of W_G . The Navier-Stokes equations reduce to the same form for both the liquid and the gas phases:

$$\frac{d^2 u}{dy^2} = -\frac{1}{\mu} \left(-\frac{dP}{dx} - \rho g \right) = -\beta \quad \text{A-1}$$

where β is constant and defined above. Integrating twice gives the velocity profiles:

$$u = -\frac{1}{2} \beta y^2 + C_1 y + C_2 \quad \text{A-2}$$

$$u_L = -\frac{1}{2} \beta_L y^2 + C_{1L} y + C_{2L} \quad \text{A-3}$$

where no subscript indicates vapor phase, subscript L indicates liquid phase, and C_1 and C_2 are constants of integration. The boundary

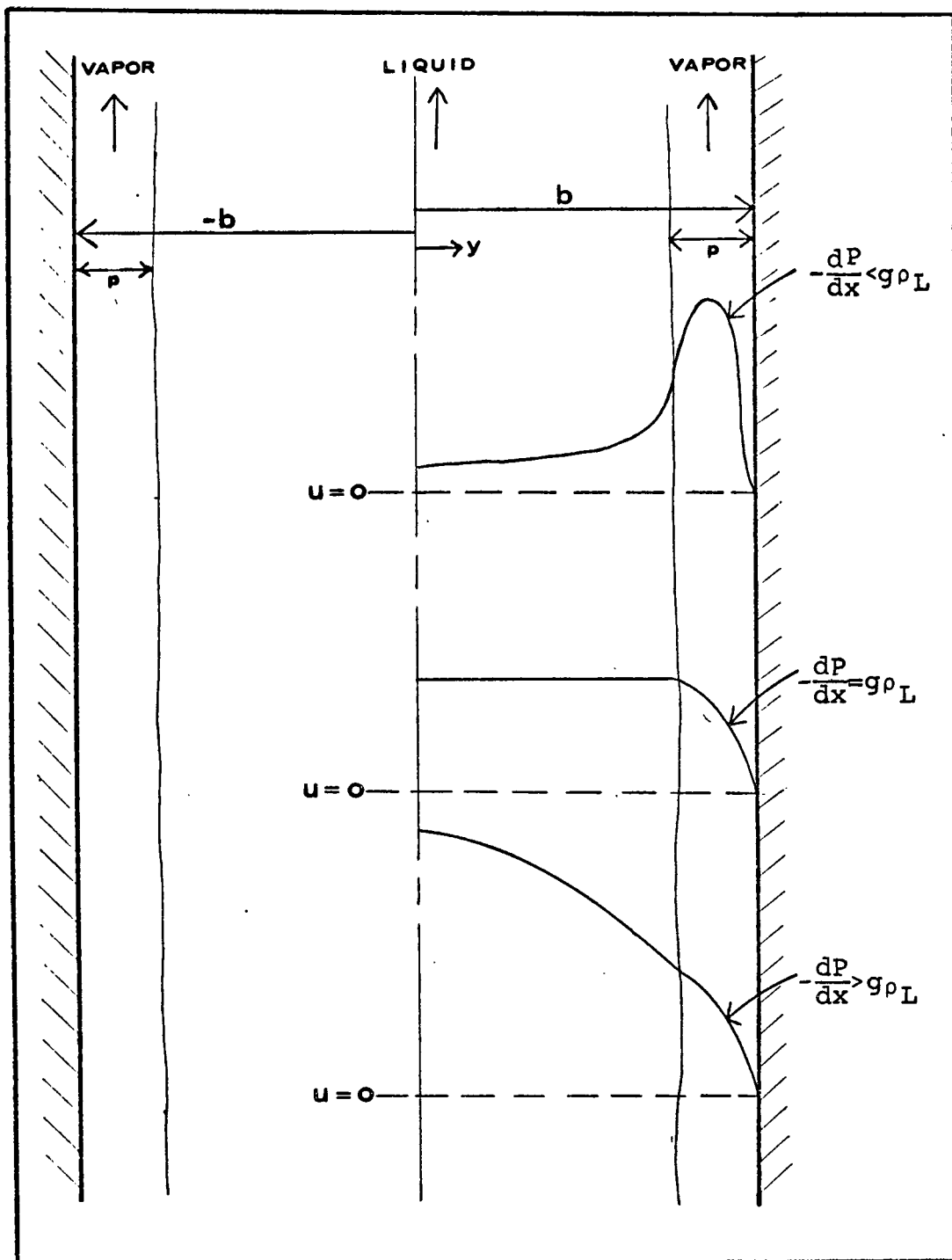


FIGURE A-1. SYMMETRICAL FILM BOILING WITH LAMINAR FORCED CONVECTION FLOW BETWEEN PARALLEL PLATES

conditions to be applied are:

$$y = b, \quad u = 0 \quad \text{A-4}$$

$$y = b - p, \quad u = u_L = u_i \quad \text{A-5}$$

$$y = b - p, \quad \tau = \tau_L = \tau_i \Rightarrow \mu \frac{du}{dy} = \mu_L \frac{du_L}{dy} \quad \text{A-6}$$

$$y = 0, \quad \tau_L = 0 \Rightarrow \frac{du_L}{dy} = 0 \quad \text{A-7}$$

Applying these boundary conditions gives the velocity profiles as functions of the geometric parameters, b and p , and the pressure gradient which is included in β :

$$u = \frac{1}{2} \beta (b^2 - y^2) + \left(\frac{\mu_L}{\mu} \beta_L - \beta \right) (b - p)(b - y) \quad \text{A-8}$$

$$u_L = \frac{1}{2} \beta_L [(b - p)^2 - y^2] + \frac{1}{2} \beta p (2b - p) + p(b - p) \left(\frac{\mu_L}{\mu} \beta_L - \beta \right) \quad \text{A-9}$$

For a maxima to exist in the vapor phase, the value of y_m must be greater than $(b - p)$, where y_m is the position at which du/dy of equation A-8 is zero:

$$y_m = (b - p) \left(1 - \frac{\mu_L \beta_L}{\mu \beta} \right) \quad \text{A-10}$$

Then, a vapor phase maxima occurs when:

$$\left(1 - \frac{\mu_L \beta_L}{\mu \beta} \right) \geq 1.0 \quad \text{A-11}$$

From the definition of β in equation A-1, equation A-11 reduces to:

$$-\frac{dP}{dx} \leq g\rho_L \quad \text{A-12}$$

If the pressure gradient term is broken up into two parts as follows:

$$-\frac{dP}{dx} = \left(-\frac{dP}{dx}\right)_f + g\rho_L \quad \text{A-13}$$

it is seen that a maxima exists in the vapor phase only when the frictional pressure gradient is negative, as was discussed in Chapter III, Section G. If this is the case, β_L is always negative and the velocity gradient in the liquid, found from equation A-9, is always positive:

$$\frac{du_L}{dy} = -\beta_L y > 0 \quad \text{A-14}$$

Thus, with a maxima in the vapor phase, the velocity profile in the liquid is always concave upward as given by profile number 2 on Figure 3-2.

When $g\rho_L = -\frac{dP}{dx}$, the maxima in the vapor phase velocity occurs at the interface and β_L equals zero. Then, from equation A-9:

$$u_L = \frac{\rho^2}{2\mu} \left(-\frac{dP}{dx} - g\rho\right) = \text{constant} \quad \text{A-15}$$

If $\left(-\frac{dP}{dx}\right) > g\rho_L$, no maxima exists in the vapor phase velocity profile.

Then β_L is positive and $\frac{du_L}{dy}$ is negative (see equation A-14), and the velocity profile in the liquid is concave downward as is profile number 3

in Figure 3-2. The maximum velocity in the system then occurs in the liquid at the point $y = 0$.

It now becomes of interest to determine what flow rates of vapor and liquid lead to these various cases. To accomplish this, the velocity profiles are integrated to give the mass flow rate for a plate of unit depth:

$$W_G = 2\rho \int_{b-p}^b u dy \quad \text{A-16}$$

$$W_L = 2\rho_L \int_0^{b-p} u_L dy \quad \text{A-17}$$

After much algebraic manipulation, this leads to:

$$\frac{W_G}{W_L} = \frac{\phi^2 \left(\frac{\rho}{\rho_L} \right) \left[1 - \frac{1}{3}\phi - (1-\phi) \left(\frac{1 - \frac{\rho}{\rho_L}}{\phi - \frac{\rho}{\rho_L}} \right) \right]}{(1-\phi) \left[\frac{2\mu}{3\mu_L} \cdot \left(\frac{\sigma-1}{\sigma - \frac{\rho}{\rho_L}} \right) (1-\phi^2) + \phi(2-\phi) - 2\phi(1-\phi) \left(\frac{1 - \frac{\rho}{\rho_L}}{\sigma - \frac{\rho}{\rho_L}} \right) \right]} \quad \text{A-18}$$

where $\phi = \frac{p}{b}$ and $\sigma = \frac{(-\frac{dp}{dx})}{g\rho_L}$.

For the maxima in the velocity profile to exist in the vapor phase, it is necessary that $\sigma \leq 1$. For the dividing case where $\sigma = 1$, equation A-18 reduces to:

$$\frac{W_G}{W_L} = \frac{2}{3} \frac{\phi \left(\frac{\rho}{\rho_L} \right)}{1-\phi} \quad \text{A-19}$$

The ratio of W_G to W_L will be estimated for specified values of the parameters. The maximum expected value of ϕ is no more than about 0.5, since vapor film thicknesses larger than this are certain to be unstable. For reasonably sized conduits, ϕ will be 0.2 or less, since the thickness of the vapor film is of the order of 0.05 inches. Using the larger value of 0.5 for ϕ and a density ratio on the order of 0.003, W_G/W_L is 0.001 when $\sigma = 1$. Thus, as soon as the vaporization rate of liquid reaches 0.1% of the feed, the maxima of the velocity profile will go into the vapor phase. Using a more realistic value for ϕ will reduce this figure considerably.

These estimates indicate that the maximum velocity will normally be in the vapor phase, and profiles of type 2 will prevail in laminar film boiling within a conduit. Because of mathematical complexities, such estimates would be quite difficult to make for turbulent film boiling within a conduit or for forced convection pool film boiling. However, similar conclusions would be expected for these cases.

In Chapter III, Section G, the frictional pressure drop was put in terms of the parameter, η_f , defined as follows:

$$-\frac{dP}{dx} = \left(-\frac{dP}{dx}\right)_f + g\rho_L = \eta_f g\rho_L \quad 3-80$$

$$\eta_f = 1 + \frac{\left(-\frac{dP}{dx}\right)_f}{g\rho_L} \quad 3-81$$

In terms of the definition of β from equation A-1, η_f may be restated as either:

$$\eta_f = 1 + \frac{\beta_L \mu_L}{g \rho_L} \quad \text{A-20}$$

$$\eta_f = \frac{\rho}{\rho_L} + \frac{\beta \mu}{g \rho_L} \quad \text{A-21}$$

Determining η_f requires first that β or β_L be known. These terms can be found after integration of equations A-16 and A-17 to obtain the following:

$$W_G = 2\rho p^2 \beta (b - \frac{2}{3}p) + 2\rho p \left(\frac{\mu_L}{\mu} \beta_L - \beta \right) (b-p) (b - \frac{1}{2}p) \quad \text{A-22}$$

$$W_L = \frac{2}{3} \rho_L \beta_L (b-p)^3 + 2\rho_L p (b-p)^2 \left(\frac{\mu_L}{\mu} \beta_L - \beta \right) + \rho_L p \beta (2b-p)(b-p) \quad \text{A-23}$$

A relationship between β_L and β can be derived from their definition in equation A-1:

$$\beta_L = \beta \frac{\mu}{\mu_L} - \frac{g}{\mu_L} (\rho_L - \rho) \quad \text{A-24}$$

In the design problem, the physical properties, the plate spacing of $2b$, and the mass flow rates of W_G and W_L are generally specified. Then, equations A-22 through A-24 can be solved simultaneously for the values of the three variables; the vapor film thickness, p , β and β_L . From equation

A-1, the pressure drop can then be calculated. This finally leads to the desired value of η_f from equation 3-80.

APPENDIX B

THE NATURE OF THE ROUGHNESS PARAMETER

The x-direction Reynolds equation is:

$$u \frac{du}{dx} + v \frac{dv}{dy} = -\frac{1}{\rho} \frac{dP}{dx} - g - \frac{1}{\rho} \frac{d\tau_{xx}}{dx} - \frac{1}{\rho} \left(\frac{d\tau_{yx}^l}{dy} + \frac{d\tau_{yx}^t}{dy} \right) \quad \text{B-1}$$

The superscripts refer to the laminar and turbulent shear stress terms.

For the case of fully developed flow, v , $\frac{du}{dx}$, and $\frac{d\tau_{xx}}{dx}$ are all zero.

In this case:

$$\frac{d}{dy} (\tau_{yx}^l + \tau_{yx}^t) = -\frac{dP}{dx} - \rho g = \text{constant} \quad \text{B-2}$$

For smooth conduits, the shear stress is written in terms of the velocity gradient as follows:

$$\tau_{yx}^l = \mu \frac{du}{dy} \quad \tau_{yx}^t = \rho \epsilon \frac{du}{dy} \quad \text{B-3}$$

From equations B-2 and B-3:

$$\tau_{yx} = (\mu + \rho \epsilon) \frac{du}{dy} = \left(-\frac{dP}{dx} - \rho g \right) y + C_1 \quad \text{B-4}$$

This is equivalent to the starting point in the quasi-steady state theory of Chapter III.

In the case of flow over a rough surface, the roughness elements will induce a y-direction velocity component near the wall, which in turn results in a non-zero value for $\frac{dv}{dx}$. Thus, the full equation B-1 should apply. However, in Chapter III the momentum transport equation for rough conduits was written:

$$\frac{d}{dy} \left[(\mu + \rho\varepsilon + \rho\varepsilon') \frac{du}{dy} \right] = -\rho g - \frac{dP}{dx} \quad \text{B-5}$$

By comparison with the previous equations, this is equivalent to the statement that:

$$\frac{d}{dy} (\rho\varepsilon' \frac{du}{dy}) = -\rho u \frac{du}{dx} - \rho v \frac{du}{dy} - \frac{d\tau_{xx}}{dx} \quad \text{B-6}$$

or that:

$$\varepsilon' \frac{du}{dy} = - \int \left(u \frac{du}{dx} + v \frac{du}{dy} + \frac{1}{\rho} \frac{d\tau_{xx}}{dx} \right) dy \quad \text{B-7}$$

For small roughnesses, the convective acceleration terms are likely to be significant only near the rough surface. It would be expected, therefore, that ε' has a maximum value near the wall and then decreases as the center of the conduit is approached. These considerations could also explain the experimental measurements of Worley (W-5) in which the measured shear stress distribution was linear only in the center two-thirds of the channel and began to decrease rapidly near the wall.

Although ε' has been assumed constant in this work, it will be of interest to attempt to determine its dependence on position. For mathematical convenience, it will be assumed that $\frac{d\tau_{xx}}{dx}$ is negligible.

From the continuity equation:

$$\frac{du}{dx} + \frac{dv}{dy} = 0 \quad \text{B-8}$$

it follows that:

$$u \frac{du}{dx} + v \frac{du}{dy} = -u^2 \frac{d}{dy} \left(\frac{v}{u} \right) \quad \text{B-9}$$

Then equation B-7 can be written:

$$\varepsilon' \frac{du}{dy} = \int u^2 d\left(\frac{v}{u}\right) \quad \text{B-10}$$

Since the roughness effects can be expected to occur only near the wall, it seems reasonable to suppose that u is linear with respect to y in this region:

$$u = ay \quad \text{B-11}$$

Although u and v both approach zero at the wall, it is postulated that the ratio approaches a finite limit, and decays exponentially away from the wall, so that :

$$d\left(\frac{v}{u}\right) = -k_0 e^{-k_1 y} dy \quad \text{B-12}$$

Then:

$$\varepsilon' = -a k_0 \int y^2 e^{-k_1 y} dy \quad \text{B-13}$$

And:

$$\varepsilon' = e^{-k_1 y} (a_0 + a_1 y + a_2 y^2) \quad \text{B-14}$$

Not enough experimental data is available to evaluate this approach to the determination of \mathcal{E}' , but more data of the type taken by Worley would be sufficient. Until further evidence is available, it seems reasonable to let \mathcal{E}' be some constant average value across the entire flow field.

APPENDIX C

TRUE AVERAGE VAPOR SPACE TEMPERATURE

In Chapter III, Section J, the true average vapor temperature was defined as:

$$\bar{T} = T_s + \frac{\int_0^p u(T-T_s) dy}{\int_0^p u dy} \quad \text{C-1}$$

This definition for the average temperature follows from the rigorous calculation of the total superheat, Q_{SH} , in the vapor:

$$Q_{SH} = \rho C_p \int_0^p u(T-T_s) dy \equiv \rho C_p (\bar{T}-T_s) \int_0^p u dy \quad \text{C-2}$$

It will be convenient to use the arithmetic mean film temperature, defined as:

$$\bar{T}_A = \frac{1}{2} (T_w + T_s) \quad \text{C-3}$$

Therefore, equation C-2 will be rewritten using \bar{T}_A in place of \bar{T} , and a deviation factor, β_T , will be defined to account for the error that this incurs. Then the resulting equation will be examined to determine the size of β_T . The procedure is as follows:

$$Q_{SH} = \beta_T (\bar{T}_A - T_s) \rho C_p \int_0^p u dy = \beta_T \left(\frac{\Delta T}{2} \right) \rho C_p \int_0^p u dy \quad \text{C-4}$$

where ΔT is $(T_w - T_s)$ and β_T is defined as:

$$\beta_T = \frac{(\bar{T} - T_s)}{\frac{1}{2} \Delta T} \quad \text{C-5}$$

When β_T is equal to one, the arithmetic average temperature will be the true average. From equations C-5 and C-1, it follows that:

$$\beta_T = \frac{2 \int_0^p u (T - T_s) dy}{\Delta T \int_0^p u dy} \quad \text{C-6}$$

The above integration was carried out using the velocity and temperature profiles developed by the theory of Chapter III. This gave the relationship between β_T and the parameters that define the film boiling process: Re , Pr , ϵ/ν and u_i/u_m . Before proceeding, however, equation C-6 was put into dimensionless form as described below. Define I_1 and I_2 as follows:

$$I_1 = \frac{2}{\Delta T} \int_0^p u (T - T_s) dy \quad \text{C-7}$$

$$I_2 = \int_0^p u dy \quad \text{C-8}$$

Substituting the definitions for the dimensionless terms into equations C-7 and C-8 leads to:

$$I_1 = \frac{2\nu}{T_i^+} \int_0^{y^+} u^+ (T_i^+ - T^+) dy^+ \quad \text{C-9}$$

where T^+ is defined by the wall shear stress and temperature. Also:

$$I_2 = \nu \int_0^{p^+} u^+ dy^+ = \frac{1}{2} \nu Re \quad C-10$$

Combining equations C-6 through C-10:

$$\beta_T = 2 - \frac{4}{Re T_i^+} \int_0^{p^+} u^+ T^+ dy^+ \quad C-11$$

Define, now:

$$I_3 = \int_0^{p^+} u^+ T^+ dy^+ \quad C-12$$

For symmetrical flow fields, the above integration could be simply carried to $\frac{1}{2}p^+$ and the result doubled. For the non-symmetrical case with waves, however, the integration must be carried out separately for each part of the flow field and the results put together as has been done for similar cases in Chapter III. Therefore, I_3 is broken up into two parts:

$$I_3 = \int_0^{A^+} u^+ T^+ dy^+ + \int_{A^+}^{p^+} u^+ T^+ dy^+ = I_4 + I_5 \quad C-13$$

where the dimensionless terms are still based on the wall shear stress and temperature. Equations 3-70 and 3-65 from Chapter III may be written in terms of the temperature or velocity at any point instead of at y_m :

$$T^+ = T_i^+ - T_b^+ \left(\frac{A^+}{B^+} \right)^{1/3} \quad C-14$$

$$u^+ = u_b^+ \left(\frac{B^+}{A^+} \right)^{1/3} \quad C-15$$

Since $dy = -dy_b$ and $\frac{y^+}{y_b^+} = \frac{y}{y_b} \cdot \left(\frac{\tau_w}{\tau_i}\right)^{1/2}$, it follows from equations 3-17 and 3-64 and the definition of y^+ that:

$$dy^+ = -\left(\frac{\tau_w}{\tau_i}\right)^{1/2} dy_b^+ = -\left(\frac{A^+}{B^+}\right)^{1/3} dy_b^+ \quad \text{C-16}$$

With these results, I_5 from equation C-13 may be written:

$$I_5 = T_i^+ \int_0^{B^+} u_b^+ dy_b^+ - \left(\frac{A^+}{B^+}\right)^{1/3} \int_0^{B^+} u_b^+ T_b^+ dy_b^+ \quad \text{C-17}$$

Dimensionless terms with the subscript b are defined in terms of the interfacial shear stress and temperature. The B-side Reynolds number has been defined:

$$Re_b = 4 \int_0^{B^+} u_b^+ dy_b^+ \quad \text{3-42}$$

If equation C-14 is written for the point $y = 0$, T_b^+ becomes T_{wb}^+ . This leads to:

$$\left(\frac{A^+}{B^+}\right)^{1/3} = \frac{T_i^+}{T_{wb}^+} \quad \text{C-18}$$

where T_{wb}^+ is the dimensionless wall temperature based on the interfacial conditions. With these definitions and results, equation C-11 can be written:

$$\beta_T = 2 - \frac{Re_b}{Re} - \frac{4}{Re} \left[\frac{1}{T_i^+} \int_0^{A^+} u^+ T^+ dy^+ - \frac{1}{T_{wb}^+} \int_0^{B^+} u_b^+ T_b^+ dy_b^+ \right] \quad \text{C-19}$$

The integration of equation C-19 has been made for several values of the parameters Pr , A^+ , ϵ/ν , and u_i/u_m . It was found that:

$$\beta_T = 1.0 \pm 0.1$$

except for very low Reynolds numbers (less than 500) together with values of ϵ/ν greater than 10, or except for large values of u_i/u_m (greater than 0.4). Even in these cases, the deviation of β_T from 1.0 was less than 20%. The value of β_T affects only the calculated Reynolds number, and this only slightly. Since the heat transfer rate varies slowly with the Reynolds number, these small variations in the value of β_T will have little effect. It was assumed in this work that β_T is unity.

APPENDIX D

THEORY AND CONSTRUCTION OF THE HEAT METER

The basis of the heat meter, as discussed in Chapter V, is the mathematical analogy between electric current in an RC circuit and one-dimensional heat conduction in a solid. This analogy exists because the two physical systems are governed by equivalent differential equations. When the input voltage to the heat meter is directly proportional to the surface temperature of the solid, the heat meter output voltage is directly proportional to the heat flux at the solid surface. The details of the mathematical analogy and the heat meter construction will be discussed in this section.

A. Simplification of the System

The actual heat conduction system being studied involves one-dimensional heat flow between two parallel planes spaced a distance L apart. The average heat flux across any plane is constant and equal to \bar{q} . A temperature disturbance imposed at the surface $x=L$ is here assumed to be sinusoidal for convenience:

$$x = L, \quad T = \bar{T}_L + \gamma \sin(\omega t) \quad \text{D-1}$$

where \bar{T}_L is the time average temperature at this surface. The temperature at $x=0$ is constant at the value T_0 . With these conditions, Carslaw and Jaeger (C-4) give the solution to the conduction equation:

$$\frac{\partial^2 T}{\partial x^2} = \frac{1}{\alpha} \frac{\partial T}{\partial t} \quad \text{D-2}$$

After a time sufficiently long to allow the transient effects to be negligible, the solution is:

$$T = T_0 - \frac{x}{L} (T_0 - \bar{T}_L) + A' \sin (\omega t + \phi')$$

$$A' = \gamma \left(\frac{\cosh 2Kx - \cos 2Kx}{\cosh 2KL - \cos 2KL} \right)^{1/2} \quad \text{D-3}$$

$$\phi' = \arg \left(\frac{\sinh Kx (1+i)}{\sinh KL (1+i)} \right)$$

where:

$$K = \left(\frac{\omega}{2\alpha} \right)^{1/2} \quad \text{D-4}$$

$$\bar{q} = \frac{x}{L} (T_0 - \bar{T}_L) \quad \text{D-5}$$

These equations are too cumbersome for convenient usage. Under the proper circumstances, however, this system may be accurately approximated by the case of heat flow in a semi-infinite block with the following boundary conditions:

$$x = 0, \quad T = \bar{T}_0 + \gamma \sin \omega t \quad \text{D-6}$$

$$x \rightarrow \infty, \quad T \rightarrow \bar{T}_0$$

The solution given by Carslaw and Jaeger (C-1) was adjusted to fit the

present situation:

$$T = \bar{T}_0 + \frac{\lambda}{L} (T_L - \bar{T}_0) + \gamma e^{-\lambda x} \sin(\omega t - \lambda x)$$

D-7

where λ is defined above. T_L is the constant temperature at the back wall of the actual heater and the term, $(x/L) \cdot (T_L - \bar{T}_0)$ corresponds to the time-average heat flux given by equation D-5. Of course, if the wall were actually infinite this term would have no meaning. The solution given in equation D-7 can now be applied to a specific physical situation to determine the magnitude of the error introduced by assuming an infinite thickness. For the problem at hand, L is the depth within the nickel wall for which one-dimensional heat flux exists. As seen in Figure 5-8, this is about 3/4 inches. The thermal diffusivity of nickel is about 0.02 square inches per second. The amplitude of the temperature fluctuations at the back wall ($x=L$) can be found from equation D-7:

$$\gamma_L = \gamma e^{-\lambda L}$$

Thus, if the frequency of the surface disturbance is one cps or greater:

$$\frac{\gamma_L}{\gamma} \leq e^{-\frac{3}{4} \left(\frac{2\pi}{0.04} \right)^{1/2}} = 0.0001$$

This shows that all but the very low frequency surface disturbances will be almost completely damped within the nickel wall, and the approximate solution given by equation D-7 may be used to represent the actual process with sufficient accuracy.

Proceeding then with equation D-7, the heat flux is given by:

$$q = -k \frac{dT}{dy} \quad \text{D-8}$$

$$q = -\frac{k}{L} (T_1 - \bar{T}_0) + 2^{1/2} k \gamma e^{-\lambda x} \sin(\omega t - \lambda x + \frac{\pi}{4}) \quad \text{D-9}$$

$$q = \bar{q} + q'$$

where the time average and fluctuating components, \bar{q} and q' , are defined as indicated. The fluctuating component of the heat flux is evaluated at the surface, $x=0$:

$$q'_0 = 2^{1/2} k \gamma \sin(\omega t + \frac{\pi}{4}) \quad \text{D-10}$$

This shows that the surface heat flux and the surface temperature are out of phase by 45 degrees with the flux leading, and that the net energy transfer due to the fluctuating heat flux is zero. Thus, measurements of the amplitude and frequency of a sinusoidal surface temperature variation will lead directly to the surface heat flux by equation D-10. If the surface temperature is a more complex periodic function, equation D-10 may be used for each term of its Fourier expansion.

B. The Electrical Analogy

Unfortunately, the interfacial waves that occur in vertical film boiling and the resultant variations in heat flux to the fluid are random rather than periodic processes. The complex nature of the surface temperature-time relationship precludes any analytical solution to equation D-2.

Therefore, the heat meter, a specialized analog computer, was constructed to solve this equation.

The current within an electrical system with distributed resistance and capacitance is governed by the equation:

$$\frac{d^2 v}{dx^2} = RC \frac{dv}{dt} \quad \text{D-11}$$

with the current given by:

$$i = -\frac{1}{R} \frac{dv}{dt} \quad \text{D-12}$$

where R and C are the resistance and capacitance per unit length. These equations are clearly similar to equations D-2 and D-8. The term RC is equivalent to $(1/\infty)$ in equation D-2 and R is equivalent to $(1/\kappa)$ in equation D-8. Equations D-2 and D-11 are put into dimensionless form as follows:

$$\frac{d^2 T}{dX_1^2} = \frac{dT}{d\Psi_1} \quad \text{D-13}$$

$$\frac{d^2 V}{dX_2^2} = \frac{dV}{d\Psi_2} \quad \text{D-14}$$

The dimensionless variables are defined below.

$$T = \frac{T - \bar{T}_0}{T_{or} - \bar{T}_0}, \quad X_1 = \frac{x_1}{L_1}, \quad \Psi_1 = \frac{\alpha t_1}{L_1^2} \quad \text{D-15}$$

$$V = \frac{v - \bar{v}_o}{v_{or} - \bar{v}_o} \quad , \quad X_2 = \frac{x_2}{L_2} \quad , \quad \psi_2 = \frac{t_2}{RCL_2^2} \quad \text{D-16}$$

L_1 and L_2 are characteristic lengths of the two physical systems, x and t are measures of actual length and time, and subscripts 1 and 2 refer to the heat flux and electric current systems, respectively. \bar{T}_o and \bar{v}_o are time average values of the variables at the surface ($x=0$) while T_{or} and v_{or} are the root mean square averages. They are defined in the following manner:

$$\bar{T}_o = \text{Limit}_{\theta \rightarrow \infty} \frac{1}{\theta} \int_0^\theta T_o dt \quad ; \quad T_{or} = \text{Limit}_{\theta \rightarrow \infty} \left(\frac{1}{\theta} \int_0^\theta T_o^2 dt \right)^{1/2} \quad \text{D-17}$$

The surface temperature of the solid, $T_o(t)$, is transformed into a voltage by a suitable surface thermocouple according to the relationship:

$$T(t) = a_o + a_1 v(t) \quad \text{D-18}$$

where a_o and a_1 are constant conversion factors for the thermocouple. The other characteristic functions of these variables will also follow equation D-18:

$$T_o(t) = a_o + a_1 v_o(t) \quad , \quad \bar{T}_o = a_o + a_1 \bar{v}_o \quad , \quad T_{or} = a_o + a_1 v_{or} \quad \text{D-19}$$

The boundary conditions for equations D-2 and D-11 are:

$$\begin{aligned} x_1 &= 0 \quad , \quad T = T_o \\ x_2 &= 0 \quad , \quad v = v_o = \frac{1}{a_1} (T_o - a_o) \end{aligned} \quad \text{D-20}$$

Upon transformation of these equations to the dimensionless form, the boundary conditions for equations D-13 and D-14 are seen to be identical.

$$X_1 = X_2 = 0 : \quad T = T_0 = V = V_0 \quad \text{D-21}$$

Thus, the dimensionless solutions are also identical:

$$T(X_1, \psi_1) = V(X_2, \psi_2) \quad \text{D-22}$$

A voltage v is measured at the distance x_w from the end of the cable at the time t_w , while the temperature is measured at the distance x_b from the surface of the block at the time t_b . Since the dimensionless terms have the same value for each physical situation:

$$X_1 = \frac{x_b}{L_1} = X_2 = \frac{x_w}{L_2} \quad \Rightarrow \quad \frac{x_b}{x_w} = \frac{L_1}{L_2} \quad \text{D-23}$$

and:

$$\psi_1 = \frac{\alpha t_b}{L_1^2} = \psi_2 = \frac{t_w}{RCL_2^2} \quad \Rightarrow \quad t_b = t_w \left(\frac{x_b}{x_w} \right)^2 \left(\frac{1}{\alpha RC} \right) \quad \text{D-24}$$

The time measures, t_b and t_w , must be equal so that the wire voltages will correspond to heater temperatures in "real time". For this to be true, equation D-24 indicates that the points of measurement for the two systems must be related as follows. When:

$$x_b = x_w (\alpha RC)^{1/2}, \quad t_b = t_w \quad \text{D-25}$$

Dimensionless temperatures at $x_b = x_w (\alpha RC)^{1/2}$ equal dimensionless voltages at x_w :

$$T_{x_b} = V_{x_w} \Rightarrow \frac{T_{x_b} - \bar{T}_o}{T_{or} - \bar{T}_o} = \frac{v_{x_w} - \bar{v}_o}{\frac{1}{a_1} (T_{or} - \bar{T}_o)} \quad \text{D-26}$$

From equations D-26 and D-20:

$$T_{x_b} = \bar{T}_o + a_1 v_{x_w} - a_1 \bar{v}_o = a_o + a_1 v_{x_w} \quad \text{D-27}$$

With this last equation, it has been shown that the instantaneous temperatures and voltages are uniquely related when the points of measurement are specified by equation D-25.

Equations D-13 and D-14 also possess identical derivatives:

$$\frac{dT}{dX_1} = \frac{dV}{dX_2} \quad \text{D-28}$$

From the definitions of these dimensionless groups:

$$\left(\frac{dT}{dX_1} \right)_{X_1 = X_b} = \frac{a_1}{(\alpha RC)^{1/2}} \left(\frac{dV}{dX_2} \right)_{X_2 = X_w} \quad \text{D-29}$$

where equation D-25 defines the relationship between x_b and x_w . With x_b and x_w both set to zero, the heat flux at the surface of the solid can be determined from equations D-8 and D-29.

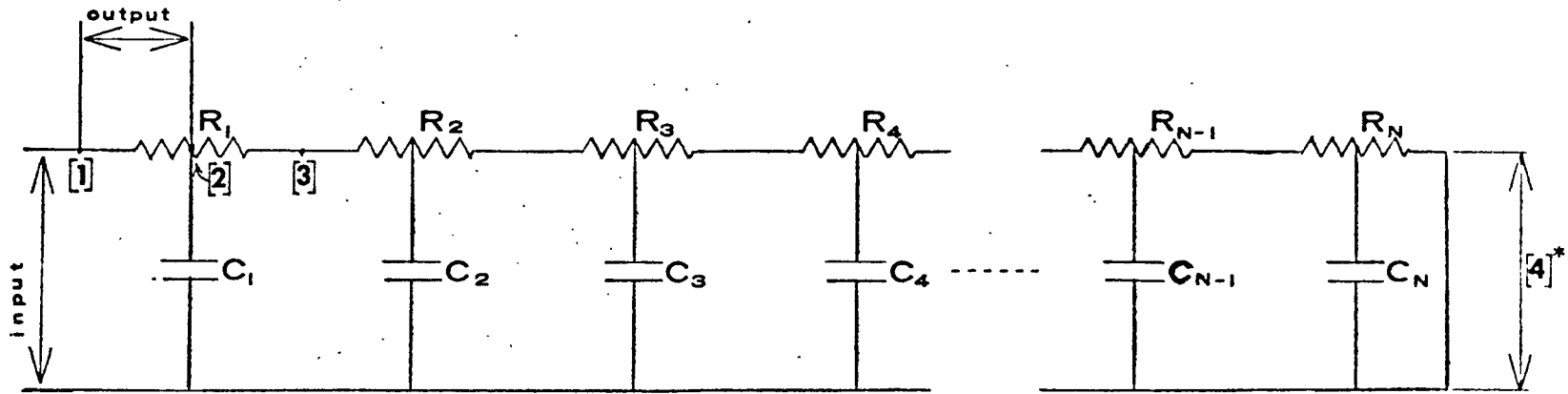
$$q_{x,=0} = - \frac{a_1 k}{(\alpha RC)^{1/2}} \left(\frac{dV}{dX_2} \right)_{X_2 = 0} \quad \text{D-30}$$

The goal of the analogy has now been achieved, in that voltage measurements in an external RC circuit are directly related to heat flux within the solid, and the electrical system may serve as a heat meter.

At this point, the practical value of assuming that the nickel block is infinitely thick becomes clear. When this assumption is valid, only one boundary condition is required for the solution of equation D-2. For the analog circuit then, only one input signal is required which is provided by the surface thermocouple. If the assumption of an infinitely thick block is not accurate enough, however, two boundary conditions would be required for the solution of equation D-2. Physically, this means that two thermocouples would be required to provide input voltages to the electrical analog circuit. The second thermocouple would be buried within the nickel block. It would be connected to point [4] in Figure D-1, which shows the lumped parameter analog circuit that will be discussed next.

C. Lumped Parameter Approximation to the Heat Meter

A typical electrical system with distributed resistance and capacitance will have a very low capacitance. The capacitance of a coaxial cable, for instance, will be on the order of 50×10^{-12} farads per foot. If its resistance were as much as 1000 ohms per foot, a cable length of about $4\frac{1}{2}$ miles would be required to model heat conduction within a $\frac{3}{4}$ inch thick nickel wall. A more practical heat meter is a lumped parameter RC circuit as shown in Figure D-1, which can serve as an approximation to the continuous cable. Each lump or section of this circuit contains a resistor and a capacitor and represents a specific length of cable. The total number of lumps required to be equivalent to a coaxial cable of length



[4]* -Input from buried thermocouple if heater block cannot be considered infinite in depth.

FIGURE D-1
Preliminary Design of Heat Meter

L_w is:

$$N = L_w \left(\frac{RC}{R_1 C_1} \right)^{1/2} \quad \text{D-31}$$

where R_1 and C_1 are the resistance and capacitance within the first lump of Figure D-1, and where the lumps are momentarily assumed to be equally sized. The length of cable equivalent to one lump is then:

$$\chi_w = \frac{L_w}{N} \quad \text{D-32}$$

Combining equations D-31 and D-32:

$$(RC)^{1/2} = \frac{1}{\chi_w} (R_1 C_1)^{1/2} \quad \text{D-33}$$

Then, based on equation D-25, one lump is equivalent to a wall thickness for heat conduction of:

$$\chi_b = (\alpha R_1 C_1)^{1/2} \quad \text{D-34}$$

The size of one section of the lumped parameter circuit must be small enough to accurately model the continuous system, yet large enough to be convenient. For the design in question, the first lump was to be equivalent to an 0.002 inch thick slice of the nickel heater wall. Thus, 350 sections would be required to represent a 3/4 inch thick wall. Meyer (M-2) suggested that the number of RC sections required for the heat meter could be reduced by increasing the RC product of successive sections. Accordingly, the values of the resistors and capacitors in successive sections were increased in an

arithmetic progression. Thus, in Figure D-1:

$$R_2 = 2R_1, R_3 = 3R_1, \dots, R_N = NR_1$$

$$C_2 = 2C_1, C_3 = 3C_1, \dots, C_N = NC_1$$

From equation D-34, successive RC sections correspond to wall thicknesses of x_b , $2x_b$, $3x_b$, and so forth. Twenty-six sections were required for the heat meter used here instead of the 351 sections that would have been needed if the sections had been equally-sized.

The capacitors in Figure D-1 could be connected to the resistors at any point, such as at positions [1], [2], or [3] on resistor R_1 . Meyer (M-2) has shown that the T-arrangement, with the capacitor connected to the center of the resistor at point [2], is the easiest to analyze and has been used here. The design now calls for two resistors between each pair of capacitors. In the construction of the heat meter, these two resistors were combined into a single physical unit, as was shown on Figure 5-16 in Chapter V. As in Chapter V, let r represent the size of the resistors actually used between capacitors. Then in terms of R :

$$\begin{aligned} r_1 &= \frac{1}{2} R_1 \\ r_2 &= \frac{1}{2} (R_1 + 2R_1) = \frac{3}{2} R_1 \\ r_3 &= \frac{1}{2} (2R_1 + 3R_1) = \frac{5}{2} R_1 \\ &\vdots \\ r_{26} &= \frac{1}{2} (25R_1 + 26R_1) = 25\frac{1}{2} R_1 \\ r_{27} &= \frac{1}{2} (26R_1) = 13R_1 \end{aligned}$$

The heat meter output is taken across r_1 in Figure 5-16, or from points [1] to [2] in Figure D-1. In terms of the nomenclature of this section, this is

half of a lump. The corresponding wall thickness for heat conduction is found from equation D-34:

$$\chi_{b,1/2} = \frac{1}{2} (\alpha R_1 C_1)^{1/2} = \left(\frac{1}{2} \alpha r_1 C_1 \right)^{1/2}$$

D-36

In the latter form, this is the dimension Δx given by equation 5-12 in Chapter V.

The parameters for the heat meter used in this work had values of: $R_1 = 28,480$ ohms, $r_1 = 14,240$ ohms, and $C_1 = 0.0102$ microfarads. The thickness of the nickel heater wall represented by r_1 can now be calculated by equation D-36. Since α is a function of temperature, the thickness is also temperature dependent, as is shown below:

<u>Temperature</u> <u>(°F)</u>	<u>$\chi_{b,1/2}$</u> <u>(mils)</u>
200	1.252
300	1.185
400	1.130
600	1.012
800	1.008
1000	1.078

D. Testing the Heat Meter

The accuracy of the heat meter in its final form (Figure 5-16) was determined by comparing its output to the output that would be expected from a distributed system. The test input signal to the heat meter was a known sinusoidal voltage:

$$E_o = \gamma \sin \omega t \quad \text{D-37}$$

With this as a boundary condition at $x = 0$ for a distributed RC system, the solution to equation D-11 can be determined from equation D-7 (which is the solution to equations D-2 and D-6):

$$E = E_o e^{-x(\frac{1}{2}\omega RC)^{\frac{1}{2}}} \sin(\omega t - x\sqrt{\frac{1}{2}\omega RC}) \quad \text{D-38}$$

The voltage drop across a small length, Δx , at $x = 0$ is equal to:

$$\Delta E = \left(\frac{dE}{dx}\right)_{x=0} \cdot \Delta x = E_o (\omega RC)^{\frac{1}{2}} \sin(\omega t + \frac{\pi}{4}) \Delta x \quad \text{D-39}$$

Now let Δx be the distance represented by the first resistor of the heat meter, $r_1 = \frac{1}{2}R_1$, which is one-half the length given by equation D-31:

$$\Delta x = \frac{1}{2} \chi_w = \frac{1}{2} \left(\frac{RC}{\omega}\right)^{\frac{1}{2}} \quad \text{D-40}$$

For this value of Δx , equation D-32 becomes:

$$\Delta E = \frac{1}{2} E_o (\omega RC)^{\frac{1}{2}} \sin(\omega t + \frac{\pi}{4}) \quad \text{D-41}$$

Thus, the voltage across r_1 in the heat meter should have an amplitude of $\frac{1}{2}E_0(\omega R_1 C_1)^{\frac{1}{2}}$ and a leading phase angle of 45° with respect to the input voltage. Test frequencies of one to 1000 cps were applied to the heat meter. Output voltage amplitudes were measured on an rms voltmeter with a rated accuracy of 1% and were found to deviate by less than 3% from the theoretical values. The phase angles were measured on the Weston-Boonshaft and Fuchs wave form analyzer which has a rated accuracy of ± 2 degrees. They were found to be within ± 4 degrees of the expected 45 degrees. Based on these tests, the simplified heat meter circuit was considered to provide an accurate representation of heat conduction within the nickel wall.

E. SUMMARY

The logic leading to the heat meter design will be briefly summarized here. Measuring the heat flux within the solid at the surface is the same as measuring the heat flux from the surface to the fluid. The surface heat flux can be calculated directly from the surface temperature-time relationship if equation D-2 can be solved. For a periodic temperature variation, the exact solution for the heater block in question is given by equation D-3. This is cumbersome to use, but it may be replaced by the solution for an infinite block, as given by equation D-7, since the block thickness is very large compared to the wave lengths of the expected surface temperature disturbances. For random temperature disturbances, however, an analytic solution to equation D-2 is not possible. In this case, a distributed resistance-capacitance electrical system can be used as an analog to the one-dimensional heat transfer system. It will give an output voltage directly proportional to the surface heat flux if its input voltage is directly proportional

to the surface temperature of the heater. For ease of construction, a lumped parameter electrical system is used as the heat meter in place of the distributed system. To reduce the number of RC sections in the lumped system, the RC products of the sections were increased in an arithmetic progression.

APPENDIX E

DETAILS OF OTHER THEORETICAL STUDIESA. The Theory of Dougall and Rohsenow (D-5)

The theory of this work was developed in terms of the dimensionless CC and Re numbers which represent the local heat transfer coefficient and the local flow rate, respectively. They are defined as follows:

$$CC = \frac{h}{k} \left[\frac{g\rho(\rho_f \rho_v - \rho)}{\mu^2} \right]^{1/3} \quad E-1$$

$$Re = \frac{2\bar{u}p}{\nu} = 2 \int_0^{p^+} u^+ dy^+ \quad E-2$$

On the other hand, Dougall and Rohsenow (designated by D-R hereafter) developed their theory in terms of a dimensionless Nusselt number defined as follows:

$$Nu_{D-R} = \frac{hD}{k} \quad E-3$$

where D is the inside diameter of the tube within which film boiling takes place. To compare the two theories, the D-R work was redeveloped in terms of the CC and Re numbers. D-R applied the universal velocity profile to a symmetrical flow field in the vapor film.

$$\begin{aligned} 0 \leq y^+ \leq 5 & & u^+ = y^+ \\ 5 \leq y^+ \leq 30 & & u^+ = -3.05 + 5.0 \ln y^+ \\ 30 \leq y^+ \leq \frac{1}{2} p^+ & & u^+ = 5.5 + 2.5 \ln y^+ \end{aligned} \quad E-4$$

Using equation E-4, they integrated equation E-2 to obtain:

$$60 \leq p^+ : Re = -256 + 6p^+ + 5p^+ \ln\left(\frac{1}{2}p^+\right) \quad \text{E-5}$$

The CC number must now be found as a function of p^+ to give a parametric relationship between the CC and Re numbers.

The heat transfer coefficient is defined as:

$$h = \frac{q}{T_w - T_i} \quad \text{E-6}$$

Based on the definition of T_i^+ , this becomes:

$$h = \frac{\rho c_p}{T_i^+} \left(\frac{T_w}{\rho} \right)^{1/2} \quad \text{E-7}$$

Since the interfacial and wall shear stresses are equal, a force balance across the entire vapor film leads to:

$$T_w = \frac{1}{2} g \rho (\eta_f \rho_L - \rho) \quad \text{E-8}$$

Considering the definition of p^+ , this becomes:

$$\left(\frac{T_w}{\rho} \right)^{1/2} = \left[\frac{\mu g (\eta_f \rho_L - \rho)}{2 \rho^2} p^+ \right]^{1/3} \quad \text{E-9}$$

Equation E-7 can then be written:

$$h = \frac{Pr}{T_i^+} \left(\frac{p^+}{2} \right)^{1/3} \left[\frac{g \rho (\eta_f \rho_L - \rho)}{\mu^2} \right]^{1/3} \quad \text{E-10}$$

This is substituted into equation E-1 to give:

$$CC = \frac{T_i^+}{Pr \left(\frac{1}{2} p^+\right)^{1/3}} \quad \text{E-11}$$

Now T_i^+ must be found in terms of p^+ .

The turbulent transport of heat flux within the vapor film is governed by the equation:

$$q_y = -\left(k + \rho c_p \epsilon_H\right) \frac{dT}{dy} \quad \text{E-12}$$

This is put into dimensionless form with the assumptions that $q_y = q_{\text{wall}}$ and $\epsilon_H = \epsilon$:

$$T_i^+ = Pr \int_0^{p^+} \frac{dy^+}{1 + Pr \frac{\epsilon}{\nu}} \quad \text{E-13}$$

Equation E-11 then becomes:

$$CC = \left(\frac{2}{p^+}\right)^{1/3} \int_0^{p^+} \frac{dy^+}{1 + Pr \frac{\epsilon}{\nu}} \quad \text{E-14}$$

The eddy viscosity distribution is implied by the universal velocity profile and can be derived therefrom by the equation:

$$\frac{\epsilon}{\nu} = \frac{\tau/\tau_w}{du^+/dy^+} - 1 \quad \text{E-15}$$

This function is given by D-R:

$$\begin{aligned}
 0 \leq y^+ \leq 5 & \quad \epsilon_D = 0 \\
 5 \leq y^+ \leq 30 & \quad \epsilon_D = \frac{1}{5} y^+ - 1 \\
 30 \leq y^+ \leq \frac{1}{2} p^+ & \quad \epsilon_D = 0.4 y^+ \left(1 - \frac{2 y^+}{p^+} \right)
 \end{aligned}
 \tag{E-16}$$

The integration of E-14 can then be broken up into three parts and integrated analytically from the wall to the center of the film. The results given by D-R for half of the vapor film when $\frac{1}{2} p^+$ is greater than 30 are:

$$\left(\frac{2}{p^+} \right)^{\frac{1}{3}} \int_0^{\frac{1}{2} p^+} \frac{dy^+}{1 + Pr \frac{\epsilon}{y}} = I_1 + I_2 + I_3
 \tag{E-17}$$

where I_1 , I_2 , and I_3 correspond to those portions of the integration that apply to the laminar, buffer, and turbulent zones of the vapor film, respectively. These terms are:

$$I_1 = 5
 \tag{E-18}$$

$$I_2 = \frac{5}{Pr} (5 Pr + 1)
 \tag{E-19}$$

$$I_3 = \frac{2.5}{\gamma Pr} \ln \left[\frac{(1+\gamma)}{(1-\gamma)} \left(\frac{120/p^+ - 1 - \gamma}{120/p^+ - 1 + \gamma} \right) \right]
 \tag{E-20}$$

$$\gamma = \left(1 + \frac{20}{p^+ Pr} \right)^{\frac{1}{2}}$$

When equations E-14 and E-17 are applied to a symmetrical vapor film:

$$CC_{\text{LBT}} = 2 \cdot (I_1 + I_2 + I_3)
 \tag{E-21}$$

D-R called this result the 'LBT' theory. To account for the interfacial waves which would reduce the resistance to turbulent energy transport, they also proposed the 'BT' and 'T' theories. The 'BT' theory assumed that the laminar sublayer at the interface provided no resistance to energy transport, so that:

$$CC_{BT} = I_1 + 2(I_2 + I_3) \quad E-22$$

According to the 'T' theory, neither the laminar or buffer regions at the interface provided such resistance, so that:

$$CC_T = I_1 + I_2 + 2I_3 \quad E-23$$

Thus, with equation E-5 and one of the equations E-21, E-22, or E-23, the CC versus Re number relationship can be found. These relationships have been plotted in Figure 6-26 in Chapter VI for the 'BT' and 'T' theories. D-R suggested that the 'BT' theory be used at low Reynolds numbers and the 'T' theory at higher values, with a smoothed transition between these two theories. This is shown by the dashed curve on Figure 6-26.

B. The Theory of Hsu (H-5)

The theoretical model of Hsu will be applied to two special cases of film boiling, and the local CC and Reynolds numbers will be determined for each case. The model was discussed in Section H-3 of Chapter VI and it was depicted in Figure 6-27. Since Hsu assumed that most of the vapor flowed in the turbulent core where its density was that of the saturated vapor, ρ_s , he used the saturated density when making a force balance. Almost everywhere

else, however, he evaluated physical properties at the arithmetic average film temperature as was done for the theory presented in this work. In order to redevelop his theory in terms of the parameters of the theory presented here, it was necessary to make some decisions as to which density to use. However, calculations based on various decisions showed that this was not a critical point, and the decisions that were made will not be justified further. Hsu also used the equation suggested by Bromley (B-9) for the effective latent heat of vaporization as was discussed in Section J, Chapter III, and that equation will be used here.

1. The Case of Constant ΔT

The first case to be investigated is that of a constant wall-to-liquid temperature difference (ΔT). Hsu gives the analytical results for the local and space average heat transfer coefficients for this case:

$$h = k \left[\frac{2}{3} \left(\frac{3A}{3B+1} \right) (L-L_0) + y_*^{-2} \right]^{\frac{1}{2}} \quad \text{E-24}$$

$$\bar{h} = \frac{1}{L} \int_0^L h dx \quad \text{E-25}$$

$$\bar{h} = \frac{2}{3} \frac{\lambda' \mu Re_t}{L \Delta T} + \frac{k}{L} \left(\frac{3B+1}{3A} \right) \left[\left\{ \frac{2}{3} \left(\frac{3A}{3B+1} \right) (L-L_0) + y_*^{-2} \right\}^{\frac{3}{2}} - y_*^{-3} \right] \quad \text{E-26}$$

where:

$$A = \frac{g \rho (\rho_L - \rho_s)}{\mu^2} \cdot \frac{\rho / \rho_s}{Re_t^2} \quad \text{E-27}$$

$$B = 1 + \frac{\lambda' \mu}{k \Delta T} \left[1 + f_i Re_t \left(\frac{\rho_s}{2\rho} \right) \right] \quad \text{E-28}$$

$$y_* = \left[\frac{2\mu^2 Re_t}{g\rho(\rho_L - \rho)} \right]^{1/3} \quad \text{E-29}$$

$$\lambda' = \Delta H_v \left[1 + \frac{0.34 c_v \Delta T}{\Delta H_v} \right]^2 \quad \text{E-30}$$

where y_* is the vapor film thickness (y_s) at the point of transition from laminar to turbulent flow, L_0 is the length of the laminar region, L is the length of the heater plate from the start to the point in question, $Re_t = 100$, and f_i can be closely approximated by a constant value of 0.01. The local Reynolds number, based on physical properties at the saturation temperature, is:

$$Re_s = \frac{2\bar{u}\rho}{\nu_s} \quad \text{E-31}$$

It can be stated in terms of the local mass flow rate, W , past the point $x = L$:

$$Re_s = \frac{2W}{f\mu_s} \quad \text{E-32}$$

where f is the perimeter of the heater surface. Then, W can be calculated from the total heat transferred between the points $x=0$ and $x=L$, since ΔT is constant:

$$W = \frac{\bar{h} f L \Delta T}{\lambda'} \quad \text{E-33}$$

The local Reynolds number used in this work, based on evaluation of the physical properties at the mean film temperature, can be written:

$$Re = Re_s \left(\frac{v_s}{\nu} \right) = \frac{2 \bar{h} L \Delta T}{\mu_s \lambda'} \left(\frac{v_s}{\nu} \right) \quad E-34$$

Then, combining equations E-34 and E-26 and using the indicated values of Re_t and f_i :

$$Re = \frac{2 \bar{k} \Delta T (3B+1) v_s}{3 \lambda' \mu_s A \nu} \left[\left\{ \frac{2}{3} \left(\frac{3A}{3B+1} \right) (L-L_0) + y_{\star}^{-2} \right\}^{3/2} - y_{\star}^{-3} \right] + 133 \left(\frac{\rho}{\rho_s} \right) \quad E-35$$

The CC number is defined here as:

$$CC = \frac{\bar{k}}{h} \left[\frac{g \rho_s (\rho_L - \rho_s)}{\mu^2} \right]^{1/3} \quad E-36$$

Combining this with equation E-24 leads to:

$$\frac{2}{3} \left(\frac{3A}{3B+1} \right) (L-L_0) - y_{\star}^{-2} = \frac{g \rho_s (\rho_L - \rho_s)}{\mu^2 (CC)^3} \quad E-37$$

This result was substituted into equation E-36, together with the definitions of A, B and y_{\star} given in equations E-27 through E-29. The result is:

$$Re = 133\left(\frac{\rho}{\rho_s}\right) + \left(2 + \frac{\rho_s}{\rho} + \frac{8k\Delta T}{3\mu\lambda}\right) \left(\frac{10,000\rho_s}{\rho \text{ CC}^3} - 50\right)$$

E-38

In arriving at equation E-38, it had been assumed that:

$$\frac{\rho_L - \rho}{\rho_L - \rho_s} = 1.$$

The relationship between the Reynolds and CC numbers given by equation E-38 was evaluated for Freon-113 boiling at one atmosphere pressure with a ΔT of 400 degrees F. The results were presented as Case 1 in Figure 6-28 in Chapter VI.

2. The Case of Negligible Acceleration Effects

In this case, the local Reynolds and CC numbers were determined as a function of p^+ , the dimensionless vapor film thickness, in much the same way as was done for the theory of Dougall and Rohsenow in Section A of this Appendix. From equations E-31 and E-34, it follows that:

$$Re = 2 \int_0^{p^+} u^+ dy^+$$

E-39

where the dimensionless distances and velocity are based on the wall shear stress. Hsu postulated that the dimensionless thickness of the laminar sub-layer was 10. Therefore:

$$0 \leq y^+ \leq 10 \quad u^+ = y^+$$

$$10 < y^+ \quad u^+ = u_c^+ = 10$$

E-40

Using the velocity profile of equation E-40 in the integration of equation E-39 leads to:

$$Re = 20\rho^+ - 100$$

E-41

The heat transfer coefficient is governed by conduction only across the laminar sublayer, so that:

$$h = \frac{k}{y_s}$$

E-42

Since y_s^+ is equal to 10, its definition leads to:

$$y_s = \frac{10\nu}{\left(\frac{\tau_w}{\rho}\right)^{1/2}}$$

E-43

Upon combining equations E-42, E-43, and E-36:

$$CC = \frac{10\nu}{\left(\frac{\tau_w}{\rho}\right)^{1/2}} \left[\frac{g\rho_s(\rho_L - \rho_s)}{\mu^2} \right]^{1/3}$$

E-44

It remains to determine τ_w as a function of p^+ to complete the solution. This is accomplished by making a force balance over the differential element, where the forces acting are the results of the interfacial and wall shear stresses, gravity, and pressure. The pressure force is the hydrostatic liquid head. (A complete analysis would include the rate of momentum change in the force balance.) The force balance leads to:

$$gp(\rho_L - \rho_S) = \tau_w + \tau_i \quad \text{E-45}$$

It follows from equations 6-39 and E-40 and the definition of u^+ that:

$$\tau_i = \frac{1}{2} f_i \rho_S u_c^2 = \frac{1}{2} f_i \rho_S \left(100 \frac{\tau_w}{\rho}\right) \quad \text{E-46}$$

Since f_i is about 0.01, the previous two equations lead to:

$$\tau_w \left(1 + \frac{1}{2} \frac{\rho_S}{\rho}\right) = gp(\rho_L - \rho_S) \quad \text{E-47}$$

Considering also the definition of p^+ :

$$\left(\frac{\tau_w}{\rho}\right)^{1/2} = \left[\frac{p^+ g \mu (\rho_L - \rho_S)}{\rho^2 \left(1 + \frac{1}{2} \frac{\rho_S}{\rho}\right)} \right]^{1/3} \quad \text{E-48}$$

Substituting equation E-48 into equation E-44 gives:

$$CC = 10 \left[\frac{\frac{\rho_s}{\rho} \left(1 + \frac{1}{2} \frac{\rho_s}{\rho} \right)}{\rho^+} \right]^{1/3} \quad \text{E-49}$$

Finally, combining equations E-49 and E-41 gives the desired result:

$$Re = \frac{20,000 \rho_s}{\rho CC^3} \left(1 + \frac{\rho_s}{\rho} \right) - 100 \quad \text{E-50}$$

Equation E-50 was presented in Figure 6-28 of Chapter VI as Case 2. The ratio of ρ_s/ρ was again calculated for Freon-113 boiling at atmospheric pressure with a ΔT of 400 degrees F.

APPENDIX F

PHYSICAL PROPERTIES

Tables F-1 and F-2 on the following pages contain values of the various physical properties that were required for this work.

TABLE F - 1

Physical Properties of Nickel - 200 and "Pyrex" GlassA. Nickel - 200

T ($^{\circ}\text{F}$)	ρ (LB_M/in^3)	C_p ($\text{Btu}/\text{LB}_M^{\circ}\text{F}$)	k ★	α (ft^2/hr)
200	0.320	0.113	33.9	0.542
400	0.318	0.126	30.5	0.441
600	0.316	0.140	27.0	0.354
800	0.314	0.138	26.4	0.351
1000	0.312	0.130	28.4	0.404
1200	0.310	0.135	30.5	0.422

Source: Reference (H-4)

B. "Pyrex" GlassT = 25 $^{\circ}\text{C}$

$$\rho = 139 \text{ LBM}/\text{ft}^3$$

$$C_p = 0.20 \text{ Btu}/\text{LB}_M^{\circ}\text{F}$$

$$k = 0.56 \text{ Btu}/\text{hr}^{\circ}\text{F}\text{-ft}$$

$$\alpha = 0.020 \text{ ft}^2/\text{hr}$$

Source: Reference (C-12)

★ Units are ($\text{Btu}/\text{hr}^{\circ}\text{F}\text{-ft}$)

TABLE F - 2

Physical Properties of Freon - 113 at one AtmosphereA. Vapor Pressure (psia)¹

$$P = (T - 120) \times 0.282 + 15.4 \quad (T \text{ in } ^\circ\text{F})$$

B. Latent Heat of Vaporization (Btu/LB_M)

$$\Delta H_v = 0.0825 \times (T - 120) + 62.9 \quad (T \text{ in } ^\circ\text{F})$$

C. Liquid Properties

<u>T (°F)</u>	<u>ρ_L(LB_M/ft³)</u>	<u>μ_L(cp)</u>	<u>k̄ (Btu/hr-°F-ft)</u>	<u>c_p(Btu/LB_M-°F)</u>
40	100.6	0.876	0.045	0.20
60	99.0	0.747	0.044	0.21
80	97.4	0.646	0.042	0.21
100	95.8	0.564	0.041	0.22
120	94.1	0.497	0.039	0.22
140	92.3	0.442	0.038	0.23

D. Vapor Properties

$$(1) \quad c_p = .1455 + 0.000111 \times T \quad (\text{Btu/LB}_M\text{-}^\circ\text{F}), (T \text{ in } ^\circ\text{F})$$

(2) <u>T (°F)</u>	<u>μ (cp)</u>	<u>k̄ (Btu/hr-°F-ft)</u>	<u>c_p/c_v</u>
120	0.0108	5.1 x 10 ⁻³	
160	0.0113	5.7	1.077
200	0.0118	6.4	1.073 (210°F)
240	0.0123	7.1	
300	0.0130	8.1	1.070 (260°F)
350	0.0134	8.9	
400	0.0141	9.7	
450	0.0147	10.6	
500	0.0152	11.4	
550	0.0158	12.2	

¹ This equation is accurate for T = 120 ± 10°F

TABLE F - 2 (Continued)Physical Properties of Freon-113 at One Atmosphere(3) Density (LB_m/ft³)

Beattie - Bridgeman Equation:

$$P = (T \times 5 \times 10^{-5} - 0.0214) \times \rho^3 \\ + (T \times 2.618 \times 10^{-3} - 4.035) \times \rho^2 + 0.05728 \times T \times \rho$$

T (°R) , P (psia)

Source: References (E-1) and (E-2)

APPENDIX G

BIBLIOGRAPHY

- A-1 Avitts, L. A., American Packing and Gasket Co., Private Communication.
- B-1 Bankoff, S. G., and V. S. Mehra, "A Quenching Theory for Transition Boiling", Ind. and Eng. Chem. Fund., 1, 38 (1962)
- B-2 Bendersky, D., "A Special Thermocouple for Measuring Transient Temperatures", Mechanical Engineering, 117 (1953)
- B-3 Borishanskii, V. M., and B. S. Fokin, "Correlation of Heat Transfer Data in Stable Film Boiling on Vertical Surfaces in the Presence of Free Liquid Convection in Large Volumes", Int. Chem. Eng., 5, 666 (1965)
- B-4 Borishanskii, V. M., P. A. Maslichenko, and B. S. Fokin, Teplo - i Masso - perenos (Heat and Mass Transfer), 2, Izd - vo Akad. Nauk BSSR, Minsk, 128 (1962)
- B-5 Bradfield, W. S., "Wave Generation at a Stagnation Point in Stable Film Boiling", Symposium on Two Phase Flow, 2, A301, U. of Exeter, Devon, England (1965)
- B-6 Bradfield, W. S., R. O. Barkdoll, and J. T. Byrne, "Film Boiling on Hydrodynamic Bodies", Research Note 37, Convair Scientific Research Lab. (1960)
- B-7 Brand, Louis, Advanced Calculus, 497, John Wiley & Sons, Inc., New York (1960)
- B-8 Bromley, L. A., "Heat Transfer in Stable Film Boiling", Chem. Eng. Prog., 46, 221 (1950)
- B-9 Bromley, L. A., "Heat Transfer in Condensation, Part II, Effect of Heat Capacity on Condensate", Ind. and Eng. Chem., 44, 2966 (1952)
- B-10 Bromley, L. A., N. R. LeRoy, and J. A. Robbers, "Heat Transfer in Forced Convection Film Boiling", Ind. and Eng. Chem., 45, 2639 (1953)
- C-1 Carslaw, H. S., and J. C. Jaeger, Conduction of Heat in Solids, 2nd edition, 65, Oxford at the Clarendon Press (1959)

- C-2 *ibid.*, p 71
- C-3 *ibid.*, p 88
- C-4 *ibid.*, p 105
- C-5 Cashler, F., "Solutions of the Boundary Layer Equations for Turbulent Forced Convection Film Boiling", Master's Thesis, U. of Houston (1965)
- C-6 Cess, R. D., and E. M. Sparrow, "Film Boiling in a Forced-Convection Boundary - Layer Flow", Trans. ASME, J. Heat Transfer, 83, 370 (1961)
- C-7 Cess, R. D., and E. M. Sparrow, "Subcooled Forced-Convection Film Boiling on a Flat Plate", Trans. ASME, J. Heat Transfer, 83, 377 (1961)
- C-8 Chi, J. W. H., "A Correlation for Forced Convective Boiling Heat Transfer to Hydrogen", Preprint 38e, AIChE 57th Annual Meeting, Boston (1964)
- C-9 Class, C. R., J. R. DeHaan, M. Piccone, and R. B. Cost, "Pool Boiling Heat Transfer to a Cryogenic Liquid", WADC Technical Report 58-528, Wright-Patterson Air Force Base, Ohio (1958)
- C-10 Concus, P., "Standing Capillary-Gravity Waves of Finite Amplitude", J. Fluid Mechanics, 14, 568 (1962)
- C-11 Corcoran, W. H., F. Page, W. G. Schlinger, and B. H. Sage, "Temperature Gradients in Turbulent Gas Streams", Ind. and Eng. Chem., 44, 410 (1952)
- C-12 Corning Glass Works, "Properties of Selected Commercial Glasses", Corning, New York (1963)
- D-1 Deissler, R. G., "Analytical and Experimental Investigation of Adiabatic Turbulent Flow in Smooth Tubes", NACA Technical Note 2138 (1950)
- D-2 Deissler, R. G., "Analysis of Turbulent Heat Transfer and Flow in the Entrance Regions of Smooth Passages", NACA Technical Note 3016 (1953)
- D-3 Deissler, R. G., and A. L. Loeffler "Analysis of Turbulent Flow and Heat Transfer on a Flat Plate at High Mach Numbers with Variable Fluid Properties", NASA Report R-17 (1959)
- D-4 Dougall, R. S., Private Communication (1966)

- D-5 Dougall, R. S., and W. M. Rohsenow, "Film Boiling on the Inside of Vertical Tubes with Upward Flow of the Fluid at Low Qualities", EPL Report No. 9079-26, MIT Dept. of Mech. Eng. (1963)
- D-6 Dukler, A. E., "Fluid Mechanics and Heat Transfer in Vertical Falling-Film Systems", C.E.P. Symposium Series, 56, No. 3, 1, (1960)
- D-7 Dukler, A. E., and M. Wicks, "Gas-Liquid Flows in Conduits", Chap. 8, Modern Chemical Engineering, 1, Editor, A. Acrivos, Reinhold Publishing Corp., N. Y. (1963)
- E-1 E. I. du Pont de Nemours & Co., " 'Freon' Technical Bulletin No. B-9A", Wilmington, Delaware
- E-2 E. I. du Pont de Nemours and Co., "Thermodynamic Properties of 'Freon-113' ", Bulletin No. T-113A, Wilmington, Delaware (1938)
- E-3 Ellion, M. E., "A Study of the Mechanism of Boiling Heat Transfer", Memorandum No. 20-88, Jet Propulsion Lab., Calif. Ins. of Tech.
- F-1 Frederking, T. H. K., "Stability of Film Boiling Two-Phase Flow in Cryogenic Systems", Preprint 216, 52nd National Meeting, AICHE, Memphis (1964)
- G-1 Gill, W. M., and M. Scher, "A Modification of the Momentum Transport Hypothesis", A.I.Ch.E. Jour., 7, 61 (1961)
- G-2 von Glahn, U. H., "A Correlation of Film-Boiling Heat-Transfer Coefficients Obtained with Hydrogen, Nitrogen, and Freon-113 in Forced Flow", NASA TN D-2294 (1964)
- H-1 Hamill, T. D., and S. G. Bankoff, "Growth of a Vapour Film at a Rapidly Heated Plane Surface", Chem. Eng. Science, 18, 355 (1963)
- H-2 Hendricks, R. C., R. W. Graham, Y. Y. Hsu, and R. Friedman, "Experimental Heat Transfer and Pressure Drop of Liquid Hydrogen Flowing through a Heated Tube", NASA TN D-765 (1961)
- H-3 Hottel, H. C., "Heat Transmission by Radiation from Non-Luminous Gases", Ind. and Eng. Chem., 19, 888 (1927)
- H-4 Huntington Alloy Products Division, The International Nickel Co., Inc., "Handbook of Huntington Alloys", Huntington, W. Va. (1963)
- H-5 Hsu, Y. Y., "Film Boiling on Vertical Surfaces", PhD Dissertation, U. of Illinois (1958)

- H-6 Hsu, Y. Y., and J. W. Westwater, "Approximate Theory for Film Boiling on Vertical Surfaces", Preprint No.103, 3rd National Heat Trans. Conf., ASME - A.I.Ch.E., Conn. (1959)
- J-1 Jakob, Max, Heat Transfer, 1, 124, John Wiley & Sons, N. Y. (1956)
- J-2 Johnson, V. J., "A Compendium of the Properties of Materials at Low Temperature (Phase 1), Part 1: Properties of Fluids", WADD Technical Report, 60-56 (1960)
- K-1 Kapitsa, P. L., "Undular Flow of Thin Layers of a Viscous Liquid, I. Free Flow", In translation from: Zh. E K Sperim. (Theor. Fiz.), 18, p. 3 (1948)
- K-2 Kinsman, Blair, Wind Waves, Prentice-Hall, Inc., Englewood Cliffs, N. J. (1965)
- K-3 Koh, J. C. Y., "Analysis of Film Boiling on Vertical Surfaces", Trans. ASME, J. Heat Transfer, 84, 55 (1962)
- L-1 Lamb, H., Hydrodynamics, 6th edition, Dover Publications, N. Y. (1945)
- L-2 Laverty, W. F., and W. M. Rohsenow, "Film Boiling of Saturated Liquid Flowing Upward Through a Heated Tube: High Vapor Quality Range", Report No. 9857-32, M.I.T. Dept. of Mech. Eng. (1964)
- L-3 Lavin, J. G., and E. H. Young, "Heat Transfer to Evaporating Refrigerants in Two-Phase Flow", Preprint 21e, 52nd National Meeting, A.I.Ch.E. (1964)
- L-4 Levich, V. G., Physicochemical Hydrodynamics, Chap. 12, Prentice-Hall, Inc., Englewood Cliffs, N. J., (1962)
- L-5 Lewis, J. P., J. H. Goodykoontz, and J. F. Kling, "Boiling Heat Transfer to Liquid Hydrogen and Nitrogen in Forced Flow", NASA TN D-1314 (1962)
- L-6 Lilleleht, L. U., PhD Dissertation, U. of Illinois (1961)
- L-7 Lilleleht, L. U., and T. J. Hanratty, "Measurements of Interfacial Structure for Co-current Air-Water Flow", J. Fluid Mechanics, 11, 65 (1961)
- M-1 Massot, C., F. Irani, and E. N. Lightfoot, "Modified Description of Wave Motion in a Falling Film", A.I.Ch.E. Jour. 12, 445 (1966)
- M-2 Meyer, R. F., "A Heat-Flux-Meter for use with Thin Film Surface Thermometers", Aeronautical Report LR-279, National Research Council of Canada, Ottawa (1960)

- M-3 Miles, J. W., "On the Generation of Surface Waves by Shear Flows", J. Fluid Mechanics, 3, 185 (1957)
- M-4 Moore, F. D., and R. B. Mesler "The Measurement of Rapid Surface Temperature Fluctuations During Nucleate Boiling of Water", A.I.Ch.E. Jour., 7, 620 (1961)
- M-5 Moore, R. K., Wave and Diffusion Analogies, McGraw-Hill Book Co., N. Y. (1964)
- M-6 Morgan, C. D., "A Study of Film Boiling from Vertical Surfaces", PhD Dissertation, Lehigh Univ., (1965)
- M-7 Myers, J. A., "Condensation Inside a Horizontal Pipe Studied with a Heat Meter", PhD Dissertation, U. of Kansas (1964)
- N-1 Nishikawa, K., and T. Ito, "Two-Phase Boundary-Layer Treatment of Free-Convection Film Boiling", Int. J. Heat and Mass Transfer, 9, 103 (1966)
- P-1 Padilha, Jose, "Similarity Solutions of the Boundary Layer Equations for Laminar Film-Boiling and Turbulent Single Phase Flow", Master's Thesis, U. of Houston (1964)
- P-2 Polomik, E. E., S. Levy, and S. G. Sawochka, "Film Boiling of Steam-Water Mixtures in Annular Flow at 800, 1100 and 1400 psi", Trans. ASME, J. Heat Transfer, 81, (1964)
- R-1 Rankin, S., "Heat Transfer to Boiling Liquids under Conditions of High Temperature Difference and Forced Convection", Tech. Report No. UD-FB-13, U. of Delaware, Dept. of Chem. Eng.
- R-2 Roder, H. M., and R. D. Goodwin, "Provisional Thermodynamic Functions for Para-Hydrogen", National Bureau of Standards Technical Note 130 (1961)
- S-1 Sachs, P., and R. A. K. Long, "A Correlation for Heat Transfer in Stratified Two-Phase Flow with Vaporization", Int. J. Heat and Mass Transfer, 2, 222 (1961)
- S-2 Sakiadis, B. C., "Boundary - Layer Behavior on Continuous Solid Surfaces", A.I.Ch.E. Jour., 7, Part 1, p.26; Part 2, p.221 (1961)
- S-3 Schiesser, W. C., "Statistical Uncertainty of Power Spectral Estimates", Bulletin 711-C-1, Westen-Boonshaft and Fuchs, Hatboro, Pa.

- S-4 Sellers, J. P., "Thermocouple Probes for Evaluating Local Heat Transfer Coefficients in Rocket Motors", Temperature; Its Measurement and Control in Science and Industry, 3, 673, Reinhold Publishing Corp., N. Y. (1962)
- S-5 Shand, E. B., Glass Engineering Handbook, 2nd edition, McGraw-Hill Book Co., New York (1958)
- S-6 Simoneaux, R. J., and F. F. Simon, "A Study of Velocity and Buoyancy Effects on Boiling Nitrogen", NASA Motion Picture C-245, Lewis Research Center.
- S-7 Sparrow, E. M., E. R. G. Eckert, and W. J. Minkowycz, "Heat Transfer and Skin Friction for Turbulent Boundary-Layer Flow Longitudinal to a Circular Cylinder.", J. App. Mech., Trans. ASME, 85, 37 (1963)
- S-8 Sparrow, E. M., "The Effect of Radiation on Film-Boiling Heat Transfer", Int. J. Heat and Mass Transfer, 7, 229, (1964)
- S-9 Stock, B. J., "Observations on Transition Boiling Heat Transfer Phenomena", Report ANL-6175, Argonne Nat'l. Lab. (1960)
- S-10 Swenson, H. S., J. R. Carver, and G. Szoeko, "The Effects of Nucleate Boiling Versus Film Boiling in Power Boiler Tubes", ASME Paper No. 61-WA-201 (1962).
- T-1 Telles, A., Private Communication (1965)
- T-2 Telles, A., "Liquid Film Characteristics in Vertical Two-Phase Flow", PhD Dissertation, U. of Houston (1968)
- U-1 Ursell, F., "Wave Generation by Wind", Surveys in Mechanics, Edited by G. K. Batchelor and R. M. Davis, Cambridge University Press, Cambridge (1956)
- W-1 Westwater, J. W., "Boiling of Liquids", Advances in Chemical Engineering, I, Chap. 1, Edited by J. Drew and J. Hoopes, Academic Press Inc., New York (1956)
- W-2 ibid., Vol. 2, Chap. 1
- W-3 Westwater, J. W., and Y. Y. Hsu, Motion Picture, "Film Boiling from Vertical Tubes", U. of Illinois (1957)
- W-4 Wicks, M. III, "Liquid Film Structure and Drop Size Distribution in Two Phase Flow", PhD Dissertation, U. of Houston (1967)

- W-5 Worley, F. L., "A Study of Roughness Effects in Turbulent Flow",
 PhD Dissertation, U. of Houston (1965)
- Y-1 York, J. L., H. E. Stubbs and M. R. Tek, "The Mechanism of Dis-
 integration of Liquid Sheets", Trans. ASME, 75, 1279 (1953)
- Z-1 Zuber, Novak, "Hydrodynamic Aspects of Boiling Heat Transfer",
 PhD dissertation, U. of California, Los Angeles (1959)

APPENDIX HNOMENCLATURE

a	constant in ϵ_{GS}
A	thickness of vapor film on wall side of plane of zero shear stress
A^+	dimensionless value of A: $A (\tau_w/\rho)^{1/2}/\nu$
b	constant in ϵ_{GS}
B	thickness of vapor film on interface side of plane of zero shear stress
B^+	dimensionless value of B: $B (\tau_i/\rho)^{1/2}/\nu$
c_p	specific heat
CC	dimensionless heat transfer parameter, defined by equation 3-56
CC_a, CC_b	CC defined for symmetrical flows by equations 3-57 and 3-58
f	frequency; perimeter of heater surface
g	gravitational constant
ΔH_v	latent heat of vaporization
h	heat transfer coefficient
\bar{h}	time average heat transfer coefficient
H	fluctuating component of heat transfer coefficient
k	wave number; constant in ϵ_{GS}
k	thermal conductivity
K	driving force on vapor film, defined by equation 3-3
l'	roughness mixing length
L	wall height

n	angular frequency
Nu	Nusselt number
Nua, Nub	Nu defined for symmetrical flows by equations 3-52 and 3-53
\overline{Nu}	Nusselt number based on total surface area
p	vapor film thickness
P	pressure
Pr	Prandtl number
q	heat flux
q_r	heat flux by radiation
Q	total local heat flux; volumetric flow rate
r	electrical resistance of heat meter resistors
R	electrical resistance of resistors in preliminary heat meter design
Re	Reynolds number
Rea, Reb	Reynolds number defined for symmetrical flows by equations 3-41 and 3-42
t	time
T	temperature; surface tension coefficient
\overline{T}	average vapor film temperature
T^+	dimensionless temperature: $(T - T_0) \rho c_p (\gamma_0 / \rho)^{1/2} / q_0$
u	x-direction component of velocity
u^+	dimensionless velocity: $u / (\gamma_0 / \rho)^{1/2}$
v	voltage; y - direction component of velocity
v_{mb}	maximum B-side velocity when interfacial velocity is zero
V	gas velocity in Kelvin - Helmholtz stability analysis
V_c	critical gas velocity

W	mass flow rate
x	position coordinate
y	position coordinate
y^*	dimensionless length: $y(\tau_0/\rho)^{1/2}/\nu$

Greek letters

α	thermal diffusivity
γ	ratio of eddy conductivity to eddy viscosity
ϵ	eddy viscosity
ϵ_{GS}	eddy viscosity distribution proposed by Gill and Scher
ϵ'	wall eddy viscosity
ϵ_H	eddy conductivity
ϵ_w	emissivity of heater wall
η	wave shape function
η_0	initial displacement of wave; height of a roughness element
η_f	relation between frictional pressure drop and liquid density defined by equation 3-81
λ	wave length
λ'	effective latent heat of vaporization
μ	viscosity
ν	kinematic viscosity
ρ	density
ρ_s	density of saturated vapor
$\Delta\rho$	effective buoyancy factor, defined in equation 4-4

σ	Stephan - Boltzmann constant
τ	shear stress
ϕ	term in ϵ_{GS} , defined by equation 3-81
ϕ_r	heat flux factor to account for radiation, defined by equation 3-87
Φ	velocity potential
Φ_{ii}	spectral density function
Φ_{ij}	cross-spectral density function
Ψ_{99}	mean square average of fluctuations in surface heat flux
ω	angular frequency

Subscripts

a	absolute temperature
b	B-side
i	interface
L	liquid
m	term evaluated at point of zero shear stress
Ni	nickel
o	boundary
rms	root-mean-square average
s	values determined by the quasi-steady state theory
sc	subcooled
x	x-direction component
y	y-direction component
w	wall